INTERNATIONAL DOCTORAL
SCHOOL OF THE USC

Marwan Yassir Kamel
Ajoor

PhD Thesis

STUDY OF COSMIC RAY DATA WITH THE TRISTAN AND TRAGALDABAS DETECTION SYSTEMS

Santiago de Compostela, 2022

Doctoral Programme in Nuclear and Particles Physics

USC
UNIVERSIDADE
DE SANTIAGO
DE COMPOSTELA

TESIS DE DOCTORADO

STUDY OF COSMIC RAY DATA WITH THE TRISTAN AND TRAGALDABAS DETECTION SYSTEMS

Marwan Yassir Kamel Ajoor

ESCUELA DE DOCTORADO INTERNACIONAL DE LA UNIVERSIDAD DE SANTIAGO DE COMPOSTELA

PROGRAMA DE DOCTORADO EN FÍSICA NUCLEAR Y DE PARTÍCULAS

SANTIAGO DE COMPOSTELA

2022

USC
UNIVERSIDADE
DE SANTIAGO
DE COMPOSTELA

DECLARACIÓN DEL AUTOR/A DE LA TESIS

D./Dña. **Marwan Yassir Kamel Ajoor**

Título de la tesis: **Study of Cosmic Ray data with the TRISTAN and TRAGALDABAS detection systems**

Presento mi tesis, siguiendo el procedimiento adecuado al Reglamento y declaro que:

1) La tesis abarca los resultados de la elaboración de mi trabajo.
2) De ser el caso, en la tesis se hace referencia a las colaboraciones que tuvo este trabajo.
3) Confirmo que la tesis no incurre en ningún tipo de plagio de otros autores ni de trabajos presentados por mí para la obtención de otros títulos.
4) La tesis es la versión definitiva presentada para su defensa y coincide la versión impresa con la presentada en formato electrónico.

Y me comprometo a presentar el Compromiso Documental de Supervisión en el caso que el original no esté depositado en la Escuela.

En **Santiago de Compostela**, **02 de febrero de 2022**.

Firma electrónica

USC
UNIVERSIDADE
DE SANTIAGO
DE COMPOSTELA

AUTORIZACIÓN DEL DIRECTOR DE LA TESIS

D./Dña. JUAN PABLO GARZÓN HEYDT

En condición de: Director

Título de la tesis: **Study of Cosmic Ray data with the TRISTAN and TRAGALDABAS detection systems**

INFORMA:

Que la presente tesis, se corresponde con el trabajo realizado por D. **Marwan Yassir Kamel Ajoor**, bajo mi dirección, y autorizo su presentación, considerando que reúne os requisitos exigidos en el Reglamento de Estudios de Doctorado de la USC, y que como director de esta no incurre en las causas de abstención establecidas en la Ley 40/2015.

En Santiago de Compostela, 28/03/2022

Firma electrónica

USC
UNIVERSIDADE
DE SANTIAGO
DE COMPOSTELA

AUTORIZACIÓN DEL DIRECTOR DE LA TESIS

D./Dña. PABLO CABANELAS EIRAS

En condición de: Director

Título de la tesis: **Study of Cosmic Ray data with the TRISTAN and TRAGALDABAS detection systems**

INFORMA:

Que la presente tesis, se corresponde con el trabajo realizado por D. **Marwan Yassir Kamel Ajoor**, bajo mi dirección, y autorizo su presentación, considerando que reúne os requisitos exigidos en el Reglamento de Estudios de Doctorado de la USC, y que como director de esta no incurre en las causas de abstención establecidas en la Ley 40/2015.

En Santiago de Compostela, 28/03/2022

Firma electrónica

USC
UNIVERSIDADE
DE SANTIAGO
DE COMPOSTELA

AUTORIZACIÓN DEL TUTOR DE LA TESIS

D./Dña. HÉCTOR ÁLVAREZ POL

En condición de: Tutor

Título de la tesis: **Study of Cosmic Ray data with the TRISTAN and TRAGALDABAS detection systems**

INFORMA:

Que la presente tesis, se corresponde con el trabajo realizado por D. **Marwan Yassir Kamel Ajoor**, bajo mi tutorización, y autorizo su presentación, considerando que reúne os requisitos exigidos en el Reglamento de Estudios de Doctorado de la USC, y que como tutor de esta no incurre en las causas de abstención establecidas en la Ley 40/2015.

En Santiago de Compostela, 28/03/2022

Firma electrónica

USC
UNIVERSIDADE
DE SANTIAGO
DE COMPOSTELA

Dedication

I am dedicating this thesis to the soul of my parents, whose loving memories will remain in my mind forever. To my second half and my companion in life, my darling wife, **Nour**. To the apple of my eyes and the spirit of my life, my lovely daughter, **Zaina**. Finally, to my brothers and sisters: **Kamel**, **Kamal**, **Mohammad**, **Suha**, **Maha**, **Rana** and **Hana'a**.

USC
UNIVERSIDADE DE SANTIAGO DE COMPOSTELA

USC
UNIVERSIDADE
DE SANTIAGO
DE COMPOSTELA

Acknowledgement

All praise and thanks are due to the Almighty Allah, who always guides me to the right path and has assisted me to accomplish this journey of my life.

First and foremost, I cannot express enough thanks and my sincere gratitude and appreciation to my Ph.D. supervisors, Prof. Juan A. Garzón Heydt and Prof. Pablo Cabanelas Eiras, for their unwavering support of my Ph.D. study and research, patience, enthusiasm, encouragement, motivation, dedication and immense knowledge. Throughout the research and writing of this thesis, their advice was invaluable. I could not have imagined having better supervisors and mentors for my Ph.D. study.

Besides my Directors, I present my sincere gratitude to the tutor of this Doctoral Dissertation, Prof. Hector Alvarez Pol, for his tremendous effort in the administrative aspects of my Ph.D. study he has made to accomplish this work. He was always available for help and advice. I also offer my sincere appreciation for the learning opportunities provided by the examination committee members for their encouragement and insightful comments.

My sincere thanks also go to the Galician Institute of High Energy Physics (Instituto Galego de Física de Altas Enerxías, IGFAE) and my supervisor Prof. Juan Pablo Garzón Heydt for offering me the summer internship opportunities at Coimbra University, Portugal, my experience there was very fruitful and interesting. And also, I would like to express my heartfelt thanks to Prof. Alberto Blanco for his good hospitality at Coimbra University and for his time in invaluable suggestions and useful discussions. As a result, I gained more skills and knowledge. And special thanks to all members of the LIP group.

USC
UNIVERSIDADE DE SANTIAGO DE COMPOSTELA

Heartfelt gratitude to Prof. Teresa Kurtukian Nieto for her continued support, encouragement and efforts in some aspects of this thesis.

Special thanks to Prof. Diego Gonzalez Diaz for his efforts, especially when I arrived at Santiago de Compostela for the first time and from the beginning of my Ph.D. march.

I would also like to express my thanks and appreciation to Marcos Antonio Seco for his continued encouragement, support and efforts to answer the questions and doubts about programming and other technical computer-related topics.

My completion of this thesis could not have been accomplished without the encouragement and support of my group-mates. In particular, I would like to mention Prof. Georgy Kornakov, Damian Garcia, Yanis Fontenla, Juan Xuna, Irma Riadigos, Miguel Cruces and all members of the LABCAF group and the whole community of Santiago de Compostela Unversity.

Profound, heartfelt credit also goes to my beloved family back home. My family was the motivational source during my whole research journey. No words can express my gratified feelings for my darling wife, my companion in life and my soulmate, Mrs. Nour and the apple of my eyes, my lovely daughter Zaina. Through both of them, I see everything gorgeous and beautiful in life. Their passion, generous giving, love and sentiment have given me the will and power throughout my research. Moreover, I take this opportunity to express my profound and warmest thanks to my father-in-law Mr. Hisham awadallah and my mother-in-law Mrs. Wejdan awadallah for their unconditional encouragement and massive support in all my endeavors.

I also sincerely thank my brothers, Kamel, Kamal, Mohammad and my sisters, Suha, Maha, Rana and Hana'a, for encouraging and supporting me all the time and for being my friends and soulmates forever. I also will not forget to thank my brother-in-law, Mr. Mahmmoud Al sarayreh, for always supporting and encouraging me.

USC
UNIVERSIDADE DE SANTIAGO DE COMPOSTELA

My acknowledgment would be incomplete without thanking families that provided all the support, encouragement and everything they can offer to all Jordanian students in Santiago de Compostela, especially Dr. Sami Ashour's family and Dr. Khalid Abu amira's family. They constantly motivate us to keep proceeding on the way to success.

Last but not least, I would like to thank all the dear friends who have had a significant impact and played a vital role in my study. Mainly I offer my best regards and blessings to my close friends in Jordan and as well in Spain for their intense stimulus, valuable pieces of advice and reassuring words.

Finally, I would like to confirm that the journey of accomplishing the doctoral thesis was a fabulous experience in Spain. Particularly in Santiago de Compostela city, whose residents were very kind and friendly and welcomed us with love and respect.

USC
UNIVERSIDADE DE SANTIAGO DE COMPOSTELA

USC
UNIVERSIDADE
DE SANTIAGO
DE COMPOSTELA

TABLE OF CONTENTS

List of Figures **XXI**

List of Tables **XXIII**

Introducción **XXXV**

Introduction **XLIII**

Objectives and Methodology XLIX

1 Cosmic rays **55**

1.1 Historical glance about the discovery of the cosmic rays. 55
1.2 Some general characteristics of cosmic rays 57
1.2.1 Energy spectrum 57
1.2.2 Composition and abundances 58
1.3 Sources of cosmic rays 63
1.3.1 Extragalactic and Solar cosmic rays 64
1.3.2 Cosmic rays in the atmosphere 65
1.3.3 Terrestrial cosmic rays (Cosmic rays at Earth surface) 67

2 Resistive Plate Chambers detectors **73**

2.1 General introduction 73
2.2 Parallel plate chamber detectors 73
2.3 Operation modes 77
2.3.1 Streamer mode 77
2.3.2 Avalanche mode 77
2.4 Timing RPC (tRPC) 78
2.5 The TRASGO project 79
2.5.1 The TRAGALDABAS detector 81
2.5.2 The TRISTAN detector 84

USC
UNIVERSIDADE DE SANTIAGO DE COMPOSTELA

3 Tracking with Timing (TimTrack) algorithm 89

3.1 Introduction and motivation 89
3.2 Description of the method..... 91
3.2.1 Non-linear TimTrack 98
3.2.2 Non-linear TimTrack with constraints 101
3.3 Models example and some applications..... 106
3.3.1 Linear model 106
3.3.2 Non-linear model 108
3.3.3 Super-saetas..... 110
3.3.4 TimTrack inside a pad with drift velocity..... 116
3.4 The models with numerical examples..... 121
3.4.1 Example of a linear model for TRAGALDABAS detector 122
3.4.2 Example of a linear model for TRISTAN detector..... 127

4 Analysis of simulated and real data with the TRAGALDABAS detector 131

4.1 Introduction 131
4.2 Software frameworks for simulation 134
4.2.1 Structure of EnsarRoot 137
4.2.2 Cosmic ray shower generator (CRY) 139
4.3 TRAGALDABAS simulations 141
4.3.1 TRAGALDABAS simulation geometry 142
4.3.1.1 Data levels 142
4.3.1.2 Generators of the particles..... 144
4.3.1.3 Control the simulation parameters..... 145
4.4 Particle Identification (PID) with TRAGALDABAS..... 148
4.4.1 Definition of physical observables 149
4.4.2 Description of the particle identification method..... 151
4.4.3 Simulation data and real data 151
4.4.4 Configuration of three active planes without a lead layer 152
4.4.5 Configuration of three active planes with a lead layer156
4.4.6 Angular distribution 161

USC
UNIVERSIDADE DE SANTIAGO DE COMPOSTELA

5 Preliminary analysis of the TRISTAN detector 165

5.1 Introduction 166
5.2 Atmospheric properties 167
5.2.1 Barometric effect 167
5.2.2 Temperature Effect 171
5.3 Geometric acceptance 175

6 Calibration and performance analysis of the STRATOS Cosmic Ray detector 179

6.1 Introduction 179
6.2 Position calibration 184
6.2.1 Position calibration in coordinates and Width to Charge Calibration 186
6.2.2 Position calibration in coordinates 190
6.3 Efficiency and position resolution 193
6.3.1 Position resolution 193
6.3.2 Efficiency 195
6.4 Time resolution 198

7 Analysis of the performance of Trasgo detectors for estimating the energy of primary cosmic rays 203

7.1 Introduction 203
7.2 Events generation method 204
7.3 The clusters 216
7.4 Analysis of the clusters 218
7.5 Results of the clusters 221
7.5.1 Results of the clusters at different energy ranges 221
7.5.2 Results of the clusters at different angle ranges 228
7.6 Future perspective for Trasgo detectors 252

8 Analysis of the cosmic ray background in the Faculty of Physics building at the USC using a COSMIX detector 255

8.1 Introduction 255

USC
UNIVERSIDADE DE SANTIAGO DE COMPOSTELA

8.2 Structure of the COSMIX detector 255
8.3 Radiation length 257
8.4 Electromagnetic showers 258
8.5 Measurements and taking data 261
8.6 Data analysis and results 264
8.7 Estimation of electron energy distribution in physics faculty at USC 281
8.8 Discussion and outlook 295

Conclusions **297**

Resumo da tese en Galego **303**

Resumen da tese en Español **317**

References **335**

Appendix The acceptance in particle physicis detectors **349**

1 Introduction 349
2 Geometrical acceptance and mean acceptance 349
3 Dead time corrections 355

USC
UNIVERSIDADE DE SANTIAGO DE COMPOSTELA

LIST OF FIGURES

1.1: Differential energy spectrum $F(E)$ as a function of the energy per nucleon as has been measured by different spectrometers and observatories.....57

1.2: The relative abundance of Galactic cosmic rays compared to those of the Solar System.....60

1.3: Cosmic ray flux of individual nuclei per nucleus as a function of kinetic energy.....63

1.4: quasars: The brightest objects in the Universe.....66

1.5: Showers of cosmic ray reactions with particles of the atmosphere. taken from www.antarticglaciers.com 68

1.6: Cosmic ray energy spectrum, and the most common detection methods.....69

1.7: Vertical flux of the cosmic ray in the atmosphere with energy greater than estimated from Equation's nucleon flux (1.2). The points show measurements of negative muons with muons energy greater than [27–32]. ... 71

2.1: Shows a schematic of an RPC detector. In this case, there are two gas gaps. The gas ionization causes electrical avalanches, which emit a signal sent to the read-out electronics.....76

2.2: A Trasgo with several RPC detector planes arranged one on top of the other inside the main box (a), many RPC detectors placed to cover more extensive surfaces (b), and one on top of the other as a column to improve resolutions and efficiency (c). The is taken from [61].....80

2.3: The TRAGALDABAS detector is depicted schematically. It is made up of four RPC planes that are separated into rectangular detection pads.....82

2.4: A single plane's FEE electronics layout. Four MBs receive the amplified and digitized signal from the DBs, read out by a TRB, and sent via Ethernet to the acquisition computer. 83

2.5: Left: the path of different particles (electrons, muons, gammas) across the active size of the detector; right: a layer of lead is placed under the second plane.....85

2.6: The internal layout of the RPC. 86

2.7: The TRISTAN detector in the Sarmiento de Gamboa oceanographic vessel...88

USC
UNIVERSIDADE DE SANTIAGO DE COMPOSTELA

3.1: A saeta in a generic strip detector is shown geometrically. A saeta (blue line) represents several kinematic characteristics related to particle propagation through the various components of our experimental set-up. [74] provided the illustration. 92

3.2: Scheme of the modeling of the matrices required in the TimTrack algorithm that applied to the different number of detectors, each of them following a specific model for their measurements. 98

3.3: Schematic illustration of the TimTrack method's solution search for a non-linear model. The first answer, , is proposed. At each step, the original vector is adjusted until a converged vector is obtained. A global minimum of the functional is attained for those parameter values. 99

3.4: Searching for a solution to a non-linear model with parameter restrictions. The problem is solved iteratively in the same way that a conventional non-linear problem is solved. Still, the final values of the parameters must satisfy the constraints of a constraint function (blue line).....105

3.5: A particle detected in two pads is shown schematically. Rectangular areas divide the detection areas of the planes. The signal readout is in the pad's center () and must go from the hit to the pad's center. As a result, the signal's drift velocity inside the pad is considered in the data model.....117

3.6: TRAGALDABAS experimental setup for numerical demonstration of TimTrack method. The distances between the RPC's are in mm. The origin of , is located at the center of each RPC plane. 122

3.7: TRISTAN experimental setup for numerical illustration of TimTrack method. 127

4.1: An example of a TTree generated by EnsarRoot following a simulation. The Monte Carlo simulation's variables are organized into several data levels. 138

4.2: CRY input parameters. 141

4.3: shows how the EnsarRoot framework represents a simulated cosmic ray event over the detector system. A primary electron with an energy of around 500 MeV interacts with the floor's concrete, and secondary particles produce mainly photons with low energy interacting with three active planes. 147

USC
UNIVERSIDADE DE SANTIAGO DE COMPOSTELA

4.4: Representation of a simulated cosmic ray event over the entire detector system inside the building within the EnsarRoot framework. A primary muon with an energy equal to interacts with the building materials and with a lead layer of thick installed at under the third plane...147

4.5: illustrates a simulated event over the three planes in the TRAGALDABAS detector with a lead layer within the EnsarRoot framework. A electron crosses the detector interacting with the detector, and a shower is produced and arrives at the third plane of the detector. The geometry includes three active RPC planes and a thickness of lead layer after the third plane. 148

4.6: the scheme of the TRAGALDABAS detector illustrates an example of how to calculate the total multiplicity and weighted range 150

4.7: Distributions of the three physical observables for simulated data for three operated planes of TRAGALDABAS with a geometry without a lead layer. 153

4.8: Flowchart of the particle identifications algorithm for the TRAGALDABAS detector when planes are operated without a lead layer. 154

4.9: Distributions of the three dedicated physical observables for real data for three operated planes of TRAGALDABAS with a geometry without a lead layer. 155

4.10: Distributions of the three physical observables for simulated data for three operated planes of TRAGALDABAS with a lead layer geometry. 157

4.11: Flowchart of the particle identification algorithm for the TRAGALDABAS detector with a lead layer when three planes are operated.....158

4.12: Distributions of the three dedicated physical observables , , and for real data for three operated planes of TRAGALDABAS detector with a lead layer geometry.....159

4.13: 2-Dimensional histograms for the probability of the detected particles being a particular particle for the configuration of the TRAGALDABAS without lead layer (up) and with lead layer (down) versus the identity number of the particles, where the identity number of the electrons is and for the muons. 160

4.14: The histogram of the angular distribution for the TRAGALDABAS real data without using a lead layer and the geometric acceptance calculated by the simulation when the trigger between the first and the third plane. 162

USC
UNIVERSIDADE DE SANTIAGO DE COMPOSTELA

4.15: Normalized angular distribution for the incident polar angles corrected by the acceptance in the TRAGALDABAS detector. The red line is the best fit for the distribution. We observe an angular variation as of the polar angle.....162

5.1: Represent the path of the TRISTAN detector (one red triangle per day) during the first trip of the detector from Vigo, Spain, to Punta Arenas, Chile. The is taken from [5]. 165

5.2: The anticorrelation between the relative cosmic ray rate variation and the pressure deviation observed in the first trip of the TRISTAN detector from Vigo, Spain to Punta Arenas, Chile. 168

5.3: shows the linear fit method used to obtain the barometric coefficient for every days of data for the rate of the cosmic rays and the pressure deviation measured by the TRISTAN detector.....169

5.4: Illustrates the cosmic ray rates corrected by efficiency (a), the atmospheric pressure (b), (c) and (d) uncorrected and corrected rates of the cosmic rays with pressure, respectively, in the period from November 15th to December 23rd, 2018. 170

5.5: Time evolution of the temperature recorded by the TRISTAN detector. An air conditioner failure occurred when the detector was near the Equator, where the temperature increased about through hours. 172

5.6: Example of the linear fit method used to obtain the temperature coefficient for the anticorrelation between the relative variation of the cosmic ray rates and the temperature deviation measured in the first trip of the TRISTAN detector. 173

5.7: Represents the linear fit method used to get the barometric coefficient for every 3 days of data for the rate of the cosmic rays and the temperature deviation measured by the TRISTAN detector. 174

5.8: The cosmic ray relative variations uncorrected by temperature (left) and the cosmic ray relative variations corrected by both pressure and temperature (right) from November 15th to December 23rd, 2018.....175

5.9: The pads in the TRISTAN detector are separated by grounded insulator rings 6 mm wide to eliminate crosstalk between neighboring pads. 176

5.10: Shows an example for the map of the generated (hit) events in the first plane (left) in the TRISTAN detector and the map of the detected events in the third plane (right). We can see the effect of the electrical insulator between the pads.....177

USC
UNIVERSIDADE DE SANTIAGO DE COMPOSTELA

5.11: Geometric acceptance at different distances for the TRISTAN detector, when the trigger between the first and second plane, (left) and when the trigger between the first and the third plane, (right). 177

5.12: The acceptance as a function of the incident angle for the TRISTAN detector, when the trigger between the first and second plane, (left) and when the trigger between the first and the third plane, (right). 178

6.1: View of the RPC design of STRATOS detector. Each plane of the four planes is divided into strips, with an active area of , in a transversal dimension, and in a longitudinal dimension. 180

6.2: Schematic diagram of the STRATOS detector (left) and a photograph of the real system (right) 181

6.3: The internal configuration of the RPC in STRATOS detector. 182

6.4: RPC plane of the STRATOS detector, each one of the four RPCs is composed of 4 MBs connected to 1 TRB at the center, and 8 DBs connected to each MB, As illustrated in the figure 183

6.5: Histogram of the charge for one channel chosen arbitrary for one RPC of the detector. Where the black dashed line refers to the most frequent charge (q_binmax) and the green dashed line represents the fit for the charge bins to the left of q_binmax (green dots) to calculate the pedestal (the red dashed line). 187

6.6: Histograms illustrate the real position distributions of coordinates for all planes in 188

6.7: Charge distributions for all the strips in each RPC of the detector after subtracting the pedestal. 188

6.8: Hit multiplicity distributions in all the planes of STRATOS detector. 189

6.9: The position offset was described using the distribution. Take note of the offset in the distribution for each strip. 191

6.10: distribution for the time difference after correction. 191

6.11: 2-dimensional histograms for the position versus the position before correction (left) and after correction (right) in the time difference for all the detector planes. 192

6.12: Residual distributions in X and Y for the four planes in the STRATOS detector. They are fitted to a double Gaussian method to obtain the spatial resolutions, given by the sigma of the fit. 194

6.13: Hit events distribution for entire detector's planes. 196

USC
UNIVERSIDADE DE SANTIAGO DE COMPOSTELA

6.14: Detected events distribution for all the detector planes.....196

6.15: The efficiency for each individual plane for STRATOS detector.....197

6.16: The distribution of the half-time difference for two overlapping strips before correction. 198

6.17: Slewing correction in RPC strips. The red line shows the phenomenological fit applied to the data. 200

6.18: distribution for two overlapping strips after correction. 200

7.1: Main sources of muons and electrons of cosmic origin arriving to the ground level. 208

7.2: Effects that modify the flux of cosmic rays measured on the Earth's surface. The curved lines indicate the distortion in the path of primary cosmic rays caused by magnetic fields. Red straight lines represent the trajectory of muons of the EAS. Gamma-rays are represented by dashed blue lines, while solid blue lines represent electrons and positrons. The path of a neutron is depicted in purple. 209

7.3: Example of the cluster finding strategy. Starting from point P1, the cluster composed of particles P1, P2, and P3 is found. P4 is not accepted because it is out of the circle centered in CG2 with radius sigrmx.....217

7.4: The differential intensity of particles (Flux) of primary cosmic rays as a function of the energy. 219

7.5: The distribution of detector counting rate at the given energy of a specific primary nucleus. 221

7.6: The average multiplicity function for the electrons at different energy ranges per shower energy as a function of the primary energy in logarithmic scale for H, He, C, and Fe nuclei. 222

7.7: The response function of the electrons produced in the atmosphere at different energy ranges for the primary nuclei Hydrogen, Helium, Carbon, and Iron, respectively. The solid lines in the do not represent any fit for the data. It has been drawn to guide the eyes. 223

7.8: Average number of clusters for the primary four nuclei (H, He, C, and Fe) corresponding to the primary energy of the produced clusters for the electrons (top), muons (middle), and mixed (bottom).....224

7.9: A comparison between the number of clusters for electrons, muons, and mixed clusters as a function of the primary energy for the proton.....225

USC
UNIVERSIDADE DE SANTIAGO DE COMPOSTELA

7.10: represents the number of electromagnetic (EM) clusters per shower for the primary proton interacting with the atmosphere with different primary energies as a function of the first interaction altitude. 226

7.11: The ratio between Muonic and electromagnetic clusters and between Mixed and electromagnetic clusters as a function of the energy of a proton as a primary cosmic ray. 227

7.12: The ratio of the numbers between electromagnetic and mixed clusters as a function of the primary energy. 228

7.13: The response function of the electrons produced for the Proton as a primary cosmic ray with different energy ranges as a function of the primary energy in logarithmic scale at various incident zenith angles in degrees. The energy ranges of the electrons are given in 229

7.14: The response function of the electrons produced for the Helium nucleus as a primary cosmic ray with different energy ranges as a function of the primary energy in logarithmic scale at various incident zenith angles in degrees. The energy ranges of the electrons are given in 230

7.15: The response function of the electrons produced for the Carbon nucleus as a primary cosmic ray with different energy ranges versus the primary energy in logarithmic scale at various incident zenith angles in degrees. The energy ranges of the electrons are given in 231

7.16: The response function of the electrons produced for the Iron nucleus as a primary cosmic ray with different energy ranges versus the primary energy in logarithmic scale at various incident zenith angles in degrees. The energy ranges of the electrons are given in 232

7.17: Represents the response function of the produced electrons, muons, neutrons, and protons for the Proton as primary cosmic rays versus the primary energy at different incidence zenith angles. 233

7.18: Shows the response function of the produced electrons, muons, neutrons, and protons for the Helium nucleus as primary cosmic rays versus the primary energy at different incidence zenith angles.....234

7.19: Illustrates the response function of the produced electrons, muons, neutrons, and protons for the Carbon nucleus as primary cosmic rays as a function of the primary energy at different incidence zenith angles. 235

7.20: Shows the response function of the produced electrons, muons, neutrons, and protons for the Iron nucleus as primary cosmic rays as a function of the primary energy at different incidence zenith angles.....236

USC
UNIVERSIDADE DE SANTIAGO DE COMPOSTELA

7.21: The response function of the electron clusters, muon clusters, and mixed clusters for the primary Proton versus the primary energy in logarithmic scale at different incidence zenith angles. 237

7.22: The response function of the electron clusters, muon clusters, and mixed clusters for the Helium nucleus as primary cosmic rays as a function of the primary energy in logarithmic scale at different incidence zenith angles. 238

7.23: Shows the response function of the electron clusters, muon clusters, and mixed clusters for the Carbon nucleus as primary cosmic rays as a function of the primary energy in logarithmic scale at different incidence zenith angles. 239

7.24: The response function of the electron clusters, muon clusters, and mixed clusters for the primary Iron nucleus as a function of the primary energy in logarithmic scale at different incidence zenith angles. 240

7.25: The primary energy at the maximum of the response function for different primary nuclei to produce electrons as a secondary particle at different arrival zenith angles with varying energy ranges. The energy ranges of the electrons are given in 241

7.26: Represents the primary energy at the maximum response function to produce electrons with varying energy ranges at different arrival zenith angles for Proton, Helium, Carbon, and Iron, respectively. The energy ranges of the electrons are given in. 242

7.27: The primary energy at the maximum response function for different primary nuclei (H, He, C, and Fe) to produce different secondary particles at various zenith angles. 243

7.28: The primary energy at the maximum response function for various primary nuclei (H, He, C, and Fe) at various arrival zenith angles to produce different clusters of particles. 244

7.29: Illustrates the primary energy at the maximum of the response function for different nuclei to produce different secondary particles with various arrival zenith angles. 245

7.30: Represents the primary energy at the maximum response function for various nuclei to produce different clusters of particles with different arrival zenith angles. 246

7.31: The threshold energy for various primary nuclei (H, He, C, and Fe) to produce electrons with different energy ranges at varying arrival zenith angles. The energy ranges of the electrons are given in 247

USC
UNIVERSIDADE DE SANTIAGO DE COMPOSTELA

7.32: shows threshold energy to produce electrons with varying energy ranges at different arrival zenith angles for Proton, Helium, Carbon, and Iron, respectively, where the energy ranges for the produced electrons are given in 248

7.33: Presents the threshold energy required to produce secondary particles for different primary nuclei (H, He, C, and Fe) at different arrival zenith angle ranges. 249

7.34: Illustrates the threshold energy required for producing different clusters of particles for various primary nuclei (H, He, C, and Fe) at different incident zenith angle ranges. 250

7.35: The threshold energy required for different nuclei to create secondary particles with various arrival zenith angles. 251

7.36: The threshold energy needed for various nuclei to produce clusters of particles with different arrival zenith angles. 252

7.37: Energy thresholds of different particles or bundles of particles can be measured with an area of about using Trasgo detector. 253

7.38: The area obtained by the superposition of the three response functions of the Trasgo detector provides the estimated energy of the primary cosmic rays. 254

8.1: COSMIX detector, where detector (bar) was placed over detector (bar). The dimension of detector is in length, in width, and in thickness. Detector has the same dimension, but it is longer. 256

8.2: The simplified electromagnetic shower model. The values of denote the successive radiation lengths. 259

8.3: An example of a theoretical prediction of the variation of the detected particle rates of the expected behavior for a single detector (left) and two detectors in coincidence (right) as a function of the ratio between the thickness of the lead and the radiation length 260

8.4: Main processes expected with cosmic rays after adding the lead layers gradually with the two configurations for studying the coincidence rate of the cosmic rays. The expected processes depicted in the vertical configuration could take place in the horizontal configuration. 262

8.5: An example of a Poisson distribution of the histogram for the coincidence counts per second detected by the COSMIX detector. The y-axis for the inserted plot is in the logarithmic scale. 265

USC
UNIVERSIDADE DE SANTIAGO DE COMPOSTELA

8.6: The distribution fit using the TimTrack algorithm (left) to find the coincidence rate for the COSMIX detector without using any absorbers. The best fit corresponded to the lowest uncertainty for the slope of the fit. The histogram of the time difference between the coincidence event and the next event (right). 266

8.7: The distribution fit for the rate of detector 1 with different thicknesses of a lead layer in the vertical position. 267

8.8: The distribution fit for the rate of detector 2 with different thicknesses of a lead layer in the vertical position. 268

8.9: The distribution fit of the coincidence rate for the COSMIX detector with different thicknesses of a lead layer in the vertical position. 269

8.10: The normalized rate of detector 1 obtained by the horizontal position versus the lead thickness at all the altitudes in the physics faculty. 270

8.11: The normalized rate of detector 2 versus the lead thickness at all the levels obtained by the horizontal position. 271

8.12: The normalized coincidence rate of the COSMIX detector where detector 2 placed over detector 1 versus the lead thickness obtained in the horizontal position at different floors of the physics faculty. 272

8.13: The normalized rate of detector 1 versus the lead thickness at all the levels obtained by the vertical position....273

8.14: The normalized rate of detector 2 obtained by the vertical position versus the lead thickness at all the altitudes in the physics faculty....274

8.15: The normalized coincidence rate of the COSMIX detector where detector 2 placed over detector one versus the lead thickness obtained in the vertical position at different floors of the physics faculty. 275

8.16: A summary of the results for all the gathered data in both positions at different levels using different thicknesses of the lead layers for the rate of detector 1, the rate of detector 2, and the coincidence rate of the COSMIX detector. 276

8.17: A comparison between the average coincidence rates for the COSMIX detector with both configurations for all the collected data. 279

8.18: A comparison between the normalized coincidence rates for the COSMIX detector with the horizontal and vertical configuration for all the collected data....280

8.19: Represents the attenuation of electrons in the lead using the rate of detector one and detector two as a function of the lead thickness. 285

USC
UNIVERSIDADE DE SANTIAGO DE COMPOSTELA

8.20: Shows the range of the electrons in several numbers of the lead plates used in our work as a function of the energy of the electrons.....286

8.21: Illustrates the attenuation of electrons in the lead layers as a function of the estimated energy thresholds. The solid line represents the linear regression fit of the data for different levels. 287

8.22: Shows the estimated TRAGALDABAS efficiency versus the energy of the electrons. The red dashed line represents the fit of the data given in Table 8.12. 293

10.1: Fotografía dos tres detectores de tipo TRASGO avaliados neste traballo. Arriba: ..... o detector TRAGALDABAS xunto cun esquema dos seus planos detectores. Centro:..... fotografía do sistema TRISTAN instalado na Antártida, tamén xunto co seu esquema de planos. Abaixo: ..... fotografía do detector STRATOS recentemente desenvolvido no LIP-Coimbra. 306

10.2: Visualización dun evento simulado de raios cósmicos incidindo sobre tres planos activos do detector TRAGALDABAS, situado na súa posición nominal dentro do edificio da Facultade de Física, cuxa estructura foi tamén simulada. 308

10.3: Separación entre electróns e muóns con TRAGALDABAS antes e despois de colocar a lámina de chumbo entre os dous últimos planos. Esta lámina aumenta significativamente o número de muóns identificados (electróns ID=11; muóns ID=13) e aumenta a probabilidade de ter acertado coa identificación.....309

10.4: Esquerda: distribución angular de raios cósmicos medida con TRAGALDABAS e curva de aceptancia calculada. Dereita: distribución angular final corrixida e axustada a unha curva 310

10.5: Arriba: representación do percorrido de TRISTAN na súa viaxe dende Vigo ata Punta Arenas. Cada triángulo representa un día de viaxe. Abaixo: variación relativa de raios cósmicos observada na viaxe. Pode verse claramente como a tasa é menor nas rexións da Terra próximas ao ecuador.....311

USC
UNIVERSIDADE DE SANTIAGO DE COMPOSTELA

10.1: Fotografía de los tres detectores tipo Trasgo evaluados en este trabajo. Arriba: el detector TRAGALDABAS instalado en la Facultad de Física de la Universidad de Santiago de Compostela, junto con un esquema de sus planos detectores. Centro: fotografía del detector TRISTAN instalado en la Antártida, junto a su esquema de planos detectores. Abajo: fotografía del sistema STRATOS recientemente desarrollado en el LIP – Coimbra. 321

10.2: Visualización de un evento simulado de rayos cósmicos incidiendo sobre tres planos activos del detector TRAGALDABAS, situado en su posición nominal dentro del edificio de la Facultad de Física, cuya estructura está también simulada.....324

10.3: Separación entre electrones y muones con TRAGALDABAS antes y después de colocar la lámina de plomo entre los últimos planos. Se observa como la lámina aumenta sustancialmente el número de muones identificados (electrones ID=11; muones ID=13) y se mejora sustancialmente la probabilidad de haber acertado. 325

10.4: Izquierda: Distribución angular de Rayos Cósmicos medida con TRAGALDABAS y curva de aceptancia calculada. Derecha: ..... distribución angular final corregida por aceptancia y ajustada a una curva . 326

10.5: Arriba: representación de la trayectoria seguida por TRISTAN en su primer viaje de ida desde Vigo (España) a Punta Arenas (Chile). Cada triángulo representa un día de viaje. Abajo: variación relativa de Rayos Cósmicos observados a lo largo de ese viaje. Se puede ver claramente como la tasa de Rayos Cósmicos es menor en las regiones de la Tierra próximas al ecuador. 328

USC
UNIVERSIDADE DE SANTIAGO DE COMPOSTELA

LIST OF TABLES

2.1: Components of RPC plane for TRAGALDABAS, as well as their width and radiation length. 84

6.1: Components of RPC plane for STRATOS detector. 183

6.2: Data sample of STRATOS detector. The data in the table is not in the same order as the data in the saved file. 185

6.3: Values of the spatial resolutions obtained after applying the Gaussian fit method. 195

6.4: Values of the efficiency of the STRATOS detector for all the planes. 197

7.1: The number of events generated for each mass of the primary cosmic ray and each energy range. 205

7.2: Summary of the main processes that take place in the development of Extended Air Showers induced primary cosmic rays. 206

7.3: Integrated mean flux of the most abundant secondary cosmic rays arriving the Sea Level for different thresholds of energy. 207

7.4: Summary of the shower energy required for different nuclei to produce one electron with a different energy range according to the shower energy. 222

8.1: Data sample recorded by a COSMIX detector. 263

8.2: Represents a summary for all the results of the data in the horizontal configuration at different floors heights of the physics building using various thicknesses of the lead layers for the average rate of detector 1, the average rate of detector 2, and the average coincidence rate of the COSMIX detector. 277

8.3: Summarizes all the data results in vertical configuration at different floors heights of the physics building using different thicknesses of the lead layers for the average rate of detector 1, the average rate of detector 2, and the average coincidence rate of the COSMIX detector. 278

8.4: A summary of all the data results in horizontal configuration at different floors heights of the physics building using different thicknesses of the lead layers for the normalized average rate of detector 1, the normalized average rate of detector 2, and the normalized average coincidence rate of the COSMIX detector. 279

USC
UNIVERSIDADE DE SANTIAGO DE COMPOSTELA

8.5: A summary for all the results of the data in vertical configuration at different floors heights of the physics building using various thicknesses of the lead layers for the normalized average rate of detector 1, the normalized average rate of detector 2, and the normalized average coincidence rate of the COSMIX detector. 280

8.6: Shows the electromagnetic rates measured for detector S1 after subtracting the rate measured with a brick of lead wide. 282

8.7: Displays the electromagnetic rates measured for detector S2 after subtracting the rate measured with a brick of lead wide. 283

8.8: Presents the analysis results comparing the compatibility of both detectors. 283

8.9: Shows the results of combining the data of both detectors, giving in a single sample with lower statistical errors. 284

8.10: Shows the values for both parameters, and , and the maximum energy of the electrons at different levels of the physics building. 290

8.11: Illustrates the values for both parameters, and , when a second-order fit was applied for the data at different levels of the physics building. 291

8.12: Represents the estimation of the reconstruction efficiency of electrons in the TRAGALDABAS detector. 293

8.13: Summary of the calculations for estimating the electron background in the TRAGALDABAS detector. Where is the energy of electrons in , the efficiency has been calculated using the fit described in the text, is the expected rate of electrons estimated from the COSMIX data, contents their associated uncertainties, diff is a number of electrons in the different energy intervals, diff is the expected rate per in , in each energy interval at laboratory 106 after interpolating the efficiency between the lateral values. The last columns R_TR and R_TR show the expected rates in the TRAGALDABAS detector, taking into account both its size and the geometrical acceptance and their corresponding uncertainties, where the uncertainty is the square root of the summation for all elements in the last column. 294

USC
UNIVERSIDADE DE SANTIAGO DE COMPOSTELA

INTRODUCCIÓN

Los comúnmente conocidos como Rayos Cósmicos (CR) juegan hoy en día un importante papel en el estudio y comprensión de muchos de los interesantes fenómenos físicos que tienen lugar por ejemplo en el sol, factor principal de los procesos atmosféricos terrestres, o en otras estrellas, galaxias y el universo en general. No podemos negar que se ha aprendido mucho en los últimos tiempos sobre muchos de estos fenómenos y sus propiedades, pero todavía los Rayos Cósmicos esconden muchos secretos que necesitan ser descubiertos.

Los Rayos Cósmicos fueron descubiertos en las primeras décadas del siglo pasado por el físico austríaco Victor Hess. Se puede decir que, en general, tienen la misma composición que el resto del universo. Partículas de muy alta energía procedentes incluso del espacio más profundo bombardean continuamente la Tierra. Son los Rayos Cósmicos primarios. La contribución principal es de protones de muy alta energía, con contribuciones menores de otros núcleos ligeros como helio o carbono, los cuales pueden alcanzar energías de hasta unos cuantos Julios, electrones e incluso otros núcleos pesados, principalmente hierro. El origen de estos núcleos pesados no es del todo conocido, y pueden proceder de las etapas finales de la nucleosíntesis estelar en procesos astrofísicos. Los llamados Rayos Cósmicos secundarios se producen cuando los primarios interaccionan, colisionan y decaen en la atmósfera terrestre. Se producen entonces, principalmente, grandes cantidades de protones, piones, kaones y electrones. Los kaones y piones son partículas no estables y continúan desintegrándose. El resultado final es una cascada de partículas a nivel de la superficie terrestre formada principalmente por muones, con contribución de electrones y gammas. La observación y el estudio de toda esta radiación a nivel de la superficie terrestre puede ser clave en

USC UNIVERSIDADE DE SANTIAGO DE COMPOSTELA

el estudio tanto de la estructura de objetos extragalácticos como en el de los fenómenos atmosféricos.

El rango energético de los Rayos Cósmicos es realmente grande, llegando en casos hasta los $10^{20}\ eV$. La componente menos energética se produce en fenómenos violentos de la superficie solar, como las llamadas *coronal mass ejections* (CME), en donde se aceleran partículas hasta unos pocos GeV que llegan a la superficie de la tierra como parte del viento solar, con una tasa aproximada de $10^3\ Hz/m^2$. A energías mayores, el origen de los Rayos Cósmicos se encuentra bien en nuestra galaxia como en galaxias exteriores. Se clasifican como Rayos Cósmicos Galácticos (GCR). Para energías menores de $10^{17}\ eV$ se puede asumir que los CR no tienen energía suficiente para abandonar la galaxia y permanecen confinados. Así, por encima de esa energía, se puede decir que todos los CR que llegan tienen un origen extragaláctico. Un efecto fascinante es la interacción del viento solar con los CR galácticos, modulando así el flujo de llegada a la Tierra. Esto da pie a que la medida del flujo de CR en la superficie de la tierra sea una monitorización indirecta de la actividad solar y pueda ser usada en la predicción de, por ejemplo, tormentas solares electromagnéticas.

Los CR primarios pueden ser observados y medidos con detectores localizados en satélites o globos estratosféricos, mientras que los millones de CR secundarios producidos en las interacciones de los primarios en la atmósfera, produciendo las llamadas *Extended Air Showers* (EAS), se detectan con sistemas como monitores de neutrones o telescopios de muones, localizados próximos a la superficie terrestre, o en ella misma; y aquellos más energéticos y penetrantes (muones, neutrinos, etc.) son medidos incluso en estaciones situadas bajo tierra.

Los CR primarios con energías superiores a $10^{14}\ eV$ se pueden considerar eventos raros, y sus propiedades físicas tales como la masa, energía o dirección de llegada, pueden ser estimadas a través de las medidas de las EAS producidas y detectadas a nivel del suelo. En general, los CR se ven afectados por varios efectos tanto antes como después de alcanzar la atmósfera terrestre, como los campos

USC UNIVERSIDADE DE SANTIAGO DE COMPOSTELA

magnéticos interplanetarios, tormentas solares o el propio campo magnético de la Tierra. Todo esto dificulta la predicción de las propiedades de los CR primarios, pero aún así se obtiene una información muy valiosa sobre su comportamiento y características. Además, las EAS pueden llegar a cubrir superficies de hasta cientos de kilómetros cuadrados en la superficie de la Tierra, lo que representa todavía un desafío técnico más a la hora de detectar y estimar las propiedades tanto de CR primarios como secundarios. Como complemento a las medidas directas, es habitual también estudiar y reconstruir las propiedades de CR mediante el uso de simulaciones, más o menos elaboradas.

Hace unos años, J.A. Garzón y colaboradores estudiaron y analizaron las características de algunas EAS y su microestructura durante la instalación y puesta en marcha del muro de tiempo de vuelo de detectores de RPCs para el espectrómetro HADES del GSI, Darmstadt, Alemania. Para ello, dos detectores de RPCs con una superficie aproximada de $1.25\ m^2$ cada uno fueron instalados uno sobre el otro, con una distancia de separación entre ellos de unos $33\ cm$. Se recogieron datos de CR haciendo coincidencias de al menos un hit en ambos planos de detectores. Las trayectorias de estos eventos fueron reconstruidas dentro de ventanas temporales y de posición, dada la buena granularidad del detector y su alta resolución temporal. El objetivo final de este muro de tiempo de vuelo es la medida del momento y la identificación de partículas a través de una medida precisa de la velocidad y tiempo de vuelo de las partículas entre el propio muro y el lugar de interacción o producción de dichas partículas en reacciones nucleares de blanco fijo.

Una vez los dos detectores mencionados alcanzaron sus puntos estables y correctos de operación, se estuvo tomando datos de CR durante un período largo de tiempo. Se analizaron cuidadosamente sobre 40 millones de eventos de EAS, viéndose con una resolución combinada de unos pocos cm^2 en posición, unos pocos grados en la dirección de llegada y un par de centenas de picosegundos en el tiempo de llegada.

USC
UNIVERSIDADE DE SANTIAGO DE COMPOSTELA

Nunca antes ningún detector de CR había registrado datos con esta precisión a nivel de la superficie terrestre.

Aunque los resultados obtenidos no eran definitivos desde el punto de vista de la física de CR, sí se observaron importantes comportamientos: aunque la mayoría de los eventos de EAS tenían multiplicidad 1 sobre la superficie de los dos detectores, se llegaron a observar eventos de EAS de multiplicidades muchísimo más altas; en esos eventos de altas multiplicidades, las partículas llegaban en ventanas de tiempo de unos cuantos nanosegundos; todavía después de 10 o 20 ns de que llegase el grueso de una EAS se podían observar partículas aisladas; algunos de estos eventos de alta multiplicidad agrupaban sus partículas en pequeños *clusters* espacio-temporales; en algunos casos se observaron eventos con multiplicidades muy diferentes en uno u otro detector, lo que podía dar lugar a pensar en la llegada y/o producción de pequeñas casacadas electromagnéticas bien de muy alta o de muy baja energía; la partícula más rápida, típicamente tenía una dirección de incidencia perpendicular al plano de llegada formado por el resto de sus compañeras, lo que indicaba que la partícula más rápida era un indicador de la dirección de incidencia del frente de la EAS.

Los resultados de estas medidas condujeron al diseño conceptual de una nueva familia de detectores llamados TRASGOs: *TRAck recoSntructinG mOdule,* con altas prestaciones espacio-temporales, y específicamente pensados para la medida y el estudio regular de Rayos Cósmicos y EAS.

Junto al propio diseño de los detectores TRASGOs, se incluyó un desarrollo de la electrónica de Front-end de Hades, una tarjeta de adquisición de datos basada en la actual TRB del GSI, y sobre todo establecer todas las herramientas de *software* relacionadas con la simulación de los detectores, monitorización y control de datos recogidos, reconstrucción de eventos y trayectorias, calibraciones de carga, posición y tiempo, etc. Después de iniciar estos desarrollos, se construía el primer detector de la familia: TRAGALDABAS. Este sistema fue instalado en la Facultad de Física de la Universidad de

USC UNIVERSIDADE DE SANTIAGO DE COMPOSTELA

Santiago de Compostela (USC), España, en 2013, y continúa desde entonces tomando datos de forma casi ininterrumpida hasta la actualidad. Un poco después, se unía un nuevo detector a la familia: TRISTAN, con el objetivo de analizar CR a nivel del mar en diferentes puntos del planeta. Este sistema realizó primeramente un recorrido de ida y vuelta desde Vigo (España) hasta la base antártica española Juan Carlos I, pasasndo por Punta Arenas (Chile), a bordo del buque Sarmiento de Gamboa, a principios de 2019, tomando datos durante todo el recorrido. Unas semanas después de su regreso en Octubre de 2019, realizó un segundo viaje con trayecto solo de ida a bordo del buque nacional oceanográfico Hespérides. Se encuentra, pues, actualmente instalado tomando datos en la base antártica española Juan Carlos I, situada en la isla de Livingston en el continente Antártico.

Poco después, más recientemente, los diseños existentes de TRAGALDABAS y TRISTAN fueron mejorados y se construyó un nuevo miembro de la familia: el detector STRATOS. Este sistema se desarrolló en colaboración con el Laboratorio de Instrumentación de Partículas (LIP) de la Universidad de Coímbra (Portugal), el propio Instituto Gallego de Física de Altas Energías (IGFAE) y la empresa tecnológica Hydronav (Vigo, España). El objetivo principal de este nuevo sistema es la descripción y predicción de fenómenos atmosféricos a través del análisis detallado de Rayos Cósmicos.

El trabajo presentado a continuación trata del análisis de datos y prestaciones de los tres sistemas mencionados, intentando describir la naturaleza de los Rayos Cósmicos detectados. Así, el Capítulo 1 describe la naturaleza y descubrimiento de éstos, la influencia de los campos magnéticos, los flujos a nivel del suelo y otras propiedades. Incluye también una descripción de las EAS, sus componentes hadrónica y electromagnética, y la interacción de sus partículas con la materia, con el objetivo de entender mejor su comportamiento y mejorar el diseño de nuevos detectores de partículas.

El Capítulo 2 presenta una descripción detallada de los detectores de tipo RPC (Resistive Plate Chambers). Los detectores de RPC son la

USC
UNIVERSIDADE DE SANTIAGO DE COMPOSTELA

base de la familia TRASGO y se convirtieron en los últimos años en uno de los tipos de detectores más usados y extendidos en los experimentos de Física Nuclear y de Partículas. Se presenta también una descripción un poco más detallada de los casos particulares de RPCs de TRAGALDABAS, TRISTAN y STRATOS.

En el Capítulo 3 se introduce el algoritmo de *TimTrack*. Este método matemático desarrollado por investigadores del IGFAE es usado a lo largo de todo el trabajo para la reconstrucción de trayectorias en todos los sistemas analizados, y es también esencial en la caracterización de los detectores propiamente dichos ya que es utilizado en los métodos de calibración, cálculos de eficiencia y aceptancia, ajuste de datos, etc.

El Capitulo 4 presenta otra parte de las herramientas utilizadas en el análisis de datos. En concreto el entorno de *software* EnsarRoot, desarrollado también por investigadores del IGFAE, y que constituye el entorno de trabajo dentro del cual se han desarrollado e implementado todas las simulaciones de los detectores y parte del análisis de datos. EnsarRoot incluye métodos basados en Monte Carlo, propagación de partículas usando GEANT y proporciona una implementación simple de la geometría de los detectores. A partir de simulación, se describe el método de identificación de partículas desarrollado a partir de contribuciones previas de investigadores del IGFAE, y finalmente el análisis de datos reales del detector TRAGALDABAS incluyendo la mencionada indentificación.

En el Capítulo 5 se investigan efectos atmosféricos de presión y temperatura sobre Rayos Cósmicos medidos con el detector TRISTAN a lo largo de su primer viaje de ida y vuelta a la Antártida, cruzando de norte a sur y de sur a norte el océano Atlántico. Incluye también un análisis de datos simulados en TRISTAN y los cálculos de aceptancia geométrica del sistema.

El Capítulo 6 presenta el detector STRATOS. Se describen sus sistemas de RPCs, diseño, electrónica, y todos sus componentes en general. A continuación, se discute toda la calibración desarrollada y obtenida del

USC
UNIVERSIDADE DE SANTIAGO DE COMPOSTELA

sistema, correcciones de tiempo y carga, calibración de coordenadas geométricas, cálculos de eficiencia y aceptancia y finalmente, la resolución temporal medida.

En el Capítulo 7 se presentan las investigaciones sobre las estructuras de las EAS a nivel del suelo usando el simulador CORSIKA de eventos de Rayos Cósmicos: se simularon CR primarios de núcleos de H, He, C y Fe interaccionando en las diferentes capas de la atmósfera a diferentes energías incidentes, y se observaron los efectos de los secundarios a nivel del suelo. Se obtuvieron así las funciones de respuesta de *clusters* de partículas a nivel del suelo para diferentes sistemas y configuraciones de detección.

El trabajo se completa y complementa con un pequeño análisis de los CR en el entorno de la Facultad de Física de la Universidad de Santiago de Compostela con el fin de corroborar datos medidos por TRAGALDABAS y TRISTAN. Este análisis fue realizado con un pequeño sistema portátil llamado COSMIX, desarrollado en el laboratorio CNRS/IN2P3, Francia, consistente en dos detectores de CsI(Tl) leídos por fotomultiplicadores, que admiten diferentes configuraciones, y optimizados para medidas de tasas de Rayos Cósmicos. Se presentan análisis de medidas de CR en diferentes localizaciones de la Facultad, diferentes configuraciones de los detectores, y diferentes espesores de absorbentes de Pb con el objetivo de aislar la componente electromagnética de los CR.

Finalmente, los Capítulos 9 y 10 incluyen, respectivamente, una breve conclusión del trabajo y un resumen global del mismo en Castellano.

USC
UNIVERSIDADE DE SANTIAGO DE COMPOSTELA

USC
UNIVERSIDADE
DE SANTIAGO
DE COMPOSTELA

INTRODUCTION

Cosmic rays (CR) are high-energy atomic nuclei and other subatomic particles coming from outer space. After they travel through interstellar space, they collide with the Earth's atmosphere, where they produce up to billions of secondary particles, the so-called secondary cosmic rays. Cosmic rays are the most energetic particles ever measured in the Universe, reaching energies above $10^{20}\ eV$ (tens of Joules!). Where are the cosmic rays produced and how they reach such high energies is still an unknown. Recent discoveries related to the existence of black holes in the center of the galaxies and also with the merging of black holes or of black holes and high mass neutron stars suggest them as new possible candidates.

Cosmic rays were discovered at the beginning of the 20th century by Vector Hess after having measured the air ionization at high altitudes in several balloon flights. He discovered that the ion content of the air starts to grow at high altitudes unveiling the presence of unknown extraterrestrial radiation. Analyzing the data taken during a solar eclipse, he also ruled out the Sun as the source of such radiation. Later this radiation received the name of cosmic rays and since they have been studied systematically without a pause. Some of the consequences were, for example, the discovery of the antimatter, the Yukawa mesons, a new family of leptons (the muons), a new quantum number called strangeness, or, more recently, the existence of a significative anisotropy in the production of very high energy cosmic rays in the near surroundings of the local group of galaxies. Also, indirectly, the cosmic rays have shown their applicability, for example, in the real-time monitoring of solar activity.

Presently there are a large number of cosmic ray detectors or arrays of cosmic ray detectors of different technologies, sizes and accuracies,

USC
UNIVERSIDADE DE SANTIAGO DE COMPOSTELA

taking data permanently all around the world and placed in satellites, in the ISS Space Station, on the ground and in underground stations. Now, we know that cosmic rays have the same mean composition as the whole Universe. They are composed mainly of protons and a smaller amount of helium and other nuclei around the most stables ones: C and Fe. There is also a small number of electrons and positrons with energies up to around $10^3\ GeV$. The rate of the high-energy cosmic nuclei arriving at the Earth decreases dramatically with the energy, being its rate at energies above $10^{14}\ eV/nucleon$ smaller than $\sim 1/m^2\ s$. Such a low rate makes it very difficult to measure them out of the atmosphere and can only be studied indirectly.

High energy cosmic protons and nuclei interacting with the nuclei of the atmospheric atoms, mainly N and O, may induce a chain of nuclear collisions being their final sub-products showers of subnuclear particles called secondary cosmic rays. They can be detected and measured at the Earth's surface or underground, allowing the indirect study of the primary cosmic rays with the highest energies. This secondary radiation is composed mainly of neutrons, muons and a smaller number of protons. There is also a significant amount of an electromagnetic background composed of electrons and gammas with energies up to a few GeV.

As has been already commented, the origin of the primary cosmic rays is not well known. Most of the cosmic rays having energies below a few hundreds of MeV are produced in eruptive processes in the Sun. They are usually called solar cosmic rays, SCR. They very rarely reach energies above a few GeV, that is, the minimum energy needed to produce secondary cosmic rays reaching the Earth's surface. When this happens, they produce the so-called ground-level enhancements, GLEs, detectable only in regions with low geomagnetic fields at high latitudes. The rate of cosmic rays above 1 GeV is around $10^3/m^2\ s$ at the top of the atmosphere.

Cosmic rays of the highest energies come either from our galaxy or from other galaxies, receiving the generic name of galactic cosmic rays,

USC UNIVERSIDADE DE SANTIAGO DE COMPOSTELA

GCR. It is possible to conclude that, considering the mean value of the magnetic field and the size of our galaxy, cosmic rays below $10^{17}\ eV$ cannot leave the galaxy and remain confined within it. Above those energies, it is assumed that cosmic rays have an extragalactic origin.

The study of cosmic rays is of interest for many reasons. On the one hand, looking for a better understanding of their origin and the diffusion and accelerating processes they suffer before arriving at the Earth's atmosphere. On the other hand, after they travel through the inter galaxy and the interstellar spaces, the heliosphere, the interplanetary region and the Earth's atmosphere, cosmic rays may act as a kind of privileged high energy "X-ray" radiation able to provide information of all the regions of the Universe having been traversed. The quest is how to extract form them all this hidden information. One of the most common examples is that the solar wind does interact with the lower energy galactic cosmic rays, modulating their arrival flux. Then on-ground detectors are used to monitor the solar activity indirectly and to predict the arrival of magnetic storms. Also, a fascinating result is the one observed at energies above $8 \times 10^{18}\ eV$, which has shown a very significant anisotropy in the origin of cosmic rays, compatible with a dipole angular distribution in the near extragalactic Universe.

Neutron monitors, muon telescopes and water Cherenkov detectors are the most common techniques used to measure the secondary cosmic rays on ground-based stations. Neutrons are the most common particles used for measuring solar activity through their effect in the modulation of small energy cosmic rays. As neutral particles, neutrons are very penetrating and hardly affected by the atmosphere. Primary protons need only 2 or $3\ GeV$ of kinetic energy for producing neutrons with enough energy to reach sea level. Another significant advantage is that the variations in the attenuation effect of the atmosphere due to the changes in its pressure (an easy way of measuring the air thickness) are almost linear and, as a consequence, it is straightforward to be corrected just by measuring the barometric pressure at the detector position. As a handicap, typical neutron detectors only measure integral fluxes being insensitive to their arrival direction.

USC
UNIVERSIDADE DE SANTIAGO DE COMPOSTELA

Secondary muons arriving at the Earth's surface need primary cosmic rays of higher energies to be produced. The main reason is that muons produced in the decay of meson ejected in the nuclear reactions induced by low-energy primary cosmic rays do not have enough energy for reaching the ground before decaying in electrons. Another important inconvenience is that their measure rate depends not only on the barometric pressure (that is very easy to correct) but also on the temperature profile of the whole atmosphere on top of the detector that is unknown in real-time. As a consequence, the rates can only be corrected afterward. As a significant advantage, muons are charged particles and are very easy to measure with tracking detectors, informing about their arrival direction and the region where they were produced. They are also affected by small changes in Earth's magnetic field, being, as a consequence, very useful for the early forecasting of magnetic storms.

Water Cherenkov Detectors (WCD) are very simple and robust detectors, sensitive to both muons and electrons at a very affordable cost. They are optimal detectors for building big area arrays and indirectly studying the arrival of high-energy primary cosmic rays through the measurement of the shower of secondary cosmic rays reaching the Earth's surface.

As a complement to the above commented techniques, the detectors of the TRASGO (TRAck reconStructinG bOx) family we analyze in this work do offer several new and unexplored features that may be very helpful in several of the cosmic ray research fields. Unlike other detectors, Trasgos do offer a very high granularity and time resolution being sensitive not only to single particles but also to groups or bundles of both muons and electrons. It opens the possibility of scanning in real time the arrival of primary cosmic rays to the Earth’s atmosphere in different energy ranges. Also, a large amount of information they provide (muon and electron identification, arrival directions, size of the clusters of particles, time width, Etc.) opens the possibility, not yet explored but suggested by the simulations, of looking for new

USC UNIVERSIDADE DE SANTIAGO DE COMPOSTELA

observables that could inform in real-time about the temperature in the highest levels of the atmosphere.

The TRASGO project started a few years ago, when the LABCAF research group at the USC analyzed some of the cosmic ray air shower's inner characteristics and some of the microstructure's effects, during the commissioning of the RPC (Resistive Plate Chambers) ToF (Time of Flight) Wall of the HADES Nuclear Physics experiment at GSI laboratory in Darmstadt, Germany. For this purpose, two RPC detectors with a surface area of about $1.25\ m^2$ were stacked on top of one another at a distance of approximately $33\ cm$. Cosmic rays were measured via a trigger between coincidences of at least one hit in the upper and lower planes. In both detectors, tracks were reconstructed to match hits and ask for a velocity consistent with light speed. The role of ToF is to measure the time it takes for a particle to travel to the TOF wall from the starting detector at the target, allowing the speed of the particle to be measured. A signal is produced when the particle passes the starting detector. The time is then estimated when the particle hits the TOF wall. Having a good time resolution is very important to reject bad reconstructed tracks.

Around 40 million events were chosen for a careful analysis of showers after taking data from the detectors operating in a very stable condition. A joint resolution of a few cm^2 in position, a few hundred picoseconds at the time of arrival and a few degrees in the direction of arrival were shown in the sample. No cosmic ray detector on the surface of the Earth had ever met these values together.

Although the research outcomes were not definitive from the cosmic ray physics point of view, some interesting features were observed: although most events have multiplicity equal to one, often multiplicities were much higher than that. In high multiplicity events, the fastest particle is typically perpendicular to the plane defined by the arrival times of the rest of the particles showing that it may be a good estimator or the arrival direction of the cosmic ray shower's front end. Most of the particles arrived in a time window of a few nanoseconds in high

USC
UNIVERSIDADE DE SANTIAGO DE COMPOSTELA

multiplicity events. Sometimes, single particles arrive around 20 nanoseconds behind the main particle bundle. Several events showed high granularity, with bundles of a few particles arriving in well-defined space-time clusters. The hit multiplicity was often very different in the first and second detectors, showing either a huge increase or a huge decrease. Both cases will presumably lead to electromagnetic showers with high energy or low energy, respectively.

The encouraging and inspiring results were obtained during the analysis of the cosmic ray data obtained when commissioning the RPC ToF wall of the HADES experiment at GSI. That is led to the development of a new family of specific detectors named TRASGOs, an acronym to TRAck reconStructinG mOdule for the microstructure's regular cosmic rays survey of cosmic ray showers of particles with improved performances.

Along with the design of the detector based on RPC chambers, the HADES Front End Electronics (FEE) and TRB reading board, another significant objective was to establish all the relevant tools relating to the simulation of the detector and its environment, the monitoring of data collection, the reconstruction of tracks and events. After all these efforts, the TRAGALDABAS detector has introduced as the first member of the TRASGOs family. TRAGALDABAS was installed in the Faculty of Physics of the University of Santiago de Compostela (USC), Spain, in 2013 and regularly working in appropriate circumstances until today. A few years later, another detector joined the TRASGOs family, named TRISTAN, to analyze and survey the cosmic ray at sea level. The detector made a two-way trip between Vigo (Spain) and Punta Arenas (Chile) onboard the Spanish vessel Sarmiento de Gamboa, continuously monitoring the Atlantic's cosmic-ray rate crossing. TRISTAN was installed in the Faculty of Physics of the University of Santiago de Compostela in October 2019 for around three weeks. After that, it moved to Antarctica in the Spanish part and working in different circumstances and from that time, TRISTAN taking data continuously and regularly.

USC
UNIVERSIDADE DE SANTIAGO DE COMPOSTELA

Later on, the existing TRAGALDABAS and TRISTAN designs were improved to develop the third member of the Trasgo family called STRATOS. The STRATOS detector was developed as an initiative of the company Hidronav technologies for atmospheric studies as a collaboration of the LIP group in Coimbra University, Galician Institute of High Energy Physics (IGFAE) at Santiago de Compostela University (USC).

Objectives and Methodology

The main objective of this work is the comparative analysis of the cosmic rays measured in different locations by the two opperative Trasgo-like detectors TRISTAN and TRAGALDABAS and make the first data commissioning for the newest STRATOS detector. For the intended study, all the calibration and correction tools necessary to obtain absolute rates, as well as those for the study of correlations and joint analysis with detectors, were developed and fine-tuned.

The aim was to study cosmic ray arrivals with unprecedented precision at various acceptance angles, which will allow to study, among other effects, their possible relationship with the temperature profile of the upper atmosphere above the vertical of the detectors and also perform and test a method for cosmic ray particle identification based on the information provided by those detectors, simulated data and tracking reconstruction.

Some of the tasks carried out were the following:

1- To study and understand the response of the detectors with atmospheric pressure and other variables related to the detectors themselves, such as the room temperature, high voltage, operation thresholds or calibrations.

2- To study the corrections for acceptance, charge and dead time of those detectors separately and as well as the effects of radiation and building attenuation.

USC
UNIVERSIDADE DE SANTIAGO DE COMPOSTELA

3- To measure the muon, electron and gamma-ray background in several locations using a Cosmix type auxiliary detector, developed by the University of Bordeaux.

4- Determine the possible effects of temperature variation at different levels of the atmosphere on the measured rates as well as their correlation with the cosmic ray background measured by the global network of neutron monitors.

5- To set up and commission the STRATOS detector, thus characterizing its main performances.

In this work we have applied the typical working methodology when analyzing experimental data with detector systems and also the systematic steps necessary to develop and characterize a new detector system.

For completeness, part of the work was carried out by means of simulated data. Then, we developed the methods for simulated data analysis, tracking reconstruction and generation of simulated geometries in order to obtain results which can be compared later with the same for real data. One of the key points in this work is the development and improvement of the already existing method for particle identification, based on the systematic study of cosmic ray tracks over the TRAGALDABAS detector with simulated data and extend the method to real data analysis, which was never done before.

In the real data analysis itself, all tools and methods were prepared in advance. Once the data is taken, it must be calibrated and corrected by the different contributions that affect to the detector performances, such as charge collection, time and position calibration, fake tracks removal and angular acceptance, among others. Then, the final analysis is done and conclusions are extracted.

Regarding the new STRATOS detector, which was recently developed, once it was set up in the laboratory, their performances were addressed

USC
UNIVERSIDADE DE SANTIAGO DE COMPOSTELA

by measuring cosmic ray data. They were calculated the detector efficiency, angular acceptance, charge and position calibrations and time and position resolution.

Finally, a comparative analysis of cosmic data is done with a different device: a small, compact and portable cosmic ray detector is used to monitor the cosmic ray flux at different locations and compare later with data collected with TRASGO-like detectors.

This thesis is organized as follows:

We have covered a few aspects of some of the Trasgo detectors in this work. We have explained new feasibilities that can open new research possibilities using their capability to detect particle clusters.

The nature and discovery of cosmic rays, the influence of solar and Earth magnetic fields on galactic and extragalactic cosmic rays, the particle flux that arrives on Earth and other properties are discussed in Chapter 1. The study of atmospheric showers and their hadronic and electromagnetic components, as well as the interaction of charged particles from electromagnetic showers with the matter in general, with the goal of better understanding their interactions to aid in the design of particle physics detectors.

Chapter 2 will describe the Resistive Plate Chambers detectors (RPC) designed and built at the LIP group in Coimbra University, which became one of the most widely used detectors in particle physics experiments. Thus, the models of the RPC were used in Trasgo detectors like TRAGALDABAS, TRISTAN and STRATOS.

In Chapter 3, we introduce the TimTrack algorithm. This mathematical algorithm tool is used to reconstruct the trajectory of the particles associated with a specific event across the experimental setup. These trajectories are essential for estimating the physical characteristics of our detectors, such as efficiency, calibration and acceptance and also for identifying the nature of particles.

USC
UNIVERSIDADE DE SANTIAGO DE COMPOSTELA

We present the tools we used to simulate a model of our experimental set-up in Chapter 4. The EnsarRoot framework, developed at the Universidad de Santiago de Compostela, was used for all simulations. This software includes Monte Carlo simulation and analysis tools and straightforward implementation of the detector geometry.

In Chapter 5, we will investigate the effects of atmospheric pressure and temperature on a real data of the cosmic ray detected by the cosmic ray detector TRISTAN during the first journey of the detector measuring the secondary cosmic-ray rate continuously throughout crossing the Atlantic Ocean on board the Spanish vessel Sarmiento de Gamboa from Vigo, Spain to Punta Arenas, Chile. Moreover, we introduce a simulation part about the geometric acceptance using PYTHON software for the TRISTAN detector.

In Chapter 6, we present a description of the structure of the planes (RPC) for the STRATOS detector and their components. Furthermore, we will discuss the position calibration in X and Y coordinates of the detector, the calculation of the efficiency and the time resolution.

Using simulations with the CORSIKA package developed at KIT, Chapter 7 investigates the structure of the electromagnetic shower over large areas at ground level. The study generates events with primary cosmic rays for four nuclei (H, He, C and Fe) interacting in the atmosphere's upper layers. It enables researchers to determine the distribution of secondary particles at ground level. Moreover, we study the response function for electron clusters detected by the detector at different angles for a proton as a primary cosmic ray. We also perform the response function for the electron clusters at different energy ranges.

In Chapter 8, the COSMIX detector developed by France's Gradignan CNRS/IN2P3 laboratory is composed of two scintillators Cesium Iodide CsI(Tl) bars one of them is movable. The detector was placed in the physics building in USC to study the cosmic ray rates and the background and contributions of the electrons at four different levels of

USC UNIVERSIDADE DE SANTIAGO DE COMPOSTELA

the building. Moreover, we introduce how the coincidence rate varied with a thickness of lead placed gradually above both counters at different floors with two configurations provided by the detector.

Finally, in Chapter 9, a short conclusion is introduced and a global summary in Spanish in Chapter 10.

USC
UNIVERSIDADE DE SANTIAGO DE COMPOSTELA

USC
UNIVERSIDADE
DE SANTIAGO
DE COMPOSTELA

1 COSMIC RAYS

1.1 Historical glance about the discovery of the cosmic rays.

Cosmic rays have been discovered after the natural radioactivity of the ground was uncovered. Some elements of the Earth are radioactive, such as radon and uranium. The spontaneous discharge of the electroscopes was observed in the experiments carried out by Coulomb and Faraday. After the experiments performed by Crookes, it was clear that this discharge resulted from ambient air ionization. Pierre Becquerel and Marie Curie demonstrated that radioactive substances emit ionizing particles and so, it was obvious to assume that the ground's radioactivity induced the ionization of the air and then the subsequent spontaneous discharge of the electroscopes.

The ionization source of the air was of interest to Theodor Wulf, a German physicist who developed the most accurate electroscopes at the time. In 1909 he invented a very sensitive device able to measure electrical charges with very high precision. During several measurements done in the top of the Eiffel tower [1] he observed that ion contents in the air was higher than the value that could be expected if the ionization were produced by the natural radioactive substances existing in the ground. Consequently, it should be assumed that the air ionization should have a different origin and new measurements should be done at higher altitudes.

Also, several experiments were carried out by Domenico Pacini between 1907 and 1911. He studied the ionization when the electroscopes are placed underwater. He used two electroscopes, one on the ground surface and the other at a depth of 3 meters below the

USC UNIVERSIDADE DE SANTIAGO DE COMPOSTELA

Bracciano lake's surface and noticed simultaneous variations of the ionization between both electroscopes. He also observed that the radiation's intensity at a 3 meters depth was lower than the one existing at the surface. Therefore, the assumption that there is a source of radiation independent of the source on the Earth's surface has been accepted.

In 1912, Victor Hess carried out numerous experiments on balloon flights using several Wulf electrometers [2]. He observed an increase in air ionization above the altitude of around 1 km, demonstrating the extraterrestrial origin of the ionizing radiation. One of his flights took place during a complete solar eclipse. Hess noticed the same rise in the intensity of radiation as in previous flights. He then assumed that the Sun is not the source of this radiation and that if they came from outer space. Such radiation must have a great capacity of penetration so that they can hit the Earth's surface and underwater detectors.

After several flights about 9 km above sea level, the hypothesis of Hess was confirmed later by Kolhörster. Hess was awarded in 1936 the Nobel prize in Physics for this contribution.

Along the 20th century, the cosmic rays have been extensively measured and analyzed. Currently, to study the cosmic ray properties, many detectors of very different technologies have been designed and are taking data around the World providing us very useful information about the Earth's surroundings and the rest of the Universe. Wide array detectors, such as those at Auger Observatory [3], were designed to cover large areas, collecting information from the highest energy cosmic rays ever measured.

A new family of devices, the Trasgo detectors, such as the TRAGALDABAS [4], TRISTAN [5] and STRATOS [6] detectors, described in this work, have been proposed to conduct complementary approaches to cosmic ray flux studies. A deeper investigation of the relationship between cosmic ray flux and atmospheric properties [7, 8] can be done by studying some observables.

USC
UNIVERSIDADE DE SANTIAGO DE COMPOSTELA

1.2 Some general characteristics of cosmic rays

Many experiments have studied the cosmic rays since their discovery, assembling many characteristic properties of these ionizing particles. Before reaching the Earth's surface the cosmic rays are affected by the magnetic fields of the Sun and the Earth, which modify the measured rates using ground-based detectors. A tremendous physical challenge is detecting cosmic rays on the Earth's surface and the Earth's upper atmosphere. This section will discuss the energetic spectrum, composition and abundance of cosmic rays, which may tell us more about their origin.

1.2.1 Energy spectrum

The solar system is continuously exposed to a flux of high energy cosmic rays. The energy spectrum of those particles up to the highest energies of around $10^{20}\,eV$ is shown in Figure 1.1. With a little deviation across this wide energy range from a constant power law $\frac{dN(E)}{dE} \propto E^{-\gamma}$, the spectrum is strikingly featureless. As the cosmic-ray energy increases, the flux of cosmic rays decreases rapidly.

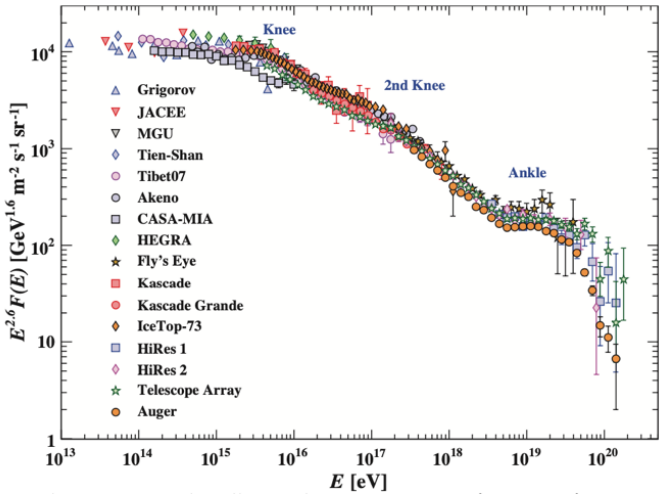

Figure 1.1: Differential energy spectrum $F(E)$ as a function of the energy per nucleon as has been measured by different spectrometers and observatories.

USC UNIVERSIDADE DE SANTIAGO DE COMPOSTELA

In order to show the characteristics of the steep spectrum that are otherwise hard to distinguish, the differential energy spectrum has been multiplied by $E^{2.6}$ [9]. It has a distinctive leg shape and it is typical to distinguish between the regions of the knee and the ankle. Particles up to several hundreds of $10^6\ eV$ are typically originated from the solar wind. Cosmic rays are modulated even those up to an energy of $10^{10}\ eV$ by solar activity. The rate of particles with energy $E > 10^6\ eV$ arriving to the Earth's atmosphere is around 10^4 per square meter per second and the rate is only one particle per square meter per second for energies above $10^{12}\ eV$. The steepening occurs between 10^{15} and $10^{16}\ eV$ because the flux of cosmic rays starts to decrease even more rapidly around $3 \times 10^{15}\ eV$, leading to a small change in slope, from $E^{-2.7}$ to $E^{-3.0}$ is referred to as the spectrum knee. There are just a few particles per square meter per year at these energies. The feature about $10^{18.5}\ eV$ is called the spectrum ankle, where the flux of cosmic rays is much higher than expected. The slope changes here to a value of -2.8. A cut-off, a theoretical upper limit of cosmic rays from distant sources, is expected from this energy. Kenneth Greisen [10], Vadim Kuzmin and Georgiy Zatsepin [11] computed this limit, called the GZK-limit, in 1966, based on predicted interactions between cosmic rays and cosmic microwave background (CMB) radiation photons; the magnitude of this limit is equivalent to approximately 8 Joules for protons. They predicted that to generate pions, cosmic rays with energies over the threshold energy of $5 \times 10^{19}\ eV$ would interact with cosmic microwave background photons. This will continue until their energy dropped below the threshold of pion production. Therefore, extragalactic cosmic rays can never be detected on Earth with energies greater than this threshold energy.

1.2.2 Composition and abundances

The chemical abundances of cosmic rays offer significant indications of their origin and propagation mechanisms from their origins to the Earth. The composition of cosmic rays up to $1\ TeV$ energy is well known. Around 98% of the particles are nuclei and 2% are electrons. Furthermore, roughly 87% of the nuclei are protons,

USC UNIVERSIDADE DE SANTIAGO DE COMPOSTELA

12% are helium nuclei and the remaining 1% are heavier nuclei. The relative abundance of the various cosmic ray elements compared to those of the Solar System can be seen in Figure 1.2 [12]. The figure shows that the abundances of cosmic ray elements is not so different from typical solar systems abundances. Both distributions have peaks at carbon, nitrogen, oxygen and at the iron group. This could be explained by the fact that particles of cosmic rays must have been accelerated from material with a chemical composition approximately identical to that of the abundances of the Solar System. As a special feature, elements such as lithium, beryllium, boron and other elements just below the iron peak, the so called the sub-Fe group, show an excess in the abundance in cosmic rays. It can be explained as being the spallation products of higher more stable elements. Also, the abundance of hydrogen and helium is lower in the cosmic rays than the abundance in the solar system. The reason can be a consequence of the dependence of the propagation mechanisms on the electrical charge of the nuclei in the interstellar medium. The first ionization energies of helium and hydrogen atoms are relatively high. Therefore, a relatively big amount of these atoms is not ionized and hence, they are not accelerated. Therefore, the abundance of these elements decreases in the cosmic rays compared to their abundance in the solar system. In general, in cosmic rays, light elements as lithium, beryllium and boron are more abundant than in the solar system and, so, the elements below iron ($Z = 26$) and below lead ($Z = 82$).

USC
UNIVERSIDADE DE SANTIAGO DE COMPOSTELA

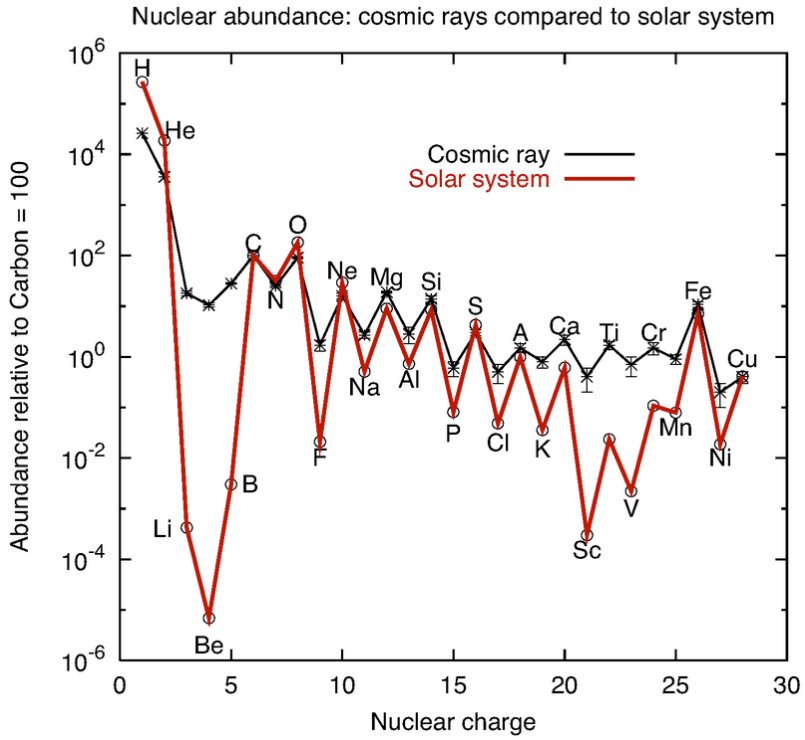

Figure 1.2: The relative abundance of Galactic cosmic rays compared to those of the Solar System.

The spectrum of the components of cosmic radiation may be listed in four different ways: 1) By particles per unit rigidity. Propagation by cosmic magnetic fields and possibly also acceleration, depends on the gyroradius or the magnetic rigidity R, which is the gyroradius multiplied by magnetic field strength, that depends also on the p/Z ratio :

$$R = \frac{p\,c}{Z\,e} = r_L\,B \tag{1.1}$$

2) By nucleons per energy-per-nucleon. The production in the atmosphere of secondary cosmic rays depends on the intensity of the arrival nucleons and the energy per nucleon, roughly irrespective of

USC UNIVERSIDADE DE SANTIAGO DE COMPOSTELA

whether the incident nucleons are free protons or are bound in nuclei. 3) By particles per energy-per-nucleon. Energy per nucleon depends on the fragmentation of nuclei propagating through the interstellar gas since that amount is roughly retained when the interaction with the gas breaks up a nucleus. 4) By particles per energy-per-nucleus. Air shower experiments using the atmosphere as a calorimeter typically measure a quantity per particle that is related to the total energy.

The differential intensity, I, has a unit $[m^{-2}\ s^{-1}\ sr^{-1}\ \mathcal{E}^{-1}]$, where $\mathcal{E}$ represents the unit of one of the above four variables. In the energy range from the several GeV with somewhat above $100\,TeV$, the intensity of primary nucleons is roughly given by

$$I_N(E)\ \approx 1.8\ \times\ 10^4\ (E/1\ GeV)^{-\alpha}\ \frac{nucleons}{m^2\ s\ sr\ GeV} \qquad (1.2)$$

where E is the energy-per-nucleon, including rest mass-energy and the differential spectral index of the cosmic ray flux is $\alpha \equiv\ \gamma\ + 1\ \cong 2.7$, being γ the integral spectral index [13].

For kinetic energies approximately greater than $0.2\ GeV/$nucleus, Figure 1.3 summarizes the important nuclear components. A useful set of experimental data is mentioned in [14] for cosmic ray nuclei and electrons.

Usually, nuclei's composition and energy spectra are represented in the sense of propagation models in which the primary cosmic radiation sources are located within the galaxy [15]. With increasing energy, the ratio of secondary to primary nuclei is observed to decrease. A fact sometimes interpreted to mean that the lifetime of cosmic rays in the galaxy decreases with energy.

USC
UNIVERSIDADE DE SANTIAGO DE COMPOSTELA

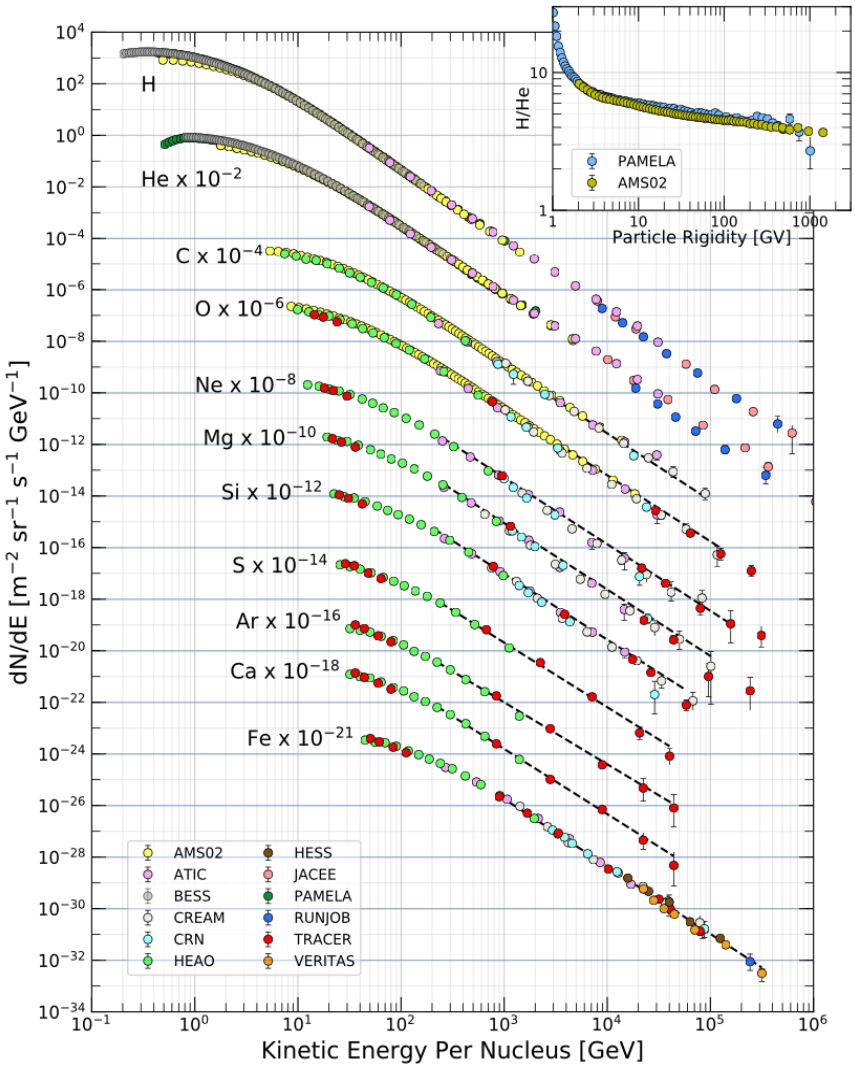

Figure 1.3: Cosmic ray flux of individual nuclei per nucleus as a function of kinetic energy.

In cosmic rays, all of the elements of the periodic table have been observed. Energy spectra for individual elements were measured for relatively abundant elements up to nickel [16, 17]. As shown in Figure

USC UNIVERSIDADE DE SANTIAGO DE COMPOSTELA

1.3, most of the energy of the particles is greater than 10 GeV because of the interaction between the solar wind and the cosmic rays. The primary radiation is decelerated by the charged particles that are ejected from the Sun. Thus, these primary particles are screened, which produces an anti-correlation between intensity and solar activity at the low energy spectrum.

It is possible to obtain information on the composition at the source from the refractory nucleus abundance measurements. They seem to have been subjected to limited elemental fractionation relative to each other. Comparing the derived abundance at the source with the solar system's abundance shows a striking resemblance between the two samples over a wide range [18]. The abundances of particular isotopes are consistent with being within 20 percent of solar values when uncertainties are considered; this means that cosmic rays are accelerated out of a sample of well-mixed interstellar matter. Thus, cosmic rays are natural and regular matter but accelerated to incredibly high energies.

1.3 Sources of cosmic rays

As has been already shown, cosmic rays are charged particles of extremely high energy that travel at almost the speed of light and any magnetic field alters their paths. Some come from the Sun (solar energy particles), while supernova explosions and other still nt well known energetic events expel those in the interstellar and intergalactic spaces. Primary cosmic rays create showers of "secondary particles" when they collide with the Earth's atmosphere. This section will talk briefly about the cosmic ray's source and describe the cosmic radiation separating in different regions.

USC
UNIVERSIDADE DE SANTIAGO DE COMPOSTELA

1.3.1 Extragalactic and Solar cosmic rays

Identifying the properties of the cosmic rays could provide important information about the processes that occur inside our galaxy and the entire universe in general, including the events that produce them and the mechanisms by which they pass to reach us. The highest-energy cosmic rays have long been thought to originate outside our galaxy. In contrast, lower-energy cosmic rays come from within the Milky Way, our Sun, clusters of stars and supernova events.

As mentioned before, most of the cosmic radiation is produced predominantly outside the Solar System. When a star's life comes to an end, it is possible to eject the materials produced during the nucleosynthesis processes to the interstellar medium. For instance, the particles acquire energy inside the remnant after a supernova explosion and this energy enables the particles to escape. This radiation consists mainly of carbon, iron, helium, or protons, nuclei that are usually formed in stars.

Supernovae are not considering the only source of cosmic radiation. Quasars[1] (See the Figure 1.4), galactic nuclei, or gamma-ray bursts are probable sources of cosmic rays. Other studies carried out by large observatories, such as PAMELA satellite data [19] or the Pierre Auger [3], could be the key to understanding the origins of cosmic rays. New Ice Cube data [20] indicates that star-forming galaxies are a significant cosmic neutrinos source [21].

The presence of magnetic fields influences this ejected material and can interact with the interstellar medium as well. Nuclei such as lithium or boron are obtained alongside antimatter after such interactions. In our galaxy, the Earth or outer space, the presence of magnetic fields dramatically influences the direction of these particles.

[1] Quasar (as a quasi-stellar object is also known; the acronym QSO) is an extremely luminous Active Galactic Nucleus (AGN). A gaseous accretion disk surrounds a supermassive black hole with a mass ranging from millions to billions of times the Sun's mass.

USC UNIVERSIDADE DE SANTIAGO DE COMPOSTELA

This reality makes the location of the origin of cosmic rays with energies below around 10^{18} eV very difficult.

Figure 1.4: Quasar artistic image. The brightest objects in the Universe.

The Sun is the nearest cosmic radiation source to the Earth. When there is a reconfiguration of the Sun's magnetic field or a shock, solar flares and coronal mass ejections are generated. There is an anticorrelation between solar activity and the arriving flux of galactic cosmic rays. When the Sun's ejections deflect a big portion of the arriving galactic cosmic rays, a sharp decrease is produced in detection rate; this phenomenon is known as a Forbush decrease or FD.

1.3.2 Cosmic rays in the atmosphere

High energy primary cosmic rays interact with the atomic nuclei in the air, primarily nitrogen and oxygen. The results of the interactions depends on the air's density and the energy of the primary cosmic ray. The most energetic particles will travel further, allowing for more secondary particles production along their paths. The strong interaction

USC UNIVERSIDADE DE SANTIAGO DE COMPOSTELA

mediates the collisions between hadrons and air atomic nuclei. As shown in Figure 1.5, particles in the Earth's atmosphere are created when primary cosmic rays interact with atoms in the atmosphere. As a result of these interactions, cascade reactions occur, resulting in the generation of other particles. There are three main components to the cosmic ray cascade:

1- The meson component. It is made up of kaons, K, and pions, π, where pions make up most secondary particles. Both of them decay either directly or indirectly to produce muons, μ. They are very short-lived, lasting just a few hundredths of a nanosecond. For example, charged pion with an energy order of $1\ GeV$ travels 60 meters and lives just $26\ ns$ [22]. As a result, the majority of pions decay near the altitude at which they were produced. Depending on the charge of the pion, their decay will produce either muons and photons:

$$\pi^{\pm} \rightarrow \mu^{\pm} \nu_{\mu} (\bar{\nu}_{\mu})$$

$$\pi^{0} \rightarrow 2\,\gamma$$

2- The electromagnetic component. It is composed of electrons and gammas or photons, $\gamma's$, coming from the decay of neutral pions, π^0. If the photons have energy greater than $1\ MeV$, they have a big chance of creating electron-positron pairs:

$$\gamma \rightarrow e^{+}\, e^{-}$$

These positrons and electrons are losing their energy by the Bremsstrahlung process producing new photons that can create new electron-positron pairs. This process continues until the energy of the electrons is smaller than the so-called critical energy at which the probability of losing their energy by ionization is higher than producing new photons.

3- The hadronic component. Protons and neutrons form the hadronic component. As seen in Figure 1.5, a fraction of nucleons can interact

USC UNIVERSIDADE DE SANTIAGO DE COMPOSTELA

with the atomic nuclei ejecting new nucleons and mesons that can produce further nuclear interactions [23]. Finally, all mesons decay in muons, electrons and neutrinos, whereas neutrons and protons are either absorbed in the air or reach the Earth's surface.

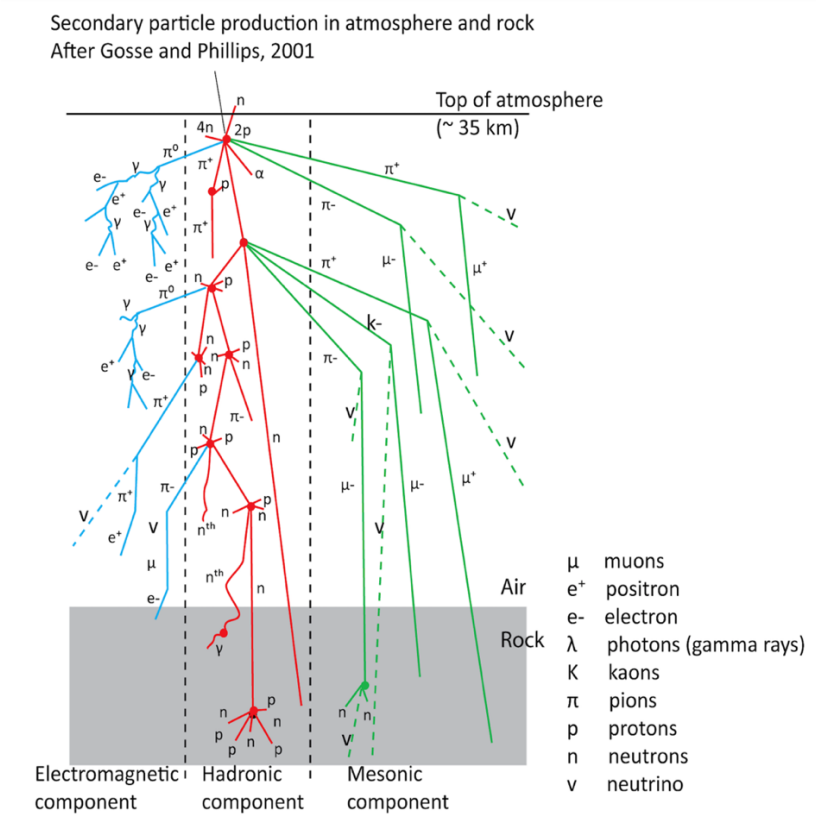

Figure 1.5: Showers of cosmic ray reactions with particles of the atmosphere. Figure taken from www.antarticglaciers.com

1.3.3 Terrestrial cosmic rays (Cosmic rays at Earth surface)

The interaction of cosmic ray particles with the terrestrial atmosphere induces both atmospheric ionization and nuclear reactions, resulting in creating a cascade of secondary particles, the direct or

USC UNIVERSIDADE DE SANTIAGO DE COMPOSTELA

indirect measurements near the ground could be used to research the physical processes involved in the cosmic ray particle's journey, including the conditions of originating of the lower energetic particles and the propagation of the higher energetic particles [24]. The composition of cosmic ray showers formed in the atmosphere is summarized schematically in Figure 1.5.

The energy spectrum of cosmic rays is represented in Figure 1.6 [4]. The spectrum depicts cosmic ray flux as a function of the primary cosmic ray's energy, sources and common cosmic ray detection methods. The altitude, density and composition of the Earth's atmosphere are illustrated on the figure's right-hand side. Using all these parameters could provide a reasonable explanation and description of cosmic radiation.

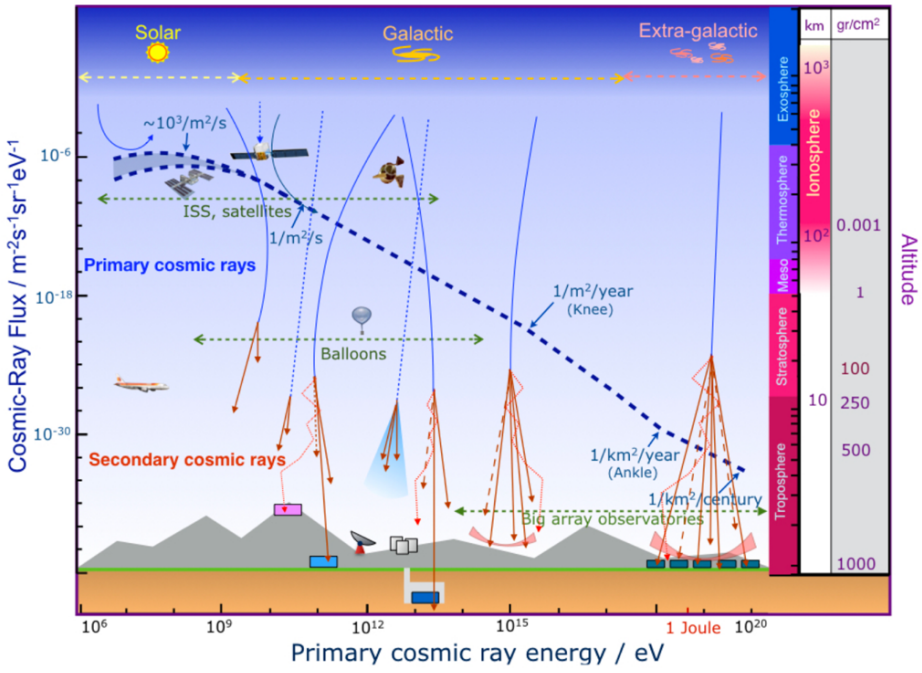

Figure 1.6: Cosmic ray energy spectrum and the most common detection methods.

USC UNIVERSIDADE DE SANTIAGO DE COMPOSTELA

Due to their relatively high fluxes, primary cosmic rays with energies up to around $10^5\ GeV$ can be measured directly using detectors placed in satellites or balloons. Above that energy, the flux is so tiny that it can only be measured indirectly using ground-based detectors.

The energy of galactic cosmic rays arriving to the Earth ranges between around $10^{10}\ eV$ and $10^{17}\ eV$. They interact mainly around the tropopause region, resulting in secondary cascades that propagates along the atmosphere. In order to overcome their attenuation effect, several detectors or arrays of detectors, like the ones placed in Sierra Negra in Mexico [25] or in Tibet [26], at altitudes higher than 4 kilometers above sea level. New projects are on the way for installing new observatories at high altitudes mainly in South America.

Wide cascades are produced on the Earth's surface by highly energetic cosmic rays from extragalactic sources. Although these cosmic rays' flux is just one per km^2 per century, they are the most energetic. The detection of cascades is only possible with large arrays of detectors because of their immense amplitude. Observatories like P. Auger [3] cover vast detection areas and investigate the sources of these cosmic rays.

Muons are the most abundant charged particles at the sea level, as it is shown in Figure 1.7. The figure illustrates the mean vertical fluxes of the main cosmic-ray components in the atmosphere in the energy area where the particles are most abundant, except for electrons, which are most numerous near their critical energy around $81\ MeV$ in the air [13]. And also, except for protons and electrons at the top of the atmosphere. The energy cutoff E is greater than $1\ GeV$.

The majority of measurements are made at ground level or near the top of the atmosphere, but muons and electrons can also be measured from airplanes and balloons. The measurements of negative muons are also shown in Figure 1.7. Since $\mu^+(\mu^-)$ are emitted in combination with $\nu_\mu\ (\bar{\nu}_\mu)$, the measurement of muons near the limit of the intensity curve

USC UNIVERSIDADE DE SANTIAGO DE COMPOSTELA

for the parent pions helps to calibrate the atmospheric ν_μ beam [33]. The

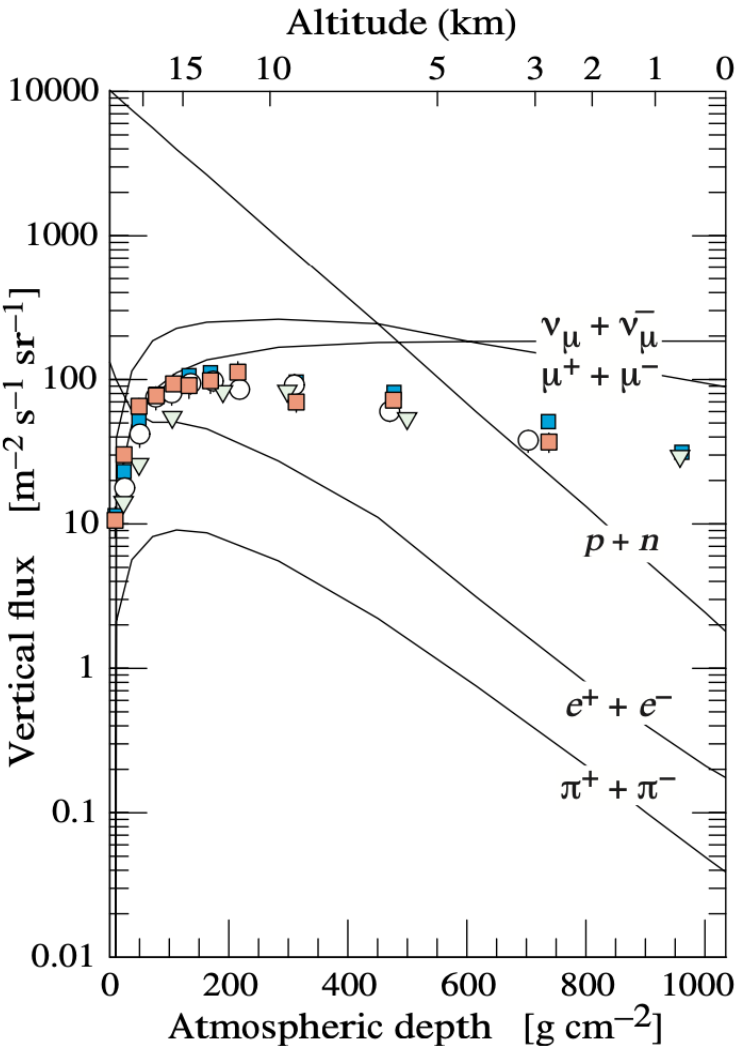

Figure 1.7: Vertical flux of the cosmic ray in the atmosphere with energy greater than $1\ GeV$ estimated from Equation's nucleon flux (1.2). The points show measurements of negative muons with muons energy greater than $1\ GeV$ [27-32].

USC UNIVERSIDADE DE SANTIAGO DE COMPOSTELA

comparison near the production altitude is essential for the sub-GeV range of ν_μ ($\bar{\nu}_\mu$) energies since muons usually lose almost $2\ GeV$ in passing through the atmosphere.

In this context, detectors of the Trasgo family do provide new ingredients for a better understanding of the properties of cosmic rays arriving to the Earth's atmosphere and the Earth's surface. Their capability of measuring at the same time the arrival rates of muons, electrons and bundles of particles could open a broad spectrum of improvements in several areas as, for instance, a direct estimation of the energy of the primary cosmic ray using ground-based detectors and, in addition, a more accurate correction of the atmospheric effect or, even, an estimation of the mass of the primary cosmic ray using a small array of detectors.

USC
UNIVERSIDADE DE SANTIAGO DE COMPOSTELA

USC
UNIVERSIDADE
DE SANTIAGO
DE COMPOSTELA

2 Resistive Plate Chambers detectors

2.1 General introduction

Resistive Plate Chambers detectors, the acronym (RPCs), play a significant role at the beginning like counter detectors and later like timing detectors (tRPCs) thanks to developing its technology. Therefore, it is possible to use RPCs to perform particle tracking. These days, it is one of the most widely used detectors in particle physics experiments. These detectors, which were first produced in the early 1980s [34, 35], can cover large detection areas at a low cost per information channel. RPCs have commonly been used as counter trigger detectors in experiments like ATLAS [36].

Particle detection necessitates the use of a detector with a few distinct characteristics. The time resolution, for instance, must be in the order of a nanosecond. We will be able to classify and assign an individual track to each particle with this resolution and we will be able to rule out any random coincidences [37].

2.2 Parallel plate chamber detectors

The RPCs belong to gaseous detectors. That implies the particles interact with the detector in a gaseous medium. Whenever a charged particle crosses the detector, a signal is generated as a result of this interaction.

The number of ionizations (primary clusters) per unit of length follows a Poisson distribution, assuming that ionization's probability is independent of the previous collision. The average number of clusters, given by $\bar{n} = g/\lambda$, varies depending on the gas mixture used, with g being the length travelled by the particle within the gas and λ being the

USC
UNIVERSIDADE DE SANTIAGO DE COMPOSTELA

mean free path. It can range from less than one cluster per millimeter to about ten clusters per millimeter [38]. Also, worth noting that more than one electron may be expelled in a single collision, implying that the cluster size is represented by distribution. According to simulation results [38], more than 80% of the clusters in a tRPC configuration using a standard gas mixture have a size of one.

The origin of the RPCs is the Parallel Plate Chamber (PPC) filled with a gas, which consists of two parallel metallic electrodes operated at high voltage to provide a uniform electric field across its volume. Electron-ion pairs are formed when a charged particle passes between two electrodes. At least one electrode must be coated with a high resistivity material to prevent discharges or perturbations in gas ionization. The released electrons are accelerated towards the anode if the field is high enough, regaining enough energy to induce more ionizations in a cascading process known as avalanche (gas multiplication [39]). This simple method will produce measurable charge from a reduced number of initial charges. The high-speed drifting electrons emit a prompt signal that can be used for timing purposes, while the ions drift to the cathode at much slower speeds due to their higher masses.

The first application of a parallel plate geometry for a timing device was developed in 1948 and was named after its inventor, Keuffel Sparks [40]. It had a time resolution of $1\,ns$ but, due to the massive amount of charge emitted by the sparks, a long recovery time of several milliseconds was needed, limiting the device's rate capability.

In 1971, the first parallel geometries with electrodes covered in high resistivity materials were operated [41]. Working in quenched spark mode, Pestov's team used a highly resistive material (glass) to restrict the progress of the spark produced. Despite its great technological difficulty, the so-called 'Pestov counter' [41] eventually achieved a time resolution of $25\,ps$.

The Resistive Plate Chambers (RPCs) [35] developed by R. Santonico and R. Cardarelli solidified this technology in 1981, as mentioned

USC UNIVERSIDADE DE SANTIAGO DE COMPOSTELA

before. The idea was to overcome the Pestov counter's difficulties while maintaining its core virtues.

The high resistivity material (on the order of $10^{10}\ \Omega.cm$) prevents sparks from forming and prevents the avalanche from spreading throughout the gas. As a result, it aids in the cleaning of the gas after the avalanche finishes.

The time it takes for the high resistivity material to recover its properties is the main limitation of RPC detectors, particularly in the early models of Cardarelli [34]. When a particle interacts with the gas and generates a signal, it takes some time for the detection region to clean up the avalanche. This time is measured in milliseconds and varies depending on the material. Because of the avalanche, the effective electric field is weaker at this period. As a result, there is some dead time in the detector, which affects the time resolution. Indeed, if the particle flux is high compared to the RPC's dead time, some interactions will be lost, which will reduce the detector's efficiency. Multiple gas gaps are used in modern RPCs to increase the probability of particle-gas interaction and thus improve efficiency and time resolution see Figure 2.1. The increase in efficiency is roughly expected to be [42]

$$\varepsilon = 1 - (1 - \varepsilon_n)^n \tag{2.1}$$

where n denotes the number of gaps and ε_n is the efficiency per single gap. Typical values of the single efficiency, ε_n are of the order of 75% as displayed in [43].

The time resolution, on the other hand, can be estimated by [43].

$$\sigma t = \frac{\sigma_{t,n}}{\sqrt{n}} \tag{2.2}$$

USC
UNIVERSIDADE DE SANTIAGO DE COMPOSTELA

where the behavior of the contributions to the total fluctuations is presumed to be infinitesimal and thus the time response is Gaussian.

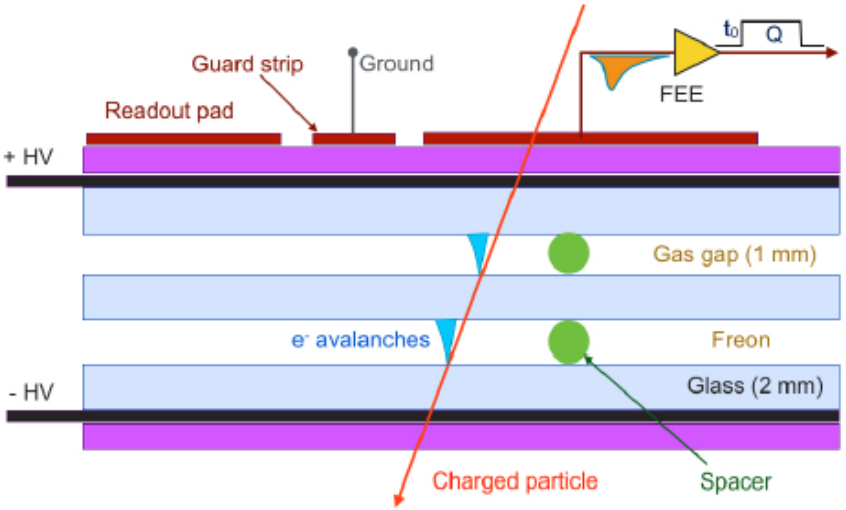

Figure 2.1: shows a schematic of an RPC detector. In this case, there are two $1\,mm$ gas gaps. The gas ionization causes electrical avalanches, which emit a signal sent to the read-out electronics.

Different gases, such as Argon mixtures, were used as an active medium in the first RPC models. Tetrafluorethane $(C_2H_2F_4)$[2], mixed with other gases such as isobutane or sulphur hexafluoride, is the most commonly used gas in modern RPC detectors. The proportions of the mixture are essential for controlling avalanches and the detector's efficiency. The ATLAS and CMS experiments, for example, used RPC detectors with a gas mixture of $95.2\%\ C_2H_2F_4$, $4.5\%\ i-C_4H_{10}$ and $0.3\%\ SF_6$ [44]. The existence of non-environmentally friendly gases like SF_6 and $C_2H_2F_4$ is one of the significant drawbacks of this gas mixture. Alternative gas mixtures based on Helium have recently been proposed [45]. The use of a closed-circuit gas system is also a

[2] Freon sometimes is used as a generic name to any fluorocarbon. The chemical formula of the Freon-134a (R-134a) is $C_2H_2F_2$.

USC UNIVERSIDADE DE SANTIAGO DE COMPOSTELA

reasonable solution. This mechanism extracts the impurities in the gas and it is not released into the atmosphere [46].

2.3 Operation modes

The RPC detectors can operate in one of two modes: avalanche or streamer. The only difference between the two modes is the intense of the avalanche.

2.3.1 Streamer mode

A streamer is a process that differs from avalanche multiplication (see section 2.2). It releases a large amount of charge compared to a regular avalanche process; therefore, it limits the rate capability that becomes a potential problem for RPCs operated in this mode. A high operation voltage is required. The charge produced by the secondary ionizations is so high that it distorts the electric field, ultimately causing a streamer in the detector gas. Compared to the avalanche mode, this mode provides more significant signals that can be discriminated against without amplification, simplifying the readout electronics. RPCs in streamer mode are well suitable for experiments that operate at low rates, such as BELLE at KEK, which operates at 1 Hz/cm^2[47], or BaBar at SLAC [48]. And also, for cosmic rays experiments as ARGO at YangBaJing [49].

This mode was previously known as ‘spark mode’ [50], but it is probably not a good choice and the term ‘streamer mode’ has gained popularity [51].

2.3.2 Avalanche mode

In 1993 [52], the avalanche mode was implemented to increase rate capacity by lowering the charge released per avalanche ($0.2\ pC$). It was also known as ‘proportional mode’ [51], but that was too ambitious, so the word ‘avalanche mode’ prevailed [50]. In this mode, lower-amplification gas mixtures are used, necessitating integrating high-gain

USC UNIVERSIDADE DE SANTIAGO DE COMPOSTELA

fast amplifiers into the Front-End Electronics (FEE) to compensate for this effect, making the FEE more complex than in the streamer mode.

RPCs that operate in avalanche mode has been used in high-energy physics like ATLAS [53] or CMS [54] at the Large Hadron Collider (LHC). They are known as 'trigger RPCs,' and their rate capabilities range from 100 to 1000 Hz/cm^2. Timing detectors have also benefited from these RPCs, such as ALICE [55] at LHC or FOPI at GSI [56].

Modern RPC detectors use avalanche mode with a multigap configuration. With these detectors, time resolutions of the order of 90 ps and below are possible. Because of their high time resolution, RPC detectors are ideal for particle tracking in high multiplicity environment.

An RPC detector, for example, is depicted schematically in Figure 2.1. A two-gap configuration in avalanche mode corresponds to this particular case. R-134a is used to fill each gas gap, which has a 1 mm width. With 2 mm of glass, the gas gaps are isolated. The two gaps are inside a high voltage created by two parallel planes. Ionization occurs within the gas gaps when a charged particle passes through the RPC. As a result, an avalanche occurs. The electric field is affected by the avalanche in the gas gap if its scale is large enough. The anode will attract the electrons in the gas, while the cathode will attract the ions. As a result, a perturbation in the electric field occurs around the avalanche's development region. This generates a signal that can be read. The induction is produced in a rectangular region in this case. Other methods of detection divide the detection area into layers of strips. The electronic devices process this signal and convert it to relevant physical information.

2.4 Timing RPC (tRPC)

The relevance of gap mechanical homogeneity concerning high precision timing and the development of fast amplification electronics enabled the operation of a multi-gap RPC in avalanche mode with tiny

USC UNIVERSIDADE DE SANTIAGO DE COMPOSTELA

gaps of less than $1\,mm$ and glass electrodes at fields as high as $100\,kV/cm$. In the year 2000, this was accomplished by P. Fonte, A. Smirnitski and M.C.S. Williams [57]. A new branch of the field was opened, with a time resolution of $120\,ps$, while the ability to go down to $50\,ps$ for small detectors was soon verified [58]. The use of large size tRPCs was eventually validated [59], with resolutions below $100\,ps$ and good homogeneity.

The high resistivity material has caused further changes in the mechanical structure of the RPCs. Originally, Bakelite electrodes were applied to prevent sparks from generating inside the gas. Nowadays, for timing RPCs a type of glass is preferred as a standard with a resistivity of $10^{12} - 10^{13}\ \Omega.cm$.

The parallel plates must be exposed to a high voltage. It must be strong enough to achieve high efficiency, but not so high that streamers are produced and the avalanche mode is broken. There are tRPCs that work in avalanche mode with $100\,kV/cm$ voltages and a low probability of streamers. By this reason, usually, multigap detectors are built in order to increase their total efficiency.

2.5 The TRASGO project

The characteristics of primary cosmic rays with an energy of more than $100\,TeV$ can only be studied indirectly using detector arrays on the Earth's surface. Only a small fraction of these particles reaches the ground on surfaces ranging from 0.1 to $100\,km^2$ [60]. Because of the Insufficient information about the primary interaction and the low density of particles at the detection level, event-by-event analysis is extremely difficult. Therefore, simulation programs are required for this type of analysis.

After observing cosmic rays in the HADES spectrometer at GSI (Institute in Darmstadt, Germany) [61], the Trasgos (acronym TRAck sreconStructinG mOdule) were suggested. The goal was to create a high-performance, affordable cosmic rays detector sensitive to muons

USC UNIVERSIDADE DE SANTIAGO DE COMPOSTELA

and electromagnetic showers and based on RPC detectors. Because of the good time and spatial resolutions that the detector provides, the Trasgos are ideal for studying the properties of cosmic rays. As a result, they are perfect detectors for particle tracking and more accurate reconstruction of secondary cascades.

The Trasgo is operating autonomously and allows to assemble or overlap many detectors to create larger constructions. Figure 2.2 shows multiple Trasgos representations. The simplest model (a) shows a single Trasgo with one RPC detector plane above the other. The simplest arrangement can be configured to cover a wider area (b) or arranged on top of the other as a column to improve efficiency and resolution (c).

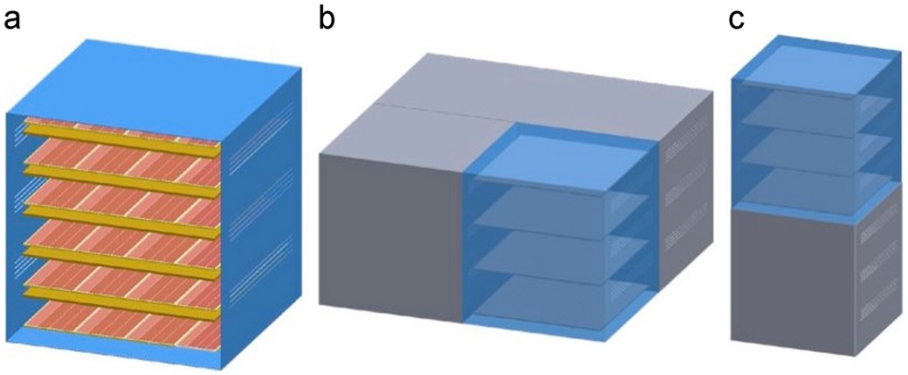

Figure 2.2: A Trasgo with several RPC detector planes arranged one on top of the other inside the main box (a), many RPC detectors placed to cover more extensive surfaces (b) and one on top of the other as a column to improve resolutions and efficiency (c). The figure is taken from [61].

And also, TRASGO would provide for a more precise and better reconstruction of air shower properties, either working stand-alone or in large surface arrays.

Now, in this subsection, we present some of the TRASGO family, starting with the TRAGALDABAS detector.

USC
UNIVERSIDADE DE SANTIAGO DE COMPOSTELA

2.5.1 The TRAGALDABAS detector

The TRAGALDABAS detector (acronym TRAsGo for the AnaLysis of the nuclear matter Decay, the Atmosphere, the Earth B-Field[3] And the Solar activity) [62] is a cosmic rays telescope of the Trasgo family.

The detector is located in the LabCAF research laboratory of the Faculty of Physics at the University of Santiago de Compostela (USC). The detector is devoted to analyzing the structure of the cosmic rays, the atmospheric properties and solar activity. It was installed on the first floor of a two-floor building and so will reject a fraction of the electromagnetic component of the showers in the geographical coordinates (N 42° 52' 34", W 8° 33' 37") at about $260\ m$ above sea level [4, 63]. Since 2013, the detector is taking data regularly with a rate of about 7 million registered events per day, around 80 triggers per second.

The TRAGALDABAS detector is shown schematically in Figure 2.3. It comprises four RPC planes with an external area of $1.285 \times 1.650\ m^2$ separated into rectangular pads. Only three of the four detectors are currently fully instrumented and operational.

The TRAGALDABAS RPCs were designed and built at the LIP-Coimbra using the same technology as the P. Auger observatory [64]. The RPC's internal structure is similar to that seen in Figure 2.1. They are composed of two 1 mm gaps filled with R-134a (Freon) gas. A high voltage of $\pm 5600\ V$ is applied between the outer sides of the RPC at each plate, equating to $5600\ V/mm$ in each gap. In avalanche mode, this voltage creates an electric field. Copper pads are used to read out the induced signals.

The TRAGALDABAS Front-End Electronics (FEE) were developed at GSI for the HADES experiment. The induced signals in

[3] where B refers to the Earth's magnetic field.

USC UNIVERSIDADE DE SANTIAGO DE COMPOSTELA

the pads for each RPC are first amplified and integrated and then digitized in 4-channels daughter boards (DB). Every 8 DBs are connected to a motherboard (MB) that provides low voltage and the output for both the digital read-out and the trigger signals[4]. The four MBs for each RPC plane collected all the signals and sent them to a read-out board (TRB.V2) before registering on a computer (see Figure 2.4).

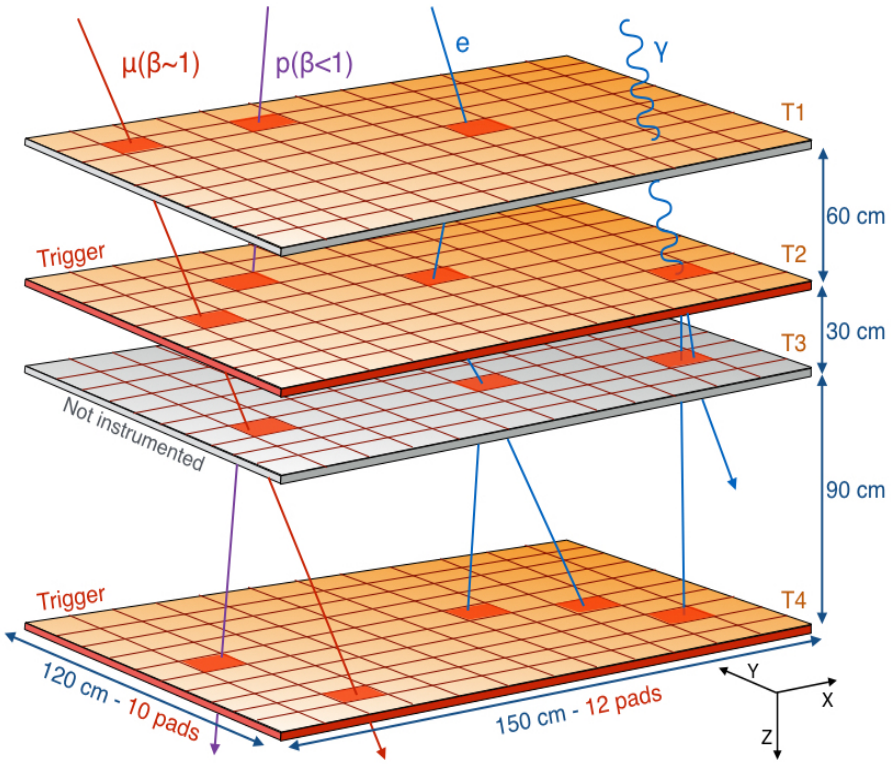

Figure 2.3: The TRAGALDABAS detector is depicted schematically. It is made up of four RPC planes that are separated into rectangular detection pads.

[4] The trigger signal is the coincidence signal between any two RPC planes.

USC UNIVERSIDADE DE SANTIAGO DE COMPOSTELA

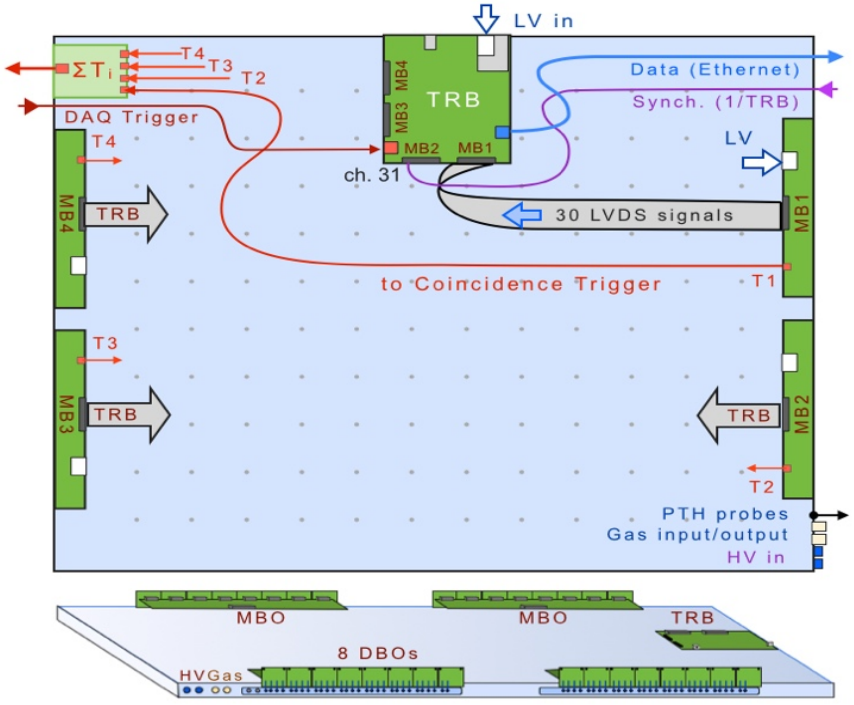

Figure 2.4: A single plane's FEE electronics layout. Four MBs receive the amplified and digitized signal from the DBs, read out by a TRB and sent via Ethernet to the acquisition computer.

The various materials of TRAGALDABAS RPC are listed in Table 2.1 [63], together with their width (in mm) and radiation length (in cm). The materials respectively are aluminum (Al), foam, copper (Cu), Printed Circuit Board (PCB) with a thin layer of Cu foil laminated (FR4), metacrilate, glass and R134a (Freon) gas gap.

Furthermore, later in October 2020, a layer of lead was installed with around $1 - 2$ cm of thickness under the third plane to improve the detection technique, tracking and identification capabilities of the detector.

USC
UNIVERSIDADE DE SANTIAGO DE COMPOSTELA

Table 2.1: Components of RPC plane for TRAGALDABAS, as well as their width and radiation length.

RPC layout	Width(mm)	X_0(cm)	ΔX_0
Al	3	8,9	0,034
Foam(dens=0.3)	8,7	142,0	0,006
Cu	0,03	1,4	0,002
PCB (FR4)	1,57	31,8	0,005
Metacrilate	1	40,8	0,002
Glass	1,9	3,2	0,059
Gas: R134a	1	26,5	0,004
Glass	1,9	3,2	0,059
Gas: R134a	1	26,5	0,004
Glass	1,9	3,2	0,059
Metacrilate	1,0	40,8	0,002
Al	3	8,9	0,034
Total	26		~0,27

where ΔX_0 is the width divided by the radiation length X_0.

In the following subsection, we will present the second member of the TRASGO family, which is the TRISTAN detector.

2.5.2 The TRISTAN detector

TRISTAN (TRasgo para InveSTigaciones ANtarticas) does not look much different from TRAGALDABAS in design and construction. The TRISTAN detector is a cosmic rays detector based on Resistive Plate Chambers (RPC) technology. It consists of three RPCs, each with an active area of $120 \times 150\ cm^2$, which define the detector instrumented with the fast Front-End Electronics (FEE) [65,

USC UNIVERSIDADE DE SANTIAGO DE COMPOSTELA

66]. Moreover, the detector was built in Coimbra using the expertise of the mechanical workshop and detector laboratory teams of LIP [67], including the high voltage (HV) power supplies and the gas system with monitoring capability.

Figure 2.5 [68] presents the three planes of RPCs of the detector with a layer of lead with a thickness of 1 cm placed under the second plane covering the central 12 pads around 40% of the plane surface.

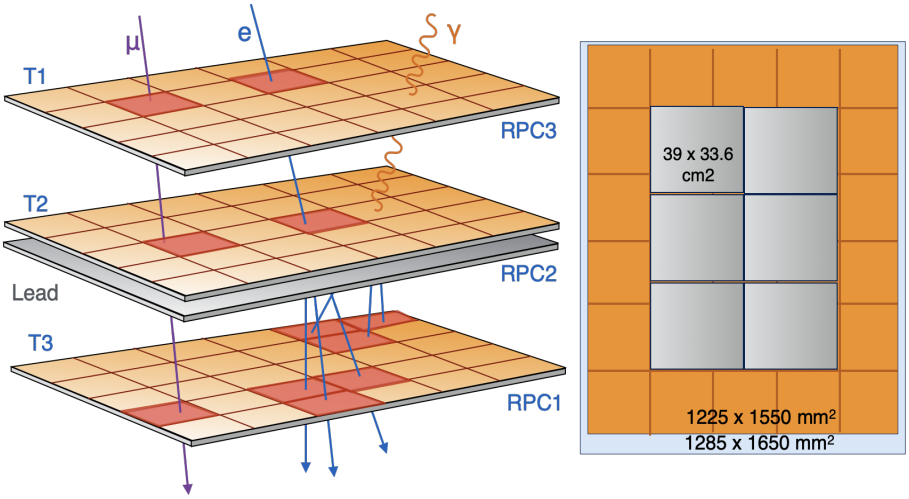

Figure 2.5: Left: the path of different particles (electrons, muons, gammas) across the active size of the detector; right: a layer of lead is placed under the second plane.

The internal configuration of each RPC plane is depicted in Figure 2.6. Three 2 mm thick layers of glass with a 1 mm gap between them are placed inside a gas-tight methacrylate box to make each plane. The glass layers are coated with a conductive layer where the high voltage of $\pm 5600\ V$ is applied. To compensate for the slight leak of the gas, Freon gas (R134a) is used to flow through each RPC. A total of 90 channels, 30 pads $24 \times 25\ cm^2$ per plane, were read out by the TRB3 readout board with a timing resolution of around $20\ ps$ [69]. Furthermore, there are grounded guard rings 6 mm wide separate the pads to prevent crosstalk.

USC UNIVERSIDADE DE SANTIAGO DE COMPOSTELA

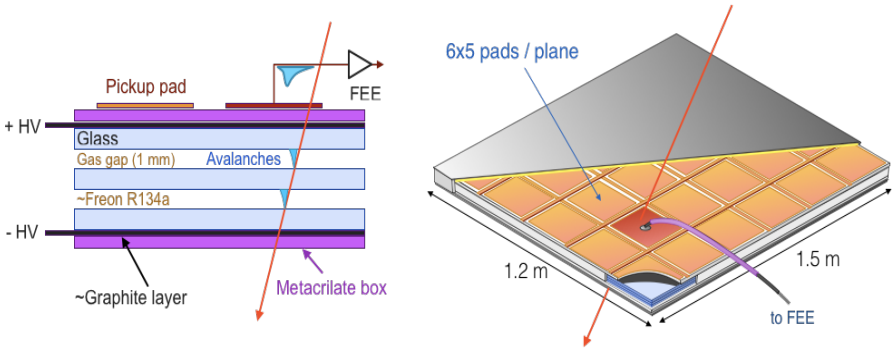

Figure 2.6: The internal layout of the RPC.

Charged particles traveling through the first and second planes will interact with the layer of lead before reaching the third one. This layer was introduced to impose electromagnetic showers related to gammas and electrons to improve electron-muon separation.

In addition, each plane has a set of sensors, five of them for the temperature and the other two for the pressure and humidity, respectively. A high voltage (HV) power supply has been connected to each plane. All of them are auto-calibrated to keep the gain nearly constant by pressure and temperature [5, 70]. As a result, any slight changes in these variables are compensated by a change in the HV increasing or decreasing. Furthermore, two independent sensors, one an optic sensor and the other a pressure sensor, continuously check the gas flow. The optic sensor counts how many bubbles are formed per minute inside the bubblers, while the other monitors pressure variations. We can calculate the high voltage according to the following equation:

$$HV[V] = \frac{E/N\,[Td]\,.\,d_{gap}[cm]\,.\,P[mbar]}{0.01138068748\,.\,T[K]} \qquad (2.3)$$

where E/N is the reduced electric field in the Townsend unit, d_{gap} is the thickness of the gap, P is the pressure and T is the temperature.

USC UNIVERSIDADE DE SANTIAGO DE COMPOSTELA

The TRBV3 readout board developed by GSI is the foundation of the TRISTAN detector's data acquisition system (DAQ). As mentioned before, each RPC has 30 channels connected to 8 daughter boards (DBs) connected to a single motherboard (MB) per plane. The same TRB was used to connect all motherboards (MBs) for all the planes. The acquisition trigger is coincidentally between at least one hit in the first plane and one in the third plane.

The TRISTAN detector achieved three journeys and collected data while crossing the Atlantic Ocean on board the Sarmiento de Gamboa and BIO Hesperides oceanographic vessels along the region where the South Atlantic Magnetic Anomaly (SAMA) is located. SAMA is a weakness in Earth's magnetic field over South America and the South Atlantic, which allows the inner Van Allen radiation belt to dip down closer to the atmosphere. The trips took place between November 2018 and December 2019.

As part of the Antarctic Cosmic-Ray Observatory (ORCA) [71]. The first two journeys that the detector made from November 2018 to April 2019 onboard the Spanish vessel Sarmiento de Gamboa between Vigo, Spain $42^{\circ}N$ and Punta Arenas, Chile $53^{\circ}S$, measuring the cosmic-ray rate continuously throughout the Atlantic crossing. After that, the detector was installed and operated in facilities of the University of Santiago de Compostela (USC), Spain, for a short time, around three weeks from the middle of October 2019 to the first week of November 2019. Figure 2.7 shows the detector installed in the Spanish boat Sarmiento de Gamboa. The results of these trips are published in 36th International Cosmic Ray Conference (ICRC 2019) [72].

The last journey of TRISTAN was from $38^{\circ}N$ Cartagena, Spain, to $53^{\circ}S$ Punta Arenas, Chile, on board of BIO Hesperides oceanographic vessel. It was the most extended trip with more than one month of data.

USC
UNIVERSIDADE DE SANTIAGO DE COMPOSTELA

Figure 2.7: The TRISTAN detector in the Sarmiento de Gamboa oceanographic vessel.

Thus, the last latitudinal scan finished. The detector TRISTAN was installed in December 2019 at the Spanish Antarctic Base Juan Carlos I ($62^{\circ}S$) in Livingston Island, joining the other detectors of ORCA. Moreover, the results of this trip are published at 37^{th} International Cosmic Ray Conference (ICRC 2021) [68].

USC UNIVERSIDADE DE SANTIAGO DE COMPOSTELA

3 Tracking with Timing (TimTrack) algorithm

3.1 Introduction and motivation

The reconstruction of the paths of the particles associated with a specific event across the experimental setup is one of the essential aspects of data processing. The ionization of a material medium causes a charged particle to lose some of its energy when it travels through it. As a result, a signal verifying the particle's detection might be conceivable. A particle detector operates in this way at its most basic level. We keep track of all particle interactions with our detectors for each occurrence. This data is necessary for describing the particle's trajectory. These trajectories are crucial for estimating the physical characteristics of our detectors (efficiency, calibration and acceptance) and for identifying the nature of particles and performing a more extensive physics investigation.

Not all detectors are built to deliver the same level of information. For example, we can include detectors that offer accurate information on the particle's velocity in our experimental setup. Some detectors provide data on the position of the interaction. A set of various detectors gathering diverse forms of information is standard in a typical experimental setup. This information must be processed to obtain a good description of the trajectories or other variables and it is the beginning point of the data analysis.

Particle trajectory information can be obtained using a variety of techniques and algorithms. Traditionally, tracking analysis is carried out in two steps: first, spatial data determines all possible particle trajectories in the detector. After then, the time information is used to

USC UNIVERSIDADE DE SANTIAGO DE COMPOSTELA

cut the events that are not compatible with the time. This two-step procedure, which treats time and spatial variables separately, has been in use for decades. One of the key reasons for this is that early detectors had inadequate or perhaps non-existent temporal resolution. In that case, a combined analysis of the variables is not necessary. Investigating correlations between spatial and time variables is impossible due to a lack of knowledge regarding time resolution.

The new RPC detectors can provide accurate spatial and temporal information. As a result, suggesting new tracking methods that eliminate the old two-step procedure in favor of a single-step analysis seems fair.

The TimTrack algorithm is described in detail in this chapter. J. Garzón and P. Cabanelas [73, 74] devised the method, which has been adopted as the Trasgo family of detectors' reference reconstruction method. In contrast to the methods outlined above, TimTrack reconstructs trajectories utilizing spatial and temporal information in a single step. This is considerable because the approach can handle data from various detectors regardless of the measured variable. If our setup, for example, comprises a combination of RPCs and plastic scintillators, the approach will combine all data and provide a concise description of the system.

TimTrack is built on the least-squares method, one of the algorithm's essential advantages from a mathematical standpoint. Because a full matrix description of the approach is possible, this information allows for a more comfortable formulation of the equations.

There are three sections to this chapter. To begin, we'll go over the TimTrack method's general concept. The models utilized in real-world physical situations are described in the second section. The method's numerical examples are shown in the third section.

USC
UNIVERSIDADE DE SANTIAGO DE COMPOSTELA

3.2 Description of the method

The least-squares method is used in the TimTrack algorithm. G. Audi's work [75] provides a detailed matrix explanation of this technique and is used as the basis for TimTrack's mathematical formulation.

TimTrack's purpose is to determine all of the parameters related to particle propagation using a set of experimental data as input. These parameters are stored in an object called **saeta**[5] (**s**m**a**llest s**e**t of p**a**rameters), where a saeta is a vector composed of the minimum of parameters required to describe a particle's trajectory:

$$\boldsymbol{s} = (X_0, X', Y_0, Y', T_0, S) \tag{3.1}$$

where $(X_0,\ Y_0)$ are the coordinates of the trajectory in the reconstruction plane (the origin), the $(X',\ Y')$ are the slopes respect the x and y propagation axes along the z-axis, $\Delta x/\Delta z$ and $\Delta y/\Delta z$, the T_0 is the time at which the particle crossed the plane referred to an external counter and S is the *slowness*, that is, the inverse of the velocity of the particle, $S = 1/V$.

The equation (3.1) shows the simplest form of a saeta that describes the propagation of a particle. With these six parameters, the trajectory of a particle can be fully explained. Depending on the situation, the parameters can be different and other parametrizations of the problem can be done.

As a result, the following are the fundamental features that distinguish TimTrack from other tracking or reconstruction algorithms:

- TimTrack always works with the six parameters that define a particle's movement: two coordinates, two projected slopes, the particle's time in a particular reference plane and the inverse of the particle's velocity. Working with all of the available parameters allows

[5] saeta, from Latin sagitta, arrow.

USC UNIVERSIDADE DE SANTIAGO DE COMPOSTELA

for the early stages of the reconstruction process to include the relationships that exist between them. Other processes, such as energy loss or multiple scattering and constraints, such as vertex location or mass, can be added to the fit in a reasonably simple method at the start. All these features make the algorithm more powerful and more sensitive.

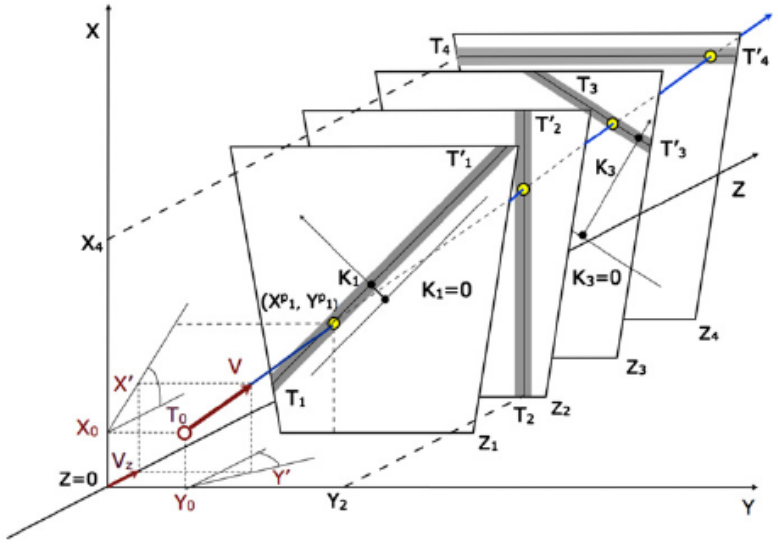

Figure 3.1: A saeta in a generic strip detector is shown geometrically. A saeta (blue line) represents several kinematic characteristics related to particle propagation through the various components of our experimental setup. [74] provided the illustration.

- TimTrack can deal with uncalibrated data and integrate the calibration steps as part of the algorithm if enough data is provided.

- TimTrack is designed in a simple matrix formalism that treats parameters and calibration constants in the same way. It means that well-known parameters can be fixed at any moment. The procedure can find calibration constants or analyze any relationships between them and the set parameters.

USC UNIVERSIDADE DE SANTIAGO DE COMPOSTELA

Figure 3.1 depicts an experimental setup with four plane parallel detectors as an example. When a particle passes through the setup, we get spatial and temporal coordinates from each detector. The parameters are presented in equation (3.1) as a saeta vector for the particle's propagation when the reconstruction is completed with TimTrack. The slope of the trajectory along the propagation direction, z, is represented by the X' and Y' parameters in the figure.

The TimTrack approach essentially connects two spaces: data and parameters. This link is made under the assumption that our measured data follows a specific model dependent on our parameters. To summarize, the TimTrack approach requires the following:

1. A set of experimental data. They are grouped into a $\boldsymbol{d}$ vector.

2. A set of parameters. They are defined as saeta $\boldsymbol{s}$.

3. A model that connects the two spaces: $\boldsymbol{m} = \boldsymbol{d}(\boldsymbol{s})$.

The dimension of $\boldsymbol{m}$ equals the dimension of $\boldsymbol{d}$, as seen above. The dimension of both spaces is referred to as n_d. It is essential to know that n_d refers to the number of coordinates that make up each element, not the size of the space. In general, we have a total number of parameters n_s that must satisfy $n_d \geq n_s$.

By minimizing a mathematical function, S, the parameters gathered in a saeta are derived. The statistical distance between the measured data and the model is referred to as this operator in the least-squares approach. As a result, the parameter values must ensure that the residual, or distance between the model and the experiment, is as little as possible.

The functions we propose have the following mathematical form:

USC
UNIVERSIDADE DE SANTIAGO DE COMPOSTELA

$$S = \sum_{i}^{n_d} \left(\frac{d_i - m_i(\boldsymbol{s})}{\sigma_i} \right)^2 \tag{3.2}$$

where σ_i is the uncertainty associated with the i variable. The method's purpose is to find the parameter values that reduce this observable to the minimum value.

The latter equation can be expressed in a matrix form [75, 76] as:

$$S = (\boldsymbol{d} - \boldsymbol{m}(\boldsymbol{s}))' \,.\, W \,.\, (\boldsymbol{d} - \boldsymbol{m}(\boldsymbol{s})) \tag{3.3}$$

where W is the matrix that contains the statistical weights of the variables (σ_i) or the inverse of the variance matrix and the apostrophe represents the transpose operation over a vector or matrix.

According to least-squares method (LSM), the set of parameters s that best describes the model is:

$$\frac{\partial S}{\partial \boldsymbol{s}} = 0 \tag{3.4}$$

The modeled data $\boldsymbol{m}(\boldsymbol{s})$ Jacobian matrix with respect to $\boldsymbol{s}$

$$G = \frac{\partial \boldsymbol{m}(\boldsymbol{s})}{\partial \boldsymbol{s}} = \begin{pmatrix} \frac{\partial m_1(s)}{\partial s_1} & \cdots & \frac{\partial m_1(s)}{\partial s_{ns}} \\ \vdots & \ddots & \vdots \\ \frac{\partial m_{nd}(s)}{\partial s_1} & \cdots & \frac{\partial m_{nd}(s)}{\partial s_{ns}} \end{pmatrix} \tag{3.5}$$

we can use a linear expansion to express the model that follows the data:

USC UNIVERSIDADE DE SANTIAGO DE COMPOSTELA

$$\boldsymbol{m}(\boldsymbol{s}) = G\,.\boldsymbol{s} + \boldsymbol{g}_0 \tag{3.6}$$

where $\boldsymbol{g}_0$ is the difference between $\boldsymbol{m}(\boldsymbol{s}) - G.\boldsymbol{s}$. As a result, S can be written as a function of the matrices G and $\boldsymbol{g}_0$:

$$\begin{aligned} S = {} & (G\boldsymbol{s})'\,.W\,.(G\boldsymbol{s}) - 2(G\boldsymbol{s})'\,.W\,.(\boldsymbol{d} - \boldsymbol{g}_0) \\ & + (\boldsymbol{d} - \boldsymbol{g}_0)'\,.W\,.(\boldsymbol{d} - \boldsymbol{g}_0) \end{aligned} \tag{3.7}$$

The following definitions can be added to this expression to make it more comfortable to read:

$$K = G'\,.W\,.G \tag{3.8}$$

$$\boldsymbol{a} = G'\,.W\,.(\boldsymbol{d} - \boldsymbol{g}_0) \tag{3.9}$$

$$\boldsymbol{s}_0 = (\boldsymbol{d} - \boldsymbol{g}_0)'\,.W\,.(\boldsymbol{d} - \boldsymbol{g}_0) \tag{3.10}$$

The functional assumes the following form with these definitions:

$$S = \boldsymbol{s}'\,.K\,.\boldsymbol{s} - 2\,.\boldsymbol{s}'\,.\boldsymbol{a} + \boldsymbol{s}_0 \tag{3.11}$$

Now, we need to minimize the chi-square functional S by applying the condition of the equation 3.4, yields:

$$\boldsymbol{a} = K\,.\boldsymbol{s} \tag{3.12}$$

consequently

$$\boldsymbol{s} = K^{-1}\,.\boldsymbol{a} \tag{3.13}$$

The called *sea* equation is obtained by calling $\mathcal{E}$ to the inverse of the K matrix:

USC UNIVERSIDADE DE SANTIAGO DE COMPOSTELA

$$\boldsymbol{s} = \mathcal{E}\,\boldsymbol{a} \tag{3.14}$$

At this point, must note the following observations:

1. The K matrix is also known as the *configuration matrix*. It is always a squared symmetric matrix of the same dimension as the set of parameters, n_s. If the model is linear, it is solely affected by the essential properties of the detectors and the uncertainty in the experimental data.

2. The matrix containing the uncertainties of the parameters $\boldsymbol{s}$ is the inverse of K. As a result, it's known as an *error matrix*:

$$\mathcal{E} = \left(\frac{1}{2}\frac{\partial^2 S}{\partial \boldsymbol{s}^2}\right)^{-1} = K^{-1}$$

3. Because $n_d \geq n_s$, the K matrix can always be inverted and the minimization problem can be solved. The problem has a unique and exact solution if $n_d = n_s$.

4. The $\boldsymbol{a}$ vector is called the *reduced data vector*. It converts the n_d data in a vector of dimension n_s.

5. $\boldsymbol{s}_0$ is always a scalar quantity.

After all experimental data has been reduced to $\boldsymbol{a}$ vector, the K matrix connects the data and parameter spaces.

One of the key benefits of the TimTrack approach is that it may be utilized with a variety of detectors simultaneously. Each experiment is made up of a collection of detectors that measure various variables. We can have, for example, Cherenkov detectors that can accurately measure velocity with a Time-Of-Flight detector that can measure time. A model $\boldsymbol{m}_i$ is used to characterize each of these detectors.

USC UNIVERSIDADE DE SANTIAGO DE COMPOSTELA

We can characterize the entire array of detectors by solving a more generic sea equation using the TimTrack technique. There are a few things to consider:

1. In our experiment, we will assume that we have n detectors. A unique model mi is assigned to each detector.

2. The models can be various because they depict different experimental data. Each detector, in general, has its own K_i matrix and $\boldsymbol{a}_i$ vector.

3. The sum of the individual vectors and matrices yields the total K matrix and total $\boldsymbol{a}$ vector that describe the entire set-up of the experiment.

4. As a result, the general *sea* equation becomes:

$$\boldsymbol{s} = \left(\sum_i^n K_i\right)^{-1} . \left(\sum_i^n \boldsymbol{a}_i\right) \tag{3.15}$$

In figure 3.2, you can see a schematic representation of the TimTrack applied to several detectors. Each detector in the figure measures different types of data. The first detector measures position (x, y), followed by the second detector (x, t), the third detector (x, y, t) and so on. As a result, each model produces a matrix K and a vector $\boldsymbol{a}$ for each set of data. The solution of the general *sea* equation (3.15) is saeta, which describes the path through all of the detectors.

USC UNIVERSIDADE DE SANTIAGO DE COMPOSTELA

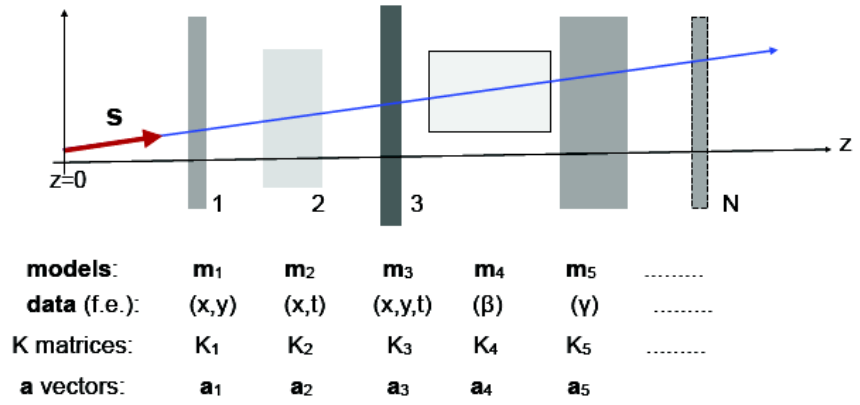

Figure 3.2: Scheme of the modeling of the matrices required in the TimTrack algorithm that applied to the different N number of detectors, each of them following a specific model for their measurements.

3.2.1 Non-linear TimTrack

If the data is described by a non-linear model, an iterative method should be used to solve the problem. The vector $\boldsymbol{g}_0$ has no dependency on the parameters in the linear case. In a nutshell, this vector represents how much our data deviates from linearity. Because the model is linear, its derivatives are constant and the Jacobian matrix's components are also constant values. As a result, the solution is not required for these mathematical objects.

In the non-linear case, however, this reliance occurs. We must iterate until convergence is discovered to get the global minimum. Figure 3.3 depicts a simple instance of this iterative process, with a proposed solution at each iteration.

At this point, we will use J. Cuenca's [77] description and notation for the non-linear case. The same method is used to get the global minimum of a function with several variables. The function to be minimized has a nearly identical form. The variance lies in the objects' dependency:

USC UNIVERSIDADE DE SANTIAGO DE COMPOSTELA

$$S(\boldsymbol{s}) = \boldsymbol{s}' \,.\, K_0 \,.\, \boldsymbol{s} - 2 \,.\, \boldsymbol{s}' \,.\, \boldsymbol{a}_0 + k_0(\boldsymbol{s}) \tag{3.16}$$

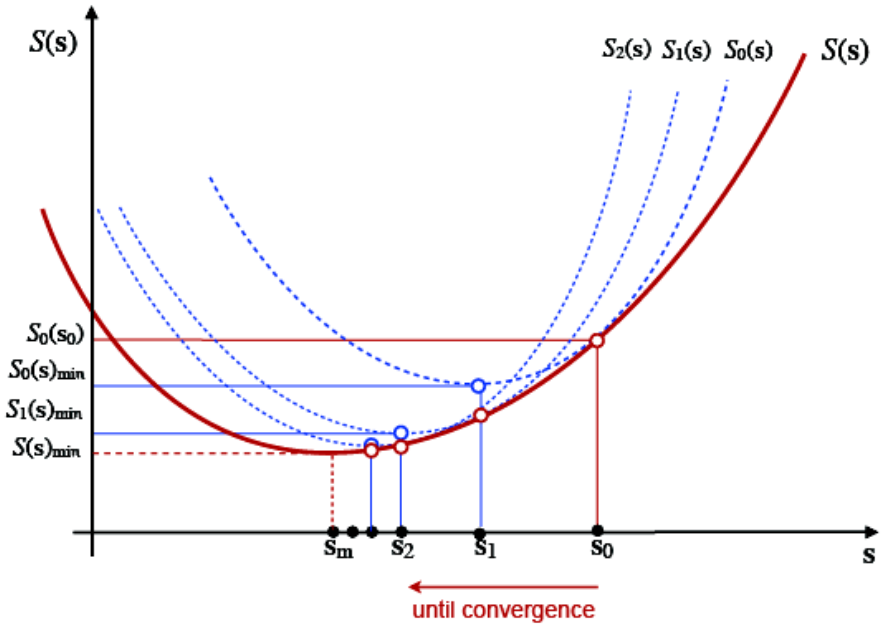

Figure 3.3: Schematic illustration of the TimTrack method's solution search for a non-linear model. The first answer, s_0, is proposed. At each step, the original vector is adjusted until a converged vector s_m is obtained. A global minimum of the functional $S(s)_{min}$ is attained for those parameter values.

Where the objects now have a dependency in $\boldsymbol{s}$:

$$K_0 = G_0' \,.\, W \,.\, G_0 \tag{3.17}$$

$$\boldsymbol{a}_0(\boldsymbol{s}) = G_0' \,.\, W \,.\, (\boldsymbol{d} - \boldsymbol{g}_0(\boldsymbol{s})) \tag{3.18}$$

$$k_0(\boldsymbol{s}) = (\boldsymbol{d} - \boldsymbol{g}_0(\boldsymbol{s}))' \,.\, W \,.\, (\boldsymbol{d} - \boldsymbol{g}_0(\boldsymbol{s})) \tag{3.19}$$

Let us suppose that a set of parameters s_0 is proposed as a solution and it is close to the global minimum that solves our problem. As a result, a Taylor expansion for the functional S about s_0 can be performed:

USC UNIVERSIDADE DE SANTIAGO DE COMPOSTELA

$$S(\boldsymbol{s}) \approx S(\boldsymbol{s}_0) + \left.\frac{\partial S(s)'}{\partial \boldsymbol{s}}\right|_{s_0} . \delta \boldsymbol{s} + \frac{1}{2}\, \delta \boldsymbol{s}' . \left.\frac{\partial^2 S(\boldsymbol{s})}{\partial \boldsymbol{s}^2}\right|_{s_0} . \delta \boldsymbol{s} + \ldots \tag{3.20}$$

where $s = s_0 + \delta s$. Because the minimum must satisfy the condition $S(\delta s) = 0$, we can write:

$$K_0\, \delta \boldsymbol{s} + (K_0 .\ \boldsymbol{s}_0 - \boldsymbol{a}_0) = 0 \tag{3.21}$$

where can you get the parameters δs:

$$\delta \boldsymbol{s} = K_0^{-1} . \boldsymbol{a}_0 - \boldsymbol{s}_0 \tag{3.22}$$

The following are the new parameters:

$$\boldsymbol{s}_1 = \boldsymbol{s}_0 + \delta \boldsymbol{s} = K_0^{-1} .\ \boldsymbol{a}_0 \tag{3.23}$$

As well as the observation that this equation has the same form as (3.13). We may recalculate the new K matrix, the new a vector and so on with these new parameter values. The new values are closer to the minimum and the iterative process continues until convergence is reached. A more generic equation that accounts for the recursive method can be written as follows:

$$\boldsymbol{s}_i = K_{i-1}^{-1} . \boldsymbol{a}_{i-1} \tag{3.24}$$

Convergence is obtained after a few iterations and the differences δs should diminish with each iteration.

To summarize, we must follow the procedures below to find a non-linear TimTrack solution:

USC UNIVERSIDADE DE SANTIAGO DE COMPOSTELA

1. As an initial vector, we suggest a collection of parameters called s_0. In general, this vector should be near the global minimum functional S.

2. After calculating the Jacobian matrix G_0, we calculate the vector $g_0(s)$.

3. We calculate the values of K_0 and a_0 using these two objects as the value of K and a evaluated at s_0.

4. To find a new set of parameters s_1, we use the sea equation.

5. Iteratively repeat the method until convergence is achieved.

3.2.2 Non-linear TimTrack with constraints

Some physical or geometrical properties may constrain the parameters of the s vector, such as energy-momentum conservation.

These parameters boundary conditions can be introduced in three different ways. One option is to apply the constraints to the parameters before performing the calculations. This redefinition could make calculating the Jacobian matrix more difficult, especially if the constraints are not linear. The covariances between the individual parameters are lost while using this method.

Extending the model is the second option to include constraints. Additional equations are used to define the boundary conditions between the parameters. An arbitrary weight factor in the W matrix related to the physical problem's uncertainty is required for this method.

The third possible option is to redefine the functional S to include a set of n_c functions containing the parameter constraints. Lagrange multipliers are used to minimize the function to its simplest form. Restrictions are always given in the following format:

USC
UNIVERSIDADE DE SANTIAGO DE COMPOSTELA

$$f_i(\boldsymbol{s}) = 0 \tag{3.25}$$

If we use the Lagrange multipliers approach and the index i runs to n_c, we must first construct the functional:

$$L(\boldsymbol{s}) = S(\boldsymbol{s}) + 2 \sum_{i}^{n_c} \lambda_i \, f_i(\boldsymbol{s}) \tag{3.26}$$

where λ_i is the set of Lagrange multipliers and for convenience, the number 2 will introduce later. Because the multipliers are arbitrary, adding one more will have no effect on the final solution and, in this case, will simplify the equations.

Using the condition, we will find the bare minimum of the functional:

$$\frac{\partial S}{\partial \boldsymbol{s}} = \frac{\partial}{\partial \boldsymbol{s}} \left[(\boldsymbol{d} - \boldsymbol{m}(\boldsymbol{s}))' \, . \, W \, . \, (\boldsymbol{d} - \boldsymbol{m}(\boldsymbol{s})) + 2 \sum_{i}^{n_c} \lambda_i \, f_i(\boldsymbol{s}) \right] = 0 \tag{3.27}$$

We can use the general non-linear method described in the preceding section to solve this problem. We can suppose the model and restriction functions can be expanded as first-order Taylor series with neglecting the high order terms of the expansion:

$$\boldsymbol{m}(\boldsymbol{s}) \approx \boldsymbol{m}(\boldsymbol{s}_0) + \left. \frac{\partial \boldsymbol{m}(\boldsymbol{s})}{\partial \boldsymbol{s}} \right|_{\boldsymbol{s}_0} d\boldsymbol{s} = \boldsymbol{m}(\boldsymbol{s}_0) + G_0 \, . \, d\boldsymbol{s} \tag{3.28}$$

and

USC UNIVERSIDADE DE SANTIAGO DE COMPOSTELA

$$\boldsymbol{f}(\boldsymbol{s}) \approx \boldsymbol{f}(\boldsymbol{s}_0) + \left.\frac{\partial \boldsymbol{f}(\boldsymbol{s})}{\partial \boldsymbol{s}}\right|_{\boldsymbol{s}_0} d\boldsymbol{s} = \boldsymbol{f}(\boldsymbol{s}_0) + R_0 \,.\, d\boldsymbol{s} \tag{3.29}$$

where R_0 is the Jacobian matrix of the constraints calculated at $\boldsymbol{s}_0$ and $\boldsymbol{f}$ is the array of functions with boundary conditions.

We may rewrite the condition of minimum (3.27) by using the definitions of $\boldsymbol{a}_0$ and $\boldsymbol{s}_1$ as:

$$K_0 \boldsymbol{s}_1 + R_0 \lambda = \delta \boldsymbol{a}_0 \tag{3.30}$$

where $\delta \boldsymbol{a}_0 = \boldsymbol{a}_0 - K_0 \boldsymbol{s}_0$. Following the same procedure as in the non-linear case, the solution of the non-linear constrained equations is given by:

$$\boldsymbol{s} = K_{i-1}^{-1} \boldsymbol{h}_{i-1} \tag{3.31}$$

where $\boldsymbol{h}_i$ was defined as $\boldsymbol{h}_i = \delta \boldsymbol{a}_i - R_i \lambda$.

The Lagrange multipliers, as we can see, play a role in the solution of the parameters. As a result, we will have to figure out their values. The solution will be useless if this is not done. We can suggest the following set of equations based on the definition of the constraint functions and the Lagrangian form:

$$K_0 \,.\, d\boldsymbol{s} + R_o \lambda = \delta \boldsymbol{a}_0 \tag{3.32}$$

$$R_0 \,.\, d\boldsymbol{s} \approx -\boldsymbol{f}_0 \tag{3.33}$$

Using these equations, the K_0 matrix, the vector $d\boldsymbol{s}$ and the vector $\boldsymbol{a}_0$ can be extended as follows:

USC UNIVERSIDADE DE SANTIAGO DE COMPOSTELA

$$\underbrace{\begin{pmatrix} K_0 & R_0' \\ R_0 & 0 \end{pmatrix}}_{\widehat{K}_0} \cdot \underbrace{\begin{pmatrix} d\boldsymbol{s} \\ \lambda \end{pmatrix}}_{d\hat{\boldsymbol{s}}} = \underbrace{\begin{pmatrix} \delta \boldsymbol{a}_0 \\ -\boldsymbol{f}_0 \end{pmatrix}}_{\delta \widehat{\boldsymbol{a}}_0} \tag{3.34}$$

The Lagrange multipliers are included in an extension of the parameters. When we use the non-linear approach again, we get the *sea* equation:

$$\delta \hat{\boldsymbol{s}}_i = \widehat{K}_{i-1}^{-1} \,.\, \delta \widehat{\boldsymbol{a}}_{i-1} \tag{3.35}$$

where $\hat{\boldsymbol{s}}_i = \hat{\boldsymbol{s}}_{i-1} + \delta \hat{\boldsymbol{s}}_i$.

The errors matrix associated with the parameters is contained in the inverse of the K matrix, just like in the other cases.

The iterative procedure is illustrated in figure 3.4. The restricted *sea* equation is used to create a new set of values, presented as an initial solution for the parameters. The solution must fulfill the restrictions contained in the constraint functions.

Finally, the algorithm for the non-linear TimTrack with constraints can be summarized as follows:

1. We add a set of n_c equations to our model to represent the constraints on our parameters. $\boldsymbol{f}_i = 0$ is the form of each restriction.

2. The equation for constructing the Lagrangian to be minimized is (3.26).

USC UNIVERSIDADE DE SANTIAGO DE COMPOSTELA

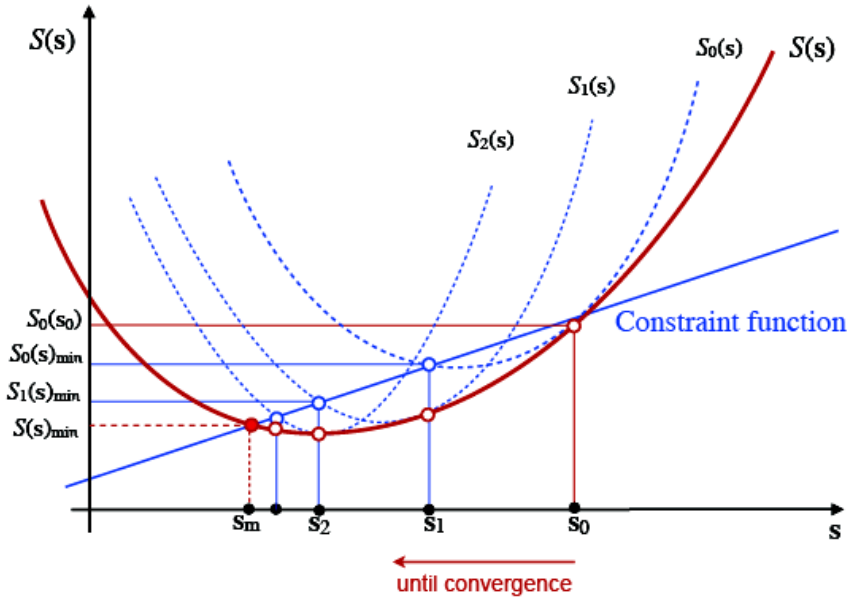

Figure 3.4: Searching for a solution to a non-linear model with parameter restrictions. The problem is solved iteratively in the same way that a conventional non-linear problem is solved. Still, the final values of the parameters s_m must satisfy the constraints of a constraint function (blue line).

3. we compute the Jacobian matrix $R = \partial_s \boldsymbol{f}(\boldsymbol{s})$.

4. There is a proposed first solution $\boldsymbol{s}_0$. Using these parameters, we evaluate the objects.

5. Now, it is time to begin the iterative process. We find the solution to:

$$\begin{pmatrix} \delta \boldsymbol{s}_1 \\ \lambda \end{pmatrix} = \begin{pmatrix} K_0 & R_0' \\ R_0 & 0 \end{pmatrix}' \cdot \begin{pmatrix} \boldsymbol{a}_0 - K_0 \boldsymbol{s}_0 \\ -\boldsymbol{f}_0 \end{pmatrix}$$

6. The new solution takes the form $\boldsymbol{s}_1 = \boldsymbol{s}_0 + \delta \boldsymbol{s}_1$.

7. The iteration process Repeats until convergence is reached.

USC UNIVERSIDADE DE SANTIAGO DE COMPOSTELA

3.3 Models example and some applications

We define the models utilized for calibration and reconstruction tasks throughout the thesis in this section. The models are based on an experimental setup that includes three parallel planes in the TRISTAN detector and four parallel planes in the TRAGALDABAS detector, each of which provides (x, y, t) coordinates, as illustrated in figure 3.1. At z_i, each plane is located. We considered z as a free independent variable because the particle is traveling along the positive z-axis.

The values of the measured quantities are grouped in the W matrix as statistical weights and their intrinsic uncertainty is associated with them. The uncertainties are σ_x, σ_y and σ_t in this case. As a result, the W matrices take the following form:

$$W = \begin{pmatrix} w_x & 0 & 0 \\ 0 & w_y & 0 \\ 0 & 0 & w_t \end{pmatrix}$$

where $w_i = 1/\sigma_i^2$. In all of the models in this section, this matrix will be the same.

3.3.1 Linear model

The linear model is the maximum straightforward representation of a particle propagating along a straight path. The model, $\boldsymbol{m}(\boldsymbol{s})$, is defined by the following equations:

$$m_x = X_0 + X' . z$$
$$m_y = Y_0 + Y' . z$$
$$m_t = T_0 + S . z$$

USC UNIVERSIDADE DE SANTIAGO DE COMPOSTELA

the x, y coordinates, as seen, are the parametric representation of a straight line, with the z coordinate standing as the free parameter. A linear time dependency was also considered. This is a rough estimate that only holds if vertical particles are present.

In the saeta, the unknown parameters are grouped as follows:

$$\boldsymbol{s} = (X_0, X', Y_0, Y', T_0, S)$$

as seen in figure 3.1. The *sea* equation (3.14) must be solved in order to calculate the parameter values. The configuration matrix K and the reduced data vector $\boldsymbol{a}$ is required for this. The K matrix has the following form for each plane, based on the object definitions given in the array of equations (3.8):

$$K_i = \begin{pmatrix} w_x & w_x.z_i & 0 & 0 & 0 & 0 \\ w_x.z_i & w_x.z_i^2 & 0 & 0 & 0 & 0 \\ 0 & 0 & w_y & w_y.z_i & 0 & 0 \\ 0 & 0 & w_y.z_i & w_y.z_i^2 & 0 & 0 \\ 0 & 0 & 0 & 0 & w_t & w_t.z_i \\ 0 & 0 & 0 & 0 & w_t.z_i & w_t.z_i^2 \end{pmatrix}$$

the configuration matrix, as can be shown, is unaffected by the $\boldsymbol{s}$ parameters. It only depends on the plane's position z_i and the experimental data w_i's uncertainty. To construct $\boldsymbol{a}$ vector, we use the following definition:

$$\boldsymbol{a}_i = \begin{pmatrix} w_x \,.\, x_i \\ w_x \,.\, x_i \,.\, z_i \\ w_y \,.\, y_i \\ w_y \,.\, y_i \,.\, z_i \\ w_t \,.\, t_i \\ w_t \,.\, t_i \,.\, z_i \end{pmatrix}$$

USC UNIVERSIDADE DE SANTIAGO DE COMPOSTELA

$(x_i,\ y_i,\ t_i)$ denotes the experimental measurement in the plane i. The $\boldsymbol{a}$ vector, like the configuration matrix K, is independent of the parameters.

There are six unknowns (i.e., parameters to solve). The problem has an exact solution for two planes (we have $n_d = 3 \times 2 = 6$ data for six parameters) since each plane contributes three data. We have two additional data vectors that help us answer better since they provide the system more information.

The sums of the individual K_i and $\boldsymbol{a}_i$ vectors yield the total K matrix and total $\boldsymbol{a}$ vector. The solution is reached without an iterative method because these objects are not dependant on the parameters. The *sea* equation (3.14) is used to find the parameters.

3.3.2 Non-linear model

The previous subsection shows the linear model, the most straightforward essential representation of a particle crossing the detector in a straight line. Now, in this subsection, a non-linear model can be used to provide a more realistic description:

$$m_x = X_0 + X' \,.\, z$$
$$m_y = Y_0 + Y' \,.\, z$$
$$m_t = T_0 + S \,.\, k \,.\, z$$

where

$$k = \sqrt{1 + X'^2 + Y'^2}$$

the kinematical parameters are identical to those in the linear case:

$$\boldsymbol{s} = (X_0, X', Y_0, Y', T_0, S)$$

USC UNIVERSIDADE DE SANTIAGO DE COMPOSTELA

The non-vertical displacement is considered in this non-linear model. The quantity k denotes the direction vector's module, or the actual distance traveled by the particle in a vertical step of Δz. As in the linear case, the x, y components follow the equation of a straight line.

Unlike in a linear model, the values of the unknown parameters will affect the different objects. The K_i matrices and $\boldsymbol{a}_i$ vectors have the following format:

$$K_i = \begin{pmatrix} w_x & w_x z_i & 0 & 0 & 0 & 0 \\ w_x z_i & w_x z_i^2 + S^2 w_t X'^2 z_i^2/k^2 & 0 & S^2 w_t X' Y' z_i^2/k^2 & S w_t X' z_i/k & S w_t X' z_i^2 \\ 0 & 0 & w_y & w_y z_i & 0 & 0 \\ 0 & S^2 w_t X' Y' z_i^2/k^2 & w_y z_i & w_y z_i^2 + S^2 w_t Y'^2 z_i^2/k^2 & S w_t Y' z_i/k & S w_t Y' z_i^2 \\ 0 & S w_t X' z_i/k & 0 & S w_t Y' z_i/k & w_t & w_t k z_i \\ 0 & S w_t X' z_i^2 & 0 & S w_t Y' z_i^2 & w_t k z_i & w_t k^2 z_i^2 \end{pmatrix}$$

and

$$\boldsymbol{a}_i = \begin{pmatrix} w_x x_i \\ w_x x_i z_i + S w_t X' z_i T/k \\ w_y y_i \\ w_y y_i z_i + S w_t Y' z_i T/k \\ w_t T \\ w_t k z_i T \end{pmatrix}$$

where

$$T = t + S X'^2 z_i/k + S Y'^2 z_i/k$$

these objects, as we can see, are dependent on the parameters S, X' and Y'. We can also see correlations between the variables in the K matrix that are not present in the linear model case.

As with the linear case, the total K matrix and total $\boldsymbol{a}$ vector are determined. Iteratively solving the *sea* equation is required. To do so,

USC UNIVERSIDADE DE SANTIAGO DE COMPOSTELA

we suggest an arbitrary initial solution as close as possible to the global minimum $\boldsymbol{s}_0$ and alter it by solving the sea equation iteratively. When a convergence criterion is met, the procedure comes to an end. The difference in Euclidean modules of the solutions was employed in this thesis:

$$(|\boldsymbol{s}_{i+1}| - |\boldsymbol{s}_i|) < \mathcal{E}$$

to bring the iterative process to a halt, the value of $\mathcal{E}$ is optional in this case. In this difference of modules criteria, we utilized $\mathcal{E} = 10^{-3}$ as a convergence value.

3.3.3 Super-saetas

The multiple Coulomb scattering occurs when the particles interact with the materials of the detector. By reconstructing the interaction vertices, the material's shape can be created. A new object, super-saeta, is now defined. A super-saeta is made up of two saetas that shared the same vertex.

The data is described by two models: one for the two top planes and another for the lower planes. Each model produces a saeta and we impose that both trajectories intersect at the interaction vertex. The reference point for the calculations is the vertex (X_0, Y_0, Z_0).

The two models are as follows:

$$m_{xu} = X_0 + X_1' . (z - Z_0)$$
$$m_{yu} = Y_0 + Y_1' . (z - Z_0)$$
$$m_{tu} = T_0 + S . (z - Z_0)$$

$$m_{xd} = X_0 + X_2' . (z - Z_0)$$

USC UNIVERSIDADE DE SANTIAGO DE COMPOSTELA

$$m_{yd} = Y_0 + Y_2' . (z - Z_0)$$
$$m_{td} = T_0 + S . (z - Z_0)$$

The symbols u and d indicated for up planes and down planes, respectively. The super-saeta parameters are as follows:

$$\boldsymbol{s} = (X_0, X_1', X_2', Y_0, Y_1', Y_2', T_0, S, Z_0)$$

The parameters of both trajectories are included in this super-saeta because X_1', Y_1' are the slopes of the reconstructed trajectory in the upper planes and X_2', Y_2' are the slopes of the reconstructed trajectory in the lower planes. The vertex is represented by the points (X_0, Y_0, Z_0), the time is represented by T_0 and the slowness is represented by S. We assume that the particle's velocity is a free parameter in this model, meaning that it is not constant.

The new array of equations shows the non-zero elements of the configuration matrix K_u. We defined the quantities to make notation easier

$$k = \sqrt{1 + X_1'^2 + Y_1'^2}$$

and

$$dZ = z_i - Z_0$$

where $dZ^2 = (z_i - Z_0)^2$. Since there are nine parameters, the configuration matrices are 9×9 squared symmetric $k_{uij} = k_{uji}$. The following are the elements of K_u:

$$k_{u11} = w_x$$

USC UNIVERSIDADE DE SANTIAGO DE COMPOSTELA

$$k_{u12} = w_x \,.\, dZ$$

$$k_{u19} = -w_x \,.\, X_1'$$

$$k_{u22} = w_x \,.\, dZ^2 + \frac{w_t \,.\, S^2 \,.\, X_1'^2 \,.\, dZ^2}{k^2}$$

$$k_{u25} = \frac{w_t \,.\, S^2 \,.\, X_1'^2 \,.\, dZ^2}{k^2}$$

$$k_{u27} = \frac{S \,.\, w_t \,.\, X_1' \,.\, dZ}{k}$$

$$k_{u28} = S \,.\, w_t \,.\, X_1' \,.\, dZ^2$$

$$k_{u29} = -S^2 \,.\, w_t \,.\, X_1' \,.\, dZ - w_x \,.\, X_1' \,.\, dZ$$

$$k_{u44} = w_y$$

$$k_{u45} = w_y \,.\, dZ$$

$$k_{u49} = -w_y \,.\, Y_1'$$

$$k_{u55} = w_y \,.\, dZ^2 + \frac{w_t \,.\, S^2 \,.\, Y_1'^2 \,.\, dZ^2}{k^2}$$

$$k_{u57} = \frac{S \,.\, w_t \,.\, Y_1' \,.\, dZ}{k}$$

$$k_{u58} = S \,.\, w_t \,.\, Y_1' \,.\, dZ^2$$

$$k_{u59} = -S^2 \,.\, w_t \,.\, Y_1' \,.\, dZ - w_y \,.\, Y_1' \,.\, dZ$$

$$k_{u77} = w_t$$

$$k_{u78} = w_t \,.\, k \,.\, dZ$$

$$k_{u79} = -S \,.\, w_t \,.\, k$$

$$k_{u88} = w_t \,.\, k^2 \,.\, dZ^2$$

$$k_{u89} = -S \,.\, w_t \,.\, k^2 \,.\, dZ$$

$$k_{u99} = w_x \,.\, X_1'^2 + w_y \,.\, Y_1'^2 + w_t \,.\, S^2 \,.\, k^2$$

USC UNIVERSIDADE DE SANTIAGO DE COMPOSTELA

The reduced data vector $\boldsymbol{a}_u$ for a measurement $(x_i,\ y_i,\ t_i)$ in the plane z_i has the following form:

$$\boldsymbol{a}_u = \begin{pmatrix} w_x\ .\ \Delta x_i \\ -Z\ .\ \dfrac{w_x.k^2.\Delta x_i + S.w_t.X_1'.[-t_i.k + S.(Z_0.k' - z_i.q')]}{k^2} \\ 0 \\ w_y\ .\ \Delta y_i \\ -Z\ .\ \dfrac{w_y.k^2.\Delta y_i + S.w_t.Y_1'.[-t_i.k + S.(Z_0.k' - z_i.q')]}{k^2} \\ 0 \\ w_t.t_i.k.S.\dfrac{-Z_0.k' + z_i.q'}{k} \\ w_t.Z.t_i.k.S.(Z_0.k' - z_i q') \\ -S.t_i.w_t.k + w_x.X_1'.\Delta x_i + w_y.Y_1'.\Delta y_i + S^2.w_t(k'.Z_0 - q'.z_i) \end{pmatrix}$$

where

$$\Delta x_i = x_i - X_1'.Z_0$$

$$\Delta y_i = y_i - Y_1'.Z_0$$

$$k' = 1 + 2X_1'^2 + 2Y_1'^2$$

$$q' = X_1'^2 + Y_1'^2$$

The model defining the data of the two lower planes is constructed in the same way. The non-zero values of the K_d matrix have the same form as the non-zero values of the K_u matrix, but as a function of X_2', Y_2'.

The variables k and dZ have the exact definition as in the upper case:

USC UNIVERSIDADE DE SANTIAGO DE COMPOSTELA

$$k = \sqrt{1 + X_2'^2 + Y_2'^2}$$

and

$$dZ = z_i - Z_0$$

The configuration matrices K_d are 9×9 squared symmetric $k_{dij} = k_{dji}$ since there are nine parameters. The elements of K_d are as follows:

$$k_{d11} = w_x$$

$$k_{d12} = w_x \,.\, dZ$$

$$k_{d19} = -w_x \,.\, X_2'$$

$$k_{d33} = w_x \,.\, dZ^2 + \frac{w_t \,.\, S^2 \,.\, X_2'^2 \,.\, dZ^2}{k^2}$$

$$k_{d36} = \frac{w_t \,.\, S^2 \,.\, X_2' \,.\, Y_2' \,.\, dZ^2}{k^2}$$

$$k_{d37} = \frac{S \,.\, w_t \,.\, X_2' \,.\, dZ}{k}$$

$$k_{d38} = S \,.\, w_t \,.\, X_2' \,.\, dZ^2$$

$$k_{d39} = -S^2 \,.\, w_t \,.\, X_2' \,.\, dZ - w_x \,.\, X_2' \,.\, dZ$$

$$k_{d44} = w_y$$

$$k_{d45} = w_y \,.\, dZ$$

$$k_{d49} = -w_y \,.\, Y_2'$$

$$k_{d66} = w_y \,.\, dZ^2 + \frac{w_t \,.\, S^2 \,.\, Y_2'^2 \,.\, dZ^2}{k^2}$$

$$k_{d67} = \frac{S \,.\, w_t \,.\, Y_2' \,.\, dZ}{k}$$

USC UNIVERSIDADE DE SANTIAGO DE COMPOSTELA

$$k_{d68} = S\,.\,w_t\,.\,Y_2'\,.\,dZ^2$$

$$k_{d69} = -S^2\,.\,w_t\,.\,Y_2'\,.\,dZ - w_y\,.\,Y_2'\,.\,dZ$$

$$k_{d77} = w_t$$

$$k_{d78} = w_t\,.\,k\,.\,dZ$$

$$k_{d79} = -S\,.\,w_t\,.\,k$$

$$k_{d88} = w_t\,.\,k^2\,.\,dZ^2$$

$$k_{d89} = -S\,.\,w_t\,.\,k^2\,.\,dZ$$

$$k_{d99} = w_x\,.\,X_2'^2 + w_y\,.\,Y_2'^2 + w_t\,.\,S^2\,.\,k^2$$

The same is done for the reduced data vector $\boldsymbol{a}_d$ and takes the following form:

$$\boldsymbol{a}_d = \begin{pmatrix} w_x\,.\,\Delta x_i \\ 0 \\ -Z\,.\,\dfrac{w_x.k^2.\Delta x_i + S.w_t.X_2'.[-t_i.k + S.(Z_0.k' - z_i.q')]}{k^2} \\ w_y\,.\,\Delta y_i \\ 0 \\ -Z\,.\,\dfrac{w_y.k^2.\Delta y_i + S.w_t.Y_2'.[-t_i.k + S.(Z_0.k' - z_i.q')]}{k^2} \\ w_t.t_i.k.S.\dfrac{-Z_0.k' + z_i.q'}{k} \\ w_t.Z.t_i.k.S.(Z_0.k' - z_i q') \\ -S.t_i.w_t.k + w_x.X_2'.\Delta x_i + w_y.Y_2'.\Delta y_i + S^2.w_t(k'.Z_0 - q'.z_i) \end{pmatrix}$$

where the same variables as in the upper plane case were introduced:

$$\Delta x_i = x_i - X_2'.Z_0$$

$$\Delta y_i = y_i - Y_2'.Z_0$$

USC UNIVERSIDADE DE SANTIAGO DE COMPOSTELA

$$k' = 1 + 2X_2'^2 + 2Y_2'^2$$

$$q' = X_2'^2 + Y_2'^2$$

As with the $\boldsymbol{a}$ vector, the total K matrix represents the sum of the contributions for the two models:

$$K = \sum_{i=1}^{2} K_{ui} + \sum_{j=1}^{2} K_{dj}$$

$$\boldsymbol{a} = \sum_{i=1}^{2} \boldsymbol{a}_{ui} + \sum_{j=1}^{2} \boldsymbol{a}_{dj}$$

as a result, the parameter values are found by solving the *sea* equation (3.14).

By assuming that the particle's velocity remains constant, we can modify these models. In this case, there are eight rather than nine parameters grouped in the super-saeta:

$$\boldsymbol{s} = (X_0, X_1', X_2', Y_0, Y_1', Y_2', T_0, Z_0)$$

Therefore, the dimensions of the K matrices are (8×8) and the elements have a new form.

3.3.4 TimTrack inside a pad with drift velocity

Now we will look at a set of RPC planes with rectangular pads dividing their detecting area, as we saw in Chapter 2, section 5. A particle traversing two RPC planes is demonstrated in figure 3.5. The detection regions or pads on each RPC plane are rectangular. The signal propagates inside the detecting region until it is read at the center of the

USC UNIVERSIDADE DE SANTIAGO DE COMPOSTELA

cell when a particle interacts with the detector at some pad. The drift velocity (the signal's velocity inside the pad) is estimated to be roughly 60% of that of light.

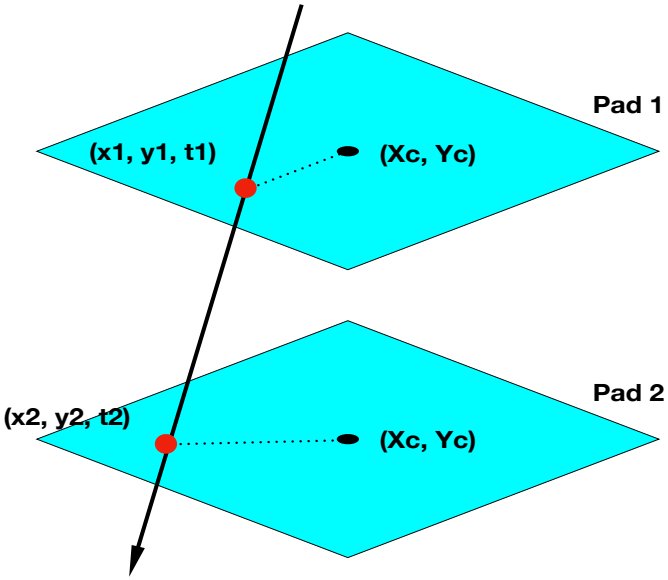

Figure 3.5: A particle detected in two pads is shown schematically. Rectangular areas divide the detection areas of the planes. The signal readout is in the pad's center (X_c, Y_c) and must go from the hit (x_i, y_i, t_i) to the pad's center. As a result, the signal's drift velocity inside the pad is considered in the data model.

As a result, a model that includes the drift velocity and represents the propagation of a particle is:

$$m_x = X_0 + X' \,.\, z$$

$$m_y = Y_0 + Y' \,.\, z$$

$$m_t = T_0 + S \,.\, k \,.\, z + S_s \,.\, r$$

USC UNIVERSIDADE DE SANTIAGO DE COMPOSTELA

where S_s is the inverse of the signal's velocity, $k = \sqrt{1 + X'^2 + Y'^2}$ and r is the distance the signal travels inside the path from the interaction site to the detection point in the pad's center:

$$r = \sqrt{(m_x - X_c)^2 + (m_y - Y_c)^2}$$

This is a non-linear model that must solve iteratively. In the saeta, the following parameters are grouped:

$$\boldsymbol{s} = (X_0, X', Y_0, Y', T_0, S)$$

For all planes, we assumed that the drift velocity is constant.

Because one pad has dimensions $(l_x,\ l_y)$ and the signal is read out in the center, x and y are random variables that are distributed uniformly. The uniform probability distribution is used to compute the uncertainty of the measurements $(\sigma_x,\ \sigma_y)$. That is lead to:

$$\sigma_x = \frac{l_x}{\sqrt{12}}$$

and

$$\sigma_y = \frac{l_y}{\sqrt{12}}$$

The configuration matrix *K* consists of the following elements:

$$k_{11} = w_x + \frac{S_s^2 \,.\, w_t \,.\, \Delta_x^2}{r^2}$$

$$k_{12} = z_i \,.\left(w_x + \frac{\Delta_x \,.\, S_s \,.\, w_t\,(\Delta_x \,.\, k \,.\, S_s + r \,.\, S \,.\, X')}{k \,.\, r^2}\right)$$

USC UNIVERSIDADE DE SANTIAGO DE COMPOSTELA

$$k_{13} = \frac{S_s^2 \,.\, w_t \,.\, \Delta_x \,.\, \Delta_y}{r^2}$$

$$k_{14} = z_i \,.\left(\frac{\Delta_x \,.\, S_s \,.\, w_t \,(\Delta_y \,.\, k \,.\, S_s + r \,.\, S \,.\, Y')}{k \,.\, r^2}\right)$$

$$k_{15} = \frac{\Delta_x \,.\, S_s \,.\, w_t}{r}$$

$$k_{16} = \frac{\Delta_x \,.\, S_s \,.\, w_t \,.\, k \,.\, z_i}{r}$$

$$k_{22} = w_x \,.z_i^2 + w_t \,.\left(\frac{\Delta_x \,.\, S_s \,.\, z_i}{r} + \frac{S \,.\, X' \,.\, z_i}{k}\right)^2$$

$$k_{23} = z_i \,.\left(\frac{\Delta_y \,.\, S_s \,.\, w_t \,(\Delta_x \,.\, k \,.\, S_s + r \,.\, S \,.\, X')}{k \,.\, r^2}\right)$$

$$k_{24} = w_t \,.\frac{(\Delta_x \,.\, k \,.\, S_s + r \,.\, S \,.\, X')\,(\Delta_y \,.\, k \,.\, S_s + r \,.\, S \,.\, Y')}{k^2 \,.\, r^2}$$

$$k_{25} = w_t \,.\left(\frac{\Delta_x \,.\, S_s \,.\, z_i}{r} + \frac{S \,.\, X' \,.\, z_i}{k}\right)$$

$$k_{26} = w_t \,.z_i^2 \,.\left(\frac{\Delta_x \,.\, k \,.\, S_s + r \,.\, S \,.\, X'}{r}\right)$$

$$k_{33} = w_y + \frac{S_s^2 \,.\, w_t \,.\, \Delta_y^2}{r^2}$$

$$k_{34} = z_i \,.\left(w_y + \frac{\Delta_y \,.\, S_s \,.\, w_t \,(\Delta_y \,.\, k \,.\, S_s + r \,.\, S \,.\, Y')}{k \,.\, r^2}\right)$$

USC UNIVERSIDADE DE SANTIAGO DE COMPOSTELA

$$k_{35} = \frac{\Delta_y \,.\, S_s \,.\, w_t}{r}$$

$$k_{36} = \frac{\Delta_y \,.\, S_s \,.\, w_t \,.\, k \,.\, z_i}{r}$$

$$k_{44} = w_y \,.\, z_i^2 + w_t \,.\left(\frac{\Delta_y \,.\, S_s \,.\, z_i}{r} + \frac{S \,.\, Y' \,.\, z_i}{k}\right)^2$$

$$k_{45} = w_t \,.\left(\frac{\Delta_y \,.\, S_s \,.\, z_i}{r} + \frac{S \,.\, Y' \,.\, z_i}{k}\right)$$

$$k_{46} = w_t \,.\, z_i^2 \,.\left(\frac{\Delta_y \,.\, k \,.\, S_s + r \,.\, S \,.\, Y'}{r}\right)$$

$$k_{55} = w_t$$

$$k_{56} = w_t \,.\, k \,.\, z_i$$

$$k_{66} = w_t \,.\, k^2 \,.\, z_i^2$$

where the quantities Δ_x and Δ_y are defined as follow:

$$\Delta_x = m_x - X_c = X_0 + X' \,.\, z_i - X_c$$

and

$$\Delta_y = m_y - Y_c = Y_0 + Y' \,.\, z_i - Y_c$$

After determining the configuration matrix K. Now, we determine the reduced data vector, $\boldsymbol{a}$ and takes the form:

USC
UNIVERSIDADE DE SANTIAGO DE COMPOSTELA

$$\boldsymbol{a} = \begin{pmatrix} w_x.x_i + \Delta_x.S_s.w_t.\left(\frac{r.S(X'^2+Y'^2)z_i + k[-r^2S_s + r.t_i + S_s(\Delta_x.m_x + \Delta_y.m_y)]}{k.r^2}\right) \\ w_x.x_i.z_i + w_t(\Delta_x.k.S_s + r.S.X')z_i.\left(\frac{r.s(X'^2+Y'^2)z_i + k[r(-S_s.r + t_i) + S_s(\Delta_x.m_x + \Delta_y.m_y)]}{k^2.r^2}\right) \\ w_y.y_i + \Delta_y.S_s.w_t.\left(\frac{r.S(X'^2+Y'^2)z_i + k[-r^2S_s + r.t_i + S_s(\Delta_x.m_x + \Delta_y.m_y)]}{k.r^2}\right) \\ w_y.y_i.z_i + w_t(\Delta_y.k.S_s + r.S.Y')z_i.\left(\frac{r.s(X'^2+Y'^2)z_i + k[r(-S_s.r + t_i) + S_s(\Delta_x.m_x + \Delta_y.m_y)]}{k^2.r^2}\right) \\ w_t.\left(\frac{r.S(X'^2+Y'^2)z_i + k[-r^2.S_s + r.t_i + S_s(\Delta_x.m_x + \Delta_y.m_y)]}{k.r}\right) \\ w_t.z_i.\left(\frac{r.S(X'^2+Y'^2)z_i + k[-r^2.S_s + r.t_i + S_s(\Delta_x.m_x + \Delta_y.m_y)]}{r}\right) \end{pmatrix}$$

by using the same definitions that were used before. The parameters are determined by solving the sea equation iteratively.

Even though this model appears to be highly comprehensive, it does have significant limits due to the computation approach. Making a perturbation on the saetas at each iteration is one such solution. If the particle enters the pad vertically, the final solution provides the pad's center, as if the drift velocity is zero. As a result, the process will seek the global minimum rather than local stable solutions.

3.4 The models with numerical examples

Undoubtedly, the numerical examples assist in understanding the physics situation that we have. Thus, this section will present two numerical examples of some models illustrated before to explain how the TimTrack algorithm works with more details, one for the TRAGALDABAS detector and the other for the TRISTAN.

The central point of each RPC for the detectors is used as the origin of the spatial components. We used the units mm and ps for the magnitudes of space and time. For each plane, we assumed that the uncertainties in position x, position y and time t are the same. The following are the values we assigned to them:

$$\sigma_x = \sigma_y = 5\ mm$$

USC UNIVERSIDADE DE SANTIAGO DE COMPOSTELA

and

$$\sigma_t = 200\, ps$$

As a result, the weight matrix remains constant:

$$W = \begin{pmatrix} 1/5^2 & 0 & 0 \\ 0 & 1/5^2 & 0 \\ 0 & 0 & 1/200^2 \end{pmatrix}$$

Now, we will start with the first example for the TRAGALDABAS detector.

3.4.1 Example of a linear model for TRAGALDABAS detector

For this example, we employed the same set-up for the TRAGALDABAD detector as in figure 3.6, consisting of four RPC planes. Each RPC measures x position, y position and t the time (x, y, t).

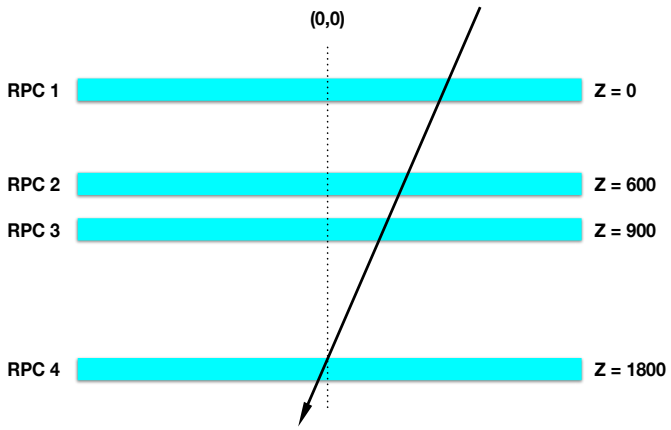

Figure 3.6: TRAGALDABAS experimental setup for numerical demonstration of TimTrack method. The distances between the RPC's are in mm. The origin of x, y is located at the center of each RPC plane.

USC UNIVERSIDADE DE SANTIAGO DE COMPOSTELA

The linear model described in subsection 3.3.1 will be evaluated numerically. We create a list of hits, as follows:

$$(x_1, y_1, t_1) = (300, -300, 1100) \text{ at } z = 0$$

$$(x_2, y_2, t_2) = (-300, -120, 3200) \text{ at } z = 600$$

$$(x_3, y_3, t_3) = (-600, -30, 4250) \text{ at } z = 900$$

$$(x_4, y_4, t_4) = (-1500, 240, 7400) \text{ at } z = 1800$$

These numbers are based on a particle traveling at the speed of light crossing the detector. As the x coordinates decrease, the y coordinates increase.

We calculate the *configuration matrix K* for each plane using the *K* matrix definitions:

$$K_1 = \begin{pmatrix} 0.04 & 0 & 0 & 0 & 0 & 0 \\ 0 & 0 & 0 & 0 & 0 & 0 \\ 0 & 0 & 0.04 & 0 & 0 & 0 \\ 0 & 0 & 0 & 0 & 0 & 0 \\ 0 & 0 & 0 & 0 & 0.000025 & 0 \\ 0 & 0 & 0 & 0 & 0 & 0 \end{pmatrix}$$

$$K_2 = \begin{pmatrix} 0.04 & 24 & 0 & 0 & 0 & 0 \\ 24 & 14400 & 0 & 0 & 0 & 0 \\ 0 & 0 & 0.04 & 24 & 0 & 0 \\ 0 & 0 & 24 & 14400 & 0 & 0 \\ 0 & 0 & 0 & 0 & 0.000025 & 0.015 \\ 0 & 0 & 0 & 0 & 0.015 & 9 \end{pmatrix}$$

USC UNIVERSIDADE DE SANTIAGO DE COMPOSTELA

$$K_3 = \begin{pmatrix} 0.04 & 36 & 0 & 0 & 0 & 0 \\ 36 & 32400 & 0 & 0 & 0 & 0 \\ 0 & 0 & 0.04 & 36 & 0 & 0 \\ 0 & 0 & 36 & 32400 & 0 & 0 \\ 0 & 0 & 0 & 0 & 0.000025 & 0.0225 \\ 0 & 0 & 0 & 0 & 0.0225 & 20.25 \end{pmatrix}$$

$$K_4 = \begin{pmatrix} 0.04 & 72 & 0 & 0 & 0 & 0 \\ 72 & 129600 & 0 & 0 & 0 & 0 \\ 0 & 0 & 0.04 & 72 & 0 & 0 \\ 0 & 0 & 72 & 129600 & 0 & 0 \\ 0 & 0 & 0 & 0 & 0.000025 & 0.045 \\ 0 & 0 & 0 & 0 & 0.045 & 81 \end{pmatrix}$$

and then the total K matrix is as follows:

$$K_{total} = \sum_{i=1}^{4} K_i$$

$$= \begin{pmatrix} 0.16 & 132 & 0 & 0 & 0 & 0 \\ 132 & 176400 & 0 & 0 & 0 & 0 \\ 0 & 0 & 0.16 & 132 & 0 & 0 \\ 0 & 0 & 132 & 176400 & 0 & 0 \\ 0 & 0 & 0 & 0 & 0.0001 & 0.0825 \\ 0 & 0 & 0 & 0 & 0.0825 & 110.25 \end{pmatrix}$$

Now, we calculate the inverse of K_{total}, which is known as the *error matrix*:

$$\mathcal{E} = K_{total}^{-1}$$

$$= \begin{pmatrix} 16.33 & -0.0122 & 0 & 0 & 0 & 0 \\ -0.0122 & 0.000015 & 0 & 0 & 0 & 0 \\ 0 & 0 & 16.33 & -0.0122 & 0 & 0 \\ 0 & 0 & -0.0122 & 0.000015 & 0 & 0 \\ 0 & 0 & 0 & 0 & 26133.33 & -19.555 \\ 0 & 0 & 0 & 0 & -19.555 & 0.0237 \end{pmatrix}$$

USC UNIVERSIDADE DE SANTIAGO DE COMPOSTELA

The same way is used to calculate the *reduced data vector* $\boldsymbol{a}$:

$$\boldsymbol{a}_1 = \begin{pmatrix} 12 \\ 0 \\ -12 \\ 0 \\ 0.0275 \\ 0 \end{pmatrix} \quad \boldsymbol{a}_2 = \begin{pmatrix} -12 \\ -7200 \\ -4.8 \\ -2880 \\ 0.08 \\ 48 \end{pmatrix}$$

$$\boldsymbol{a}_3 = \begin{pmatrix} -24 \\ -21600 \\ -1.2 \\ -1080 \\ 0.10625 \\ 95.625 \end{pmatrix} \quad \boldsymbol{a}_4 = \begin{pmatrix} -60 \\ -108000 \\ 9.6 \\ 17280 \\ 0.185 \\ 333 \end{pmatrix}$$

and then the total $\boldsymbol{a}$ vector is as follows:

$$\boldsymbol{a}_{total} = \sum_{i=1}^{4} \boldsymbol{a}_i = \begin{pmatrix} -84 \\ -136800 \\ -8.4 \\ 13320 \\ 0.39875 \\ 476.625 \end{pmatrix}$$

By solving the *sea* equation (3.14), which is the product of the total K matrix with the total $\boldsymbol{a}$ vector, the values of the parameters can be found as follows:

$$\boldsymbol{s} = K_{total}^{-1} \cdot \boldsymbol{a}_{total} = \begin{pmatrix} 300 \\ -1 \\ -300 \\ 0.3 \\ 1100 \\ 3.5 \end{pmatrix}$$

As a result, the parameters are:

USC UNIVERSIDADE DE SANTIAGO DE COMPOSTELA

$$X_0 = 300 \qquad X' = -1$$

$$Y_0 = -300 \qquad Y' = 0.3$$

$$T_0 = 1100 \qquad S = 3.5$$

Now, we present some comments and interpretations related to these parameters:

1. The point $(300, -300)$ is the initial point on plane 1 where the particle starts propagation through the detector.

2. The slopes are $X' = -1$ and $Y' = 0.3$. This means that the variables x and y changes $1\,mm$ and $0.3\,mm$, respectively, per z unit. The negative value in X' means that the variable is decreasing in z and the positive value in Y' means that the variable is increasing in z.

3. The initial time is $1100\,ps$, identical to the time measured in plane 1.

4. The velocity of the particle is $V = 1/S = 1/3.5 = 0.286\ mm/ps$. The speed of light is $c = 0.3\ mm/ps$. Therefore, the velocity of the particle agrees with the speed of light.

The last important comment about the *error matrix* in which was previously calculated is the diagonal elements of this matrix provide information about the uncertainties associated with the parameters of the saeta:

$$\sigma_i = \frac{1}{\sqrt{K_{ii}^{-1}}}$$

The covariances are contained in the non-diagonal terms, which provide information about the correlations between the parameters. The -0.0122 coefficient indicates that there is a negligible correlation

USC UNIVERSIDADE DE SANTIAGO DE COMPOSTELA

between X_0 and X' in this matrix. And the same for the rest of the parameters.

3.4.2 Example of a linear model for TRISTAN detector

With this example, we present the same set-up for the TRISTAN detector as in figure 3.7, which consists of three RPC planes. Each RPC measures $(x,\ y,\ t)$. And we apply the same procedure as the previous example.

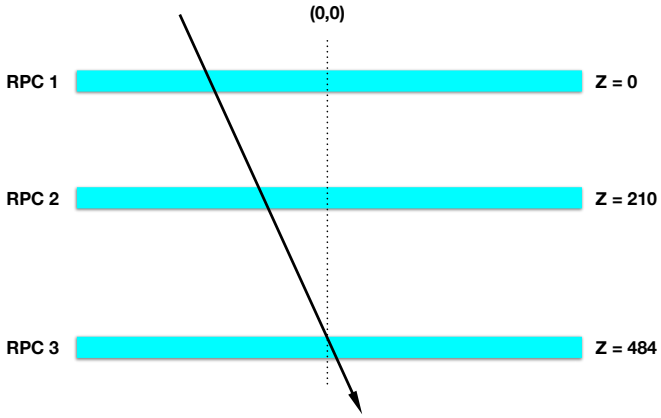

Figure 3.7: TRISTAN experimental setup for numerical illustration of TimTrack method.

We generate a list of hits, as follows:

$$(x_1, y_1, t_1) = (-100, 200, 1100) \text{ at } z = 0$$

$$(x_2, y_2, t_2) = (110, 137, 1835) \text{ at } z = 210$$

$$(x_3, y_3, t_3) = (384, 55, 2794) \text{ at } z = 484$$

And again, these numbers are based on a particle traveling at the speed of light crossing the detector. As the x coordinates increase, the y coordinates decrease.

USC UNIVERSIDADE DE SANTIAGO DE COMPOSTELA

We calculate the K matrix for each plane:

$$K_1 = \begin{pmatrix} 0.04 & 0 & 0 & 0 & 0 & 0 \\ 0 & 0 & 0 & 0 & 0 & 0 \\ 0 & 0 & 0.04 & 0 & 0 & 0 \\ 0 & 0 & 0 & 0 & 0 & 0 \\ 0 & 0 & 0 & 0 & 0.000025 & 0 \\ 0 & 0 & 0 & 0 & 0 & 0 \end{pmatrix}$$

$$K_2 = \begin{pmatrix} 0.04 & 8.4 & 0 & 0 & 0 & 0 \\ 8.4 & 1764 & 0 & 0 & 0 & 0 \\ 0 & 0 & 0.04 & 8.4 & 0 & 0 \\ 0 & 0 & 8.4 & 1764 & 0 & 0 \\ 0 & 0 & 0 & 0 & 0.000025 & 0.00525 \\ 0 & 0 & 0 & 0 & 0.00525 & 1.1025 \end{pmatrix}$$

$$K_3 = \begin{pmatrix} 0.04 & 19.36 & 0 & 0 & 0 & 0 \\ 19.36 & 9370.24 & 0 & 0 & 0 & 0 \\ 0 & 0 & 0.04 & 19.36 & 0 & 0 \\ 0 & 0 & 19.36 & 9370.24 & 0 & 0 \\ 0 & 0 & 0 & 0 & 0.000025 & 0.0121 \\ 0 & 0 & 0 & 0 & 0.0121 & 5.8564 \end{pmatrix}$$

and then the total K matrix is:

$$K_{total} = \sum_{i=1}^{3} K_i$$

$$= \begin{pmatrix} 0.12 & 27.76 & 0 & 0 & 0 & 0 \\ 27.76 & 11134.24 & 0 & 0 & 0 & 0 \\ 0 & 0 & 0.12 & 27.76 & 0 & 0 \\ 0 & 0 & 27.76 & 11134.24 & 0 & 0 \\ 0 & 0 & 0 & 0 & 0.000075 & 0.01735 \\ 0 & 0 & 0 & 0 & 0.01735 & 6.9589 \end{pmatrix}$$

we calculate the *error matrix* by taking the inverse of the K_{total} matrix:

USC UNIVERSIDADE DE SANTIAGO DE COMPOSTELA

$$\mathcal{E} = K_{total}^{-1}$$

$$= \begin{pmatrix} 19.7 & -0.05 & 0 & 0 & 0 & 0 \\ -0.05 & 0.000212 & 0 & 0 & 0 & 0 \\ 0 & 0 & 19.7 & -0.05 & 0 & 0 \\ 0 & 0 & -0.05 & 0.000212 & 0 & 0 \\ 0 & 0 & 0 & 0 & 31503.2 & -78.54 \\ 0 & 0 & 0 & 0 & -78.54 & 0.34 \end{pmatrix}$$

The same way is made with the $\boldsymbol{a}$ vector:

$$\boldsymbol{a}_1 = \begin{pmatrix} -4 \\ 0 \\ 8 \\ 0 \\ 0.0275 \\ 0 \end{pmatrix} \quad \boldsymbol{a}_2 = \begin{pmatrix} 4.4 \\ 924 \\ 5.48 \\ 1150.8 \\ 0.05 \\ 9.6 \end{pmatrix} \quad \boldsymbol{a}_3 = \begin{pmatrix} 15.36 \\ 7434.24 \\ 2.2 \\ 1064.8 \\ 0.07 \\ 33.8 \end{pmatrix}$$

and the total $\boldsymbol{a}$ vector:

$$\boldsymbol{a}_{total} = \sum_{i=1}^{3} \boldsymbol{a}_i = \begin{pmatrix} 15.76 \\ 8358.24 \\ 15.68 \\ 2215.6 \\ 0.15 \\ 43.4 \end{pmatrix}$$

We solve the *sea* equation, which is the product of the total *K* matrix with the total $\boldsymbol{a}$ vector, the values of the parameters can be as follows:

$$\boldsymbol{s} = K_{total}^{-1} \cdot \boldsymbol{a}_{total} = \begin{pmatrix} -100 \\ 1 \\ 200 \\ -0.3 \\ 1100 \\ 3.5 \end{pmatrix}$$

USC UNIVERSIDADE DE SANTIAGO DE COMPOSTELA

So the parameters are:

$$X_0 = -100 \qquad X' = 1$$

$$Y_0 = 200 \qquad Y' = -0.3$$

$$T_0 = 1100 \qquad S = 3.5$$

Some comments and interpretations related to these parameters:

1. The point $(-100, 200)$ is the initial point on plane 1 where the particle starts propagation through the detector.

2. The slopes are $X' = 1$ and $Y' = -0.3$. This means that the variables x and y changes $1\,mm$ and $0.3\,mm$, respectively, per z unit. The positive value in X' means that the variable is increasing in z and the negative value in Y' means that the variable is decreasing in z.

3. The initial time is $1100\,ps$, identical to the time measured in plane 1.

4. The velocity of the particle is $V = 1/S = 1/3.5 = 0.286\ mm/ps$. The speed of light is $c = 0.3\ mm/ps$. Therefore, the velocity of the particle is compatible with the speed of light.

The diagonal elements of the *error matrix* provide information about the uncertainties associated with the parameters of the saeta:

$$\sigma_i = \frac{1}{\sqrt{K_{ii}^{-1}}}$$

The covariances are contained in the non-diagonal terms, which give information about the correlations between the parameters. The -0.05 coefficient indicates that there is a negligible correlation between X_0 and X' in this matrix.

USC UNIVERSIDADE DE SANTIAGO DE COMPOSTELA

4 Analysis of simulated and real data with the TRAGALDABAS detector

4.1 Introduction

Simulation is defined as the execution of a software program by a computer or a group of machines to reproduce an abstract model of a physical system [78]. This mathematical model is said to be an accurate description of reality.

Because we can establish, alter, or decide the values of the parameters that play a crucial role in the system, the simulation is a controlled environment. In the sense that it must describe its equivalent in a real-world situation, a simulation should be as realistic as possible. Due to the vast number of parameters included in a given situation, this is sometimes extremely difficult to perform and in many circumstances, it is entirely impossible. In other circumstances, the model may contain equations that are impossible to solve using a computational method or algorithm. The model may have extremely restrictive boundary conditions, making it impossible to find a representative solution.

Finding a simplified physical system that behaves similarly to the real one could be one solution to overcome these challenges. If the simulation results differ significantly, that means our model is not accurately representing the real system. As a result, we must change the equations or boundary conditions in our model. This reduction would assist us in determining the relationship between system variables and writing computer code to describe it [79].

Several types of detectors and electronics are used in nuclear and particle physics experiments. Many aspects must interact and operate

USC UNIVERSIDADE DE SANTIAGO DE COMPOSTELA

together, necessitating the consideration of numerous experimental subtleties, impacts and features. Even small-scale experiments necessitate a prior simulated analysis to ensure that our models, detectors and observables are in good working order.

The Monte Carlo approach [80, 81] was selected to improve various physical problems by employing an innovative probabilistic mathematical algorithm. Integrodifferential equations and random numbers in a Monte Carlo simulation are essentially a statistical approach to a problem. A Monte Carlo simulation is roughly equivalent to repeating the same experiment many times while introducing random effects at each step. It generates an initial state, then applies our model to that starting state of the system many times before evaluating the final stage. It is feasible to give the variables a probabilistic interpretation and then connect them to the parameters of the real system model using the law of large numbers.

Monte Carlo simulations are crucial in statistical physics since, in principle, every stochastic process can be solved with the Monte Carlo method. It is widely used in many physical branches such as meteorology, Molecular Dynamics [82], nuclear physics, particle accelerators, space and medical physics. Monte Carlo simulations are also necessary for particle physics experiments. Nowadays, experimental setups in high-energy physics require a lot of staffing and infrastructure. It is therefore essential to perform a previous study on the design of the facilities. These studies can cover the behavior of our detectors to the influence of the building in the experiment.

Simulations, on the other hand, can be utilized for purposes other than structural analysis. We may be interested in a specific theory or researching a physical observable in a variety of situations. A suitable simulation is used to do a previous study of such variables. These analyses appear to be necessary because they provide preliminary information about the experiment before it is performed and assist in the understanding of the physics behind it.

USC
UNIVERSIDADE DE SANTIAGO DE COMPOSTELA

Computer simulations are currently one of the most powerful tools available for managing all of the data generated by physics investigations. A typical physics simulation can require millions of events and computers are the only method to run it. We can now run simulations on a computer in a reasonable time because of advancements in hardware and software technology. For example, in around ten minutes, a Monte Carlo simulation of a million muons or electrons interacting with a material can be completed and analyzed.

Several computer programs can perform Monte Carlo simulations. They are usually written in many different languages, including Python, C++, or any programming language. Besides the data simulation, we will need an analysis code to extract the interest information.

This chapter is devoted first to explaining the standard simulation tools for simulation and analysis and the software packages used and developed during this thesis. The introduction presented a glance at the commonly used Monte Carlo method for data generation. EnsarRoot [77], as we will see later, is an official flavor of the FairRoot framework that includes a group of software to simulate detectors, experimental setups, run Monte Carlo simulations and analyze the results.

The EnsarRoot framework and the Cosmic Ray Shower Library (CRY), were utilized to implement all geometries and custom particle generators. The implementation of the simulation and analysis software was made, taking as a reference two different setups. With simulated Extend Air Shower (EAS) data, they both give a study of the TRAGALDABAS detector system behavior and response. The two different configurations performed in TRAGALDABAS are the initial setup with three RPC active planes and a second configuration where a $1\ cm$ thick lead layer was placed between the second and the third active planes.

Our simulations are based on the interaction of secondary cosmic radiation with matter. This radiation is the result of particle interactions

USC UNIVERSIDADE DE SANTIAGO DE COMPOSTELA

in the Earth's atmosphere. Bremsstrahlung and pair formation are two mechanisms that compete after these interactions. As a result, the cosmic radiation that reaches our detector has two main components: muons on one side and electrons-photons on the other.

The following section describes the internal structure of the code and the enhancements made during this thesis, including the use and description of a Particle Identification (PID) method. Then, real TRAGALDABAS data from different time periods are analyzed. The most important results are compared with simulation and the particle identification method is used to estimate the nature of cosmic rays arriving at our detection system.

4.2 Software frameworks for simulation

This section discusses the simulation, event generation and data analysis systems and programming languages. A software framework consists of classes, scripts and templates that provide specific functions that the user can select, perform, or modify. Such a structured framework aims to maximize the efficiency of developing new software, improve the reliability of new applications and reduce programming effort.

Here is a summary of the essential software toolkits and frameworks that used in this work:

- Geant:

The Geant package developed at CERN [83, 84] is one of the most widely used software tools for simulating geometrical structures for detectors and subsequently running Monte Carlo simulations.

The Geant framework is composed of various packages that allow the definition of essential characteristics of the simulation process. Such as the system geometry, Monte Carlo event data generation, simulated particle tracking passing through the detector, particle detection by

USC UNIVERSIDADE DE SANTIAGO DE COMPOSTELA

active materials and operations management. A Monte Carlo simulation results are typically saved in files are of several gigabytes. As a result, it is required to employ appropriate software to analyze large data files with effective computer memory management. Moreover, the user interface facilitates interaction with the computer and later the data is analyzed with the ROOT program.

- ROOT:

The ROOT package [85] was developed at CERN as a platform for developing data analysis applications. The Root is an object-oriented framework written in the C++ programming language and one of its advantages is that it can encapsulate information more efficiently because it is object-oriented. Root allows the management of large amounts of data and creates customizable histograms. The TClonesArray data type allows storage and manages many objects while optimizing the amount of memory used on the computer. As can be seen, every simulation process is divided into two parts: one is devoted to generating simulated data and the other is responsible for analyzing those data. The Root is currently being used to monitor, store and analyze data in major High Energy and Nuclear Physics laboratories worldwide.

- FairRoot:

The FairRoot framework [86] was designed as an interface between the information provided by the Geant simulation package and the Root analysis tools. The FairRoot framework is based on the Root system. The objective is that the user gets access to the experiment's geometry, may alter and set the simulation parameters and then gets a file that Root can understand at the end of the process.

Because the FairRoot framework provides access to a collection of services and they are available to us at any time, utilizing the FairRoot is more convenient than using a pure Geant simulation combined with

USC
UNIVERSIDADE DE SANTIAGO DE COMPOSTELA

Root or another analysis tool. In this situation, a service creates the geometry, while others adjust the simulation parameters.

In FairRoot, the simulations are run by executing a task list file. This file allows the user to change and set parameters, choose a particle generator, select a specific geometry and reconstruct trajectories.

Many experiments have customized the framework to their specific detectors and geometries since FairRoot's inception in 2004. For example, Panda, R3B and CBM have chosen to join the FairRoot structure and develop their geometries, detectors and data management systems. All these flavors share the framework's core structure, but the simulated data is handled differently in each of them.

- EnsarRoot:

The simulation and analysis framework for ENSAR [87] is called EnsarRoot [88]. It shares the core structure of the original code but is readapted for different experiments. It has written in C++, is based on the FairRoot framework libraries and loads the Root libraries to create a ROOT-like output structure. The EnsarRoot implements several detectors and experimental setups and the representation of our experimental setups is included in these customized programs.

The EnsarRoot code makes it straightforward to implement these adaptations. Because it is built on existing tested codes, this significantly lowers programming time and effort.

All simulations and data analysis for this work were done with EnsarRoot because the setting of the TRAGALDABAS detector was built as a module inside its structure. We will go over how to run an EnsarRoot simulation in the next subsection.

The ingredients that must combine in a simulation process can be summarized as follows:

USC
UNIVERSIDADE DE SANTIAGO DE COMPOSTELA

In the beginning, we must determine the geometry of the detectors, detecting materials and other components. The second thing we need is the simulation script. This script contains all the steps in the process that must be completed and must include the type of particles to be generated and the rest of the specifications. And then, we need to organize the data and the results of the simulation. After that, we need to describe the simulated data in detail. Typically, the simulated data does not reflect real-world conditions. At this point, the simulated data must convert into real-like measurements. Finally, proceed to the data analysis.

4.2.1 Structure of EnsarRoot

The objects defined within the EnsarRoot framework will be presented in this subsection. The Trasgo detector families are used as a reference for our simulations, as previously mentioned. The code implementations will be described in detail.

Before getting into the specifics of the simulations, there are a few things to keep in mind about the EnsarRoot code's internal structure. Following this introduction, we will discuss how a Trasgo family detector is simulated to show how the simulation components combine. The RPC plane detector utilized in the TRAGALDABAS detector at USC is an example of this type of detector. The EnsarRoot code contains classes that allow us to simulate detector characteristics and further analyze the simulations.

The essential software dependencies can be installed automatically because the EnsarRoot structure utilizes all the FairRoot libraries. That means all the Root framework's classes can be used conventionally. For example, we can use TTree structures or TClonesArray of Root to organize our data levels, minimizing memory usage and execution time. The following are EnsarRoot's general characteristics:

1- Scripts are used to run the simulations and analyze the data. That

USC UNIVERSIDADE DE SANTIAGO DE COMPOSTELA

means no executables are required; everything may be accomplished using a script and run with Root.

2- The geometry of our detectors is built using Root's TGeo class. The execution script calls the setup, which is included in a root file.

3- The simulation engines Geant3 and Geant4 are both available. Virtual Monte Carlo (VMC) is an EnsarRoot interface that connects simulated events with analysis tools. Ascii generators can also be used. The events are saved in a text file, which the code reads to generate the tracks.

4- TClonesArray can be used to structure simulation results. Because we can simulate millions of events, this is especially valuable. It is easier to keep all this data in a binary format rather than a text file. As illustrated in figure 4.1, the variables generated by the simulation using Geant, an Ascii file, or another way as a generator engine are stored in a Root file and shown in a TTree.

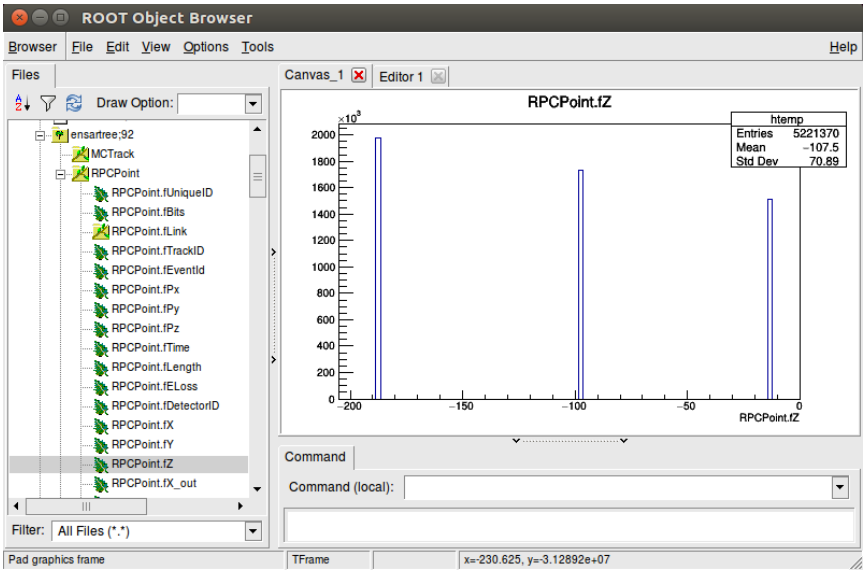

Figure 4.1: An example of a TTree generated by EnsarRoot following a simulation. The Monte Carlo simulation's variables are organized into several data levels.

USC UNIVERSIDADE DE SANTIAGO DE COMPOSTELA

5- The TEve viewer, which uses OpenGL libraries to provide a modern and interactive interface, can see all the events. The viewer shows the particle's tracks, detectors and information, such as its energy and kind. The TEve viewer generates the simulated geometry-related figures illustrated in this chapter.

As can be seen, the EnsarRoot code is nothing more than an interface between the simulated data and its translation to a Root file, where the data is more effectively arranged and displayed using trees.

4.2.2 Cosmic ray shower generator (CRY)

CRY is a software library that generates correlated particle shower distributions for cosmic rays [89]. CRY can create distributions that can be utilized as input to simulation codes for transport and detectors. That enables the generation of cosmic ray particles with data tables in a wide range of energies. The data tables are based on muons, neutrons, protons, electrons, photons and pions simulations with MCNPX 2.5.0 [90] at various altitudes. Shower multiplicity and the time of arrival and zenith angle of secondary particles are generated by the CRY software package within a specified area (up to $300\,m \times 300\,m$). It enables working with a geomagnetic limit based on the latitude of the principal cosmic ray spectrum and its modification over time depending on the average solar cycle. It lets to choose between three elevations: $sea\ level$, $2100\,m$ and $11300\,m$. The program operates in the $[1\,GeV - 100\,TeV]$ and $[1\,MeV - 100\,TeV]$ energy ranges for primary and secondary particles, respectively.

To create the software library `lib/libCRY.a`. type `make` from the top-level directory of the software distribution. That will also compile and run the `test/testMain.cc` program, then compare the results to a reference. The test results will be identical to those of the reference on most systems. The input file `setup.file`, found in CRY's test folder, is used to set the simulation input parameters, as we will see later. The following command is used to generate data:

USC UNIVERSIDADE DE SANTIAGO DE COMPOSTELA

```
g++ -I. -I../scr -o testMain testMain.cc -L../lip -
lRCY
```

In case we made changes in the test program testMain.cc we should run the command above to be sure that the changes are saved.

Another important program in the test folder is an ASCII input file `setup.file`. This file enables us to set and change the default behavior of CRY so that we can choose the type of secondary particles that we need to generate in the simulation processes. All secondary particle types are returned by default. Each of these flags $n = 1$ return the particle and 0 do not return the particle can be independently deactivated as the following illustration:

```
returnNeutrons n
returnProtons n
returnGammas n
returnElectrons n
returnMuons n
returnPions n
altitude A
latitude L
date month-day-year
subboxLength S
```

where the allowed values for A are 0 (default), 2100 m and 11300 m. and S is a box (square plane surface) its area S by S m^2, the particles are returned inside it. Some tables provide the data for 1, 3, 10, 30, 100 and 300 m for box sizes between these values.

For example, suppose that we need to generate 100 secondary particles with the input parameters as illustrated in figure 4.2 after made the required changes in the file `setup.file` we run the following command:

```
./testMain setup.file 100
```

USC UNIVERSIDADE DE SANTIAGO DE COMPOSTELA

```
returnNeutrons 1
returnProtons 1
returnGammas 1
returnElectrons 1
returnMuons 1
returnPions 0
altitude 2100
latitude 42.0
date 12-05-2020
subboxLength 3
```

Figure 4.2: CRY input parameters.

We can also save the output file produced from the generation process with a specific name and with dat or txt extension by running this command:

```
./testMain setup.file 100 >> filename.dat
```

We developed an interface that treats the CRY generator's output file as an Ascii generator adapted for the TRAGALDABAS reference system.

4.3 TRAGALDABAS simulations

As mentioned before, a complete study of the TRAGALDABAS detector system behavior and response under simulated EAS data will present in this section.

The geometric modifications in EnsarRoot were varied and the second plane, RPC2, is not operating so, we have three RPC's working. Furthermore, implementing the relevant geometry of the Faculty of

USC UNIVERSIDADE DE SANTIAGO DE COMPOSTELA

Physics building and implementing a thickness of lead layer after the third plane of the detector for a TRAGALDABAS. Adding a lead layer to the detector allows us to improve the calorimetric capabilities of the experiment. As it is expected that most electrons are stopped in the lead layer and thus, almost only muons reach the last detector plane. The simulations present interaction behaviors between particles and the material medium of the detector.

4.3.1 TRAGALDABAS simulation geometry

EnsarRoot implements the entire TRAGALDABAS detector geometry. It was created using the Root TGeo Geometry package. We are just interested in the forms and materials of the detector's components, not in the construction of the code that represents the geometry on the physics of the detector. One of the benefits of using the TGeo classes is that the volume of the detector may be applied to standard geometrical operations. The detector may be easily rotated and duplicated by using the methods implemented in the TGeo class.

When a particle reaches the detector, it interacts with various materials based on their cross-sections. We are usually just interested in the interaction with a specific medium, not all materials. The simulation's active volume refers to this medium. The interaction of a particle with freon (R134a) gas in TRAGALDABAS generates a signal. Two gaps have been filled with freon gas in these particular RPCs. In order to simulate the final measurement, the particle leaves information in both gaps, which we must process. That allows us to present the concept of data level. This step is essential in the simulation process since they include the data needed to create a realistic experiment description.

4.3.1.1 Data levels

There is a possibility that a particle will interact with a material medium when it travels through the detector. The Geant package includes data on the probability of interaction with material media that

USC
UNIVERSIDADE DE SANTIAGO DE COMPOSTELA

provide cross-sections. Because it does not represent a physical measurement of our detector, this information presented by Geant differs from the real-world representation. Using the Geant data as input, more practical information must be produced. These two representations exemplify data levels. They are defined as point and hit data levels in TRAGALDABAS.

The data at the point level relates to the perfect information provided by the simulation engine. In our case, Geant is instructed to submit data whenever a particle interacts with active volume. This information is not real because it does not match what we see in the experiment. In other meaning, the data in the point level need calibration.

The hit level of data provides a more realistic description. The output of the simulations must be translated into our observable coordinates. In the case of the TRAGALDABAS detector, Position and time coordinates. That is known as digitization and it varies based on the detector. That means the data in the hit level is the same data in the point level but after the calibration of the position and time coordinates.

The classes **TraRPCPoint.h** and **TraRPCHit.h** in the TRAGALDABAS module included with EnsarRoot are used to implement both data levels for TRAGALDABAS. The Root classes are used to store and structure both levels of data:

1- The simulated interactions with the gas are saved in a TClonesArray at the point data level. As a result, every event has a collection of all the points formed by the incident particle's interaction. The position, momentum and detector in which the interaction took place are always available to the user. This data is saved in a computer with a unique identification of the event.

2- Hit data level: Just because a point is identified within the active volume does not mean it will yield a hit. We assumed that a cell (pad) is fired when the charge is left in the medium by a particle (which

USC UNIVERSIDADE DE SANTIAGO DE COMPOSTELA

indicates its energy) above a specific threshold. We can also debate whether the particle's track entered, passed through, or vanished within an active zone. In some circumstances, the points are processed to obtain a hit and saved in a TClonesArray. The information about the cell's center, time and charge deposited is encapsulated in a hit.

3- Saeta data level: in this level, we convert the hits processed in one event and then reconstruct the possible trajectories of the particles traveling through our detector using the TimTrack algorithm. The implementation was done in the TRAGALDABAS module's **TraRPCSaeta.h** class. This saeta object holds information on the particle's propagation, such as its initial position, slope and velocity. These saeta objects are saved in the same way as the points and hits in a TClonesArray structure.

4.3.1.2 Generators of the particles

In the TRAGALDABAS module, we can use different generators:

The first one is TraBoxGenerator and this generator was used and implemented as the first cosmic ray simulator for the TRAGALDABAS detector. It generates muons from a random point on a plane at a user-specified distance z. The next one is the Box generator. With this generator, the user can modify the type of particle, kinetic energy, multiplicity, momentum and angles of the incident particles. The particle's source can either be formed from a surface or a point located at a distance of z above the detector and also determined by the user. We used in this thesis work the Box generator to generate general cosmic ray data at the ground level, used in TRAGALDABAS detector simulations and particle identification methods. The events are written in a text file in ASCII. The particle type, energy and angles are read by the code. The code then displays the tracks and this is the third way to generate particles in the TRAGALDABAS module. The last one is the CRY generator and we explained this generator in detail in subsection 4.2.2.

USC UNIVERSIDADE DE SANTIAGO DE COMPOSTELA

4.3.1.3 Control the simulation parameters

The simulation process is launched with these two scripts (macros): `tragsim.C and tragall.C`. These files contain the list of tasks to be performed. The user controls both scripts:

- The script **tragsim.C** includes the list of tasks and the options to define the simulation configuration. The user can specify the particle propagation engine Monte Carlo (GEANT3, GEANT4, or Fluka), the event generator (tragbox, box, ascii, or cry), activating the TimTrack option, selecting the geometry and the number of events.

- The simulation parameters are offered by **tragall.C**. The user can specify the particle type or angular-energetic range. When the **tragsim.C** script is executing, it will call **tragall.C** script. In other meaning, we modify both codes, but we run just the **tragsim.C** script.

The following command is used to run the simulation with Root:

```
root –l –q tragsim.C
```

tragall.root is the default output file. The EnsarRoot file contains an event TTree structure whose branches match each data level in the reconstruction process. MCTrack, **RPCPoint**, **RPCHit**, **RPCSaeta** and **MCEventHeader** are the branches involved. **MCTrack** contains pertinent information about all particles generated in the simulation, regardless of whether they interact with the detector. As mentioned before, **RPCPoint** holds information on the points where the particles interact with the active volume in each plane. **RPCHit** offers information about hits for each plane. The data in the **RPCHit** branch is essentially **RPCPoint** data that has been digitized. Digitalization is a technique for analyzing simulated data in which the planes have pads. The pads have two active medium gaps. After performing the TimTrack fitting algorithm, the trajectory reconstruction from hits in the planes is

USC
UNIVERSIDADE DE SANTIAGO DE COMPOSTELA

stored in **RPCSaeta**. Finally, **MCEventHeader** gives all the technical details about the simulated event.

EnsarRoot was used to create a realistic model of the Faculty of Physics building, containing the TRAGALDABAS detector. The addition of critical aspects to constructing these geometric implementations is an essential objective of the thesis work. As a result, the code was adjusted to include the geometry of the detector's essential components in the Faculty of Physics.

Figure 4.3 depicts the most concise description of the detector inside the building of the physics faculty with three RPC planes and one electron with an energy of around $0.5\ GeV$ interacting with the concrete floor. After this interaction with the floor's materials, secondary particles are produced and pass through the detector, moving toward the usual cosmic ray angular distribution. Low-energy photons make up the majority of the secondaries. The image was displayed using the EnsarRoot framework's event viewer tool based on Root's TEve functionality. The thickness of the traces represents the energy difference between the particles. As the energy of the particles increases, the trace will be thicker.

Furthermore, in this work, we repeated the study of a calorimetric investigation of the TRAGALDABAS detector but using a layer of lead inserted at $15.1\ cm$ under the third plane. The lead layer was added to the detector's geometry with $1\ cm$ thick.

Figure 4.4 illustrates the sequential interactions of a $1\ GeV$ muon with the building's floors in its path to the detector. It is essential to notice how the muon slightly deviates in the concrete floor just above the detector before interacting with the planes of the detector system. Moreover, the muon suffered slightly from deviation again when it interacted with a lead layer of $1\ cm$ thick inserted at $15.1\ cm$ under the third plane.

USC
UNIVERSIDADE DE SANTIAGO DE COMPOSTELA

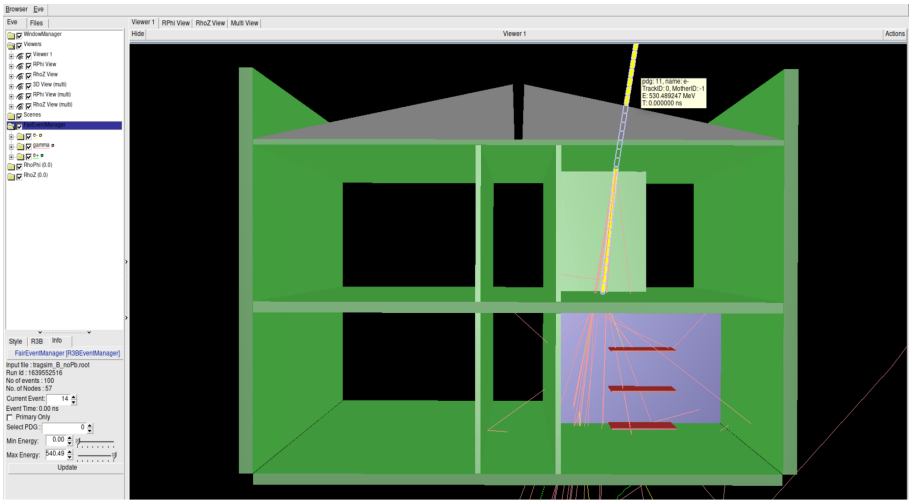

Figure 4.3: shows how the EnsarRoot framework represents a simulated cosmic ray event over the detector system. A primary electron with an energy of around 500 MeV interacts with the floor's concrete and secondary particles produce mainly photons with low energy interacting with three active planes.

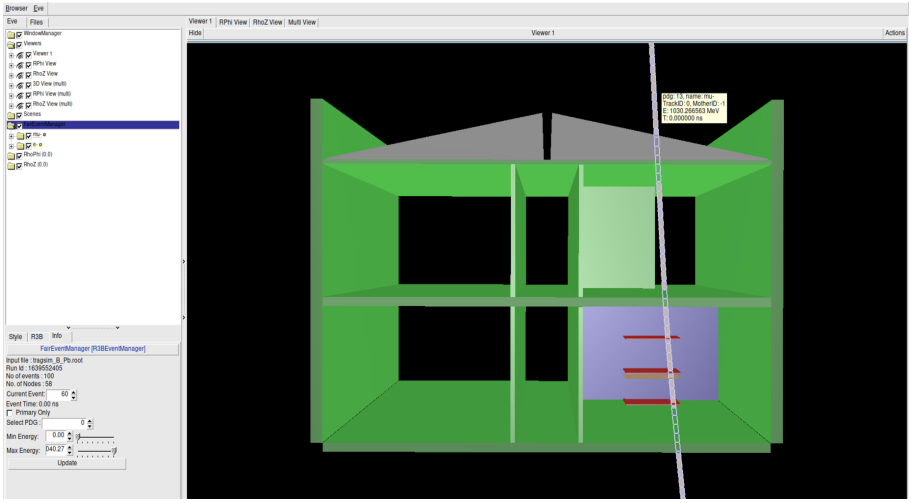

Figure 4.4: Representation of a simulated cosmic ray event over the entire detector system inside the building within the EnsarRoot framework. A primary muon with an energy equal to $1\ GeV$ interacts with the building materials and with a lead layer of $1\ cm$ thick installed at $15.1\ cm$ under the third plane.

USC
UNIVERSIDADE
DE SANTIAGO
DE COMPOSTELA

Figure 4.5 displays an incident electron with an energy of about 130 MeV over the TRAGALDABAS detector with the lead layer, as shown in the figure. The product of the interaction creates a jet of particles that collide on TRAGALDABAS. Low-energy photons and other particles, such as electrons and positrons, make up the majority of the jets. Multiple interactions related to the same secondary cosmic rays can be considered incident particles on the detector.

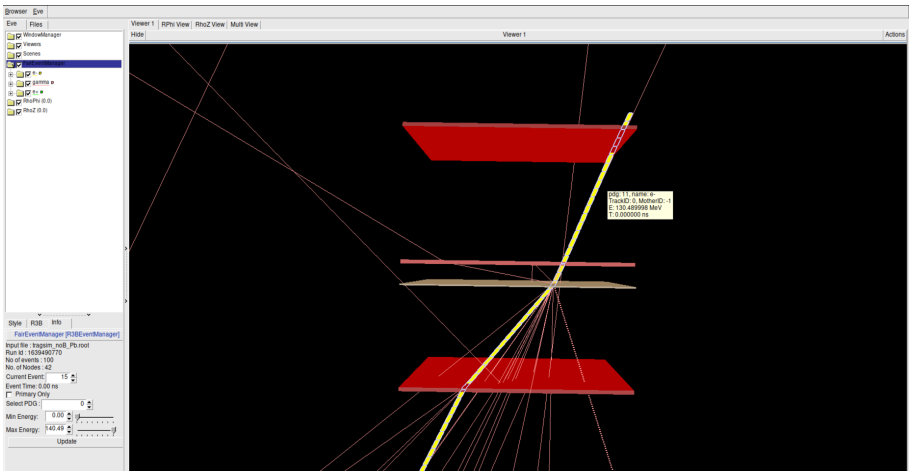

Figure 4.5: illustrates a simulated event over the three planes in the TRAGALDABAS detector with a lead layer within the EnsarRoot framework. A 130 MeV electron crosses the detector interacting with the detector and a shower is produced and arrives at the third plane of the detector. The geometry includes three active RPC planes and a 1 cm thickness of lead layer after the third plane.

4.4 Particle Identification (PID) with TRAGALDABAS

The so-called MIDAS (Multisampling IDentificAtion Software) particle identification method for Trasgo-like detectors was initially developed in [91].

One of the essential goals of this thesis was to improve and implement that technique for particle identification in the TRAGALDABAS detector, which was done in this chapter. Starting on the topology of

USC UNIVERSIDADE DE SANTIAGO DE COMPOSTELA

the event recorded by the detector, it can identify muons and electrons with a degree of accuracy. The method uses simulated and real data to analyze three physical observables: chi-square (χ^2), weighted range (a_n) and total multiplicity (TM) and then generates a behavior pattern for the particles and, after that, implemented to real data to identify the particles. Two configurations for the TRAGALDABAS detector are simulated and analyzed: three active RPC planes without a lead layer and three active planes with a lead layer of 1 cm thicknesses placed 15.1 cm below the third plane. Moreover, real data was obtained with the same configurations as the simulation ones to compare them, which was done for the first time. In the following sections, the entire approach and its outcomes are described and discussed.

4.4.1 Definition of physical observables

Some physical observables have been defined and used to analyze simulation data and real data to better understand the TRAGALDABAS event's behavior and improve a Particle Identification method. The main ones and also those on which the method is based, are:

1- **Total multiplicity** (TM) is the total number of hits (good or valid signals) across the whole detector in a single event. In other words, the total number of the signals (hits) produced in the pads in each plane in the entire detector (all the planes) for the same event.

2- **Weighted range** (a_n) is the distance traveled by a shower or a particle track in some planes, weighted by the hit multiplicity in each plane. It can be presented as $a_n = \sum_{i=1}^{n} M_i\, W_i$, where n is the planes number, M_i is the multiplicity in each plane and W_i is a weight that goes from 0 to $n-1$.

Figure 4.6 shows an example of how to calculate the total multiplicity (TM) and weighted range (a_n) in the TRAGALDABAS detector. As we can see, the RPC2 is not operated.

USC UNIVERSIDADE DE SANTIAGO DE COMPOSTELA

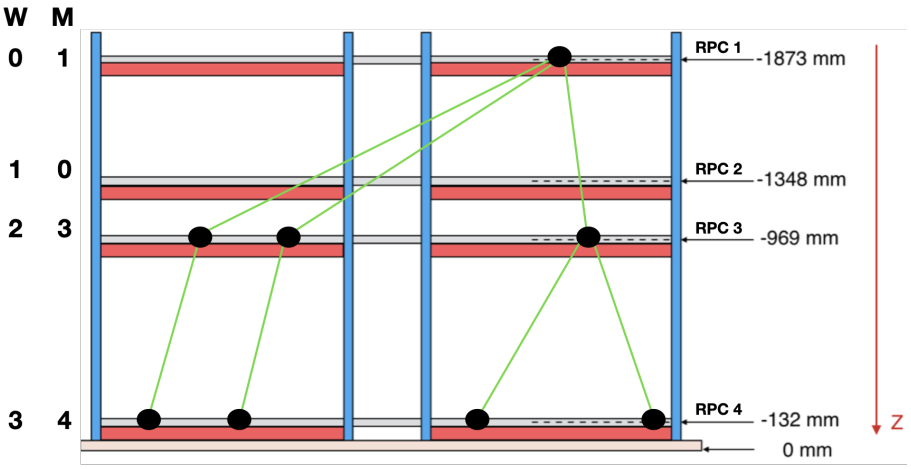

Figure 4.6: the scheme of the TRAGALDABAS detector illustrates an example of how to calculate the total multiplicity (TM) and weighted range (a_n).

According to figure 4.6, we can find the total multiplicity and weighted range as follows:

$$TM = \sum_{i=1}^{n} M_i = M_1 + M_2 + M_3 + M_4 \tag{4.1}$$

$$TM = 1 + 0 + 3 + 4 = 8$$

$$a_n = \sum_{i=1}^{n} M_i W_i \tag{4.2}$$

$$a_n = 1 \times 0 + 0 \times 1 + 3 \times 2 + 4 \times 3 = 18$$

3- **Chi-square** (χ^2) is the track fitting offered by the TimTrack algorithm. The value of the (χ^2) estimates the track's deviation from the straight line when the particle travels through certain RPC planes that can access them.

USC UNIVERSIDADE DE SANTIAGO DE COMPOSTELA

4.4.2 Description of the particle identification method

We Improved and implemented an algorithm for identifying the various particle species identified by the TRAGALDABAS detector during this work. The algorithm is based on a systematic investigation of certain particles influence on some specific physical observables. The simulation was used to parameterize the behavior of these observables, which were then applied to real data. As a result, we can determine the capacities of separation between electrons and muons for TRAGALDABAS detector in particular or any member of Trasgo's family. For the study of particle identification with Tragaldabas, choosing appropriate observables is crucial. The total multiplicity (TM), the weighted range (a_n) and the chi-square (χ^2) of the track fitting are three observable candidates for the research defined and described in the previous subsection. These three physical observables have enabled a deep study to develop and improve algorithms for identifying electrons and muons using the Tragaldabas detector. The study was carried out on three active RPC planes without a lead layer and three active planes with a $1\ cm$ thick lead layer located about $15.1\ cm$ below the third plane. Studies with lead layers reveal the experiment's calorimetric capabilities for identifying electrons and muons. The addition of lead would increase the stopping power of most electrons, forcing them to interact with it and deflecting their path, causing the physical observables to display significant variations between electron and muons and increasing the accuracy.

4.4.3 Simulation data and real data

One million 10^6 particles of electrons and the same for muons were generated using the box generator (see subsection 4.3.1.2) with a simulated configuration without lead layer and 10^5 particles for both electrons and muons with a simulated configuration with lead layer. The generated particles collide with the TRAGALDABAS detector randomly from a virtual plane with an area of about $150 \times 120\ cm^2$, it is approximately equal to the area of the RPC plane, located $12.3\ cm$ above the detector and with directions uniformly distributed in angles

USC UNIVERSIDADE DE SANTIAGO DE COMPOSTELA

θ (Theta) and ϕ (Phi), where θ is between 0 and 13° and ϕ is between 0 and 360°. Electrons have a kinetic energy range of $[10, 5620]\ MeV$, while muons have a kinetic energy range of $[100, 5620]\ MeV$. The virtual plane is large enough to collect many events in all detector planes and the number of events is high enough to provide significant statistics for effective results. For each type of simulated particle, the three dedicated observables mentioned before were analyzed to produce a behavior pattern for the particles, then applied to real data gathered with identical configurations as the simulation data to enable particle identification.

The algorithm provides particle identification (PID), probability of being a specific particle $P(ID)$ and estimated minimum energy (E_{min}) and maximum energy (E_{max}) for the particles.

4.4.4 Configuration of three active planes without a lead layer

For all energy ranges, Figure 4.7 displays the chi-square (χ^2), weighted range (a_n) and total multiplicity (TM) histograms for electrons and muons. The histograms demonstrate that electrons and muons have significant differences. Electrons have a higher value in chi-square, weighted range and total multiplicity than muons. In figure 4.7, it is clear that for χ^2 more than 12.5, a_n greater than 10.5 and TM greater than 6, the probability of electron detection is very high. For the χ^2 values in the region, less than 7 and in the region greater than 7 and less than 12.5 were studied in deep with the weighted range and total multiplicity to distinguish effectively between electrons and muons. Because the electrons and muons have the same range of χ^2 in these regions, we used other observables to separate muons and electrons. Thus, for a first electron and muon separation, the χ^2 parameter can serve and it is, in fact, the first input to the particle identification (PID) algorithm.

USC
UNIVERSIDADE DE SANTIAGO DE COMPOSTELA

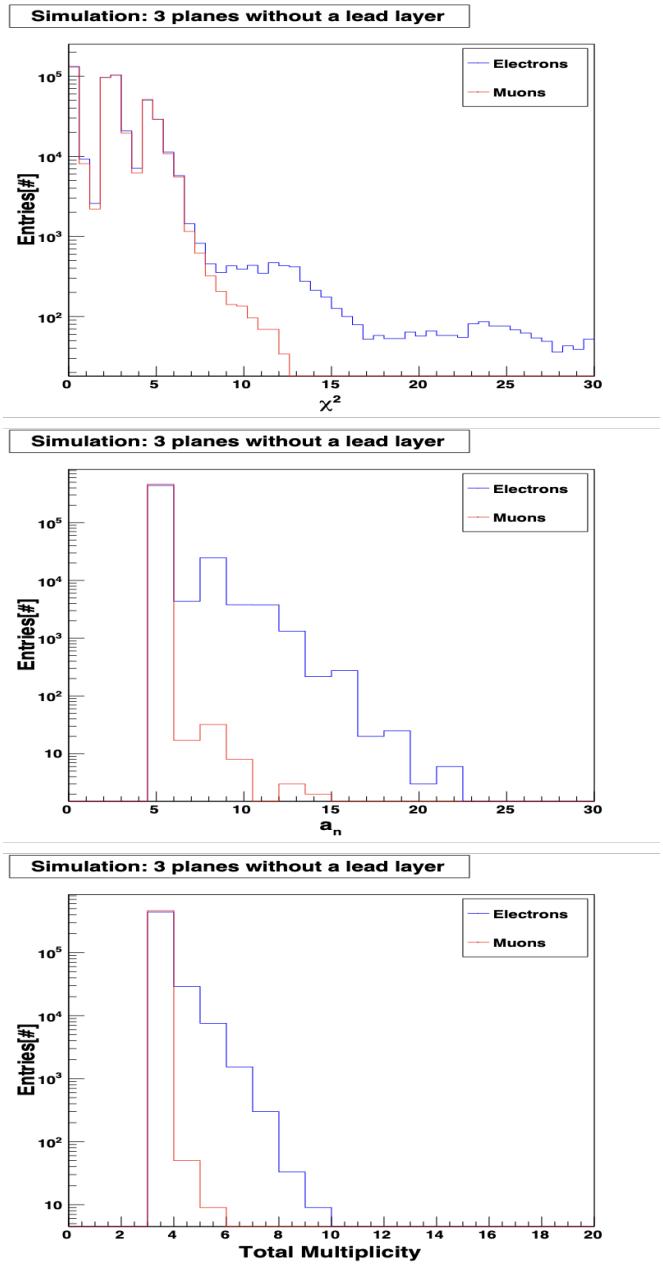

Figure 4.7: Distributions of the three physical observables for simulated data for three operated planes of TRAGALDABAS with a geometry without a lead layer.

USC UNIVERSIDADE DE SANTIAGO DE COMPOSTELA

The flowchart of the algorithm depending on the simulated data without a lead layer for three planes available in the TRAGALDABAS detector is shown in Figure 4.8. An optimal procedure and final particle identification are possible, starting with χ^2 evaluation and an appropriate combination of the three observables proposed.

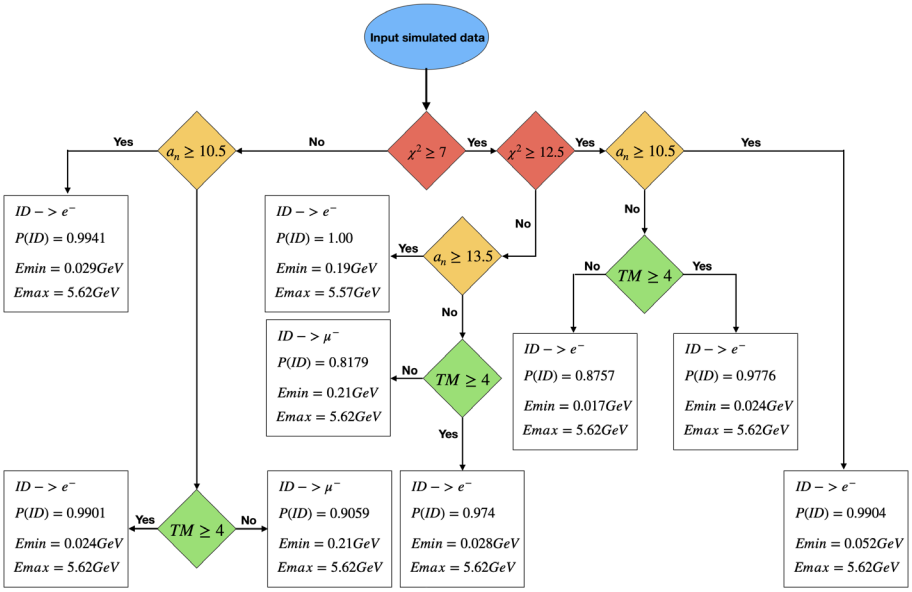

Figure 4.8: Flowchart of the particle identifications algorithm for the TRAGALDABAS detector when 3 planes are operated without a lead layer.

After analyzing the simulated data through studying and parameterizing the behavior of the three dedicated physical observables and then improving a robust algorithm for identifying the particles after that, we applied the algorithm to real data that were taken before installing the lead layer for the TRAGALDABAS detector. In figure 4.9, we can see the histograms for real data for the chi-square (χ^2), weighted range (a_n) and total multiplicity (TM) for the electrons and muons after applying the particle identifications algorithm. Again, for the real data, the algorithm provides particle identification (PID), the probability of being a particular particle $P(ID)$ and minimum energy (E_{min}) and maximum energy (E_{max}) for the particles.

USC UNIVERSIDADE DE SANTIAGO DE COMPOSTELA

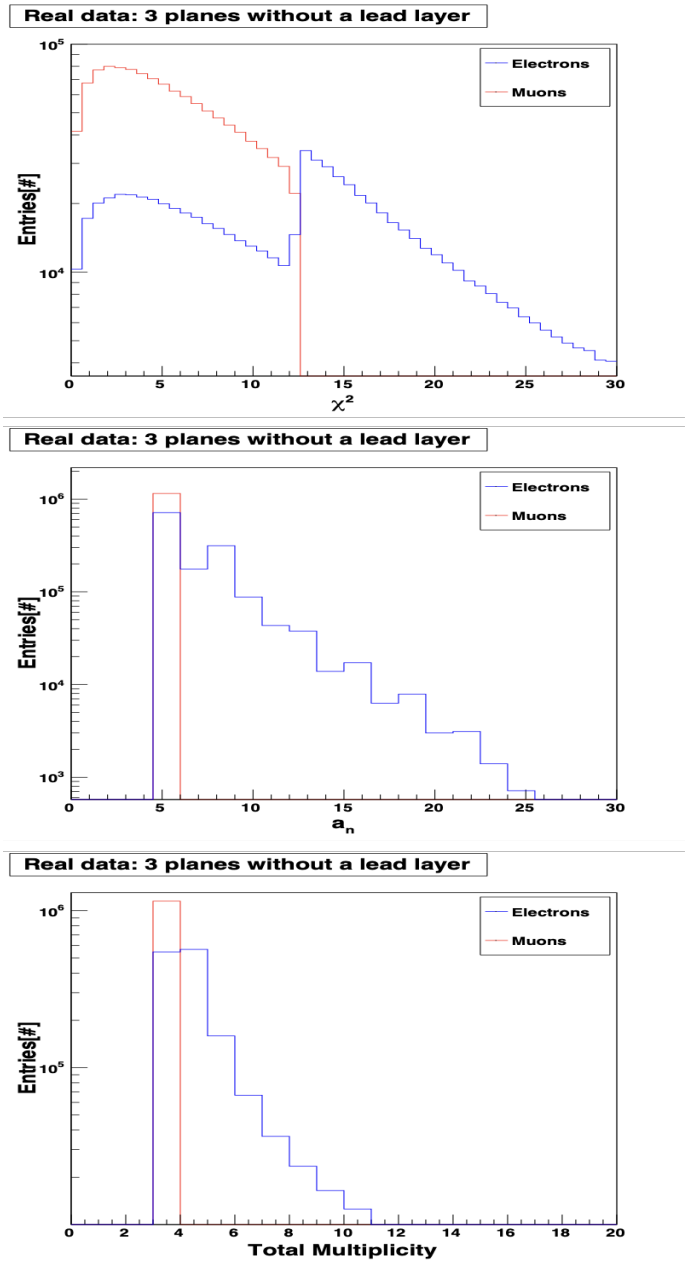

Figure 4.9: Distributions of the three dedicated physical observables for real data for three operated planes of TRAGALDABAS with a geometry without a lead layer.

USC UNIVERSIDADE DE SANTIAGO DE COMPOSTELA

The results in figure 4.9 for the chi-square (χ^2), weighted range (a_n) and total multiplicity (TM) shows great agreement with simulation data. That means that the algorithm is robust and effective in the separation between electrons and muons.

4.4.5 Configuration of three active planes with a lead layer

In this subsection, where just three operational TRAGALDABAS planes with a lead layer are available, the same analysis was performed in the previous subsection. Figure 4.10 shows the chi-square (χ^2), weighted range (a_n) and total multiplicity (TM) histograms for simulated data for electrons and muons for all energy ranges. The histograms show that electrons and muons have vast differences once again. Muons have a lower chi-square, weighted range and total multiplicity value than electrons. The probability of electron detection is very high when χ^2 is more than 17.5, a_n is greater than 7 and TM is greater than 4, as shown in figure 4.10.

Figure 4.11 shows the flowchart of the algorithm for three active planes configuration for the TRAGALDABAS detector, based on simulated data with a lead layer. The algorithm was modified to be suitable for the new configuration. An optimal process and ultimate particle identification are possible, beginning with χ^2 evaluation and a suitable combination of the three dedicated physical observables.

USC
UNIVERSIDADE DE SANTIAGO DE COMPOSTELA

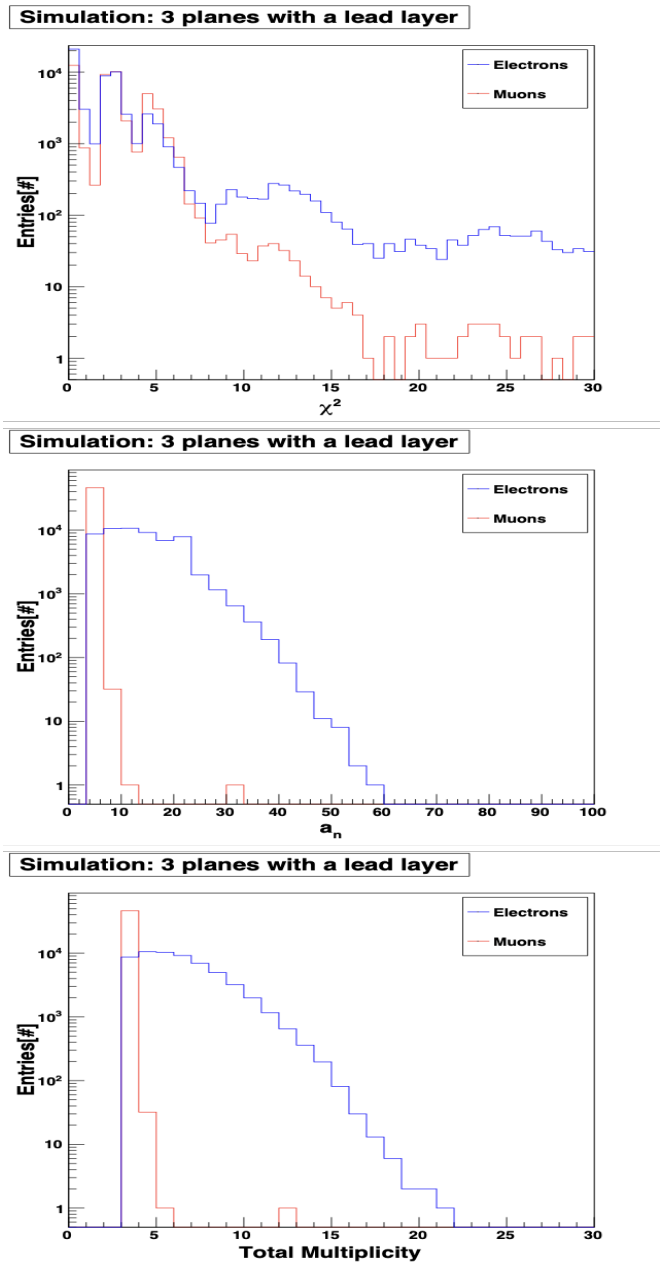

Figure 4.10: Distributions of the three physical observables for simulated data for three operated planes of TRAGALDABAS with a lead layer geometry.

USC UNIVERSIDADE DE SANTIAGO DE COMPOSTELA

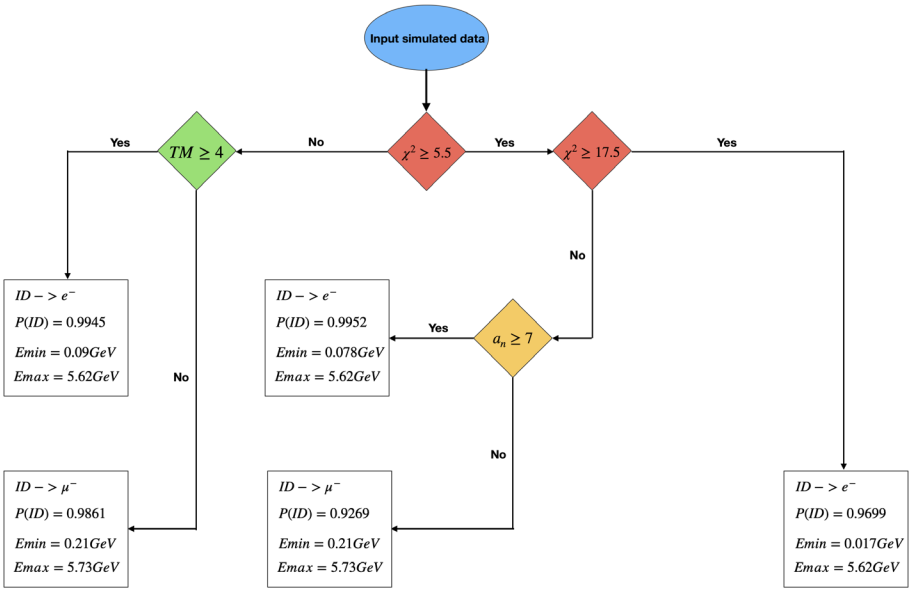

Figure 4.11: Flowchart of the particle identification algorithm for the TRAGALDABAS detector with a lead layer when three planes are operated.

We used the same previous approach to apply the algorithm to real data obtained after installing the TRAGALDABAS detector's lead layer. After applying the particle identifications algorithm, the histograms for real data for the χ^2, a_n and TM for electrons and muons are presented in figure 4.12.

Comparing the results of the simulation data in figure 4.10 with the results of real data in figure 4.12 for the chi-square (χ^2), weighted range (a_n) and total multiplicity (TM) reveals a perfect agreement between them. Moreover, we realized that the probability of the detected particles being a specific particle with a lead layer configuration is higher than the probability without a lead layer, as illustrated in figure 4.13. Furthermore, the algorithm is more effective in distinguishing between muons and electrons.

USC
UNIVERSIDADE DE SANTIAGO DE COMPOSTELA

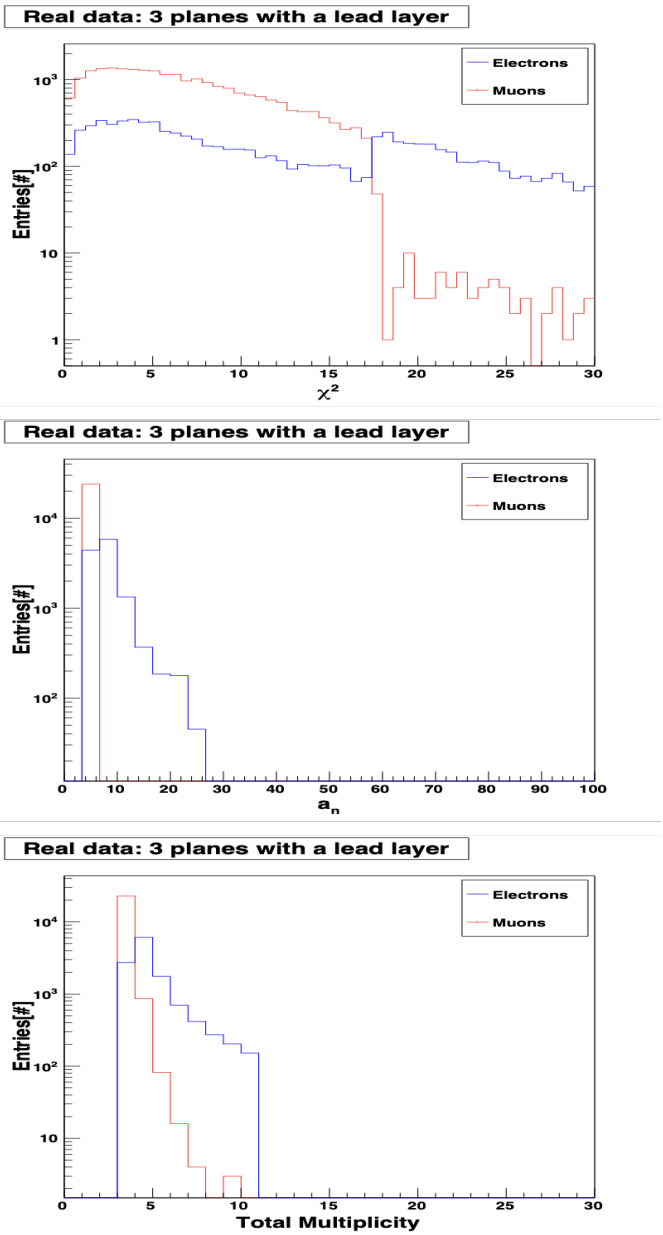

Figure 4.12: Distributions of the three dedicated physical observables χ^2, a_n and TM for real data for three operated planes of TRAGALDABAS detector with a lead layer geometry.

USC UNIVERSIDADE DE SANTIAGO DE COMPOSTELA

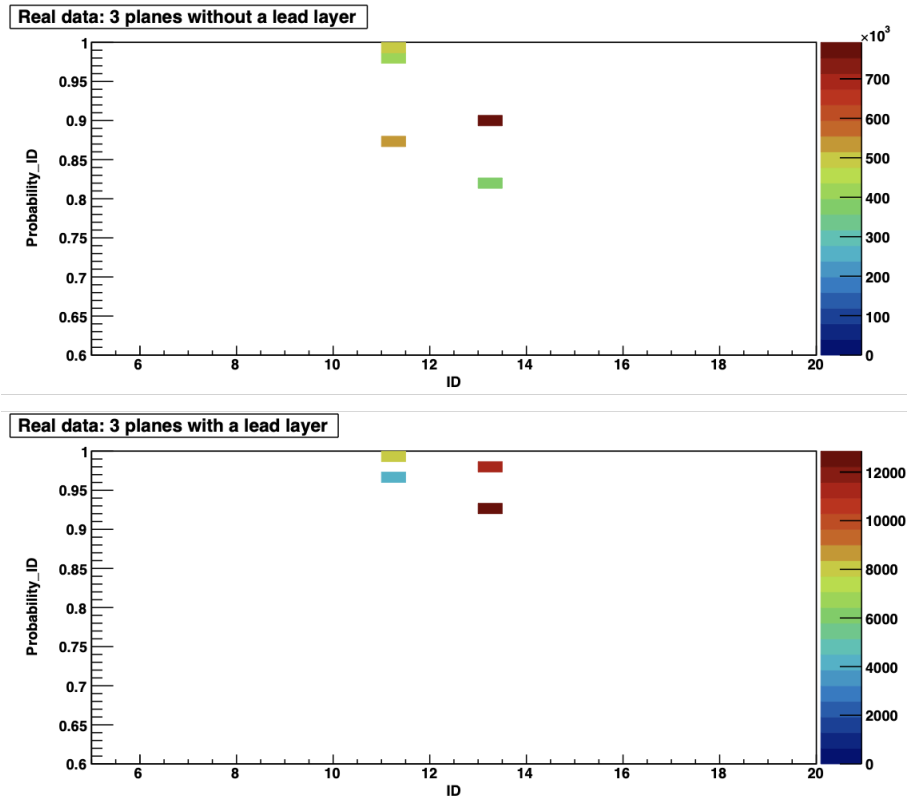

Figure 4.13: 2-Dimensional histograms for the probability of the detected particles being a particular particle for the configuration of the TRAGALDABAS without lead layer (up) and with lead layer (down) versus the identity number of the particles, where the identity number of the electrons is 11 and 13 for the muons.

Moreover, in the real data, without using a lead layer, we found that the ratio of the electrons from the total number of the detected particles is about 55% and the ratio of the muons about 45%. The probability of the most electrons is around 88% and 90% for the most muons. Whereas after using a lead layer, the ratio of the detected electrons becomes around 34% and the ratio of the detected muons about 66%. Furthermore, the probability of being the detected particle is a specific particle was improved, where the probability of the most

USC UNIVERSIDADE DE SANTIAGO DE COMPOSTELA

electrons becoming almost 100% and 94% for the most detected muons.

The aim of adding the lead layer to the TRAGALDABAS configuration for studying the experiment's calorimetric capabilities for identifying muons and electrons more effectively by increasing the stopping power of most electrons and forcing them to interact with it and deflecting their trajectory is achieved. As we can see, the physical observables show significant variations between the particles, which means increasing the accuracy of the separation between electrons and muons and increasing the probability of the detected particles being a particular particle (see figure 4.13). It would be advisable to include perhaps another lead layer behind the second plane or increase the width after the third layer.

4.4.6 Angular distribution

The real data of the TRAGALDABAS detector with a configuration including three active planes without utilizing a lead layer was used to study the angular distribution for the detected particles. Moreover, to correct the angular distribution by the geometric acceptance, 10^6 muons were generated to calculate the geometric acceptance by the simulation using the box generator with the energy around 5.6 GeV corresponding to each polar angle, as shown in Figure 4.14.

The generated muons collide with the TRAGALDABAS detector randomly from a virtual plane with an area approximately equal to the area of the RPC plane, located about 12 cm above the detector.

Figure 4.15 shows the normalized angular distribution histogram to its integral and then a fit to a cosine power law $(A\cos^n(\theta) + B$ was applied within a selected range of $(0.17, 0.7)$ $rads$. The best fit of the distribution gives a value of $n = 2.50 \pm 0.98$. This value is compatible with the typical value $n{\sim}2$ observed everywhere. The considerable uncertainty is due mainly to the small amount of data used in our

USC UNIVERSIDADE DE SANTIAGO DE COMPOSTELA

analysis and the fact that the track reconstruction algorithms still need to be improved. In any case, the method and the programs keep available to be used in the future with higher statistics and with a better sample of data.

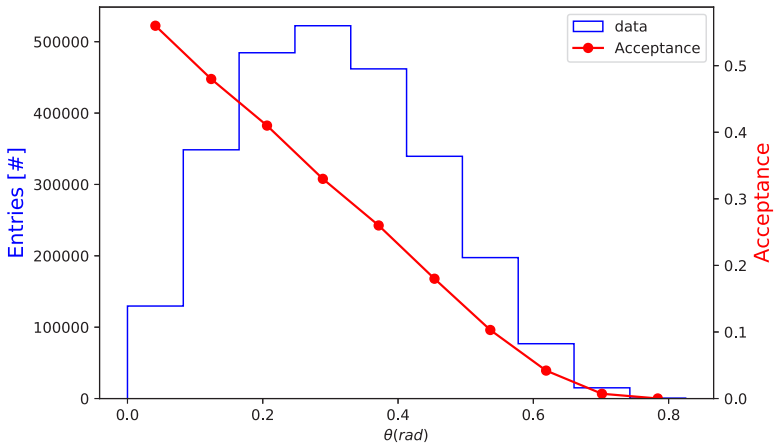

Figure 4.14: The histogram of the angular distribution for the TRAGALDABAS real data without using a lead layer and the geometric acceptance calculated by the simulation when the trigger between the first and the third plane.

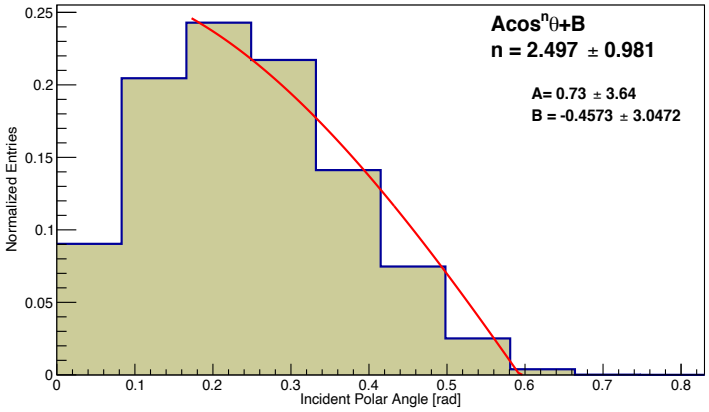

Figure 4.15: Normalized angular distribution for the incident polar angles corrected by the acceptance in the TRAGALDABAS detector. The red line is the best fit for the distribution. We observe an angular variation as $\cos^{2.497}(\theta)$ of the polar angle.

USC UNIVERSIDADE DE SANTIAGO DE COMPOSTELA

Experimentally, it is commonly accepted that the angular distribution follows a $\cos^2(\theta)$ law.

USC
UNIVERSIDADE DE SANTIAGO DE COMPOSTELA

USC
UNIVERSIDADE
DE SANTIAGO
DE COMPOSTELA

5 Preliminary analysis of the TRISTAN detector

In this chapter, we investigated the effects of atmospheric pressure and temperature on cosmic ray data recorded by the cosmic ray detector TRISTAN during the first trip of the detector as shown in Figure 5.1, on board the Spanish vessel Sarmiento de Gamboa from Vigo, Spain $42^{\circ}\ N$ to Punta Arenas, Chile $53^{\circ}\ S$, measuring the secondary cosmic-ray rate continuously throughout the Atlantic crossing from November 15th to December 23rd, 2018. Furthermore, we introduce a simulation part about the geometric acceptance of the TRISTAN detector, considering the dead zones in the structure of the detector system.

The structure of the TRISTAN detector is explained in detail in subsection 2.5.2.

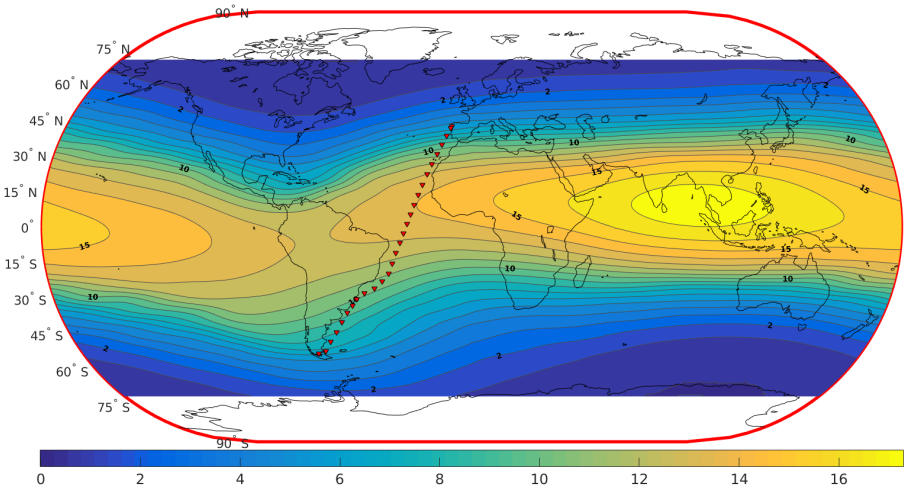

Figure 5.1: Represent the path of the TRISTAN detector (one red triangle per day) during the first trip of the detector from Vigo, Spain, to Punta Arenas, Chile. The figure is taken from [5].

USC UNIVERSIDADE DE SANTIAGO DE COMPOSTELA

5.1 Introduction

Changes in numerous atmospheric parameters, most significantly the pressure at ground level and the atmosphere's temperature profile, affect the rates of cosmic rays detected at the Earth's surface. The pressure or barometric effect is caused by energy loss from radiation absorption in the atmosphere. As a result of the more efficient absorption of secondary cosmic ray particles, the measured rates are modified in anticorrelation with the ground-level pressure. In more detail, the increased mass is related to a higher air column height, which alters the decay probabilities of the particles involved, implying a slight (but considerable) contribution to the main negative correlation [92].

In cosmic ray physics and astrophysics, investigations of the physical nature of cosmic ray changes on different time scales are a significant factor. The modulation of cosmic rays, in particular, is a helpful tool for describing disturbing circumstances in the heliosphere [93].

The modification of the density of the air column as a result of temperature variations influences cosmic ray rates even when there are no variations in ground-level pressure. The interaction (positive correlation) and decay (negative correlation) of secondary particles through the atmosphere are responsible for the temperature effect. The temperature effect can be roughly one order of magnitude smaller than the pressure effect, needing much additional control of systematic instrumental origin effects and high statistics in the first place.

When using ground-based detectors to study fluctuations in cosmic ray intensity, atmospheric influences on secondary particle fluxes must be considered. Significant background changes are produced by pressure and temperature effects. Thus, before studying the relation between ground-based data and any extraterrestrial events, it is necessary to remove these effects [94].

USC
UNIVERSIDADE DE SANTIAGO DE COMPOSTELA

5.2 Atmospheric properties

The relationship between cosmic ray measurements and atmospheric properties, namely pressure and temperature, has been studied since cosmic rays were discovered and the significant intervening phenomena are well understood [95]. In addition, many investigations revealed that the atmosphere has an integrated effect on the measured rate of cosmic rays at Earth's surface. Several experiments, such as [96] and [97], have found fascinating correlations between the rate of very high energy muons and the temperature at the stratospheric, in addition to the well-known Winter-Summer seasonal effects.

5.2.1 Barometric effect

The barometric effect (the pressure effect) on secondary cosmic ray variations is experimentally determined and a linear relation can express it:

$$\left(\frac{\Delta R}{\bar{R}}\right)_P = \beta \,.\, \Delta P \tag{5.1}$$

where $\left(\frac{\Delta R}{\bar{R}}\right)_P$ is the relative variation of the cosmic ray rates due to the pressure effect, $\bar{R}$ represents the average value of the cosmic ray rates over the period under consideration, $\Delta P = P - \bar{P}$ is the deviation of the ground-level pressure concerning its mean value $\bar{P}$ over the same period and β is the barometric coefficient, which is dependent on several factors, including the nature of the secondary component and the altitude at which the observation is done [94].

The atmospheric pressure deviation ΔP and related relative deviation of cosmic ray rates $\frac{\Delta R}{\bar{R}}$ measured by the TRISTAN detector have been analyzed after correcting the rate by efficiency. The relationship between $\frac{\Delta R}{\bar{R}}$ and ΔP is shown in Figure 5.2. A linear regression fit method was used to find the barometric coefficient β and

USC UNIVERSIDADE DE SANTIAGO DE COMPOSTELA

its value was $-0.597\ \%/mbar$, too big compared with the typical values measured with other detectors.

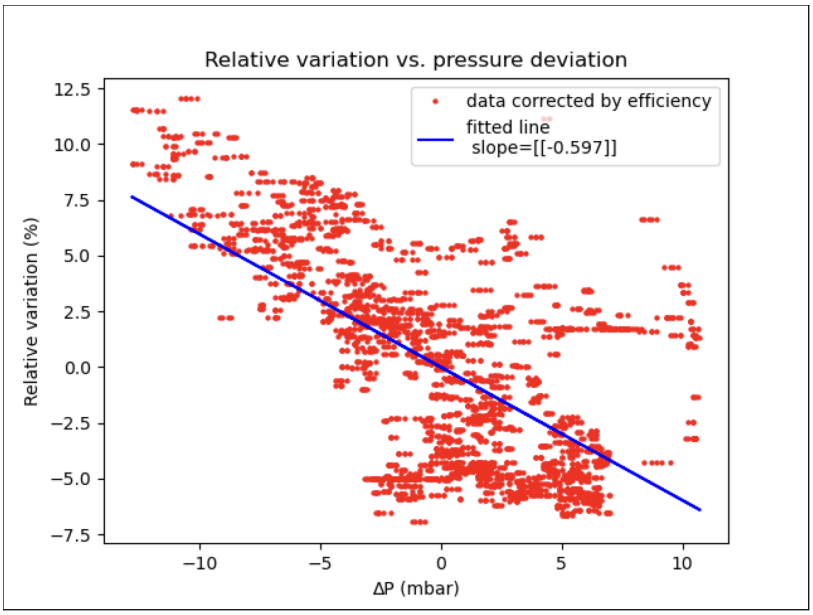

Figure 5.2: The anticorrelation between the relative cosmic ray rate variation and the pressure deviation observed in the first trip of the TRISTAN detector from Vigo, Spain to Punta Arenas, Chile.

We observed that such barometric coefficient (β) is not properly calculated because the detector was not in the same place throughout the trip. As mentioned before, atmospheric properties like pressure, temperature, latitude and geomagnetic field, among others, affect the rate of cosmic rays arriving at the Earth's surface. In other words, the cosmic rays rate that reaches the surface of the Earth differs with different atmospheric properties at these ones depending very strongly on the terrestrial latitude. That means we can not use the value of the barometric coefficient that we got to correct the rate of the cosmic rays detected by the TRISTAN detector. Alternatively, we divided the trip period into several periods to make a better correction. Each one contained 3 days of data with the mean value every 1 hour and was analyzed separately, as presented in Figure 5.3.

USC UNIVERSIDADE DE SANTIAGO DE COMPOSTELA

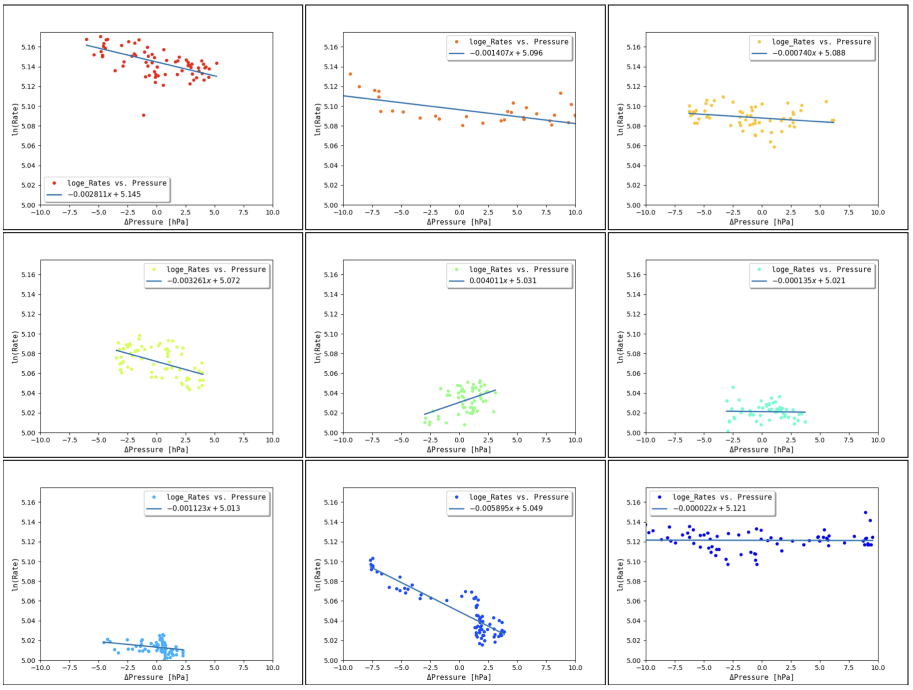

Figure 5.3: shows the linear fit method used to obtain the barometric coefficient for every 3 days of data for the rate of the cosmic rays and the pressure deviation measured by the TRISTAN detector.

Now, a preliminary barometric coefficient for the whole period achieved by the TRISTAN detector while crossing the Atlantic Ocean was calculated by calculating the mean value for the barometric coefficients for every period of 3 days of the data and the value was $-0.127\ \%/mbar$. We observe that in one of the periods, we get an unphysical positive value. In others periods, we get to big values. These discrepancies can be explained by the low quality of the data used that still needs to be corrected by some failures in the cooling system during the journey and other problems. As a consequence, our results should be taken as a first approximation.

After calculating the barometric coefficient β and using it to correct the cosmic ray rates during the journey, Figure 5.4 shows the rate of the secondary cosmic rays corrected by efficiency (a) and

USC UNIVERSIDADE DE SANTIAGO DE COMPOSTELA

presents a comparison between the cosmic ray rates without applying pressure correction (c) and corrected rates with pressure (d) and also the pressure-time variations (b). All the data presented are the mean value every 10 minutes. We see that the pressure correction improves the uncorrected distribution slightly. For instance, the sharp pick observed on the left side of the figure that was produced by the very low pressures existing during the first days of the journey disappears in the corrected distribution.

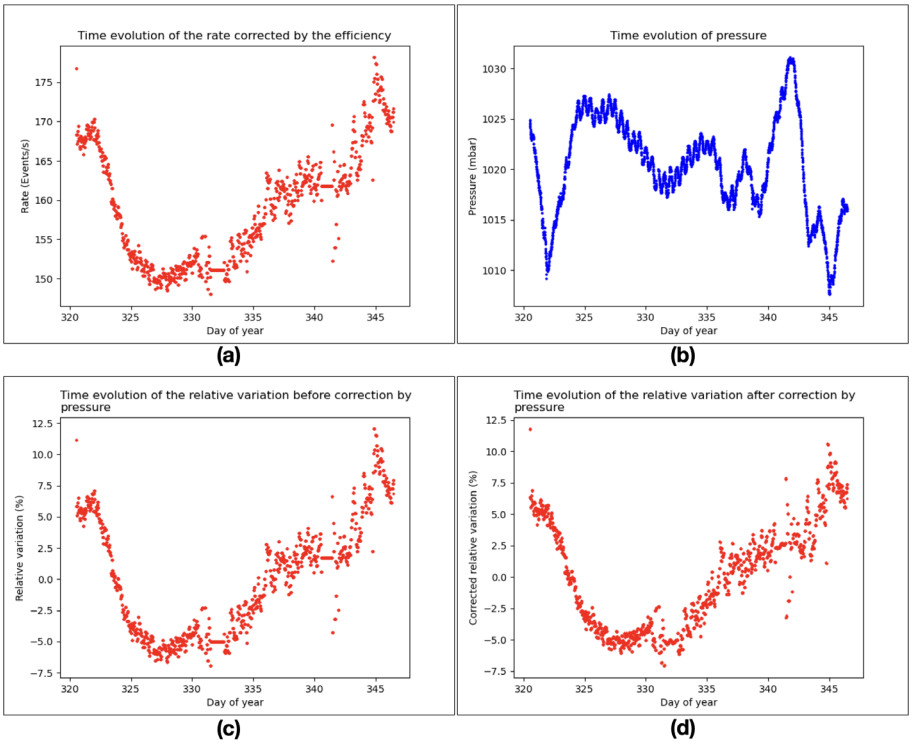

Figure 5.4: Illustrates the cosmic ray rates corrected by efficiency (a), the atmospheric pressure (b), (c) and (d) uncorrected and corrected rates of the cosmic rays with pressure, respectively, in the period from November 15th to December 23rd, 2018.

USC
UNIVERSIDADE DE SANTIAGO DE COMPOSTELA

5.2.2 Temperature Effect

The temperature influence of secondary cosmic ray particles in the atmosphere can be taken into consideration using a variety of ways [98] and [99]. The integral method [100] has been demonstrated to be one of the most precise. However, it requires knowledge of the distribution of temperature coefficients in the atmosphere. These can be calculated theoretically for various threshold energies, zenith and azimuth angles of incidence [95], or extracted from the data of the cosmic rays [101].

We will repeat the same procedure done in the previous subsection to find the temperature effect on the secondary cosmic ray. It can be represented using the following linear relationship:

$$\left(\frac{\Delta R}{\bar{R}}\right)_T = \alpha \,.\, \Delta T \tag{5.2}$$

Where $\left(\frac{\Delta R}{\bar{R}}\right)_T$ is the relative variation of the cosmic ray rates due to the temperature effect, α is the temperature coefficient and $\Delta T = T - \bar{T}$ is the deviation of the ground-level temperature concerning its mean value $\bar{T}$. $\bar{R}$ represents the average value of the cosmic ray rates over the period under consideration.

A significant increase in rates occurred due to an air conditioning failure as the boat was near the Equator. According to environmental sensors placed around the detector, the temperature increased from 20 to 30 ^{o}C in about 10 hours, as shown in Figure 5.5.

USC
UNIVERSIDADE DE SANTIAGO DE COMPOSTELA

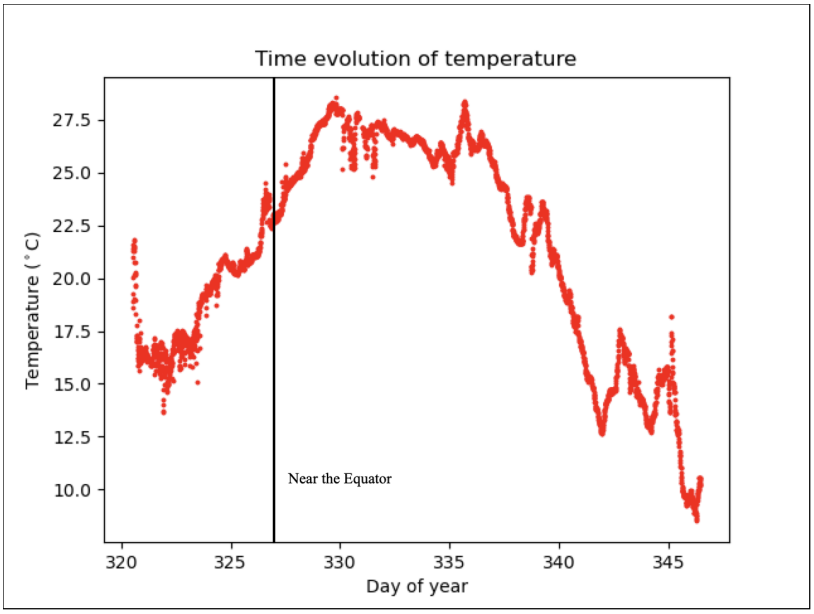

Figure 5.5: Time evolution of the temperature recorded by the TRISTAN detector. An air conditioner failure occurred when the detector was near the Equator, where the temperature increased about 10 $^{\circ}C$ through 10 hours.

Figure 5.6 shows the atmospheric temperature deviation ΔT and related relative deviation of cosmic ray rates $\frac{\Delta R}{\bar{R}}$ detected by the TRISTAN detector during the journey. We used the same data that was corrected by efficiency. A linear regression fit method was applied to calculate the temperature coefficient α and the value was $-0.688\ \%/{}^{\circ}C$.

USC
UNIVERSIDADE DE SANTIAGO DE COMPOSTELA

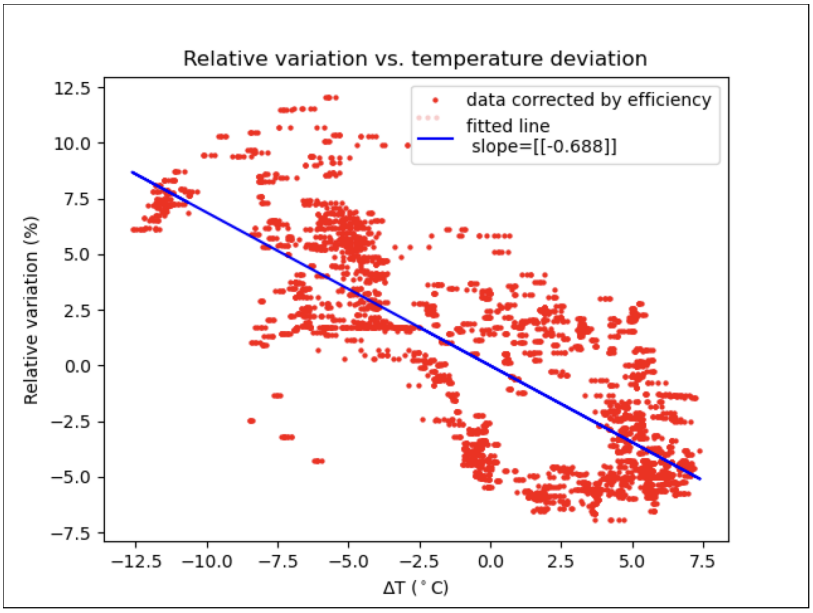

Figure 5.6: Example of the linear fit method used to obtain the temperature coefficient for the anticorrelation between the relative variation of the cosmic ray rates and the temperature deviation measured in the first trip of the TRISTAN detector.

For the reasons mentioned in the previous subsection, we did the same thing where we divided the journey period into several periods. Each one included three days of data with the mean value every 1 hour and was analyzed individually, as illustrated in Figure 5.7. The temperature coefficient (α) for the whole trip period was computed by calculating the mean value for the temperature coefficients for every period of 3 days of the data except the last two values in Figure 5.7 because it seems the data belongs to other periods. The value of the temperature coefficient that we got was $-0.1\,\%/^{\circ}C$. Again, some extreme results observed in some periods are a consequence that the data or not yet corrected by several problems that happened during the trip.

USC
UNIVERSIDADE DE SANTIAGO DE COMPOSTELA

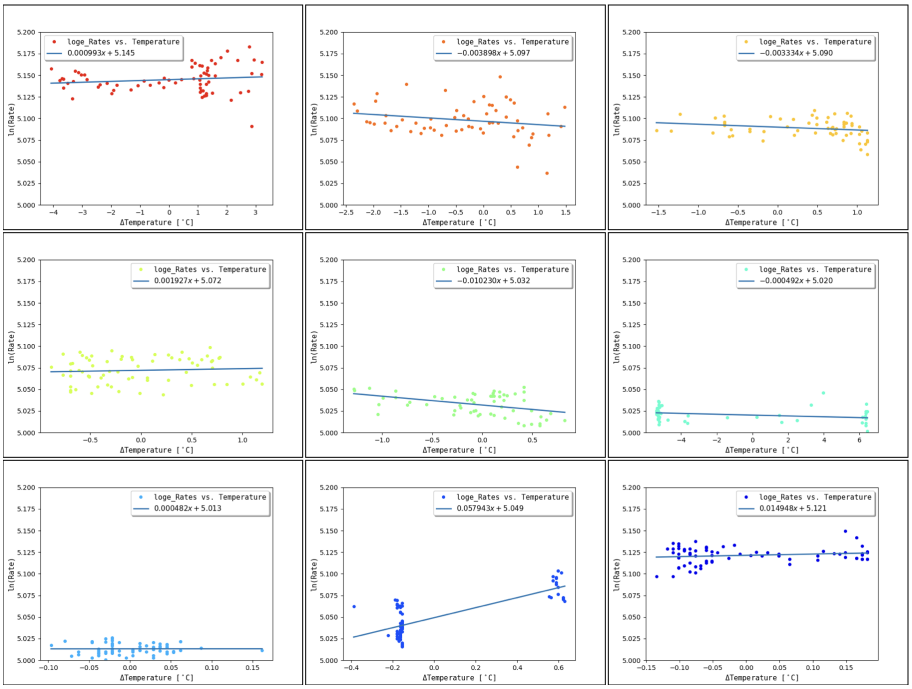

Figure 5.7: Represents the linear fit method used to get the barometric coefficient for every 3 days of data for the rate of the cosmic rays and the temperature deviation measured by the TRISTAN detector.

A comparison between the cosmic ray relative variations without applying temperature correction and corrected relative variations with temperature is shown in Figure 5.8.

USC
UNIVERSIDADE DE SANTIAGO DE COMPOSTELA

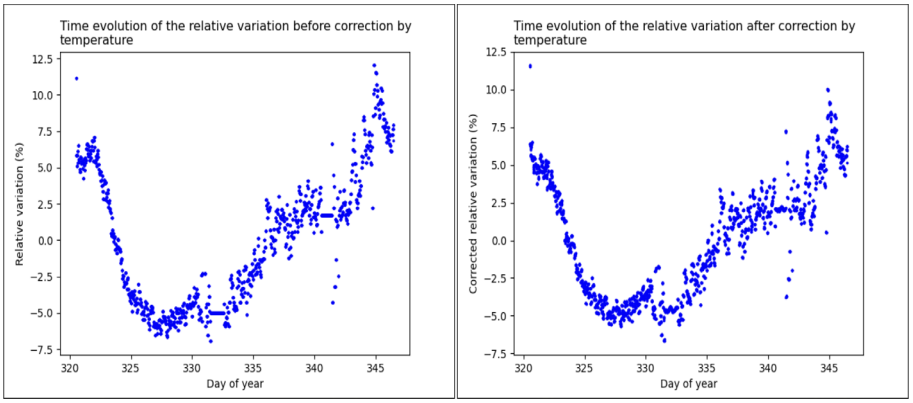

Figure 5.8: The cosmic ray relative variations uncorrected by temperature (left) and the cosmic ray relative variations corrected by both pressure and temperature (right) from November 15th to December 23rd, 2018.

As a short summary, we realize that a preliminary correction of the data by the pressure and the temperature effects after dividing the journey into short three-day periods is enough for correcting the most significant atmospheric effects in the rate measurement. However, getting better results would require a more careful analysis of all the problems affecting the measured rates, a task that is out of the scope of this work.

5.3 Geometric acceptance

The geometric acceptance of the TRISTAN detector or any member of the TRASGs family, in general, has been defined by generating all possible simulated tracks from $\cos^2\theta$ distribution over it, in other words, a probability distribution of characterizing the trajectories of particles that cross the detector. The geometric acceptance depends on the geometry of the detector and that includes the dimension of the RPC plane in the detector system, how the RPC plane is divided into pads such as TRISTAN or TRAGALDABAS or strips such as STRATOS detector and finally, the distance between the planes (d) play an essential role in the determination of the value of the geometric acceptance.

USC UNIVERSIDADE DE SANTIAGO DE COMPOSTELA

The importance of geometric acceptance determination is that it can be used to correct the real rate $Hz\,cm^{-2}$ of particles detected by the detector. In addition to the structure of the TRISTAN detector described in detail in subsection 2.5.2, proper electrical insulation with 6 mm wide was needed between the pads (known as the dead zones) to avoid the crosstalk between neighboring pads, as shown in Figure 5.9.

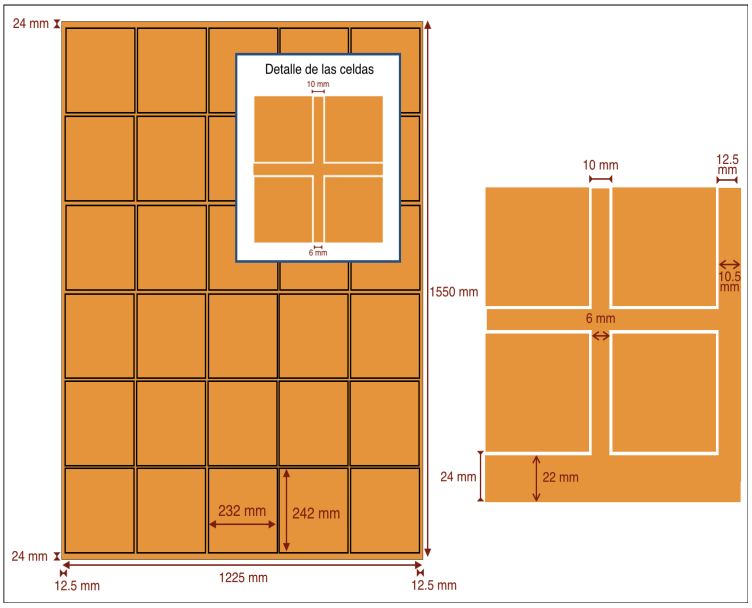

Figure 5.9: The pads in the TRISTAN detector are separated by grounded insulator rings 6 mm wide to eliminate crosstalk between neighboring pads.

The study of the geometric acceptance for the TRISTAN detector was done by simulation where was generated 10^6 particles incident randomly over the entire detector system with $\cos^2\theta$ distribution.

The geometric acceptance is studied with a configuration taking into account the dead zones of all the planes in the detector and also, the trigger between any two planes in the detector. The incoming particle with any direction is recorded as an event if the generated particle is hit the upper plane in the active regions. In case the particle hits the lower plane, it will record as a detected event, as illustrated in Figure 5.10.

USC UNIVERSIDADE DE SANTIAGO DE COMPOSTELA

Thus, the geometric acceptance calculates by the ratio between the detected events to the generated events.

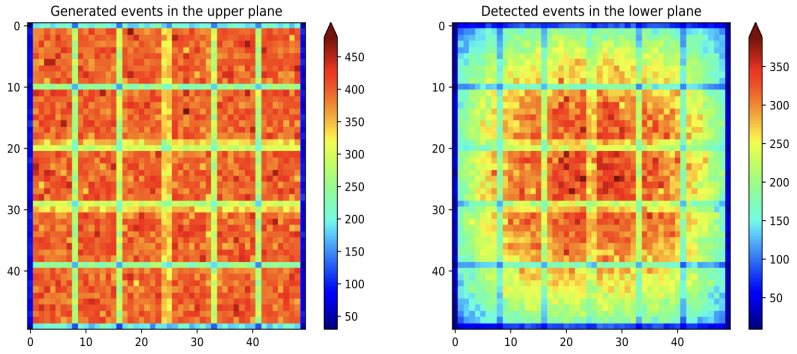

Figure 5.10: Shows an example for the map of the generated (hit) events in the first plane (left) in the TRISTAN detector and the map of the detected events in the third plane (right). We can see the effect of the electrical insulator between the pads.

Figure 5.11 represents the 3-dimensional histograms of the geometric acceptance for the TRISTAN detector at different distances between the planes.

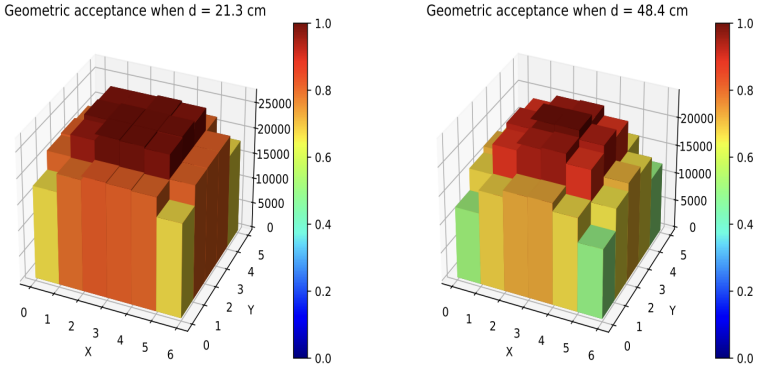

Figure 5.11: Geometric acceptance at different distances for the TRISTAN detector, when the trigger between the first and second plane, $d = 21.3\ cm$ (left) and when the trigger between the first and the third plane, $d = 48.4\ cm$ (right).

USC UNIVERSIDADE DE SANTIAGO DE COMPOSTELA

Note that the acceptance is higher in the middle of the plane and decreases with the approach to the edge of the plane. That means most particles that are incident with small angles are accepted. Thus, acceptance has the maximum value. Whereas with increasing the incident angle of the particles, the acceptance gradually decreases until it reaches zero, as shown in the Figure 5.12.

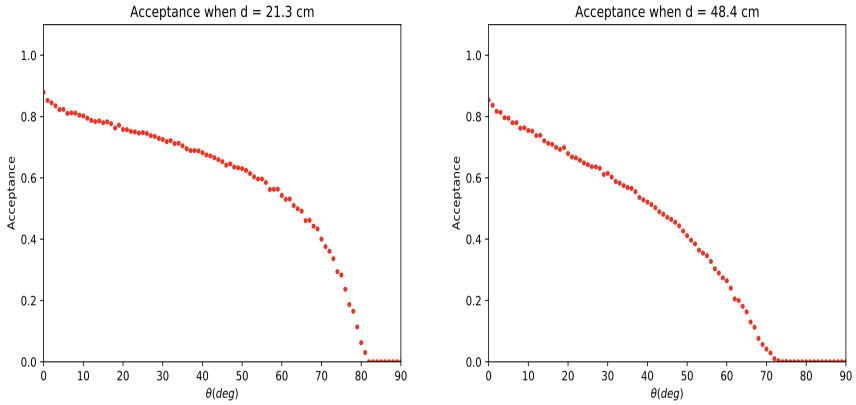

Figure 5.12: The acceptance as a function of the incident angle for the TRISTAN detector, when the trigger between the first and second plane, $d = 21.3\ cm$ (left) and when the trigger between the first and the third plane, $d = 48.4\ cm$ (right).

According to Figure 5.12, we can see that with increasing the distance between the trigger planes, the acceptance angle (θ) decreases and vice versa. The acceptance angle is found when the trigger between the first and the second plane is around 82° and 72° when the trigger is between the first and third plane. The acceptance angle is defined as the maximum angle at which the particle has to an incident to interact with all the detector planes. In other words, if a particle incident with an angle greater than the acceptance angle, that means the particle will interact with one plane or two depending on the angle but not with all the planes. Furthermore, the value of the acceptance in both cases is about 85% due to the effect of the dead zones in the planes, as mentioned before.

USC UNIVERSIDADE DE SANTIAGO DE COMPOSTELA

6 Calibration and performance analysis of the STRATOS Cosmic Ray detector

The experience obtained in the design and construction of the different detectors, as well as the excellent performance offered by RPC technology in terms of covering large areas at a reasonable price and the availability of some of the electronics used, led to the idea of proposing a new generation of cosmic ray detectors called STRATOS, the third member of the TRASGOs family. The idea was to create detectors that seem to be relatively small in size but modular enough to cover large areas or volumes. Thanks to the RPC's good timing precision, they have the ability to reconstruct the direction of incident particles using several RPCs and a particular ability to identify electrons and muons, the main components of so-called secondary cosmic rays at the Earth's surface. The main goal is to find correlations between measured cosmic ray trends and the atmosphere's temperature profile and enhance climate predictions by studying the real-time change of stratospheric temperature.

6.1 Introduction

The STRATOS detector was developed as a collaboration of the LIP group in Coimbra University (UC), Galician Institute of High Energy Physics (IGFAE) at Santiago de Compostela University (USC) and the company Hidronav technologies[6] for atmospheric studies. It is an improvement of the existing TRAGALDABAS and TRISTAN designs. As a novelty in its design, first, instead of rectangular pads, an active area per plane of $118 \times 158\ cm^2$ is separated into 64 long strips, as shown in Figure 6.1. Second, compared to prior RPC versions, the read-

[6] www.hidronav.es

USC UNIVERSIDADE DE SANTIAGO DE COMPOSTELA

out electronics design lowers the price per channel. The STRATOS detector comprises four RPCs planes. All of them are instrumented and fully operational, which defines the system equipped with fast Front-End Electronics (FEE) [65]. Furthermore, the detector was manufactured in Coimbra with the assistance of the mechanical workshop and detection laboratory teams of LIP.

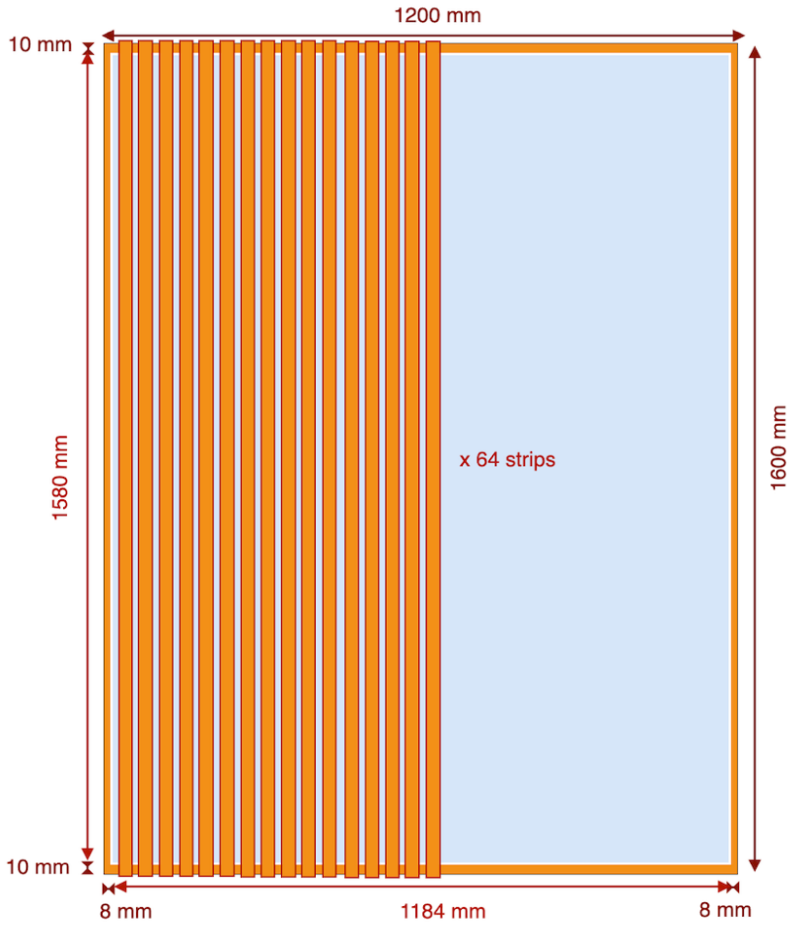

Figure 6.1: View of the RPC design of STRATOS detector. Each plane of the four planes is divided into 64 strips, with an active area of $118 \times 158\ cm^2$, $118\ cm$ in a transversal dimension and $158\ cm$ in a longitudinal dimension.

USC UNIVERSIDADE DE SANTIAGO DE COMPOSTELA

The Reference System of the STRATOS detector is chosen in the following way: the origin is located at the first plane level with equal distances of 45 cm between the four RPC planes for the detector as shown in Figure 6.2 and the Z-axis in the direction of the incident particles.

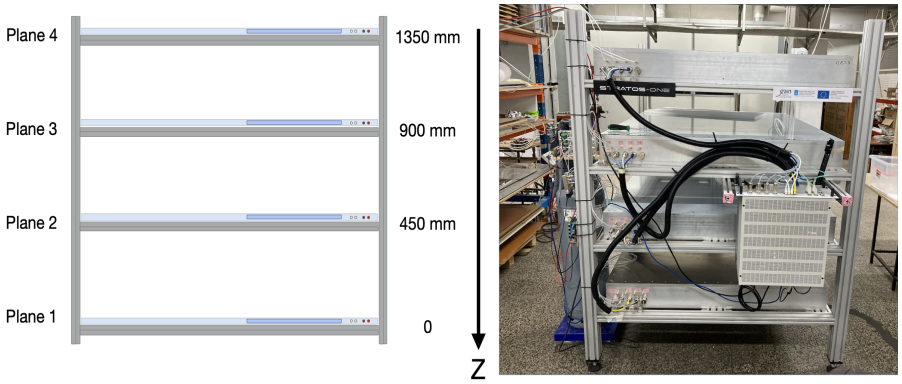

Figure 6.2: Schematic diagram of the STRATOS detector (left) and a photograph of the real system (right).

The internal configuration of each RPC plane is depicted in Figure 6.3. Six 1.9 mm thick layers of glass with four gaps of freon gas (R134a) of 1 mm width for each, two gaps between the first three layers of glass and two between the last three layers. Every three layers of glass with the two gas gaps between them are placed inside a polypropylene box. The glass layers are coated with a semi-conductive layer where the high voltage of $\pm 5600\ V$ is applied. A polystyrene layer of 80 mm thick was added from the top to fix and protect the internal components, as shown in Figure 6.3. Furthermore, all the internal components are placed inside a tight aluminum box. The different internal components of each RPC in the STRATOS detector are listed in Table 6.1.

USC UNIVERSIDADE DE SANTIAGO DE COMPOSTELA

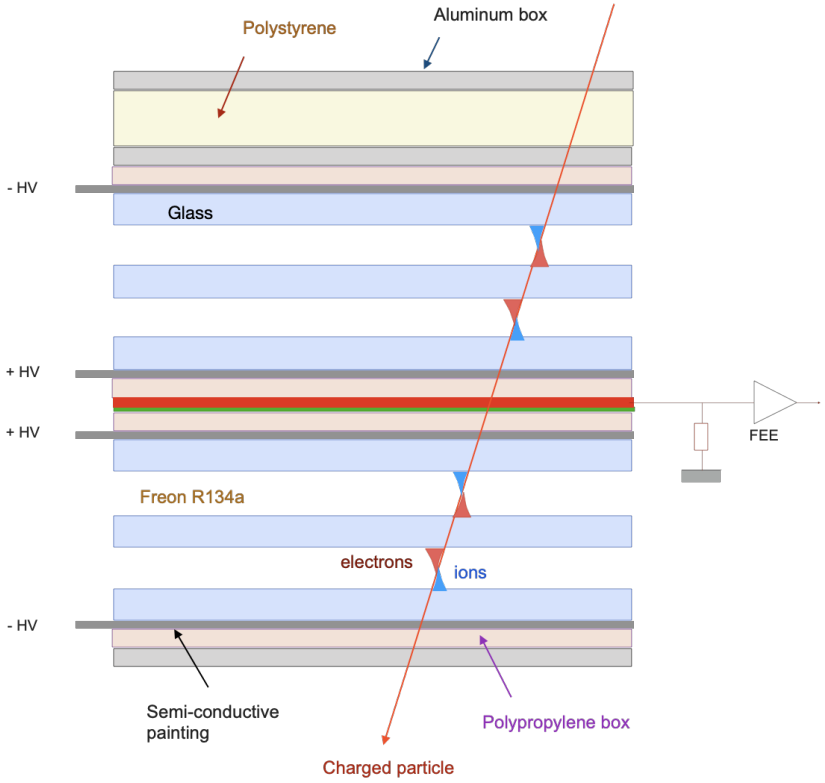

Figure 6.3: The internal configuration of the RPC in STRATOS detector.

In terms of the read-out and Front-End Electronics (FEE), each RPC holds 4 motherboards (MB), two of them located in front of the detector, two in the back and one read-out Board (TRB) at the center (see Figure 6.4). The signals generated in the RPC are first amplified and integrated and then digitized in 4-channels daughter boards (DB). The low voltage and output for both the digital read-out and the trigger signals are provided by a motherboard (MB) connected to each of the eight daughter boards (DB). A Time-To- Digital-Converter (TDC) based read-out Board (TRB) reads out the four motherboards (MB) that collect all the signals of an RPC plane [65].

USC
UNIVERSIDADE DE SANTIAGO DE COMPOSTELA

Table 6.1: Components of RPC plane for STRATOS detector.

RPC layout	Width/mm	Density/(gr/cm³)	X_0/(gr/cm²)	Mass width/(gr·cm²)	ΔX_0
Al	2	2.70	24.0	0.54	0.023
XPS (Polystyrene)	80	0.033	43.8	0.26	0.006
Al	1	2.70	24.0	0.27	0.011
Polypropilene	1	0.90	44.8	0.09	0.002
Semi-conductive painting	-	-	-	0	0
Glass	1.9	2.30	21.8	0.44	0.020
Gas: R134a	1	0.028	26,5	0.003	0
Glass	1.9	2.30	21.8	0.44	0.020
Gas: R134a	1	0.028	26,5	0.003	0
Glass	1.9	2.30	21.8	0.44	0.020
Semi-conductive painting	-	-	-	0	0
Polypropilene	1	0.90	44.8	0.09	0.002
Cu	0.018	8.96	1,4	0.02	0.011
Polyimide	0.085	1.42	40.6	0.01	0.000
Polypropilene	1	0.90	44.8	0.09	0.002
Semi-conductive painting	-	-	-	0	0
Glass	1.9	2.30	21.8	0.44	0.020
Gas: R134a	1	0.028	26,5	0.003	0
Glass	1.9	2.30	21.8	0.44	0.020
Gas: R134a	1	0.028	26,5	0.003	0
Glass	1.9	2.30	21.8	0.44	0.020
Semi-conductive painting	-	-	-	0	0
Polypropilene	1	0.90	44.8	0.09	0.002
Al	2	2.70	24.0	0.54	0.023
Total	**104.5**	**-**	**-**	**4.65**	**0.20**

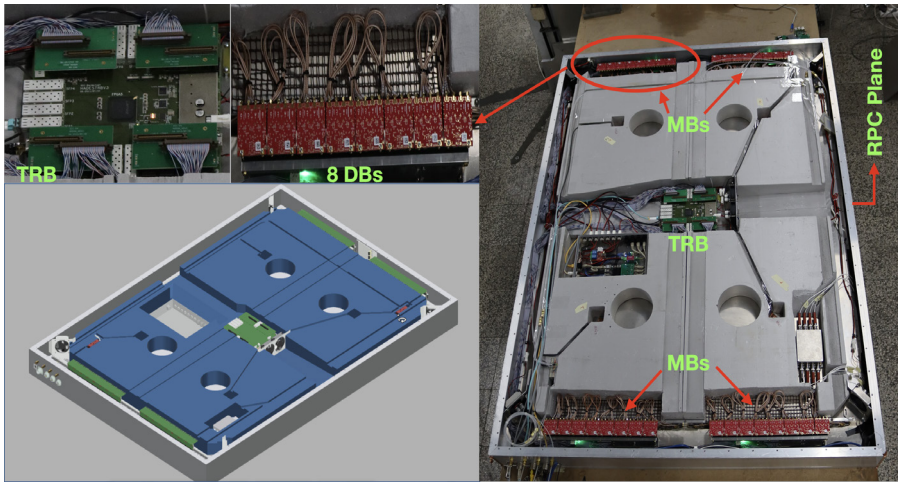

Figure 6.4: RPC plane of the STRATOS detector, each one of the four RPCs is composed of 4 MBs connected to 1 TRB at the center and 8 DBs connected to each MB, As illustrated in the figure.

USC UNIVERSIDADE DE SANTIAGO DE COMPOSTELA

The detector was located for about six months in the University of Coimbra premises, from the beginning of 2021 until the end of June 2021, under the supervision of the LIP group. In May 2021, the four RPCs of the detector were instrumented and entirely operated and it was taking data continuously and regularly. In July of the same year, the STRATOS detector was installed near the Vigo airport, Spain.

In this chapter, we presented a description of the general structure of the STRATOS detector and provided the structure of the planes (RPC) and their components. Moreover, in the following sections, we will discuss the position calibration in X and Y coordinates of the detector, the calculation of the efficiency and finally, the time resolution.

6.2 Position calibration

We will concentrate on the calibration procedure in this section. However, it is essential to keep in mind the design and the geometry of the detector, as mentioned in the previous section.

When particles interact with the active volume of the RPC, the gas will ionize and an avalanche occurs. This process generates a readable signal. These signals are processed by the Front-End Electronics (FEE), which translates them into valuable physical data such as the amount of the charge, measured time in the front and the back for each strip, the plane number in the detector, the channel number and the event number. And then, the data is saved in root or ASCII format file. Table 6.2 presents a sample of data that is saved and ready to analyze.

In Table 6.2, f/b strip means the front or back end of a given strip. When a particle hits a specific strip, both ends of the strip read the time from the place where the particle hit the strip to the strip end. Therefore, there are two measured times on both ends, one in the front of the strip and the other in the back. In Table 6.2, we referred optionally to the front of the strip with 0 and 1 for the back of the strip.

USC
UNIVERSIDADE DE SANTIAGO DE COMPOSTELA

Table 6.2: Data sample of STRATOS detector. The data in the table is not in the same order as the data in the saved file.

Event	Channel	f/b strip	Plane	Time (ns)	Charge (a.u.)
1	1	0	4	-268.5	94.3
1	1	1	4	-268.7	102.9
1	5	0	2	-247.4	90.7
1	5	1	2	-253.8	96.8
1	7	0	1	-254.9	86.3
1	7	1	1	-249.6	104.3
1	13	0	3	-261.5	90.4
1	13	1	3	-259.6	98.2
2	4	0	2	-264.5	98.0
2	4	1	2	-261.1	95.0
2	8	0	3	-262.3	99.2
2	8	1	3	-267.1	98.6
2	15	0	4	-264.9	88.1
2	15	1	4	-262.5	87.9
2	17	0	1	-257.7	96.9
2	17	1	1	-257.3	96.3
27	31	0	1	-259.8	95.9
27	31	1	1	-261.3	92.7
27	32	0	2	-260.2	97.9
27	32	1	2	-262.4	96.1
27	55	0	3	-266.9	90.6
27	55	1	3	-261.1	96.6
27	61	0	4	-265.5	100.0
27	61	1	4	-259.5	93.6
100	63	0	1	-256.7	89.1
100	63	1	1	-260.1	93.5
100	53	0	2	-256.5	94.3
100	53	1	2	-259.8	88.8
100	34	0	3	-263.5	99.3
100	34	1	3	-263.7	96.7
100	11	0	4	-260.4	111.7
100	11	1	4	-266.6	114.6

USC UNIVERSIDADE DE SANTIAGO DE COMPOSTELA

In this section, we will divide the position calibration into two parts: the first is calibration in X coordinates (transversal to the direction of the strips) and it is calculated by the charge of the avalanche produced when the particles interact with the active volume of the RPC. The second part is calibration in Y coordinates (along the direction of the strips) and it is calculated by the time difference between both ends of the fired strip for the same event.

6.2.1 Position calibration in *X* coordinates and Width to Charge Calibration

The position along the transversal coordinate of the detector, X, is obtained by utilizing prompt charge analysis. As many strips collect the charge for any single hit, the strip with the most charge gives a hint for the transversal location of the hit. Thus, calibration in the charge measurement is needed.

The charge to width algorithm encodes the induced charge by a particle giving signal in the RPC strips in the width of the FEE (LVDS) output signal, referred to as QtoW. As a result, TDC units are used for the QtoW measurement is ns. Consequently, the reverse procedure is required: first, the QtoW pedestal is subtracted from all measurements because each FEE channel has a slightly different behavior and to homogenizes each FEE channel's response. The beginning of the QtoW histogram on each channel is used to calculate these pedestals, as presented in Figure 6.5. Furthermore, Through the parameterization implemented in [102], the TDC units are converted into physical units (fC). However, we used another type of electronics that did not convert the TDC units to (fC) during this work. Consequently, we will refer to the unit of the charge with arbitrary units (a.u.).

Generally, signals below the pedestal are essentially crosstalk occurrences with no meaningful charge, so keep that in mind. Even though the RPC strips are electrically isolated, powerful signals, primarily from streamers, can cause induced crosstalk in their neighbors.

USC
UNIVERSIDADE DE SANTIAGO DE COMPOSTELA

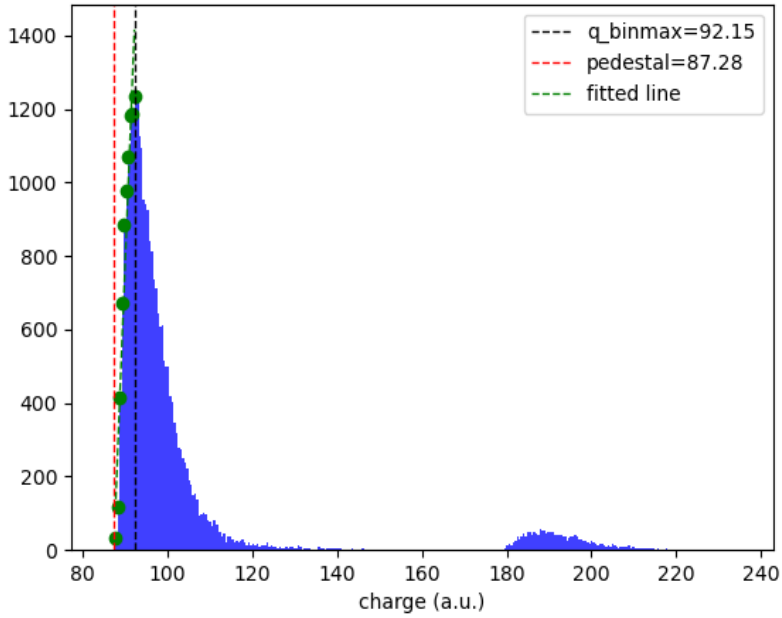

Figure 6.5: Histogram of the charge for one channel chosen arbitrary for one RPC of the detector. Where the black dashed line refers to the most frequent charge (q_binmax) and the green dashed line represents the fit for the charge bins to the left of q_binmax (green dots) to calculate the pedestal (the red dashed line).

After subtracting the pedestal from all the charge signals, the response of each Front-End Electronics (FEE) channel is homogenizing for all channels. We can easily find the largest charge produced for the same event and we do the same for all the events. At this point, we know the channel number (X_{RPC}) where the most significant charge is produced. As we also know the strip width previously, we can intuitively calculate the real position X on the RPC by multiplying the channel number by the strip width. Figure 6.6 shows the distributions of the position X for the all RPCs of the STRATOS detector.

Moreover, the charge spectra for all the strips in each plane (RPC) of the detector are presented in Figure 6.7, where the charge distributions for all the planes almost have the same distribution.

USC
UNIVERSIDADE DE SANTIAGO DE COMPOSTELA

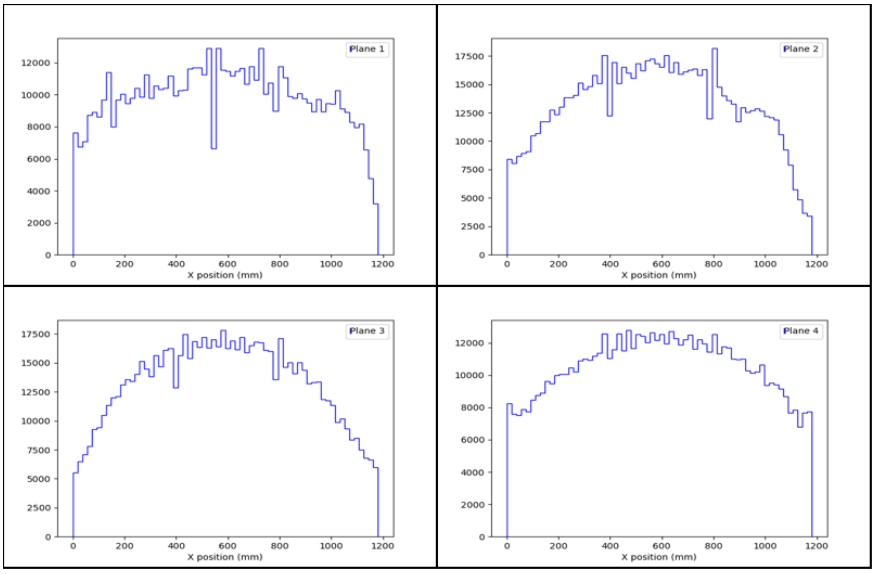

Figure 6.6: Histograms illustrate the real position distributions of X coordinates for all planes in mm.

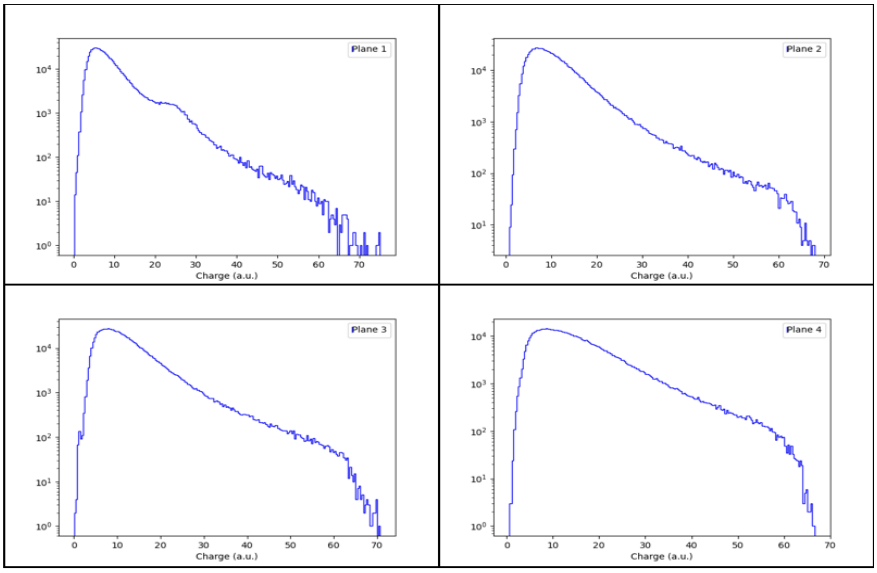

Figure 6.7: Charge distributions for all the strips in each RPC of the detector after subtracting the pedestal.

USC
UNIVERSIDADE DE SANTIAGO DE COMPOSTELA

As mentioned before, after calculating the pedestal and subtracting it from all the charge signals for the strips and determine the largest charge, which represents the position of the hit in each RPC for the detector. We can define an observable physical variable known as multiplicity (M). Multiplicity is the number of hits, defined as a valid signal in terms of charge after pedestal subtraction and calibration, across the entire detector in a single event. In brief, we can find the multiplicity by counting the number of the signals (hits) produced in all the strips for the same event. Figure 6.8 shows the hit multiplicity distributions in all the planes.

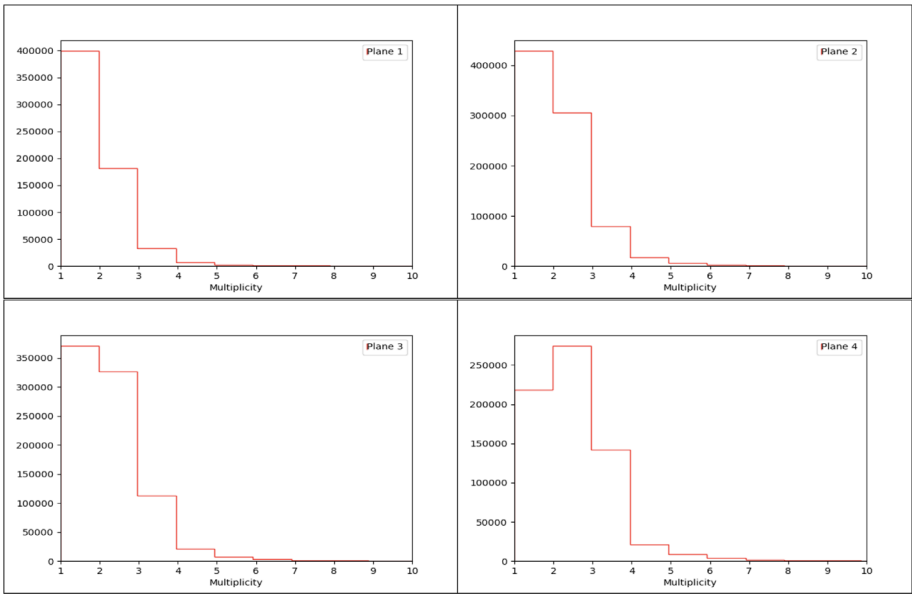

Figure 6.8: Hit multiplicity distributions in all the planes of STRATOS detector.

As a clarification, as mentioned before, an avalanche occurs when charged particles interact with any RPC of the detector. This process will produce readable signals by electronic devices. As a result, the neighbor stripes in the RPC will be affected by the charge generated and it will be fired. The number of fired strips depends on the amount of charge generated in each plane. The distribution of the strips that got fired in all the planes is presented in the figure above.

USC UNIVERSIDADE DE SANTIAGO DE COMPOSTELA

Generally, the events with multiplicity $M = 1$ have the most probability of occurrence and the probability decreases with increasing the multiplicity. Moreover, we can see that the particles with multiplicity greater than 3 ($M > 3$) have a very low probability of occurring. However, the hit multiplicity per plane does not depend on that. It depends on the charge generated in each plane. As seen in Figure 6.8, the multiplicity $M = 2$ is greater than $M = 1$ in-plane four without knowing the reason.

6.2.2 Position calibration in Y coordinates

Each RPC in the STRATOS detector is formed by sixty-four individual cables, one cable for each strip. When a particle interacts with the detector, a signal is produced and it travels through the cables to the electronic system. Each set of channels or strips have a different cable length. All the cables that form the RPC have a common point where the signal is collected in the detector. Therefore, the signal traveling by the lateral cables covers a larger distance than the central cables of the RPC. Consequently, the signal's delay has to be corrected depending on the hit position.

The time difference between measured times at both ends is used to calculate the longitudinal coordinate along the RPC strip, Y. As a result, an offset arises due to the length of the signal cable between the strip and the Front-End Electronics (FFE), as mentioned before. See Figure 6.9.

The offset can be estimated by the following method. We define the middle point of the distribution and then calculate the median for its neighbor points from both sides. We set 10% of the median value as a threshold (green line in Figure 6.9). Furthermore, we determined the right and left edges (red points) of the time-difference distribution and the following is a formula for determining the mid position:

$$Y_{mid} = (\frac{1}{2}\,[right_{edge} - \ left_{edge}]) + \ left_{edge} \tag{6.1}$$

USC UNIVERSIDADE DE SANTIAGO DE COMPOSTELA

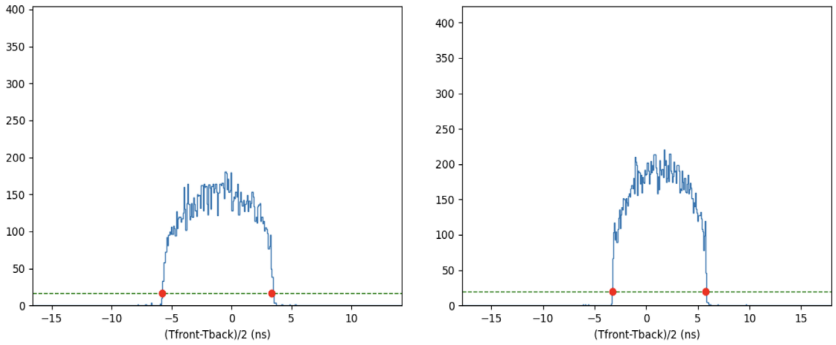

Figure 6.9: The position offset was described using the $(T_{front} - T_{back})/2$ distribution. Take note of the offset in the distribution for each strip.

and now, easily we can calculate the position of the hit in the Y coordinates after correction:

$$Y_{RPC} = Y - Y_{mid} \tag{6.2}$$

where Y is the time difference in our data (Table 6.2) and equal to $Y = (T_{front} - T_{back})/2$ for the same event and channel number. Figure 6.10 presents the distribution of the position after correction.

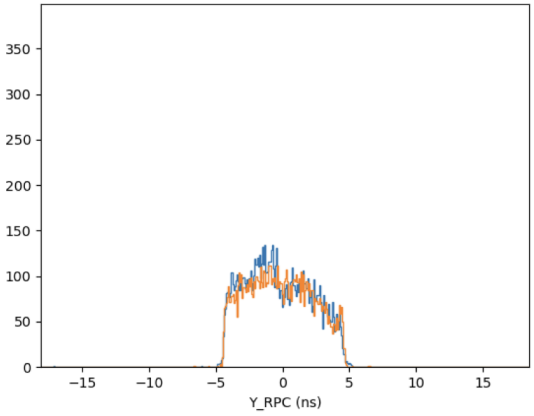

Figure 6.10: Y_{RPC} distribution for the time difference after correction.

USC UNIVERSIDADE DE SANTIAGO DE COMPOSTELA

As seen in the figure above, the offset was corrected and all the distributions for the channels are aligned precisely at the same points from $-5\ ns$ to $5\ ns$.

Figure 6.11 illustrates in 2-dimensional histograms the position Y versus the position X before and after correction in the time difference for all the planes. In figure 6.11, it is clear to notice that the RPC strips for all the planes are aligned to each other. Moreover, we can check whether the channels work or not. For instance, channel number 29 in-plane one does not work correctly.

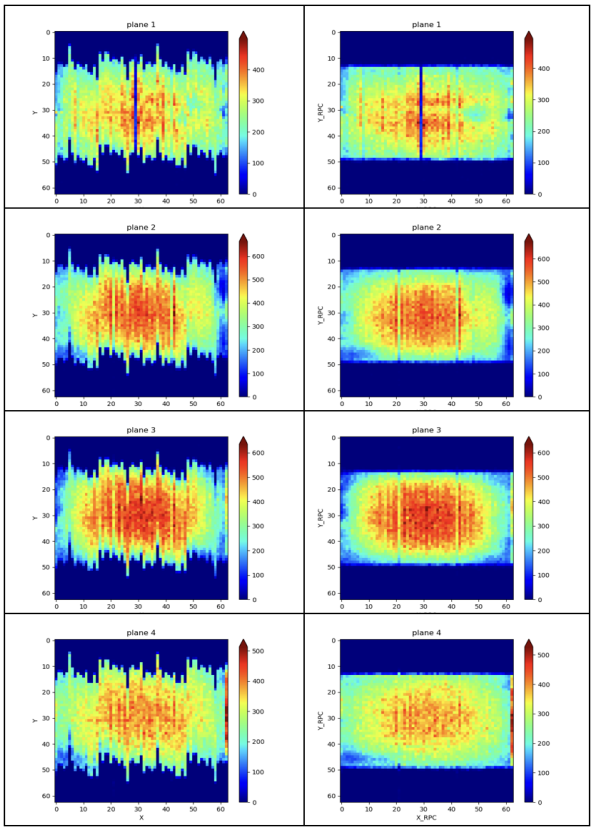

Figure 6.11: 2-dimensional histograms for the position Y versus the position X before correction (left) and after correction (right) in the time difference for all the detector planes.

USC UNIVERSIDADE DE SANTIAGO DE COMPOSTELA

6.3 Efficiency and position resolution

Each RPC event retains both the time and charge information read-out at both ends and information about the strip's position in the detector. Based on this information and after the calibration procedures, the RPC delivers two values: a time and its accompanying coordinate. Because we have front and back signals, we can calculate the longitudinal position by multiplying the half-time difference by the signal velocity in the strip, which is also known as the conversion factor ($165.7\,\frac{mm}{ns}$) [42]. The geometry determines the transversal coordinate and the strip width only determines its resolution. Thanks to the four-layer design, the quality of these measures may be determined in two ways, using the information provided by tracking or characterizing the distributions of overlapped events.

6.3.1 Position resolution

The precision of the position determination directly influences the matching between the detect and predicted events by a geometric window identified by the calculated values of the spatial resolution. As a result, the fake tracks can be eliminated if they do not match the window and in this case, we will not consider them as detect events.

In order to calculate the efficiency in a particular plane of the detector, we should first determine the position resolution in X and Y coordinates. To achieve that, a linear fit is done for the coordinate points (X, Y, Z) for the three other planes after converting their coordinates to mm units. That is done by multiplying X coordinates with the strip's width and Y coordinates by the conversion factor. Z is constant, which is the plane's height from the origin and then finding the coordinates of the predicted points for the required plane to calculate its efficiency. After that, we can easily calculate the residuals, which is the difference between the coordinate points (X, Y) and predicted points. The distributions of the residuals in X and Y coordinates for all the planes are shown in Figure 6.12. We applied a double Gaussian fit to determine the spatial resolution's final value.

USC UNIVERSIDADE DE SANTIAGO DE COMPOSTELA

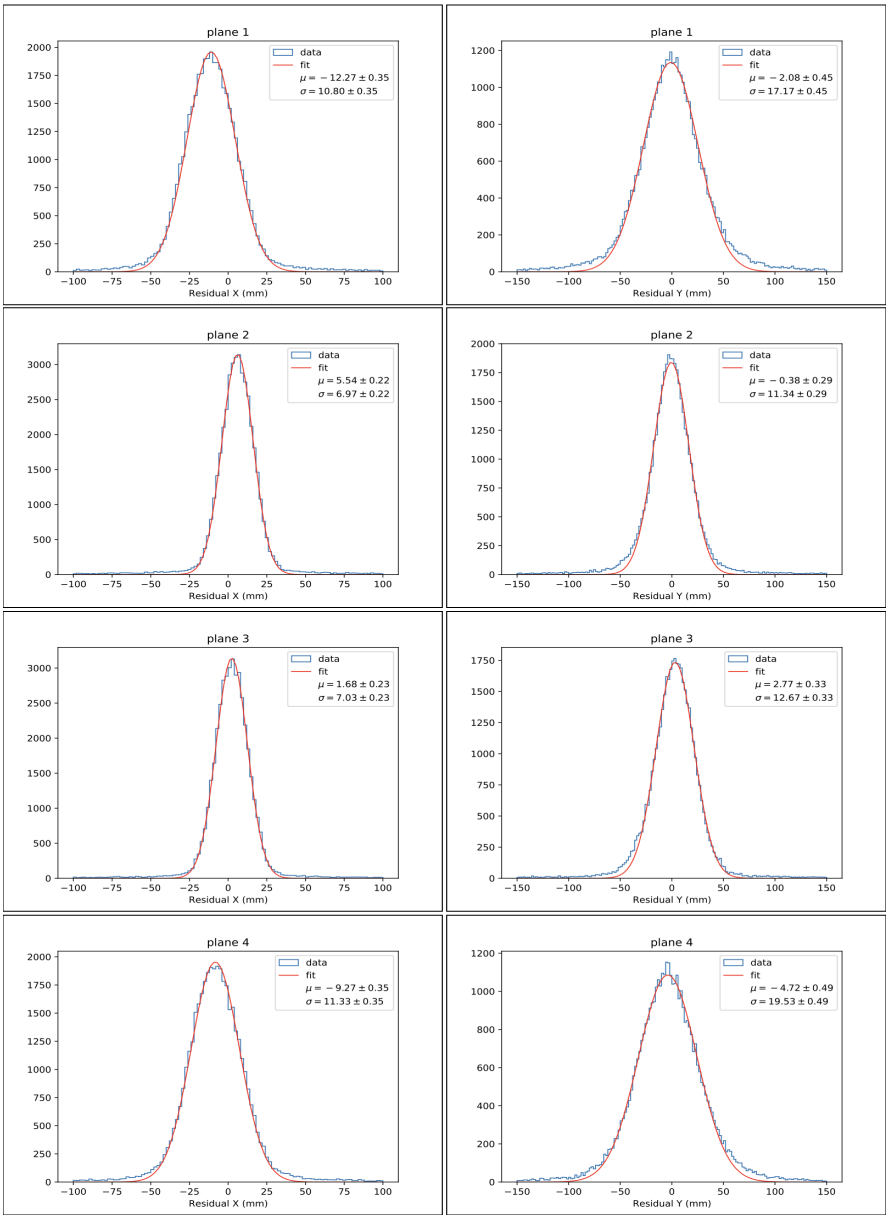

Figure 6.12: Residual distributions in X and Y for the four planes in the STRATOS detector. They are fitted to a double Gaussian method to obtain the spatial resolutions, given by the sigma of the fit.

USC
UNIVERSIDADE DE SANTIAGO DE COMPOSTELA

First, we used a Gaussian function to fit the distribution of the residuals without data range restrictions. And then, a second Gaussian fit method is performed to restrict data range limited to the full width at half maximum (FWHM) for the distribution to avoid the outliers (tails). In this case, we get a Gaussian fit on the central section of the distribution and the spatial resolutions ($\sigma_x,\ \sigma_y$) is obtained. Table 6.3 summarize the spatial resolutions for each plane.

Table 6.3: Values of the spatial resolutions obtained after applying the Gaussian fit method.

Plane	$\sigma_x\ (mm)$	$\sigma_y\ (mm)$
1	10.80 ± 0.35	17.17 ± 0.45
2	6.97 ± 0.22	11.34 ± 0.29
3	7.03 ± 0.23	12.67 ± 0.33
4	11.33 ± 0.35	19.53 ± 0.49

6.3.2 Efficiency

The efficiency of the RPC can be determined by knowing the ratio between the number of the detected particles to the hit (predict) particles in the plane, in other meaning, the magnitude of occupied space by detected particles from the volume of the detector. In order to eliminate partially fake tracks, the allowable matching window must fulfill the following criteria:

$$X_{hit} - 5\,\sigma_x \ < \ X_{RPC} \ < \ X_{hit} + 5\,\sigma_x \tag{6.3}$$

and

$$Y_{hit} - 5\,\sigma_y \ < \ Y_{RPC} \ < \ Y_{hit} + 5\,\sigma_y \tag{6.4}$$

If the hit particle achieves the above conditions, it is recorded as a detect event. In the figures 6.13, 6.14 and 6.15 are presented the distributions

USC UNIVERSIDADE DE SANTIAGO DE COMPOSTELA

of the hit events, detected events and the efficiency, respectively, for all the planes.

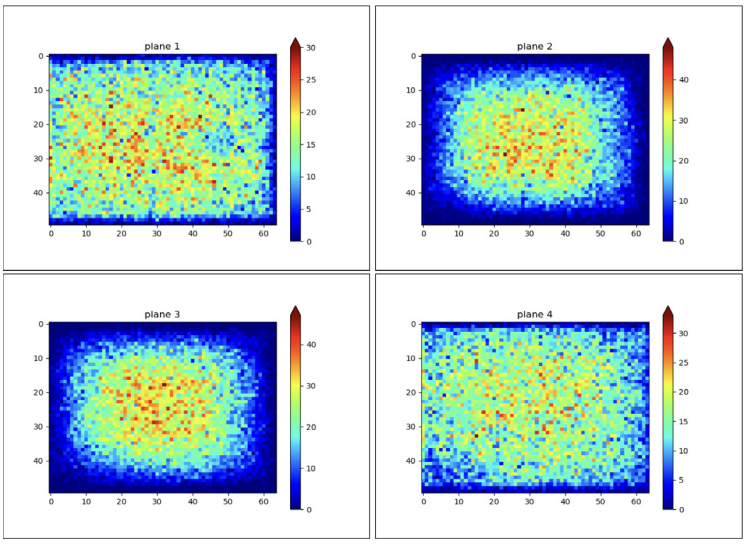

Figure 6.13: Hit events distribution for entire detector's planes.

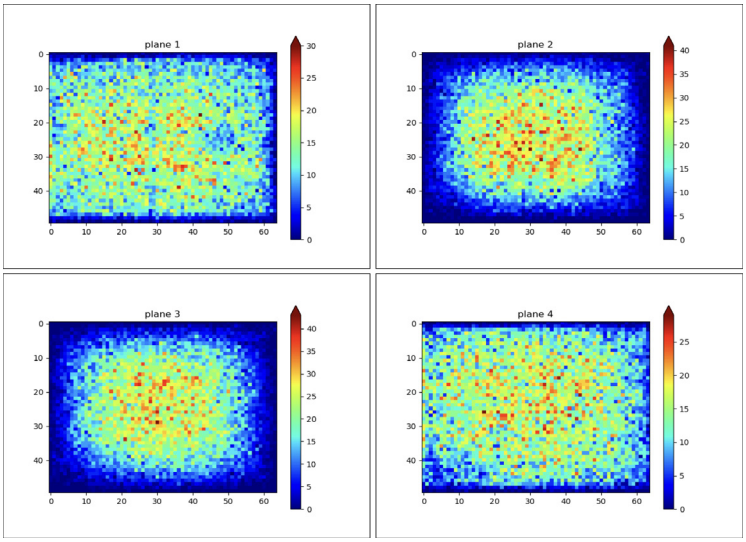

Figure 6.14: Detected events distribution for all the detector planes.

USC UNIVERSIDADE DE SANTIAGO DE COMPOSTELA

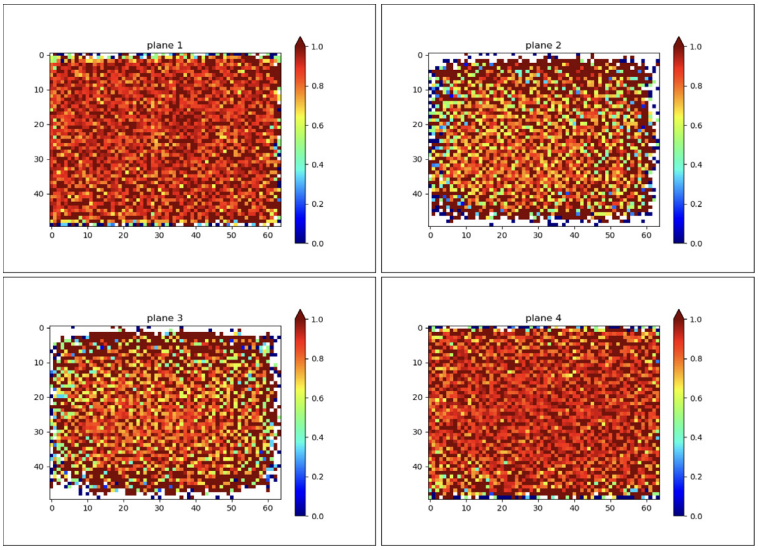

Figure 6.15: The efficiency for each individual plane for STRATOS detector.

According to the figures above, we can see some symmetry between planes 1 and 4 and between planes 2 and 3. The ratio between the number of the detected particles to the hit particles of the STRATOS detector for all the planes is calculated and shown in Table 6.4.

Table 6.4: Values of the efficiency of the STRATOS detector for all the planes.

Plane	**Efficiency** (%)
1	92.1
2	91.7
3	92.1
4	92.5

It is essential to mention that, in general, the values of the detector's efficiency are affected strongly by a parameter called geometric acceptance. The geometric acceptance is a probability distribution for describing particle trajectories that traverse the detector. The value of the acceptance depends on the detector's geometry and is customarily used to correct the particle rates for the detector.

USC UNIVERSIDADE DE SANTIAGO DE COMPOSTELA

Moreover, the efficiency can be affected by the high voltage applied on the RPCs, which means we can improve the efficiency values by increasing the high voltage applied but not to the limit that produces streamers.

6.4 Time resolution

The time resolution was calculated for the tracks that cross two overlapping strips by identifying the distribution:

$$\Delta T = \frac{1}{2}[(T_f + T_b)_{up} - (T_f + T_b)_{down}] \tag{6.5}$$

where ΔT is the half-time difference for any two planes of the detector [42]. Figure 6.16 shows the distribution of ΔT before correction for the two planes of the STRATOS detector.

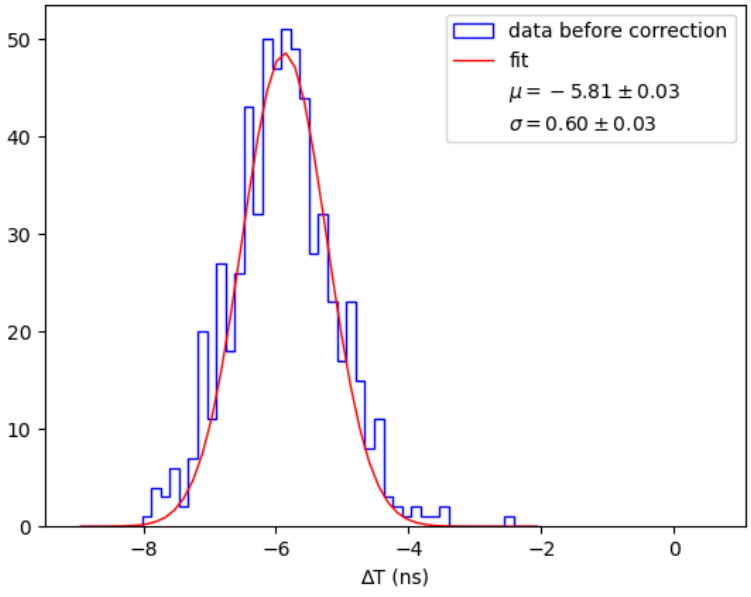

Figure 6.16: The distribution of the half-time difference for two overlapping strips before correction.

USC UNIVERSIDADE DE SANTIAGO DE COMPOSTELA

After that, the value of sigma σ_t for the distribution before correction is determined. The following equation then calculates the time resolution:

$$Time\ resolution = \frac{\sigma_t}{\sqrt{2}} \tag{6.6}$$

The value of the time resolution before correction we got for the RPC of the STRATOS detector is $424 \pm 21\ ps$.

It can improve the time resolution of RPCs by correcting the charge to time dependence [66]. This effect is known as slewing correction. The slewing is a read-out electronics effect that must be corrected. A signal is generated when a particle interacts with an RPC and the amplitude is proportional to the amount of charge integrated on the strips. The read-out electronics receive this signal, which is then processed. The signals discriminated by a constant threshold have a delay between the start of the pulse and the moment they cross the threshold. The signal's charge determines this delay to amplitude ratio. As a result, large signals arrive before the others. Consequently, there is a time shift determined by the amount of charge generating the signal.

The charge to time correction is done by two overlapped charge spectra with different behavior and the half-time difference for the related strips. Fitting the two regions to second-order polynomials rather than exponentials is used since it is more robust and less dependent on locating the exact point where the trend changes, as illustrated in Figure 6.17.

As can be seen, Figure 6.17 shows an ascendant curve shape in the lower plane. That means the events with a low charge present more time delay than the more intense signals and the opposite in the upper plane.

After correcting the half-time difference for the overlapping strips by the second-order polynomial fitting, we identified the distribution of

USC UNIVERSIDADE DE SANTIAGO DE COMPOSTELA

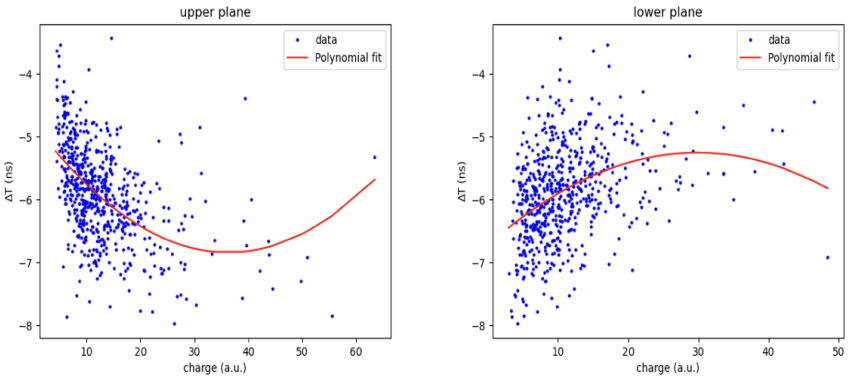

Figure 6.17: Slewing correction in RPC strips. The red line shows the phenomenological fit applied to the data.

ΔT after correction. Moreover, a Gaussian fit for the distribution is done, as shown in Figure 6.18.

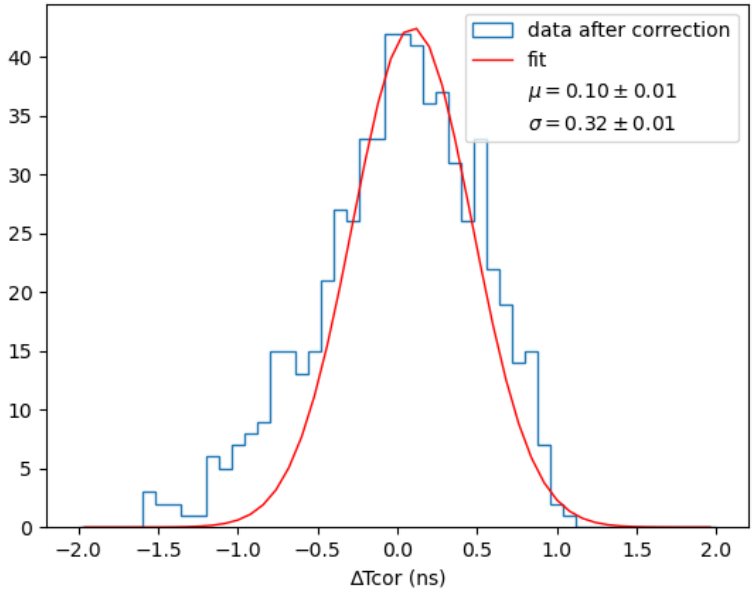

Figure 6.18: ΔT distribution for two overlapping strips after correction.

USC UNIVERSIDADE DE SANTIAGO DE COMPOSTELA

Using Equation (6.6), the value of the time resolution after correction for the RPC of the STRATOS detector is $226 \pm 7\ ps$ and the accepted value is around $300\ ps$. Moreover, tails above 3σ were found to be below 0.5%.

We can see the significant role of the correction for the half-time difference ΔT and how it affects the value of the time resolution before and after correction. As a result, that is leading to an improvement of close to a factor of 2. Furthermore, the mean value for the distribution of the ΔT is improved and becomes closer to zero.

USC
UNIVERSIDADE DE SANTIAGO DE COMPOSTELA

USC
UNIVERSIDADE
DE SANTIAGO
DE COMPOSTELA

7 Analysis of the performance of Trasgo detectors for estimating the energy of primary cosmic rays

7.1 Introduction

One of the most interesting features of Trasgo detectors is their capability to detect bundles of particles, measure their arrival directions and arrival times and even provide a hypothesis about their masses. As far as we know, all this information has not been used previously in a systematic way by other cosmic ray detectors. In our opinion, these features are very interesting. They may be used for many purposes, for instance, for getting information about the atmosphere properties or even for getting information, event by event, about the properties of the primary cosmic ray; namely, the arrival direction, the mass and the energy. In order to analyze these possibilities, we have launched a large set of simulations of primary cosmic rays of different masses and energies, impinging in the top of the atmosphere and analyzed the properties of the bundles of particles arriving on the ground. We have concentrated our effort mainly on the observables that a single Trasgo detector can measure as the multiplicity of the bundles of particles, their composition, their time distribution and the arrival angles between the particles, among others.

We have used the CORSIKA package developed at KIT [103] for our simulations. As a collision generator, we have chosen the QGSJET option starting at an energy of 1 GeV per nucleon. Although this is not the best choice at low energies and is more suitable at energies above a few thousands of GeV, we decided to use that model in order to guarantee the continuity of the results when we extrapolate them to higher energies with higher multiplicity events where we expect our

USC
UNIVERSIDADE DE SANTIAGO DE COMPOSTELA

results to be more significant[7]. In fact, at low energies, we do not expect to have many bundles of particles arriving at a small area detector.

As far as we know, this is the first time that such a systematic study has been done. We focused our priority on developing all the simulation programs, the finding algorithms of bundles or clusters of particles and the analysis programs. We made our simulations assuming an observer at the altitude of Santiago de Compostela with their corresponding magnetic field. As we are mainly interested in counting the particles that a Trasgo detector could measure, we have chosen for the ECUTS parameter of CORSIKA, defining the lowest energy threshold for accepting a particle, the values (in GeV): 0.3, 0.1, 0.05 and 0.05 for hadrons, muons, electrons and gammas respectively.

7.2 Events generation method

We have generated events with primary cosmic rays of masses: 1 (Hydrogen), 4 (Helium), 12 (Carbon) and 56 (Iron). Concerning the energies, we have generated events at four intervals per energy decade between 1 GeV and 10^4 GeV per nucleon and at constant distances in the logarithmic scale. Precisely, energy intervals followed the serial $(1.33, 2.37)$, $(2.37, 4.22)$, $(4.22, 7.50)$, $(7{,}50, 13.3)$, $(13.3, 23.7)$ and so on, where all the values are given in GeV. Those intervals were centered at the energies 1.78, 3.16, 5.6, 10, 17.8, respectively (again, all values are given in GeV). In each interval, the energy of the primary cosmic ray was chosen randomly following a probability distribution given by the well-known $E^{-2.7}$ power behavior. Finally, we repeated the generation of events for different angles of arrival to the atmosphere for the proton sample. We chose the intervals following a constant distribution in the cosine of the zenith angles, namely: $(0^\circ, 25^\circ)$, $(25^\circ, 37^\circ)$, $(37^\circ, 46^\circ)$ and $(46^\circ, 53^\circ)$. The rate of bundles of particles arriving at the ground for bigger angles was almost negligible compared with those measured at lower angles. The number of events generated for the different samples is shown in Table 7.1. For each event, the

[7] At low energies the FLUKA [fluka.cern] collision generator would be more appropriate.

USC UNIVERSIDADE DE SANTIAGO DE COMPOSTELA

shower of secondary particles (or EAS: Extended Air Shower) has been propagated until their arrival at the ground level.

Table 7.1: The number of events generated for each mass of the primary cosmic ray and each energy range.

$LogE_0/n/$	H	He	C	Fe
0.30	100K	-	-	-
0.50	100K	-	-	-
0.75	100K	100K	-	-
1.0	100K	100K	-	-
1.25	100K	100K	100K	-
1.50	100K	100K	100K	-
1.75	100K	100K	100K	-
2.00	100K	75K	75K	75K
2.25	75K	75K	75K	75K
2.50	50K	50K	50K	50K
2.75	25K	25K	25K	25K
3.00	40K	10K	10K	10K
3.25	30K	10K	10K	10K
3.50	25K	8K	8K	8K
3.75	20K	6K	6K	6K
4.00	15K	4K	4K	4K
4.25	10K	2K	2K	2K
4.50	6K	1K	1K	-
4.75	-	-	600	-

Generally, when we analyze cosmic ray data, we realize that most variables are affected by huge fluctuations and are very far from showing a Gaussian behavior. The evolution of a shower depends very significantly on the degree of centrality of the first collision and on the height at which it takes place. On the other side, the evolution of the shower depends on many processes that are summarized in Table 7.2. As can be seen, some of the processes are related to the collision probability and are mainly affected by the atmosphere's local mass width. Other processes, such as the decays of unstable particles, depending on their lifetimes and, consequently, on the space width traveled by the particle. Some particles, as high-energy neutrons, do mainly interact through elastic collisions. Other hadrons, like protons, pions, or kaons, show big probabilities of suffering an inelastic nuclear

USC
UNIVERSIDADE DE SANTIAGO DE COMPOSTELA

collision with the further production of new hadrons of lower energies. These particles would suffer further collisions with the production of new particles with lower energies. All these competitive processes make it very difficult to parameterize the development of a shower, whose behavior depends on many unknowns: the height of the first interaction, the target nucleus of the first collision (N, O, Ar or other), the type of collision (central or peripheral), etc. Consequently, for a given primary particle mass, with a given energy and a given arriving angle, the development of two different showers may be completely different, both in size and composition.

Table 7.2: Summary of the main processes that take place in the development of Extended Air Showers induced primary cosmic rays.

	Particle	Mass/ GeV	Q/q_e	$c \cdot \tau_0$	Interactions	Typical lengths				Products
						λ /g.cm^{-2}	λ (20 km)	λ (10 km)	λ (Sea level)	
First interaction	P	1	1	-	Nuclear coll.	~ 90	9000 m	2200 m	750 m	Hadrons
	He	4	2	-	Nuclear coll.	~ 40	4000 m	1000 m	330 m	Hadrons
	C	12	6	-	Nuclear coll.	~ 25	2500 m	625 m	200 m	Hadrons
	Fe	56	27	-	Nuclear coll.	~ 10	1000 m	250 m	100 m	Hadrons
Secondary interactions	Proton	1	0,1	-	Nuclear coll.	~90	9000 m	2200 m	750 m	Hadrons
	Neutron	1	0	-	Elastic int.	~60	6000 m	1500 m	500 m	Neutron
	Kaon$^{\pm}$	0.49	±1	-	Nuclear coll.	~ 140	1400 m	3500 m	1200 m	Hadrons
	Pion$^{\pm}$	0.14	±1	-	Nuclear coll.	~ 120	1200 m	3000 m	1000 m	Hadrons
Decay products	Kaon	0.490	0, ±1	3.7 m	Weak decay	-	$\gamma \cdot c \cdot \tau_0$	$\gamma \cdot c \cdot \tau_0$	$\gamma \cdot c \cdot \tau_0$	Muon (60%) Pions (40%)
	Pion$^{\pm}$	0.140	1	7.8 m	Weak decay	~60*	$\gamma \cdot c \cdot \tau_0$	$\gamma \cdot c \cdot \tau_0$	$\gamma \cdot c \cdot \tau_0$	Muons
	Pion^0	0.135	0	26 nm	EM decay	-	$\gamma \cdot c \cdot \tau_0$	$\gamma \cdot c \cdot \tau_0$	$\gamma \cdot c \cdot \tau_0$	2 gammas
	Muons	0.106	±1	660 m	Weak decay	-	$\gamma \cdot c \cdot \tau_0$	$\gamma \cdot c \cdot \tau_0$	$\gamma \cdot c \cdot \tau_0$	Electrons
	Electron	0.0005	±1	-	Bremsstrahlung	~ 37	3700 m	900 m	260 m	Gamma
	Gamma	0	0	-	Pair production	~ 37	3700 m	900 m	260 m	Electron pair

It is also worth saying that the shower development depends dramatically on the atmosphere's temperature profile. For instance, an increase in the temperature of the high atmosphere (the stratosphere) would expand it increasing the chance that the first interaction takes place at a low altitude and high-density region, with a bigger probability of producing secondary collisions and less probability for the development of the shower before reaching the Earth's surface. On the other side, increasing the temperature in the low stratosphere would

USC UNIVERSIDADE DE SANTIAGO DE COMPOSTELA

expand it increasing the chance that low energy muons have enough distance for decaying in electrons affecting their expected rates.

Muons, electrons and gammas mainly dominate the composition of the air shower when they arrive at the ground. Their approximate energy distribution is given in Table 7.3 at sea level. Although all muons have a single source and come from the decay of mesons (mainly pions and kaons), electrons and gammas may have been originated either in the decay of neutral pions produced in the nuclear collisions that took place in the high atmosphere or via the decay of high energy muons near the ground level. Also, delta electrons produced by knock-on collision of muons with atomic electrons may produce an electromagnetic shower. A summary of all these processes can be seen in Figure 7.1.

Table 7.3: Integrated mean flux of the most abundant secondary cosmic rays arriving the Sea Level for different thresholds of energy.

Mean Flux of Cosmic Rays at the Sea Level ($m^{-2}s^{-1}sr^{-1}$)
(Adapted from: Kaye&Laby. Tables of Physical and Chemical constants, www.kayelaby.npl.co.uk)

E(GeV)	Muons		Electrons[1]	Photons	Protons	Neutrons
	Flux	DifFx. %				
0.001	100	~0	60	130	2.1	
0.01	100	~0	28	60	2.1	30*
0.02	100	~0	20	40	2.1	
0.1	99	1	6.0	8	1.9	10*
0.2	97	2	3.0	3.5	1.5	-
0.5	86	11	1.0	1.1	0.9	1.5
1	69	17	0.4	0.4	0.5	0.7
2	46	23	0.1	0.1	0.25	* Estimated theoretical values
5	20	26	0.02	0.02	0.1	
10	9	11	[1] Include positrons		0.03	
20	3	6				

For each of our simulations, we have counted the number of particles of the different types arriving at the ground and some of the properties of the bundles of particles that a Trasgo detector could measure. We

USC UNIVERSIDADE DE SANTIAGO DE COMPOSTELA

counted the total number of muons, electrons and gammas concerning the single particles. Although Trasgos are not sensitive to gammas, a few percent of these particles may eject electrons or produce electromagnetic showers in the first layer of the detector, increasing the probability of detecting electrons. Also, we have counted the electrons in different energy intervals. Namely, $(0.05, 0.1)$, $(0.1, 0.15)$, $(0.15, 0.2)$, $(0.2, 0.3)$, $(0.3, 0.5)$, $(0.5, 1)$, $(1, 2)$ and (> 2), where, again, the units are given in GeV.

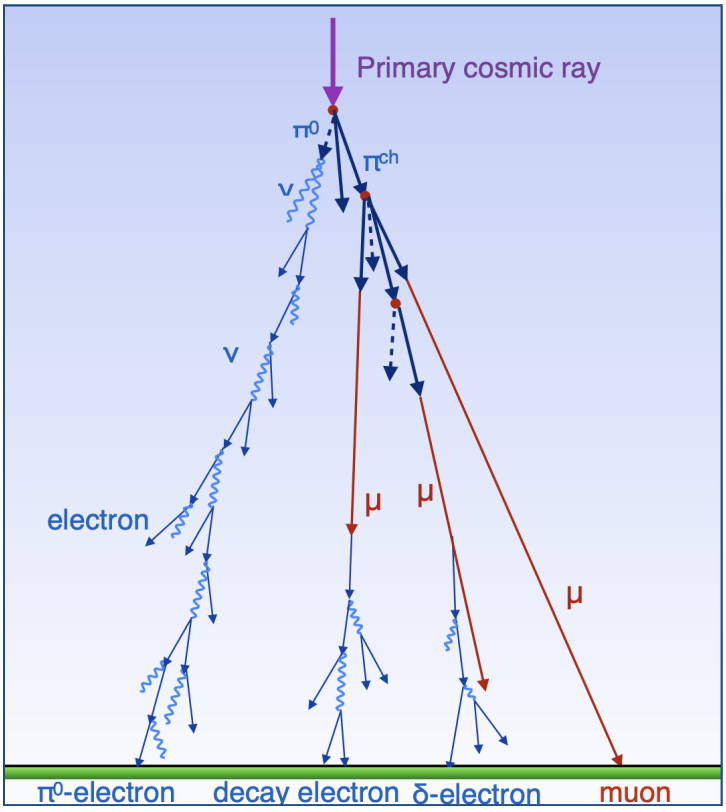

Figure 7.1: Main sources of muons and electrons of cosmic origin arriving to the ground level.

When cosmic rays collide with an air nucleus for the first time, often between 10 and 30 kilometers above the ground, a shower of secondary

USC UNIVERSIDADE DE SANTIAGO DE COMPOSTELA

particles (secondary cosmic rays) known as the Extensive Air Shower (EAS) begins.

Electromagnetic, muonic and hadronic are the three major components of the Extensive Air Shower (EAS). Muons are formed in the decay of charged pions. The decay of neutral pions into two gamma-rays may also form a pair electron-positron that can produce more gamma-rays through the Bremsstrahlung mechanism. The hadronic composes of a high-energy hadronic core feeds the muonic and electromagnetic components producing pions. Different effects influence the flux of secondary particles measured on Earth's surface [63], as shown in Figure 7.2.

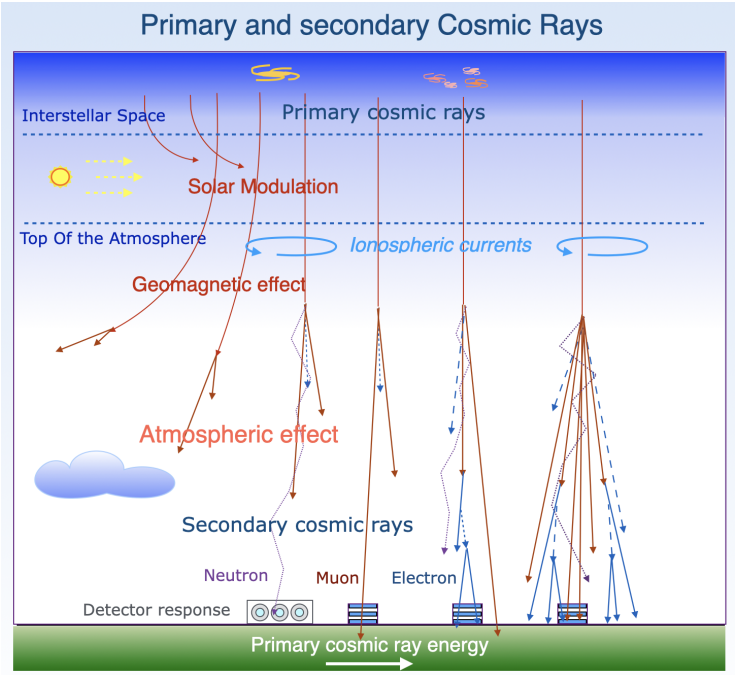

Figure 7.2: Effects that modify the flux of cosmic rays measured on the Earth's surface. The curved lines indicate the distortion in the path of primary cosmic rays caused by magnetic fields. Red straight lines represent the trajectory of muons of the EAS. Gamma-rays are represented by dashed blue lines, while solid blue lines represent electrons and positrons. The path of a neutron is depicted in purple.

USC
UNIVERSIDADE DE SANTIAGO DE COMPOSTELA

Concerning the bundles or clusters of particles, we have concentrated our efforts only on those with at least two charged particles, either muons or electrons. We have classified the clusters into the following groups:

- Electron clusters, composed by at least two electrons and any number of gammas.

- Muonic clusters, composed by at least two muons.

- Mixed clusters, composed by both muons and electrons.

Electron clusters usually are just a small portion of big electromagnetic showers cut by the small acceptance of the detector. We may assume that clusters of bigger multiplicities involve higher thresholds to the energy of the primary cosmic ray.

Concerning the muonic clusters, as mentioned before, muons are produced in the high atmosphere through the decay of mesons (mainly pions). Then, the arrival of more than one muon can only be produced by the decay of two mesons in the same shower. Then the arrival of two muons to a small size detector is very unlikely and can only be produced by high-energy primaries.

Finally, as shown in Figure 7.1, the mixed clusters do correspond probably to a high energy muon coupled with an electromagnetic shower produced by a delta electron ejected near the detector.

For each primary particle and range of energy, we have adjusted the number of simulated events according to the number of particles arriving at the ground and, consequently, to the size of the generated files. The numbers of showers ranged between one hundred thousand for the lowest energies and a few thousand for the highest energies. For each set of simulations at given energy and a given mass, we recorded four ASCII files containing summary information about all the showers, the clusters of particles and single particles (See Table 7.1).

USC
UNIVERSIDADE DE SANTIAGO DE COMPOSTELA

The variables stored in each of the files are the following:

- Shower file

This file contains in each line 26 columns containing summary information of each of the showers generated at a given energy interval. There is a line per shower. The stored variables are the following:

1. Mass of the primary cosmic ray.

2. Mean energy of the primary cosmic ray.

3. Mean height of the primary cosmic ray interaction.

4. Number of the shower.

5. Number of secondary particles.

6. Number of clusters.

7. Number of gammas.

8. Number of electrons.

9. Mean distance of the electrons to the shower center.

10. Number of muons.

11. Mean distance of the muons to the shower center.

12. Number of neutrons.

13. Number of Protons.

14. Number of other particles.

USC
UNIVERSIDADE DE SANTIAGO DE COMPOSTELA

15. Number of electron clusters.

16. Number of muon clusters.

17. Number of mixed clusters.

18. Number of with at most one charged particle.

19-26. Total number of electrons in each range of the following energy intervals, given in GeV: $(0.05, 0.1)$, $(0.1, 0.15)$, $(0.15, 0.2)$, $(0.2, 0.3)$, $(0.3, 0.5)$, $(0.5, 1)$, $(1, 2)$ and (> 2). 8 columns.

- Cluster file

This file contains a summary of the properties of all the clusters found for each of the showers generated in all the energy ranges. There is a line with 37 columns for each cluster. They are huge and heavy files for the highest energies and the information has not been used yet, but the files remain for future analysis. The stored variables are the following:

1. Mass of the primary cosmic ray.

2. Energy of the primary cosmic ray.

3. Height of the primary cosmic ray interaction.

4. Number of the generated shower.

5. Number of the cluster.

6. Identifier code of the cluster. A compact number informs about the composition of the cluster, number of gammas, electrons, muons, protons and neutrons.

7. The cluster type: electronic, muonic, mixed, or other.

USC
UNIVERSIDADE DE SANTIAGO DE COMPOSTELA

8. Number of particles in the cluster.

9. Number of electrons in the cluster.

10. Number of muons in the cluster.

11-12. Types of the first and last particles in the shower.

13-15. X and Y coordinates of the center of the cluster and radial size of the cluster, respectively.

16-19. Arrival time of the first and the last particle of the shower, the mean arrival time of all the particles in the cluster and the standard deviation of the arrival times of all the particles in the shower, respectively.

20-27. Summary of the electron properties: Arrival times of the first and last electrons, zenith and azimuth angles of the first and the last electron and momenta of the first and last electrons, respectively.

28-35. Summary of the muon properties. The exact definition as for electrons.

36. Distance of the cluster to the center of the shower.

37. the Opening angle between the first and the last particle in the cluster.

- Particle file

This file contains a compact summary of all the secondary particles arriving at the detector. It has a line per generated energy and mass with 24 columns each. Each line has the following variables:

1. Mass of the primary cosmic ray.

USC
UNIVERSIDADE DE SANTIAGO DE COMPOSTELA

2. Energy of the primary cosmic ray.

3. Mean height of the primary cosmic ray interaction.

4. The total number of simulated showers.

5. The total number of secondary particles.

6. The total number of clusters.

7-12. The total number of gammas, electrons, muons, protons, neutrons and other particles, respectively.

13-16. The total number of clusters of the different types: electronic, muonic, mixed and others.

17-24. Total number of electrons in each range of the following energy intervals, given in GeV: $(0.05, 0.1)$, $(0.1, 0.15)$, $(0.15, 0.2)$, $(0.2, 0.3)$, $(0.3, 0.5)$, $(0.5, 1)$, $(1, 2)$ and (> 2). 8 columns.

- Neural Network file

This file contains in each line 52 columns providing summary information of all the showers generated at given energy and a primary cosmic ray mass. The main goal of this file is to use it for analyzing the capability of estimating both the energy and the mass of the primary cosmic rays based on a few of the properties of the clusters of particles that a Trasgo detector could measure.

The variables we have stored are the following:

1. Mass of the primary cosmic ray.

2. Mean energy of the primary cosmic ray.

3. Number of generated showers at this energy.

USC UNIVERSIDADE DE SANTIAGO DE COMPOSTELA

4. The total number of electrons in the shower.

5. The Total number of muons in the shower.

6. The total number of electron clusters in the shower.

7. The Total number of muon clusters in the shower.

8. The Total number of mixed clusters in the shower.

9-16. The total number of electrons in each range of energy is given above (8 columns).

17-22. Number of electron clusters with their time width (time difference between the first and the last electron) classified in six-time intervals; in ns: $(0,1)$, $(1,3)$, $(3,6)$, $(6,20)$, $(20,40)$ and (>40).

23-28. The number of muon clusters with their time width is classified in six-time intervals mentioned above.

29-34. The mixed clusters with their time width are classified in the aforementioned six-time intervals.

35-40. Number of electron clusters with their angular opening (angle between the first and the last electron) classified in six angular intervals; in degrees: $(0,2)$, $(2,5)$, $(5,9)$, $(9,15)$, $(15,25)$ and (>25).

41-46. The number of muon clusters with their angular opening is classified in six aforementioned angular intervals.

47-52. The number of mixed clusters with their angular opening is classified in those mentioned above six angular intervals.

USC
UNIVERSIDADE DE SANTIAGO DE COMPOSTELA

7.3 The clusters

We define a cluster as a group of two or more particles arriving in a small area at the detector level; in our case, the one corresponding to Santiago de Compostela. To find the cluster candidates, we proceed in the following way.

For each of the simulated showers, we first looked for the fastest particle to fix a positive time reference. Then for each particle of the shower, we look for a second particle at a distance smaller than a given distance, done by a size parameter, **distmx**, the user fixes that according to the size of the detector; usually, the radius of a circle having the same area of the detector. Once a particle has been found, both particles are labeled as defining a cluster and we calculate the system's center of gravity. Then, we look among the remaining particles for new particles to be added to the cluster fulfilling the condition that the distance to the previous center of gravity is smaller than the given size parameter. Also, in order to avoid the finding of long clusters, where the new particles run too far from the first particles, for adding new particles, we require the radial standard deviation of the cluster to keep it smaller than a new parameter **sigrmx**, defined as **distmx**/2. In any case, the analysis done with a few showers has shown that this condition is not too constraining and ignoring it does not change too much the final results.

The search for new particles is done iteratively. After including a new particle in a cluster, the center of gravity of the cluster is recalculated before looking for new particles among the rest of the particles. All particles added to a cluster are labeled and are ignored while searching for new clusters.

Figure 7.3 shows an example of the strategy used in our analysis for finding a cluster. Starting from the first point, P1, a second point, P2, is found inside a radius **distmx**. The center of gravity CG1 is then estimated. In the second step, a new point P3 is found at a distance to CG1 smaller than **distmx**. Then, the new center of gravity CG2 is

USC UNIVERSIDADE DE SANTIAGO DE COMPOSTELA

calculated. A new point P4 at a distance to CG2 smaller than **distmx** is found, but it is not included in the cluster because the radial standard deviation of the three-particle system **sig3** is larger than the **sigrmx** parameter.

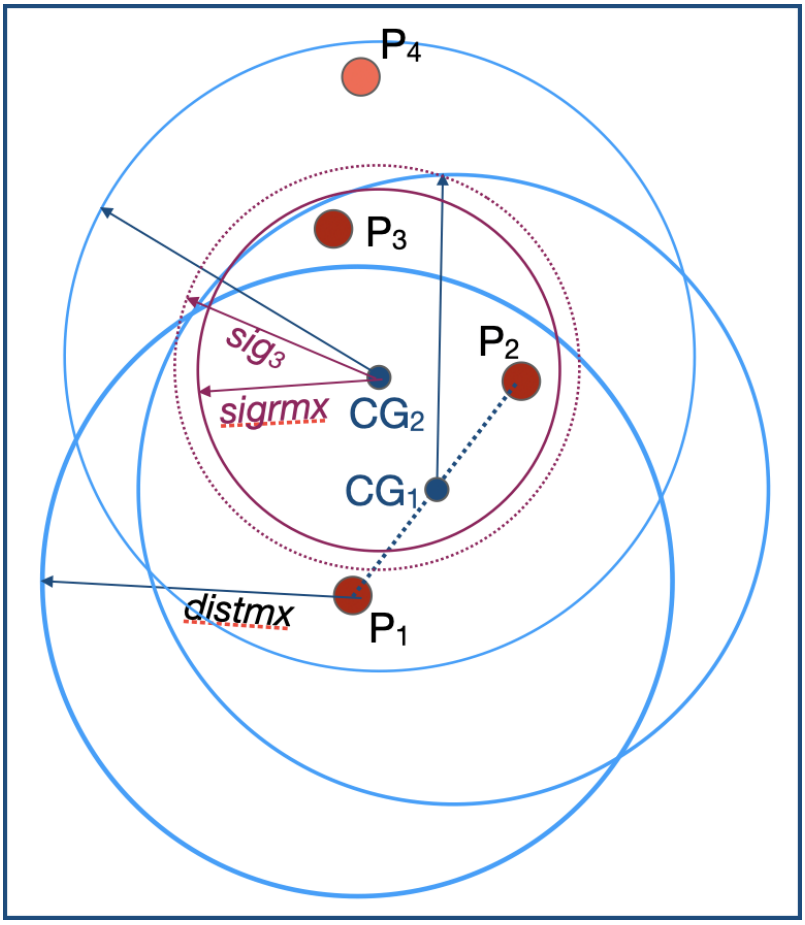

Figure 7.3: Example of the cluster finding strategy. Starting from point P1, the cluster composed of particles P1, P2 and P3 is found. P4 is not accepted because it is out of the circle centered in CG2 with radius sigrmx.

It is essential to clarify that the method used does not completely guarantee that all the particles found would arrive in the acceptance

USC
UNIVERSIDADE DE SANTIAGO DE COMPOSTELA

region of a detector that also depends on the position and arrival angle of the particles. We also did not consider the fact that the clusters we have found could not match with the position of the detector. Those circumstances were out of the scope of this work[8]. Our main goal was to estimate the number of clusters of particles of an approximate size in order to analyze their compositions, the fluctuations in their properties and how they depend on the mass of the primary cosmic ray, as well as to analyze how they behave as a function of the energy of the primary cosmic ray.

7.4 Analysis of the clusters

The research aims to use an array of Trasgo detectors at the ground level to analyze several physical observables of EAS secondary particles to determine properties of the primary cosmic ray, such as mass, energy and arrival direction.

The study in this section is carried out by generating events with primary cosmic rays for four nuclei (Hydrogen, Helium, Carbon and Iron) to study the number of electrons per shower at different energy ranges as a function of the primary energy (E_0) and also, the average number of clusters corresponding to the primary energy for the electrons, muons and mixed clusters. Moreover, the electron clusters Response Function (RF) $G(E, \theta, \phi)$ at different energy ranges was performed. And also, for different nuclei as a primary cosmic ray, we studied the response function for electron clusters detected by the detector at different angles.

Figure 7.4 shows the differential intensity of particles $\frac{dN}{dE}$ as a function of kinetic energy per nucleon (energy spectrum) for different nuclei.

[8] We know that there are many mathematical algorithms to find clusters more precisely than we did. However, none of them fulfilled directly the main requirements we needed. On the other side, using them in the way we wanted, with such a large amount of simulated showers, the number of particles and variables to store required big computer resources and processing time.

USC UNIVERSIDADE DE SANTIAGO DE COMPOSTELA

The following equation describes the intensity of the primary nuclei with the energy range from a few GeV up to a few hundred TeV:

$$I(E) \cong 1.8 \times 10^4 \times \left(\frac{E}{GeV}\right)^{-2.7} \left[m^{-2}\, sr^{-1}\, s^{-1}\, GeV^{-1}\right] \quad (7.1)$$

where E is the energy of each nucleus and the intensity of the primary nuclei is proportional to the abundance of nuclei that arrive in the atmosphere.

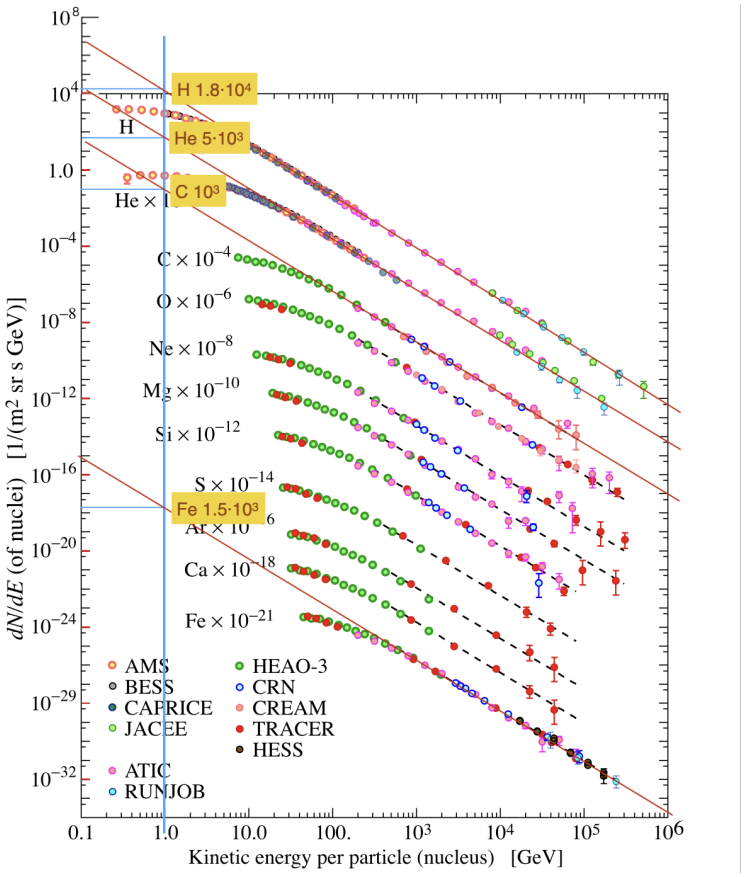

Figure 7.4: The differential intensity of particles (Flux) of primary cosmic rays as a function of the energy.

As seen in Figure 7.4, when the energy is below 10 GeV, the flux is low due to cosmic rays with low energy being blocked by the solar plasma. The values in the yellow boxes represent the slope of the linear regression fit was done for the behavior of the nuclei under study (H, He, C and Fe) that used to calculate the integral of the intensity corresponds to the energy to find the number of the particles in a specific energy range.

The Response Function (RF) $G(E,\theta,\phi)$ is the distribution of detector counting rate at the given energy of a particular primary nucleus. It can be written as:

$$G(E,\theta,\phi) = M(E,\theta)\,.\,I(E)\,.\,\Delta\, S\Omega(\theta,\phi) \tag{7.2}$$

where $M(E,\theta)$ is the multiplicity function provided by the Corsika simulations, which represents the number of particles normalized to the shower number, $I(E)$ is the intensity of the particles and $\Delta\, S\Omega(\theta,\phi)$ is the partial acceptance of the detector where it did not take into account in the simulation thus, we will ignore it.

The response function for the detector is calculated using equation (7.2) by multiplying the multiplicity function $M(E,\theta)$ with the intensity of the particles $I(E)$, as depicted in Figure 7.5. The data of differential energy spectrum were taken directly from Figure 7.4 after applying a linear regression fit to find the slope for the behavior of the nuclei under study (H, He, C and Fe) that used to calculate the intensity of primary nucleons using equation (7.1).

USC
UNIVERSIDADE DE SANTIAGO DE COMPOSTELA

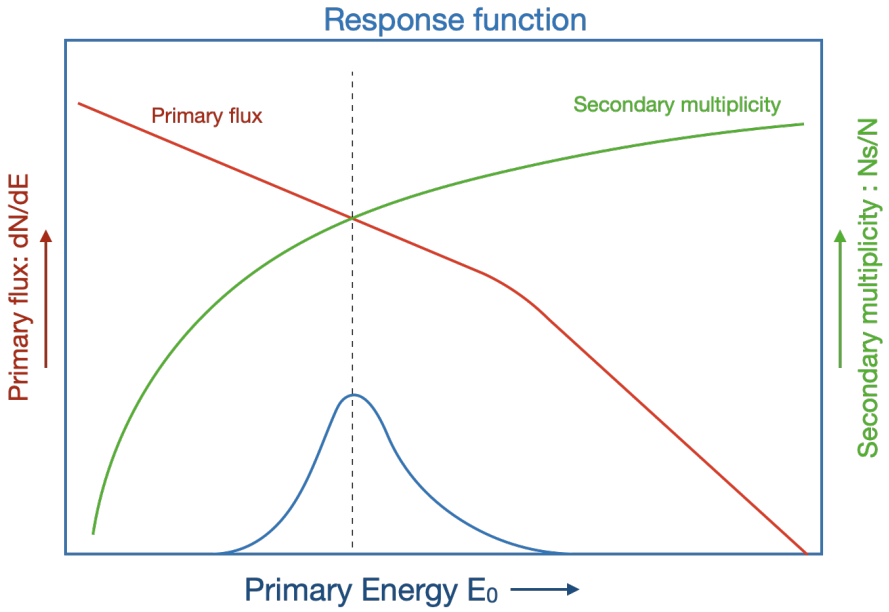

Figure 7.5: The distribution of detector counting rate at the given energy of a specific primary nucleus.

7.5 Results of the clusters

This section presents the results obtained for the clusters at different energy ranges and different incidence angle ranges.

7.5.1 Results of the clusters at different energy ranges

The average number of electrons at different energy ranges per shower energy as a function of the primary energy (E_0) in logarithmic scale for the four nuclei: Hydrogen, Helium, Carbon and Iron, respectively, are presented in Figure 7.6.

To summarize, according to Figure 7.6, the minimum shower energy required for different nuclei to produce only one electron with a different energy range according to the shower energy is listed in Table 7.4.

USC
UNIVERSIDADE DE SANTIAGO DE COMPOSTELA

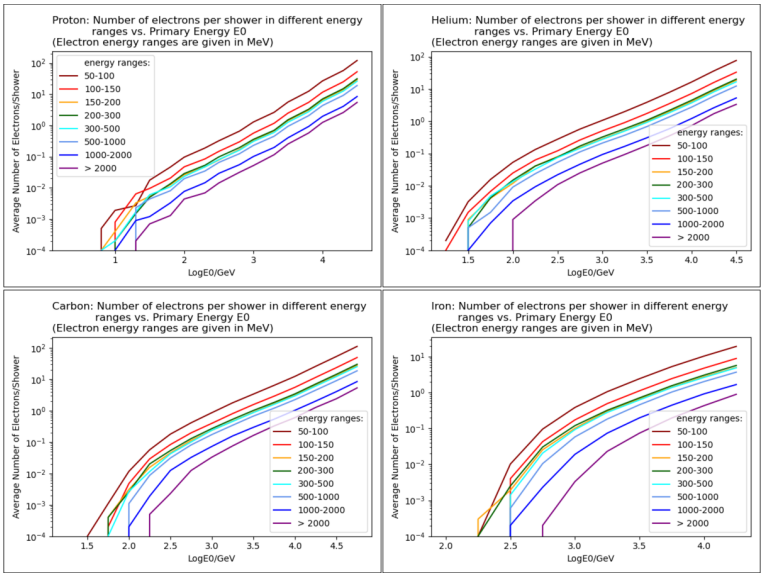

Figure 7.6: The average multiplicity function for the electrons at different energy ranges per shower energy as a function of the primary energy in logarithmic scale for H, He, C and Fe nuclei.

Table 7.4: Summary of the shower energy required for different nuclei to produce one electron with a different energy range according to the shower energy.

	Proton	Helium	Carbon	Iron
Energy (MeV)	Energy Shower $\times 10^3\ (GeV)$	Energy Shower $\times 10^3\ (GeV)$	Energy Shower $\times 10^3\ (GeV)$	Energy Shower $\times 10^3\ (GeV)$
$50 - 100$	0.8	1.0	1.1	1.8
$100 - 150$	1.6	2.0	2.2	2.8
$150 - 200$	2.5	3.2	3.1	4.0
$200 - 300$	2.5	3.2	3.1	4.0
$300 - 500$	2.8	3.5	4.0	4.5
$500 - 1000$	3.2	4.5	5.0	5.6
$1000 - 2000$	6.3	8.9	10.0	11.2
> 2000	8.9	12.6	15.8	20.0

USC UNIVERSIDADE DE SANTIAGO DE COMPOSTELA

We can observe that the shower's energy needed to produce one electron is proportional to the mass of the nuclei for the same energy range for the produced electron. For example, to produce one electron with an energy range $(50 - 100)\ MeV$, the shower should have at least an energy of about $794\ GeV$, which is for the Hydrogen nucleus. In contrast, the shower of the Helium nucleus requires the energy of about $1000\ GeV$, the shower of the Carbon nucleus needs around $1122\ GeV$. The shower of the Iron nucleus should have about $1778\ GeV$ to produce one electron with the same energy range for all the nuclei. Moreover, with increasing the energy range of the produced electron, the energy of the shower for all the nuclei increases.

After calculating the response function $G(E)$, the response function results of the electrons produced for the four primary nuclei (H, He, C and Fe) after their interactions with the atmosphere are illustrated in Figure 7.7.

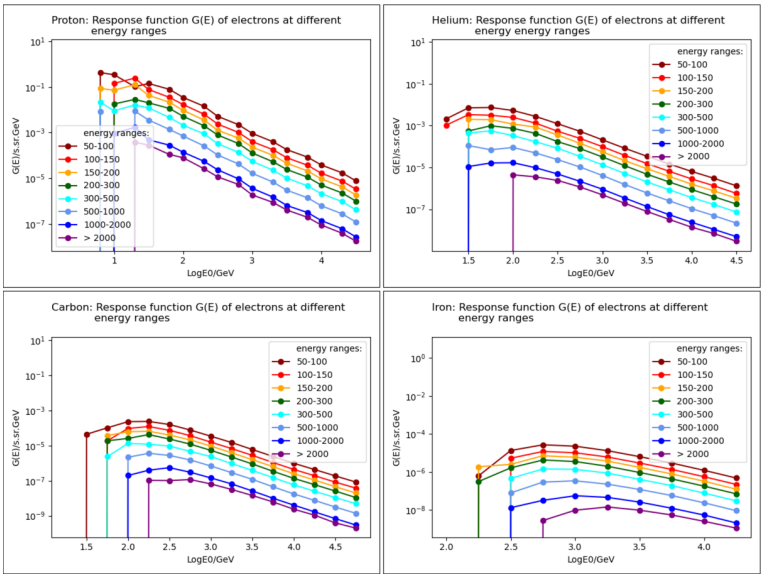

Figure 7.7: The response function $G(E)$ of the electrons produced in the atmosphere at different energy ranges for the primary nuclei Hydrogen, Helium, Carbon and Iron, respectively. The solid lines in the Figure do not represent any fit for the data. It has been drawn to guide the eyes.

USC
UNIVERSIDADE DE SANTIAGO DE COMPOSTELA

Moreover, the average number of clusters for the primary nuclei understudy corresponding to the primary energy for the produced electrons, muons and mixed clusters was studied in this section, as shown in Figure 7.8.

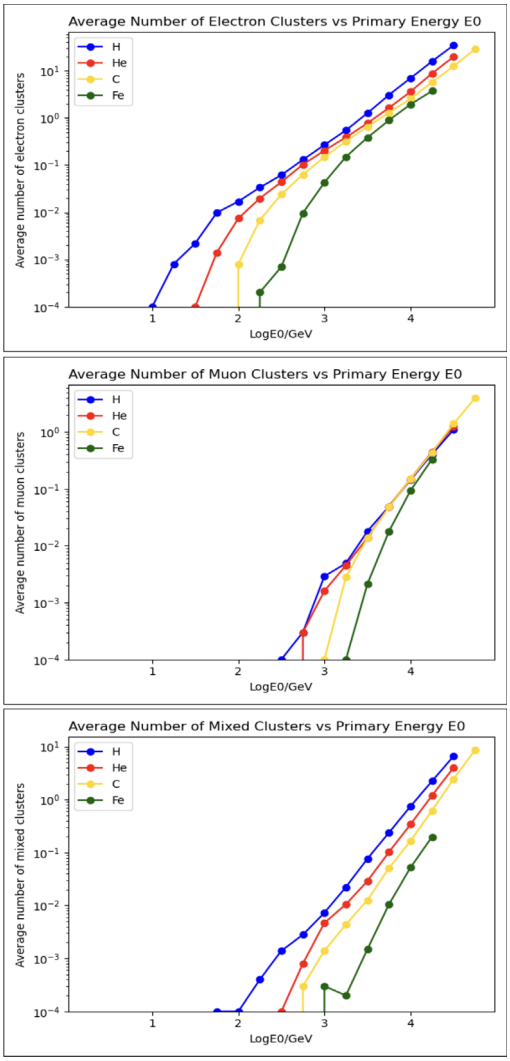

Figure 7.8: Average number of clusters for the primary four nuclei (H, He, C and Fe) corresponding to the primary energy of the produced clusters for the electrons (top), muons (middle) and mixed (bottom).

USC UNIVERSIDADE DE SANTIAGO DE COMPOSTELA

It is observed in Figure 7.8 that the heavier nucleus required more primary energy of the shower to produce the same number for the clusters of electrons, muons, or mixed clusters.

In summary, we used the Hydrogen nucleus (proton) in the simulation as a primary nucleus to compare the number of clusters for electrons, muons and mixed clusters produced corresponding to the primary energy in a range $(2-5)\ GeV$, as presented in Figure 7.9.

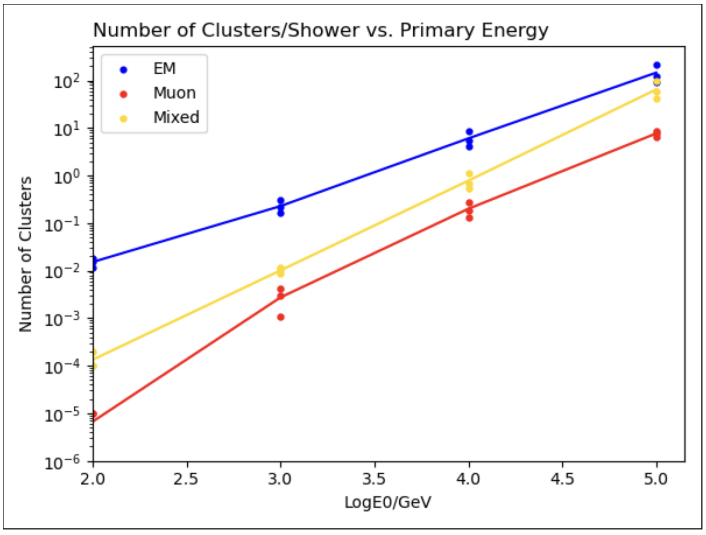

Figure 7.9: A comparison between the number of clusters for electrons, muons and mixed clusters as a function of the primary energy for the proton.

We can see in Figure 7.9, for the same primary energy, the average number of the electron clusters is greater than the muon clusters and mixed clusters and the average number of the mixed clusters is greater than the muon clusters. It could be because the mixed clusters contain electrons.

Moreover, the analysis of the variation of the number of electromagnetic (EM) clusters in time may estimate the variation of the average first interaction altitude and inform about the changes in the temperature of the high atmosphere. Among other changes could

USC UNIVERSIDADE DE SANTIAGO DE COMPOSTELA

provide the changes in the average energy of the primary cosmic rays and changes in the average mass of the primary cosmic rays. Figure 7.10 illustrates the number of electromagnetic (EM) clusters per shower produced for simulated primary proton interacting with the atmosphere with different primary energies as a function of the first interaction altitude in kilometer (km).

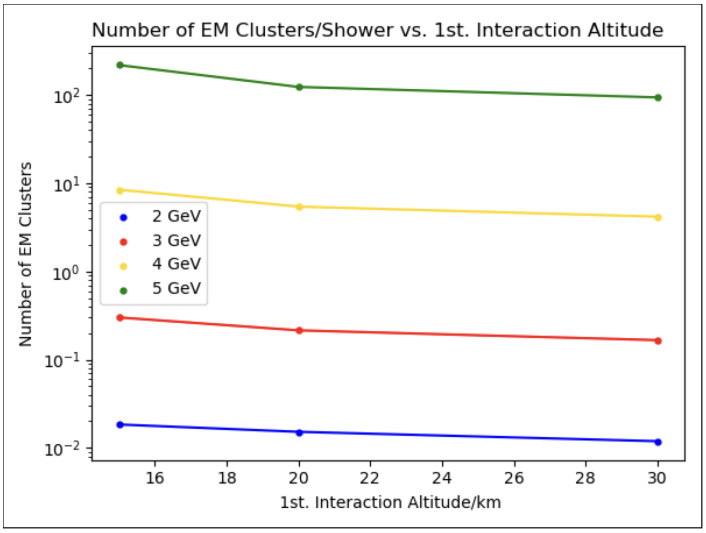

Figure 7.10: represents the number of electromagnetic (EM) clusters per shower for the primary proton interacting with the atmosphere with different primary energies as a function of the first interaction altitude.

It is obvious that the number of electromagnetic clusters per shower depends on the primary energy. The number of electromagnetic clusters per shower increases with increasing the primary energy. And also, with increasing the altitude, the number of clusters per shower slightly decreases.

In addition, the analysis of the variation of the ratio of the numbers between different types of clusters may provide information about the changes in the average energy of the primary cosmic ray and perhaps its mass. The ratio between muonic and electromagnetic clusters and

USC UNIVERSIDADE DE SANTIAGO DE COMPOSTELA

between mixed and electromagnetic clusters as a function of the energy for proton as a primary cosmic ray, as shown in Figure 7.11.

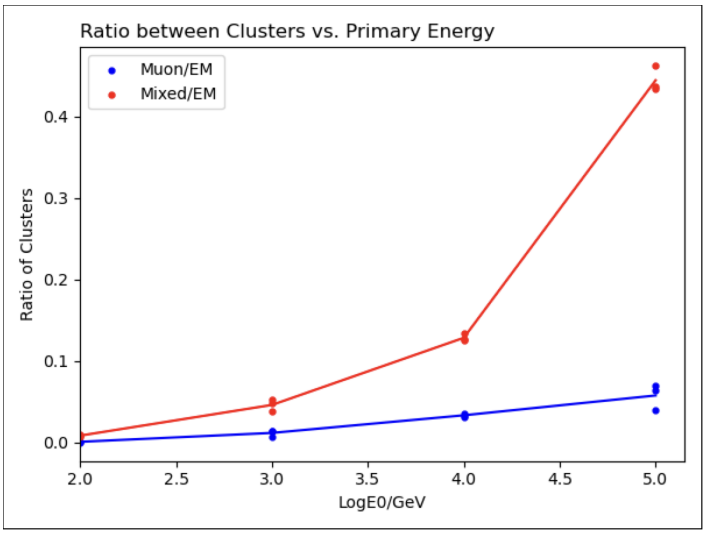

Figure 7.11: The ratio between Muonic and electromagnetic clusters and between Mixed and electromagnetic clusters as a function of the energy of a proton as a primary cosmic ray.

According to Figure 7.11, when the primary energy is below $100\,GeV$, the ratio between mixed and electromagnetic clusters is almost the same ratio between muonic and electromagnetic clusters. Nevertheless, when the primary energy is above $100\,GeV$, the ratio between different types of clusters is proportional to the primary energy. Moreover, we notice that the ratio between mixed and electromagnetic clusters is greater than the ratio between muonic and electromagnetic clusters for the same value of the primary energy.

Furthermore, Figure 7.12 shows the ratio of the numbers between electromagnetic and mixed clusters corresponding to the primary energy.

USC
UNIVERSIDADE DE SANTIAGO DE COMPOSTELA

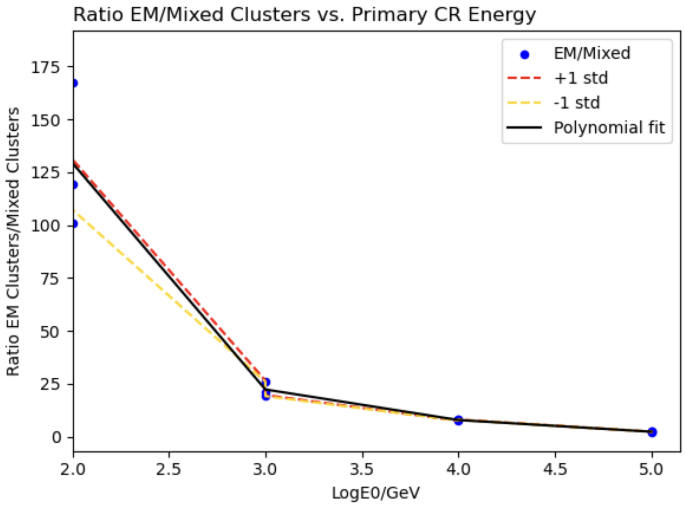

Figure 7.12: The ratio of the numbers between electromagnetic and mixed clusters as a function of the primary energy.

It is clear that the ratio decreases with the increase of primary energy. Moreover, for the same reasons that led to study the ratio of the numbers between different types of clusters previously mentioned, Analysis of the variation of that ratio in a given time period may give an estimation of the variation of the average energy of primary cosmic rays or other phenomena, as the effect of the atmosphere in that ratio.

7.5.2 Results of the clusters at different angle ranges

In this subsection, we repeated almost what was done in the previous one. We calculated the response function for different nuclei (H, He, C and Fe) at the different incident zenith angle ranges. Moreover, for the four nuclei under study at different zenith angle ranges, the primary energy of the maximum of the response function was investigated and also, threshold energy for the production of different clusters of particles, threshold energy for the production of different secondary particles and threshold energy for the production of electrons at different energy ranges.

USC
UNIVERSIDADE DE SANTIAGO DE COMPOSTELA

For this purpose, the zenithal angles have been chosen to span a large area of space where the primary cosmic rays can occur in the atmosphere. The zenithal angle has a uniform separation in four ranges between 0° and 53°, with step-in $\cos\theta$ of 0.1 according to $\cos 0 = 1$, the zenithal angle ranges employed are $[0^{\circ}, 25^{\circ}]$, $[25^{\circ}, 37^{\circ}]$, $[37^{\circ}, 46^{\circ}]$ and $[46^{\circ}, 53^{\circ}]$.

The response function results of the electrons produced for the four primary nuclei (H, He, C and Fe) after their interactions with the atmosphere with different energy ranges at various incident zenith angles are shown in the following figures.

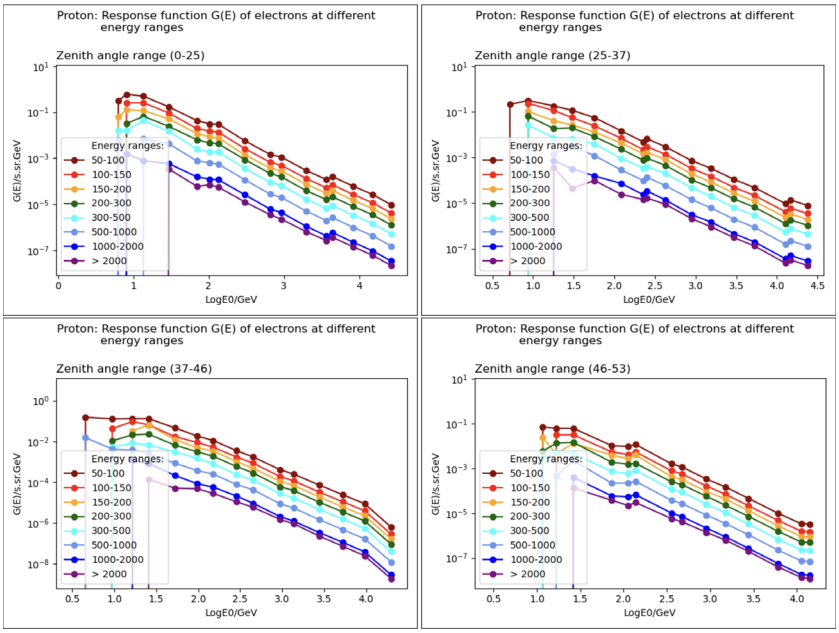

Figure 7.13: The response function of the electrons produced for the Proton as a primary cosmic ray with different energy ranges as a function of the primary energy in logarithmic scale at various incident zenith angles in degrees. The energy ranges of the electrons are given in MeV.

USC
UNIVERSIDADE DE SANTIAGO DE COMPOSTELA

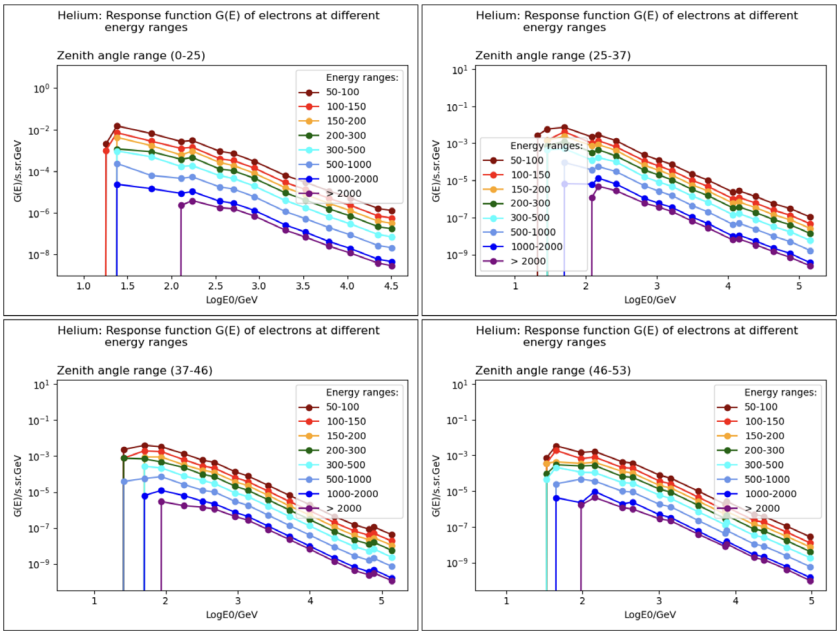

Figure 7.14: The response function of the electrons produced for the Helium nucleus as a primary cosmic ray with different energy ranges as a function of the primary energy in logarithmic scale at various incident zenith angles in degrees. The energy ranges of the electrons are given in MeV.

USC
UNIVERSIDADE DE SANTIAGO DE COMPOSTELA

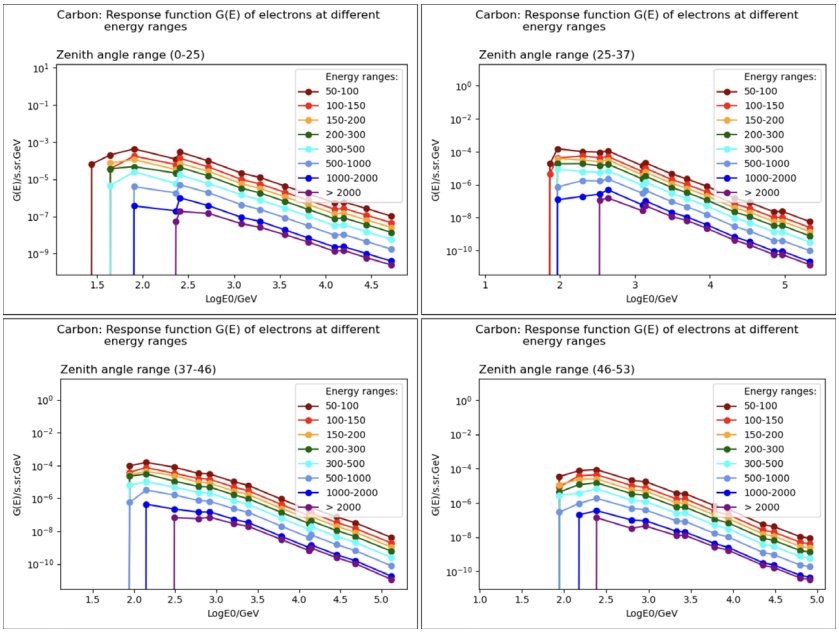

Figure 7.15: The response function of the electrons produced for the Carbon nucleus as a primary cosmic ray with different energy ranges versus the primary energy in logarithmic scale at various incident zenith angles in degrees. The energy ranges of the electrons are given in MeV.

USC
UNIVERSIDADE DE SANTIAGO DE COMPOSTELA

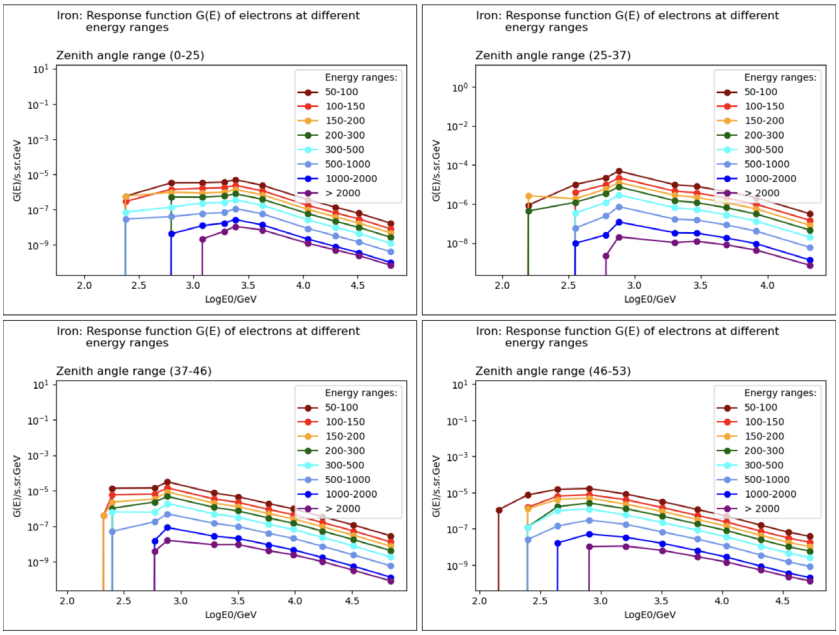

Figure 7.16: The response function of the electrons produced for the Iron nucleus as a primary cosmic ray with different energy ranges versus the primary energy in logarithmic scale at various incident zenith angles in degrees. The energy ranges of the electrons are given in MeV.

It is observed that the response function decreased with increasing the primary energy for all the nuclei. Furthermore, with increasing the incidence of zenith angles for the same nucleus used as primary cosmic rays, the results showed a discrepancy in the response function values. Some of them were increasing and others were decreasing, but in general, the response function is inversely proportional to the mass of the nucleus.

The following figures show the response function of the produced electrons, muons, neutrons and protons for various primary nuclei as a function of the primary energy at different incidence zenith angles.

USC UNIVERSIDADE DE SANTIAGO DE COMPOSTELA

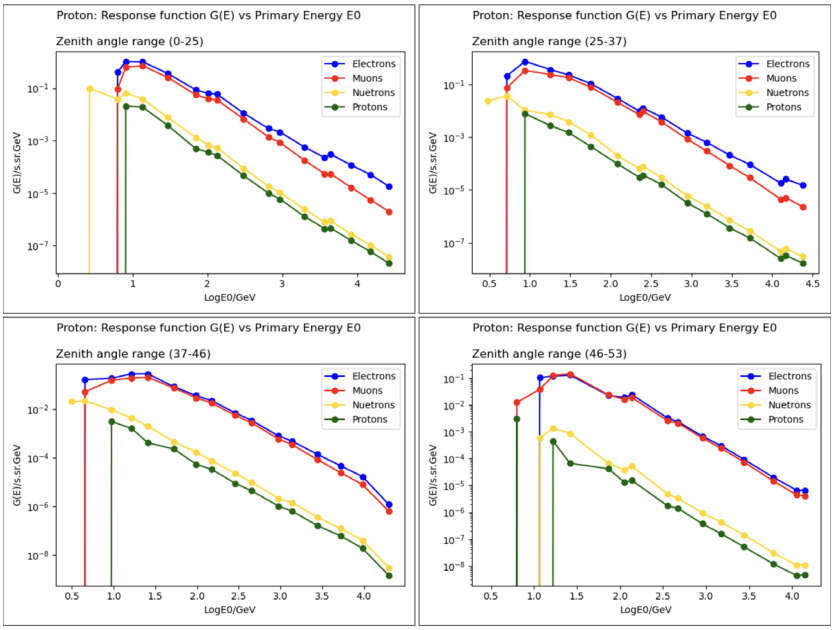

Figure 7.17: Represents the response function of the produced electrons, muons, neutrons and protons for the Proton as primary cosmic rays versus the primary energy at different incidence zenith angles.

USC
UNIVERSIDADE DE SANTIAGO DE COMPOSTELA

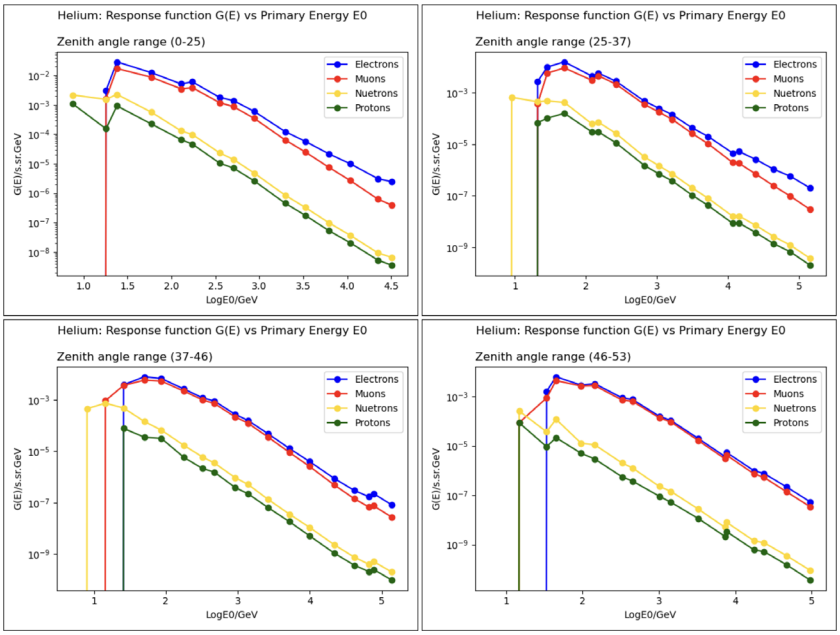

Figure 7.18: Shows the response function of the produced electrons, muons, neutrons and protons for the Helium nucleus as primary cosmic rays versus the primary energy at different incidence zenith angles.

USC
UNIVERSIDADE DE SANTIAGO DE COMPOSTELA

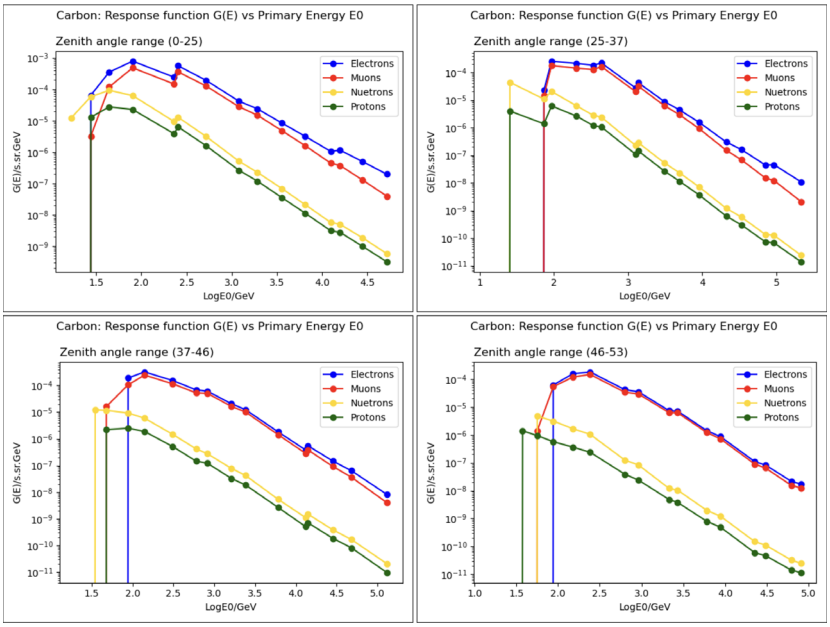

Figure 7.19: Illustrates the response function of the produced electrons, muons, neutrons and protons for the Carbon nucleus as primary cosmic rays as a function of the primary energy at different incidence zenith angles.

USC
UNIVERSIDADE DE SANTIAGO DE COMPOSTELA

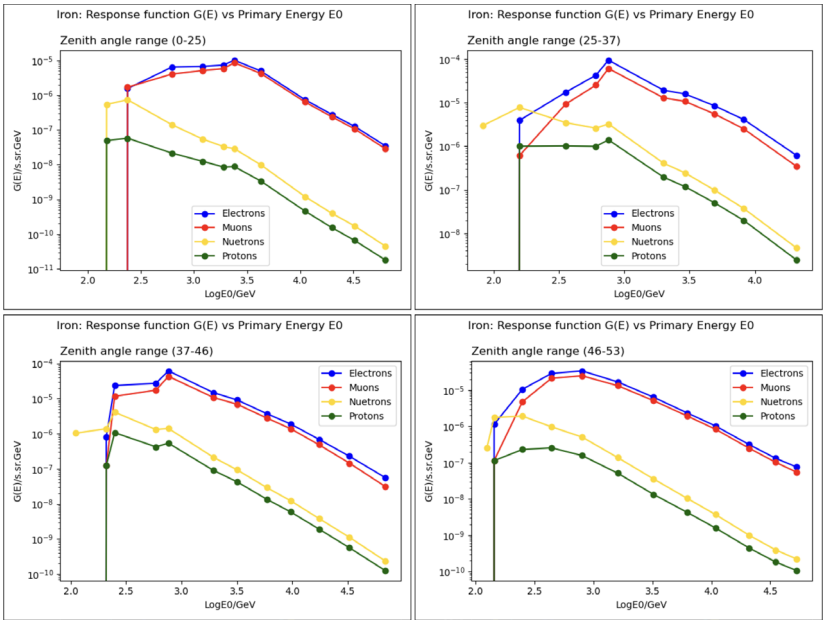

Figure 7.20: Shows the response function of the produced electrons, muons, neutrons and protons for the Iron nucleus as primary cosmic rays as a function of the primary energy at different incidence zenith angles.

It is evident that the response function depends on the mass of the nuclei, where the response function decreases with the mass of the nucleus increased for the same zenith angle ranges. Moreover, we observed that the highest value of the response function was for the produced electrons, then for the muons and then for the neutrons and the lowest value for the protons at all incidence zenith angle ranges.

Moreover, as depicted in the following figures, we studied the response function of the electron clusters, muon clusters and mixed clusters for different nuclei as primary cosmic rays versus the primary energy at different incidence zenith angles.

USC
UNIVERSIDADE DE SANTIAGO DE COMPOSTELA

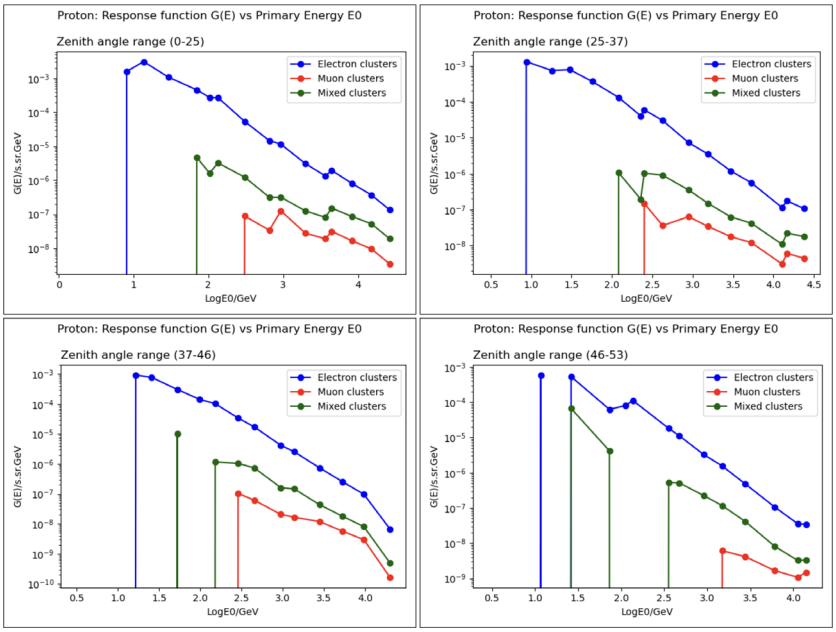

Figure 7.21: The response function of the electron clusters, muon clusters and mixed clusters for the primary Proton versus the primary energy in logarithmic scale at different incidence zenith angles.

USC
UNIVERSIDADE
DE SANTIAGO
DE COMPOSTELA

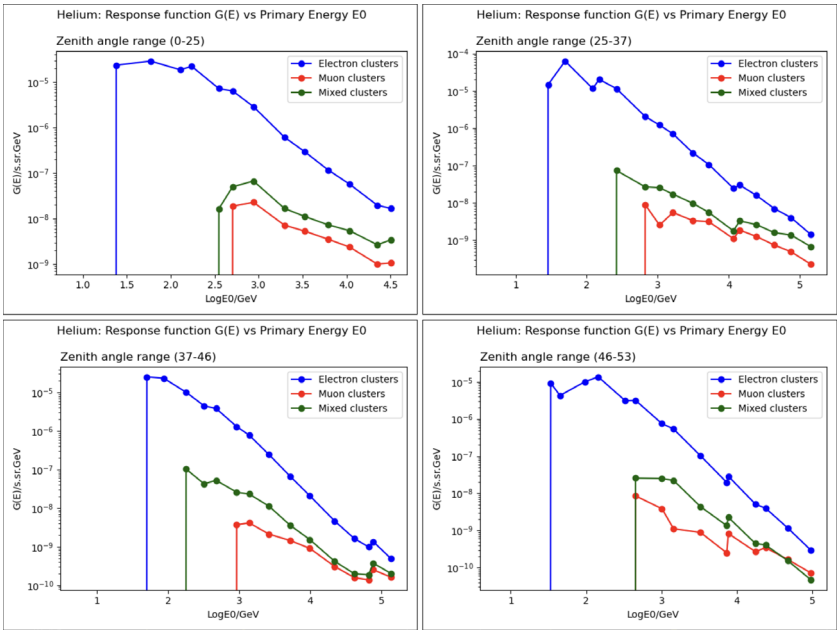

Figure 7.22: The response function of the electron clusters, muon clusters and mixed clusters for the Helium nucleus as primary cosmic rays as a function of the primary energy in logarithmic scale at different incidence zenith angles.

USC
UNIVERSIDADE DE SANTIAGO DE COMPOSTELA

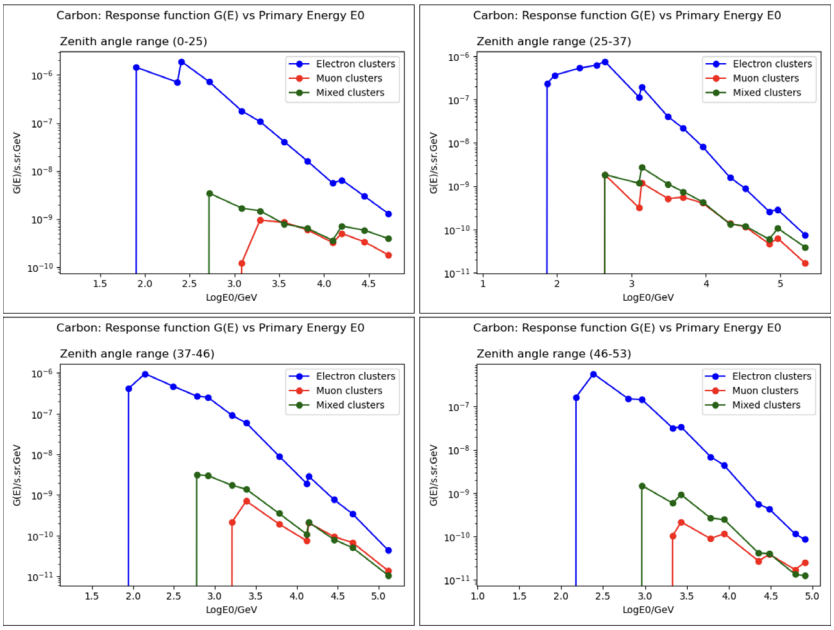

Figure 7.23: Shows the response function of the electron clusters, muon clusters and mixed clusters for the Carbon nucleus as primary cosmic rays as a function of the primary energy in logarithmic scale at different incidence zenith angles.

USC
UNIVERSIDADE DE SANTIAGO DE COMPOSTELA

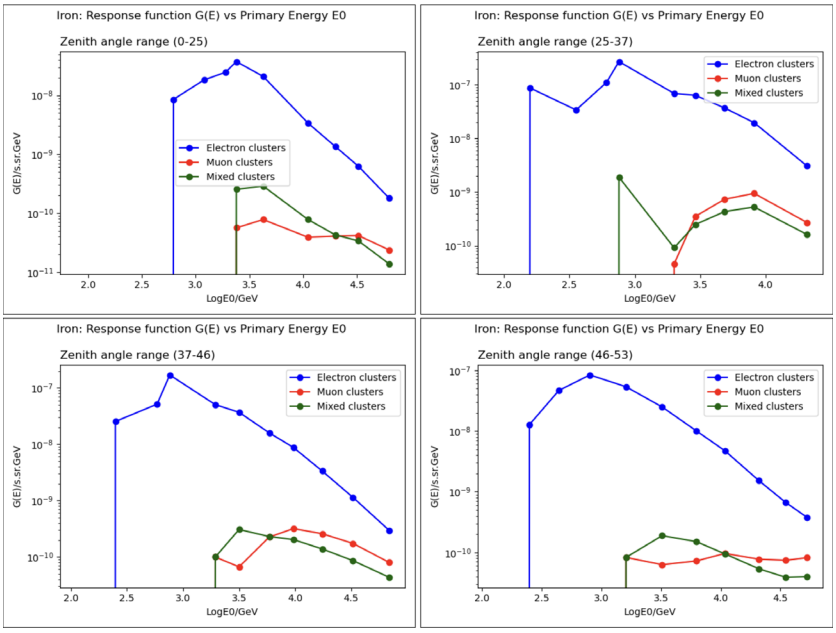

Figure 7.24: The response function of the electron clusters, muon clusters and mixed clusters for the primary Iron nucleus as a function of the primary energy in logarithmic scale at different incidence zenith angles.

The response function of the produced clusters for electrons, muons and mixed clusters does not differ from producing the secondary particles for various primary nuclei. Where we noticed that the response function for producing different types of clusters decreases with the mass of the nucleus increased for the same zenith angle ranges and the highest value of the response function was for the produced electron clusters and then for the mixed clusters and the lowest value for the muon clusters.

The primary energy was studied at the maximum of the Response Function (RF) at different zenith angles for different nuclei (H, He, C and Fe) as primary cosmic rays for the production of electrons with varying ranges of energy and production of the electron clusters, muon clusters and mixed clusters and the production of different secondary

USC UNIVERSIDADE DE SANTIAGO DE COMPOSTELA

particles such as electrons, muons, neutrons and protons, as presented in the following figures.

In the following figures, the x-axis represents either name of the nuclei or the zenith angle ranges. We referred to 1 for Hydrogen, 2 for Helium, 3 for Carbon and 4 for Iron for the nuclei names. Moreover, for the zenith angle ranges, we referred to 1 for energy range $[0^{\circ} - 25^{\circ}]$, 2 for $[25^{\circ} - 37^{\circ}]$, 3 for $[37^{\circ} - 46^{\circ}]$ and 4 for $[46^{\circ} - 53^{\circ}]$.

Figure 7.25 shows the primary energy at the maximum value of the response function $G(E)$ for different primary nuclei (H, He, C and Fe) that interact in the atmosphere to produce electrons as a secondary particle at different arrival zenith angles with varying ranges of energy.

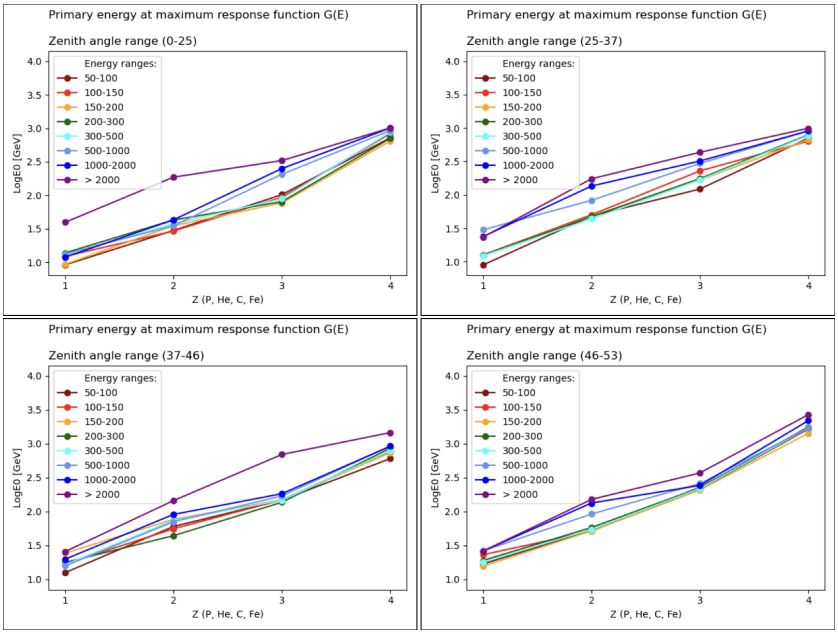

Figure 7.25: The primary energy at the maximum of the response function for different primary nuclei to produce electrons as a secondary particle at different arrival zenith angles with varying energy ranges. The energy ranges of the electrons are given in MeV.

USC
UNIVERSIDADE DE SANTIAGO DE COMPOSTELA

The primary energy at the maximum response function $G(E)$ for Proton, Helium, Carbon and Iron, respectively, to produce electrons with varying energy ranges at different arrival zenith angles, as illustrated in Figure 7.26.

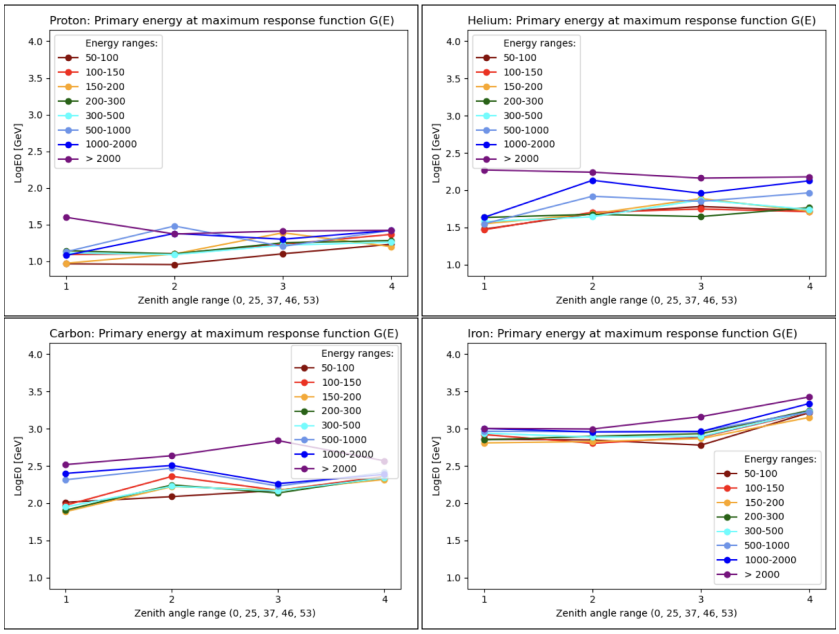

Figure 7.26: Represents the primary energy at the maximum response function to produce electrons with varying energy ranges at different arrival zenith angles for Proton, Helium, Carbon and Iron, respectively. The energy ranges of the electrons are given in MeV.

Moreover, the primary energy at the maximum response function $G(E)$ for various primary nuclei (H, He, C and Fe) to create different secondary particles and clusters of particles at different arrival zenith angles was analyzed, as depicted in the following figures.

USC
UNIVERSIDADE DE SANTIAGO DE COMPOSTELA

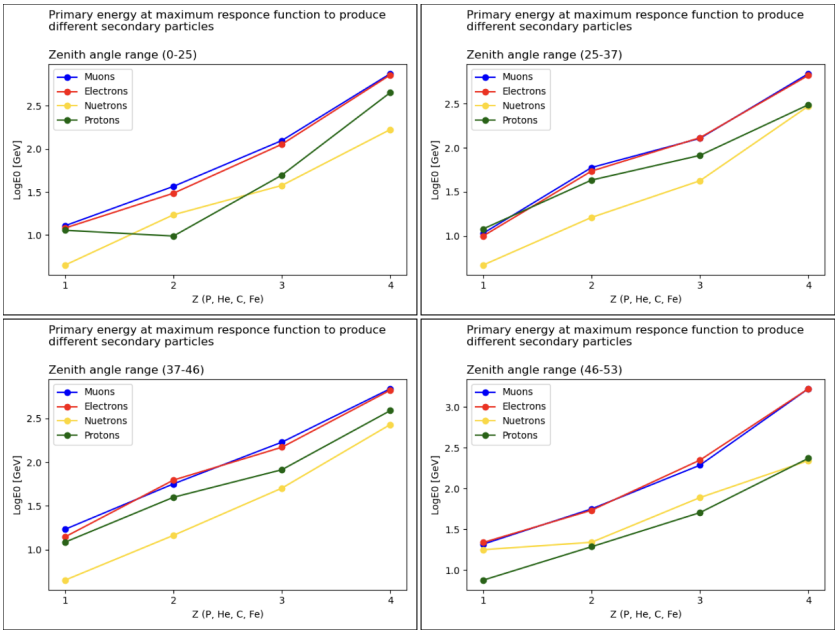

Figure 7.27: The primary energy at the maximum response function for different primary nuclei (H, He, C and Fe) to produce different secondary particles at various zenith angles.

USC
UNIVERSIDADE DE SANTIAGO DE COMPOSTELA

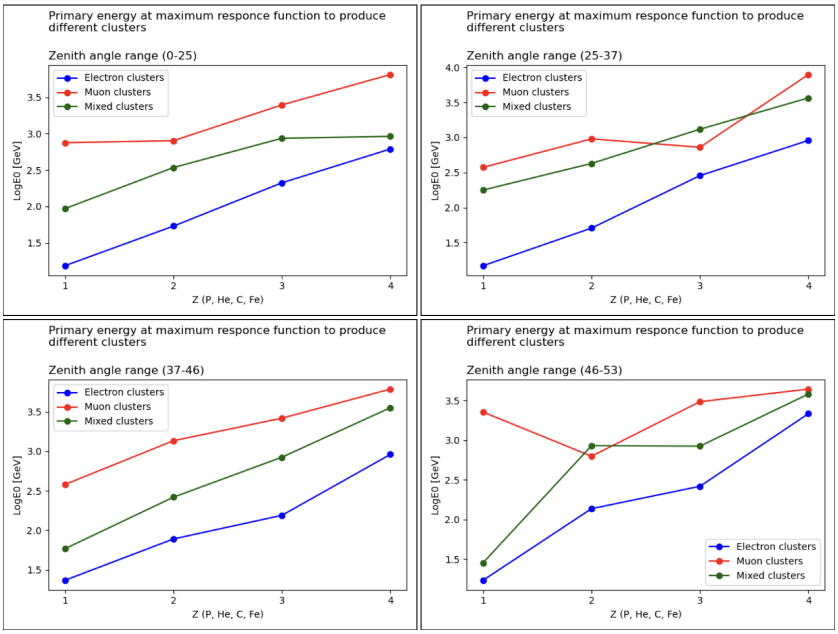

Figure 7.28: The primary energy at the maximum response function for various primary nuclei (H, He, C and Fe) at various arrival zenith angles to produce different clusters of particles.

Figures 7.29 and 7.30 show the primary energy at the highest value of the response function for different nuclei to produce the different secondary particles and clusters of particles with varying arrival zenith angles.

USC UNIVERSIDADE DE SANTIAGO DE COMPOSTELA

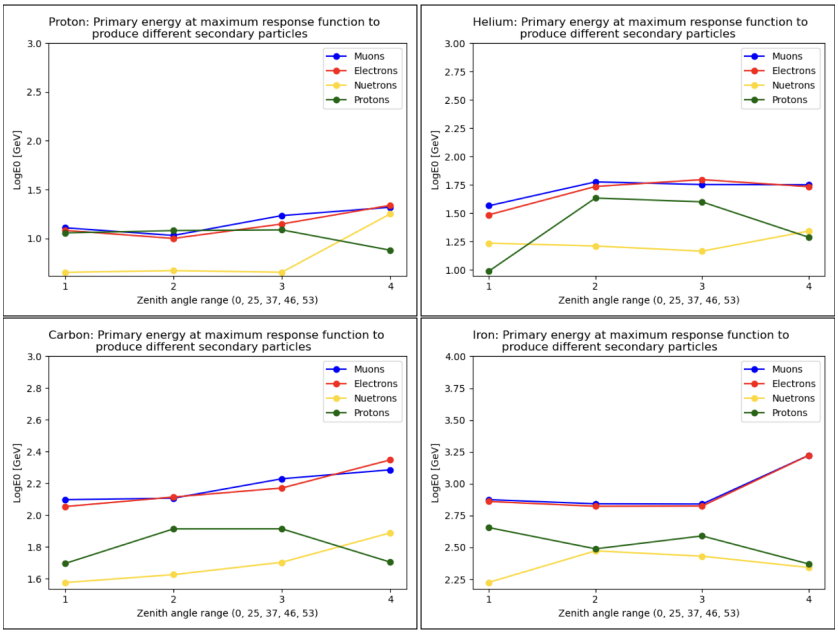

Figure 7.29: Illustrates the primary energy at the maximum of the response function for different nuclei to produce different secondary particles with various arrival zenith angles.

USC
UNIVERSIDADE DE SANTIAGO DE COMPOSTELA

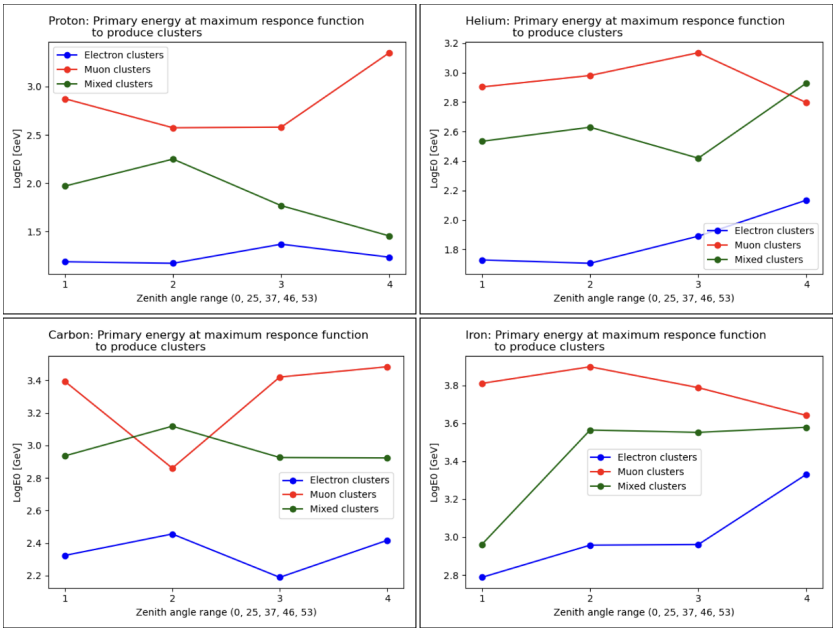

Figure 7.30: Represents the primary energy at the maximum response function for various nuclei to produce different clusters of particles with different arrival zenith angles.

Furthermore, the threshold energy, which is the minimum energy required to produce electrons with different energy ranges, various secondary particles, or different clusters of particles were investigated at different arrival zenith angles for different nuclei (H, He, C and Fe) as primary cosmic rays as shown the following figures.

Figure 7.31 shows the threshold energy for different primary nuclei (H, He, C and Fe) for producing the electrons as secondary particles with different energy ranges at various incident zenith angles.

USC UNIVERSIDADE DE SANTIAGO DE COMPOSTELA

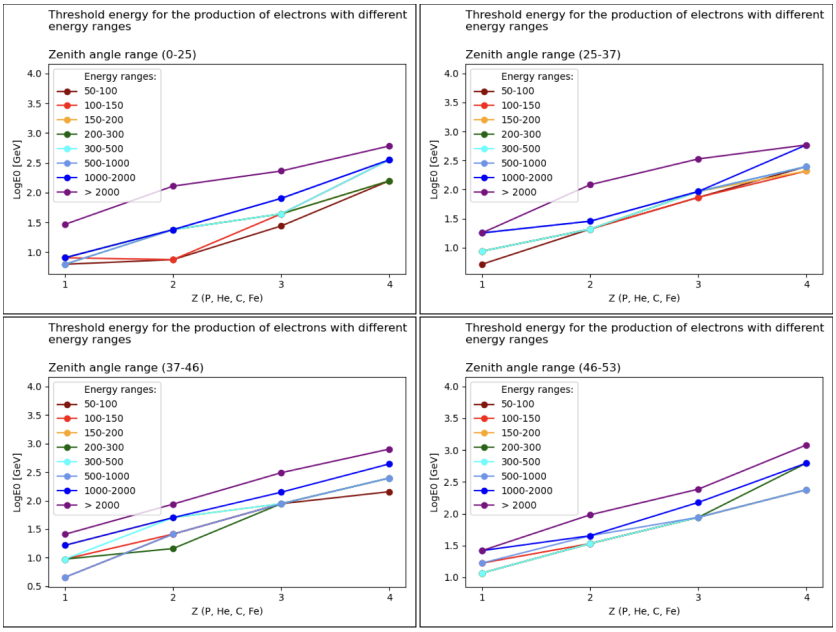

Figure 7.31: The threshold energy for various primary nuclei (H, He, C and Fe) to produce electrons with different energy ranges at varying arrival zenith angles. The energy ranges of the electrons are given in MeV.

The threshold energy for Proton, Helium, Carbon and Iron nuclei, respectively, to produce electrons with different energy ranges at different arrival zenith angles, as presented in Figure 7.32.

USC
UNIVERSIDADE DE SANTIAGO DE COMPOSTELA

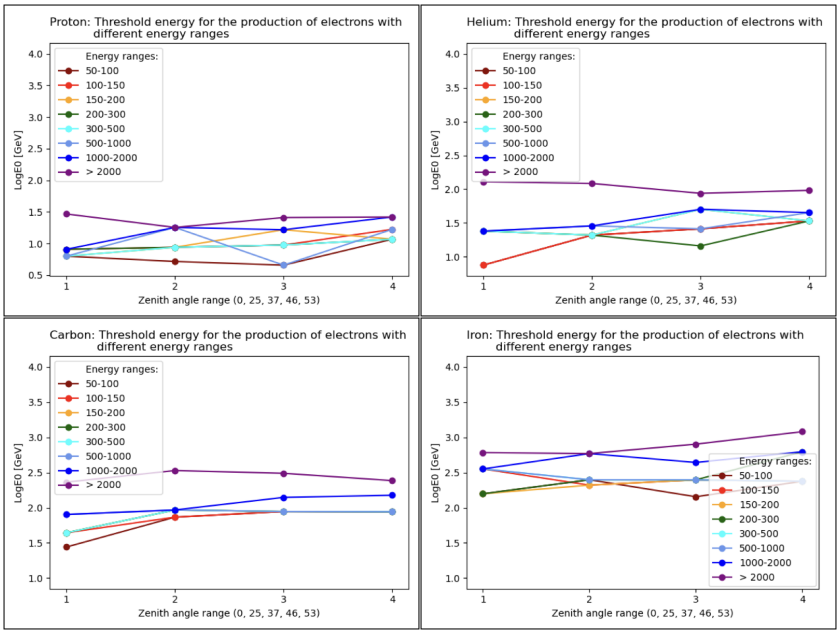

Figure 7.32: shows threshold energy to produce electrons with varying energy ranges at different arrival zenith angles for Proton, Helium, Carbon and Iron, respectively, where the energy ranges for the produced electrons are given in MeV.

Furthermore, as shown in the following figures, we analyzed the threshold energy required for producing different secondary particles and different clusters of particles for various primary nuclei (H, He, C and Fe) at different incident zenith angle ranges.

USC UNIVERSIDADE DE SANTIAGO DE COMPOSTELA

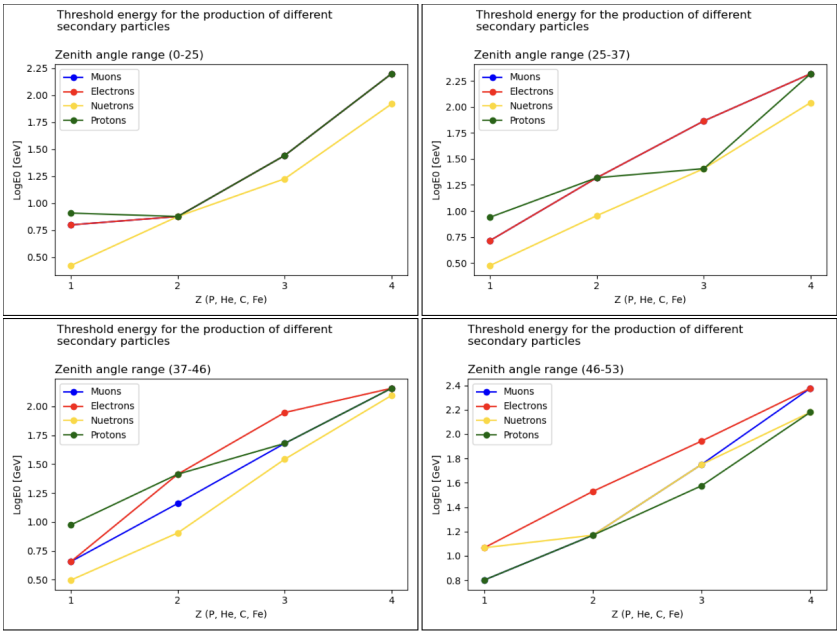

Figure 7.33: Presents the threshold energy required to produce secondary particles for different primary nuclei (H, He, C and Fe) at different arrival zenith angle ranges.

USC
UNIVERSIDADE DE SANTIAGO DE COMPOSTELA

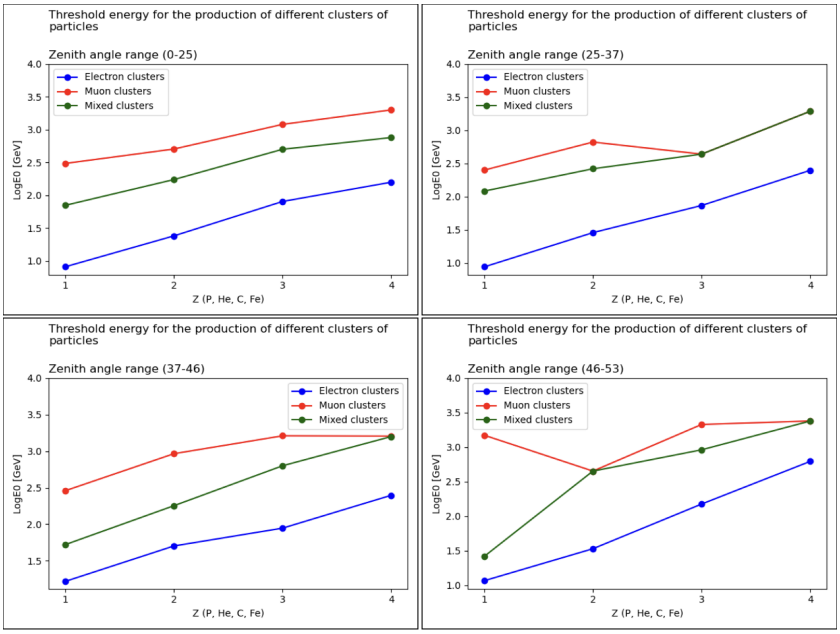

Figure 7.34: Illustrates the threshold energy required for producing different clusters of particles for various primary nuclei (H, He, C and Fe) at different incident zenith angle ranges.

The threshold energy needed for Proton, Helium, Carbon and Iron nuclei, respectively, for producing the various secondary particles and clusters of particles with different incident zenith angles, as presented in Figures 7.35 and 7.36.

USC UNIVERSIDADE DE SANTIAGO DE COMPOSTELA

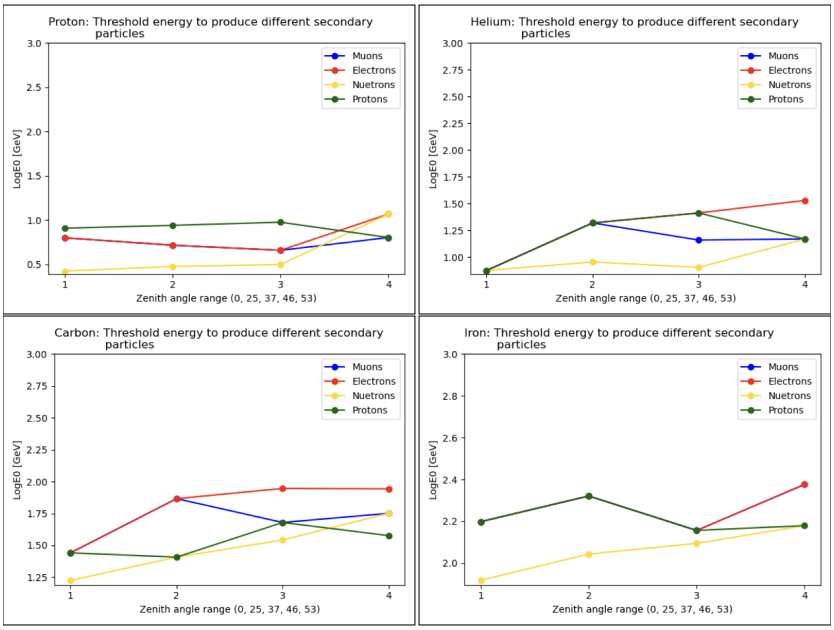

Figure 7.35: The threshold energy required for different nuclei to create secondary particles with various arrival zenith angles.

USC
UNIVERSIDADE DE SANTIAGO DE COMPOSTELA

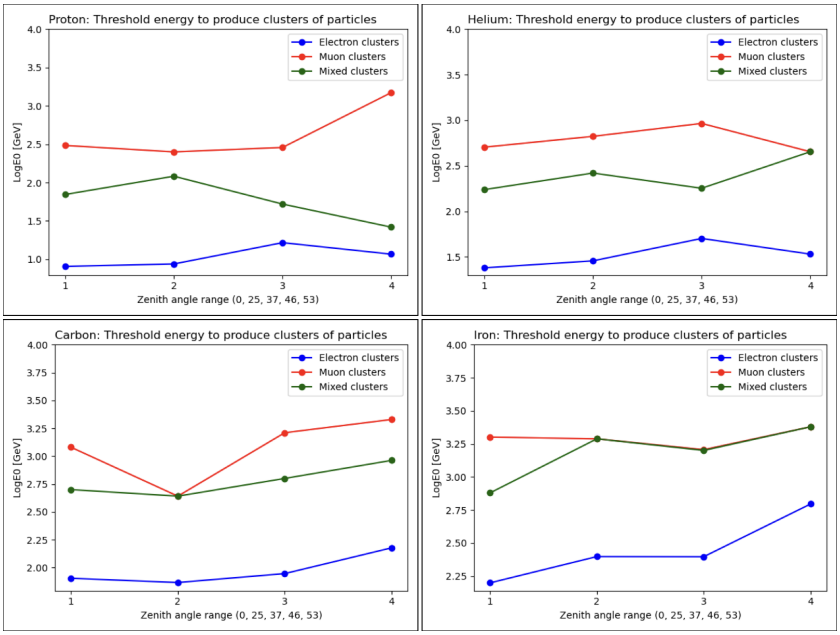

Figure 7.36: The threshold energy needed for various nuclei to produce clusters of particles with different arrival zenith angles.

It is clear that the primary energy at the maximum response function to produce electrons with differing energy ranges at various arrival zenith angles increases with increasing the mass of the nucleus. Furthermore, this also applies to the threshold energy to create electrons with varying energy ranges at different arrival zenith angles.

7.6 Future perspective for Trasgo detectors

The response function of the Trasgo family detectors enables the estimation and identification of the energy of the primary cosmic rays. A project called MEIGA (Mini Ensemble for Identifying GAlactic radiation) is developed by LabCAF with multiple Trasgo detectors at the University of Santiago de Compostela (USC) to study and understand better the properties of the primary cosmic ray. Several Trasgo detectors spread across a vast area can collect enough data to detect secondary cosmic rays from the same origin as the primary

USC UNIVERSIDADE DE SANTIAGO DE COMPOSTELA

cosmic rays. Thus, the Trasgo detectors open the door to measure new interesting observables.

Approximate energy thresholds of different particles or bundles of particles able to be measured with an area of about 1.8 m^2 using Trasgo detector at the University of Santiago de Compostela, as illustrated in Figure 7.37.

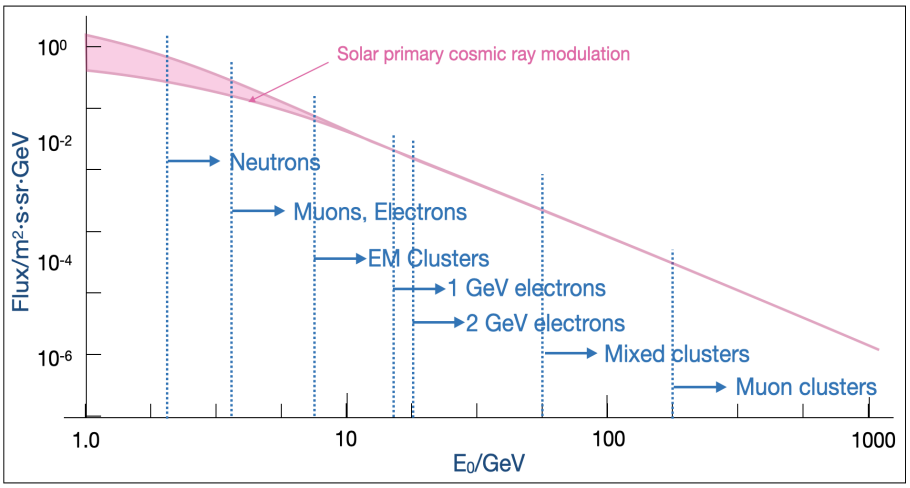

Figure 7.37: Energy thresholds of different particles or bundles of particles can be measured with an area of about 1.8 m^2 using Trasgo detector.

Figure 7.38 depicts the Response Function (RF) of three detectors, both of the flux of the cosmic ray primaries and the secondary cosmic rays multiplicity as a function of the primary energy (E0). Three response functions ($RF1, RF2, RF3$) are obtained by multiplying three multiplicity functions ($M1, M2, M3$) by the linear equation of the energy spectrum. The estimated primary energy is the area generated by superimposing the three distributions. It is a straightforward and effective method for estimating primary energy precisely and removing any possible causes of inaccuracy using statistics.

USC
UNIVERSIDADE DE SANTIAGO DE COMPOSTELA

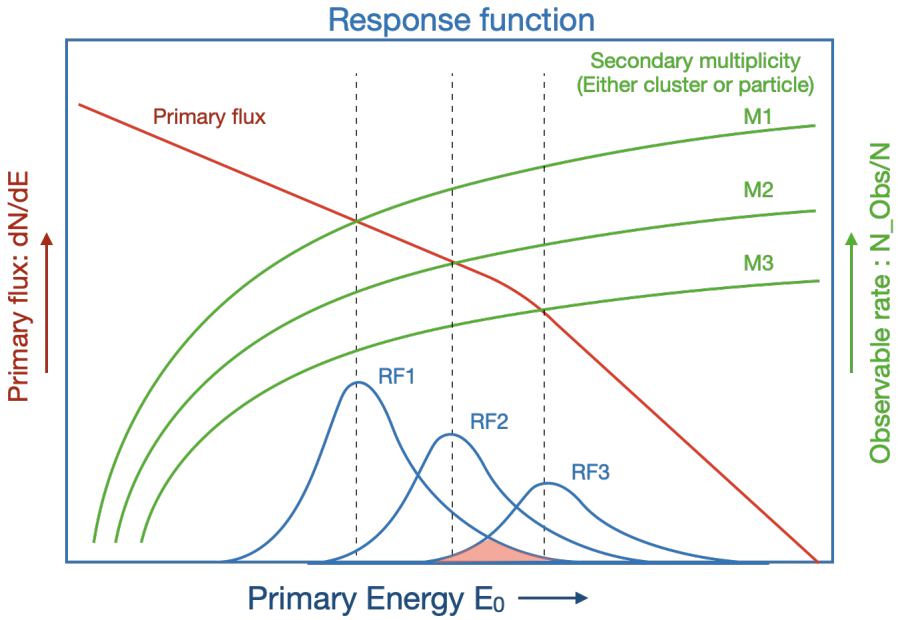

Figure 7.38: The area obtained by the superposition of the three response functions of the Trasgo detector provides the estimated energy of the primary cosmic rays.

As we can see, the joint analysis of the response functions of different observables, either for single particles or bundles of particles of the same shower measured by different detectors, may provide a precise estimation of the energy of the primary cosmic rays and perhaps their mass.

USC
UNIVERSIDADE DE SANTIAGO DE COMPOSTELA

8 Analysis of the cosmic ray background in the Faculty of Physics building at the USC using a COSMIX detector

8.1 Introduction

As discussed in previous chapters, the cosmic-ray muon flux provides a way of testing parameters of the primary cosmic-ray flux (energy spectrum, chemical composition) and particle interactions at high energies. Our TRAGALDABAS detector is placed on the first floor of the Physics Faculty of the University of Santiago de Compostela (Laboratory 106). In order to estimate the "lead equivalent thickness" of the building above the detector and to study the influence of the background and gamma and electron contributions to the observed data, a compact muon detector developed by the French CNRS/IN2P3 laboratory LP2IB (former "Centre d'Etudes Nucléaires de Bordeaux Gradignan," CENBG), called COSMIX, was used [104]. The COSMIX detector was installed at different levels of the Physics Faculty: The first level is the roof of the building, the second location is the Lab 6 on the second floor, the third position is the Lab 106 on the first floor and finally to the ground level (Lab 002). In the following section, a description of the COSMIX detector is given as well as the study of the cosmic ray rates and the background measured with this detector.

8.2 Structure of the COSMIX detector

The detector is made up of two scintillator bars cut from a spare Cesium Iodide CsI(Tl) bar from the Fermi-LAT satellite R&D test detector [105], which are connected to Hamamatsu PIN diodes and custom electronics, with the data acquisition (DAQ) system based on an Arduino microcontroller, as illustrated in Figure 8.1. It has a GPS, a pressure meter, an LCD screen showing counters and a data acquisition

USC UNIVERSIDADE DE SANTIAGO DE COMPOSTELA

system that allows data to be saved in ASCII format on an SD memory card.

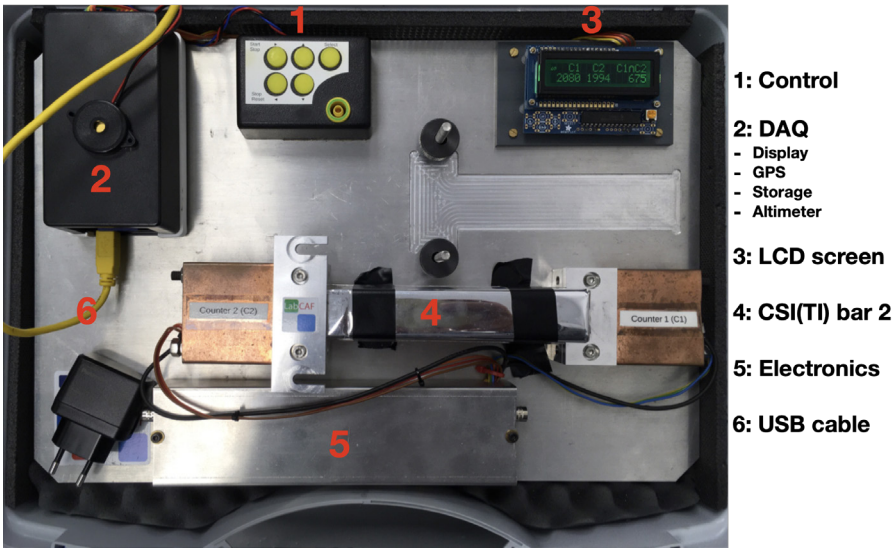

Figure 8.1: COSMIX detector, where detector 2 (bar 2) was placed over detector 1 (bar 1). The dimension of detector 1 is 10 cm in length, 2.5 cm in width and 1 cm in thickness. Detector 2 has the same dimension, but it is 2 cm longer.

Scintillator bars create visible light when a charged particle travels through it, which can be converted into an electrical pulse by a PIN photodiode. A photodiode is a semiconductor device that consists of a thin layer of silicon in which the light is absorbed, after which free charge carriers (electrons and holes) are created. PIN means that a depleted undoped Intrinsic semiconductor region separates the P and N dopped sides. Electrons and holes are collected at the anode and cathode of the diode. This results in a photocurrent that is the output of the diode. However, the charge is not amplified, making the output signal amplitude small. This makes the photodiode sensitive to electronic noise. On the other hand, the quantum efficiency for the photodiode $(60-80\%)$ compared to a photomultiplier $(20-30\%)$ gives a higher energy resolution, but for counting purposes, a PIN diode is optimal.

USC UNIVERSIDADE DE SANTIAGO DE COMPOSTELA

Each photodiode is, in fact, double (only the large surface is used in COSMIX). The collected electric charge is converted into a voltage pulse by preamplifiers in contact with the photodiode. This pulse is amplified and shaped by an amplifier. The preamplifiers are placed in copper boxes, whereas the amplifiers are placed in an aluminum box. The signals of each bar are available via BNC exits.

Each detector counts independently at a rate of about $1\ count/second$. In contrast, the coincidence rate (detector 2 is movable and thus can be placed on top of the other) decreases to about $0.4\ count/second$ [105]. The tripping thresholds must be set at $400\ mV$, which allows for observing pulses that are consistent with the counting of cosmic rays. The high noise level below this threshold may mask the physical impulses.

The detector is robust, light and portable in a small case, no tuning needed, requiring only a USB connection cable for its power supply such as that offered by a laptop or external battery (power bank) and operates about $300\ mA$. Moreover, the detector can be connected to the oscilloscope to show the signals of the detected particles.

8.3 Radiation length

The average rate of energy loss owing to the Bremsstrahlung process for relativistic electrons per cm path length is directly proportional to the particle energy (E). The equation below describes the relationship [106]:

$$-\frac{dE}{dX} = \frac{E}{X_0} \tag{8.1}$$

where the constant X_0 is denoted to the radiation length of the absorbent material and is given by the following equation:

USC
UNIVERSIDADE DE SANTIAGO DE COMPOSTELA

$$\frac{1}{X_0} = 4\left(\frac{\hbar}{mc}\right)^2 Z(Z+1)\,\alpha^3\, n_a\, ln\left(\frac{183}{Z^{1/3}}\right) \tag{8.2}$$

where n_a is material density $(atoms/cm^3)$, m is the mass of the electron, α is the fine structure constant $(1/137)$ and Z is the atomic number. It is found that the radiation length X_0 value for electrons in the lead is $0.56\ cm$.

We can calculate the energy E of the particle after crossing $X\ cm$ thickness inside absorber material with an energy E_0 by integral of equation (8.1), we got:

$$E = E_0\, e^{(-X/X_0)} \tag{8.3}$$

Equation (8.2) shows that X_0 is proportional to the particle mass square. Because the muon's mass is 200 times that of the electron, it can be predicted to have a much longer radiation length than the electron. This explains why muon energy loss by the Bremsstrahlung process is negligible compared with electron energy loss, allowing muons to traverse much longer length through absorbing material before coming to rest.

8.4 Electromagnetic showers

When electron or positron with high-energy interacts with matter, Bremsstrahlung is the dominant energy loss mechanism, while pair production is the dominant absorption mechanism for the photons produced. As a result of these two processes, the initial electron will produce a cascade of $e^{\pm}$ pairs and photons, which will continue until the secondary electron energies fall below the critical energy (E_c), at which ionization losses equal those from Bremsstrahlung [107].

USC
UNIVERSIDADE DE SANTIAGO DE COMPOSTELA

- The simplified showers model

A schematic diagram of an electromagnetic shower assuming this simple model is shown in Figure 8.2.

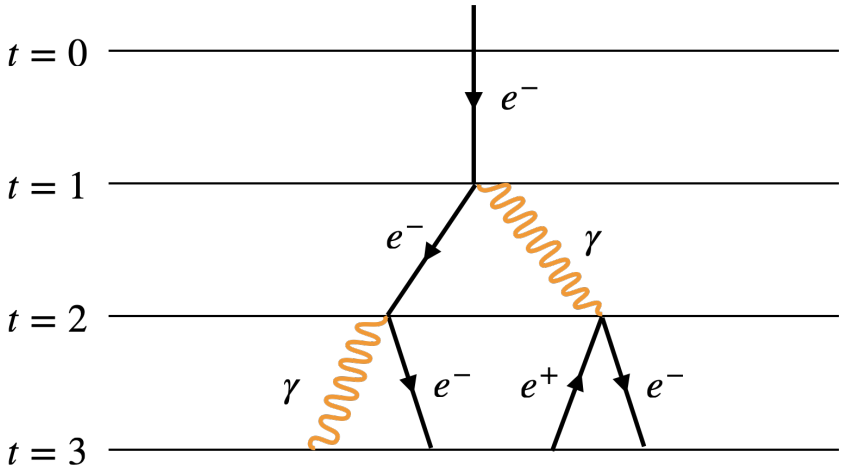

Figure 8.2: The simplified electromagnetic shower model. The values of t denote the successive radiation lengths.

The model is predicated on the following constraints:

1. Each photon with an energy $E > E_c$ travels one radiation length and forms electron-positron pairs, each with half the photon's energy.

2. Each electron with an energy $E > E_c$ travels one radiation length and loses half of its energy to a Bremsstrahlung photon.

3. Electrons with $E < E_c$ stop radiating and, by collisions, lose the rest of their energy.

4. For $E > E_c$, ionization losses are negligible.

USC
UNIVERSIDADE DE SANTIAGO DE COMPOSTELA

Suppose that the initial electron has energy $E_0 \gg E_c$, the shower will contain 2^t particles consisting of about equal numbers of electrons, positrons and photons, each with average energy given by:

$$E(t) = \frac{E_0}{2^t} \tag{8.4}$$

when $E(t) = E_c$, the absorber thickness at which the cascade ceases, t_{max}, can be expressed in terms of the critical and initial energies, as follows:

$$t_{max} = \frac{ln\frac{E_0}{E_c}}{ln2} \tag{8.5}$$

According to the model of the Electromagnetic shower, the theoretical prediction of the variation of the detected particle rates of the expected behavior for a single detector and two detectors in coincidence respectively as a function of the thickness of the lead (X) divided by the radiation length (X_0) is shown in Figures 8.3.

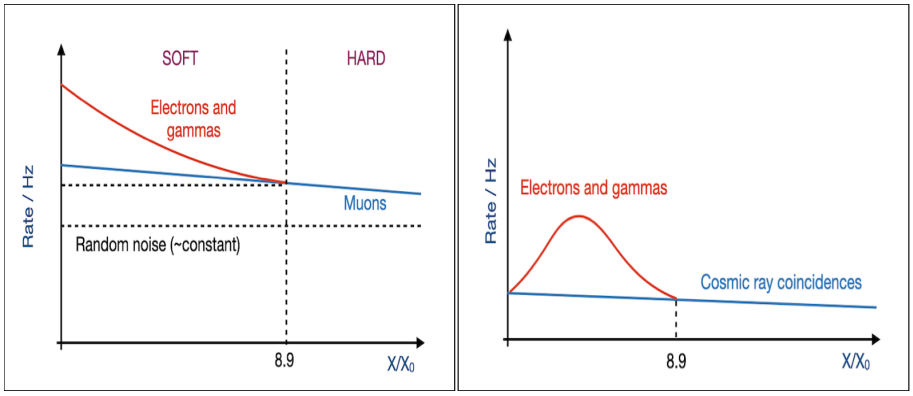

Figure 8.3: An example of a theoretical prediction of the variation of the detected particle rates of the expected behavior for a single detector (left) and two detectors in coincidence (right) as a function of the ratio between the thickness of the lead X and the radiation length X_0.

USC UNIVERSIDADE DE SANTIAGO DE COMPOSTELA

In the first approximation in a single detector, electrons and gamma-ray behave the same way. However, low-energy gammas are more penetrant than low-energy electrons because the electrons are charged particles. Several reasons cause the random noise: horizontal cosmic rays, natural radiative sources (radon, Etc.) and thermal gamma rays. Usually, we assume that cosmic electrons and gamma-ray at sea level are entirely absorbed by 5 cm of lead. This thickness of about 8.9 X_0 establishes the difference between the cosmic rays soft and hard components of the cosmic rays.

Concerning the predicted behavior of the two detectors in coincidence, it is observed that the random coincidences are almost null. Moreover, some coincidences could be produced by separated charged cosmic rays (muons, electrons) arriving simultaneously to both detectors. Electrons and gamma-rays produce the peak produced by the electromagnetic shower. The width of the peak depends on the highest energy of electrons and gamma-rays. The height of the peak depends on the number of electrons and gamma-rays. Electron and gamma-rays peaks are almost similar. The precise shape of the peak depends on the relative number of electrons and gamma-rays and their energies.

8.5 Measurements and taking data

Taking data with the COSMIX detector is easy. The users require no calibration or settings. The detector provides two modes to taking data: First, as mentioned before, detector 2 is movable, enabling the study of the detected particle rate for any detector individually. The other mode is either put detector 2 over detector 1 in a vertical position or put them beside each other in a horizontal position, as illustrated in Figure 8.4.

A set of lead layers of about 5 mm thick for each were added gradually (one layer every day, sometimes every two days) above the two detectors in both configurations (vertical and horizontal) for each building floor. Figure 8.4 shows the main processes expected with the detected cosmic rays to study the coincidence rates. The coincidence

USC
UNIVERSIDADE
DE SANTIAGO
DE COMPOSTELA

rates mean the two detectors detect two different particles simultaneously for detected particles.

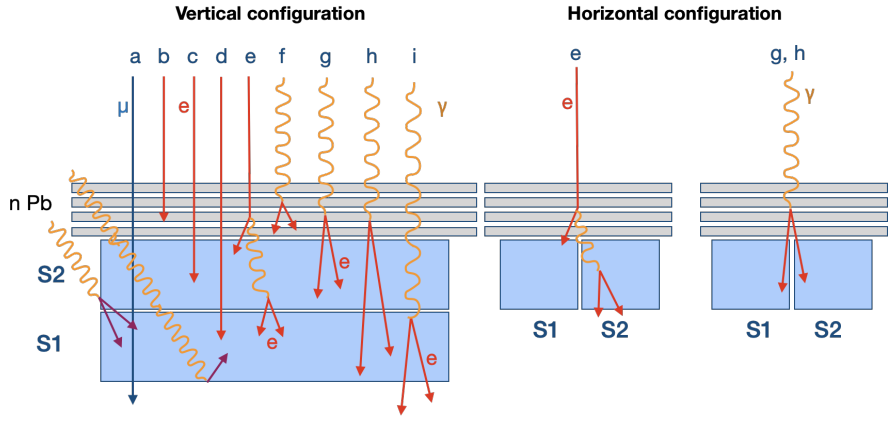

Figure 8.4: Main processes expected with cosmic rays after adding the lead layers gradually with the two configurations for studying the coincidence rate of the cosmic rays. The expected processes depicted in the vertical configuration could take place in the horizontal configuration.

where the expected processes in both configurations are:

a: Muon (coincidence).

b: Low energy electron (absorbed).

c: Medium energy electron (signal in S1).

d: High energy electron (coincidence).

e: High energy electron (coincidence).

f: Low energy gamma (absorbed).

g: Medium energy gamma (signal in S1).

h: High energy gamma (coincidence).

USC UNIVERSIDADE DE SANTIAGO DE COMPOSTELA

i: High energy gamma (some chance of signal in S2).

Visible light will produce when charged particles pass through a scintillator bar (detector). The photodiode converts the light to an electrical charge. Preamplifiers convert this electrical charge collected into a voltage pulse, then translate it into valuable physical data. And then, the data is saved on the SD memory card in an ASCII format file used later in analyzing the data. Table 8.1 shows a sample of saved and ready to analyze data.

Table 8.1: Data sample recorded by a COSMIX detector.

A	B	C	D	E	F	G	H	I	J	K	L	M	N	O	P	Q	R	S
2020	10	21	7	33	14.00	(*)	5324	42.88	-8.54	-999	23.8	97531	0	1	0	0	1	0
2020	10	21	7	33	14.00	(*)	6050	42.88	-8.54	-999	23.7	97533	1	1	0	1	2	0
2020	10	21	7	33	14.00	(*)	6145	42.88	-8.54	-999	23.7	97519	1	1	0	2	3	0
2020	10	21	7	33	15.00	(*)	6403	42.88	-8.54	-999	23.7	97528	0	1	0	2	4	0
2020	10	21	7	33	15.00	(*)	6498	42.88	-8.54	-999	23.7	97539	1	0	0	3	4	0
2020	10	21	7	33	16.00	(*)	7749	42.88	-8.54	-999	23.7	97525	1	1	1	4	5	1
2020	10	21	7	33	16.00	(*)	7943	42.88	-8.54	-999	23.8	97536	0	1	0	4	6	1
2020	10	21	7	33	17.00	(*)	8271	42.88	-8.54	-999	23.7	97531	1	0	0	5	6	1
2020	10	21	7	33	17.00	(*)	8367	42.88	-8.54	-999	23.7	97528	1	1	1	6	7	2
2020	10	21	7	33	18.00	(4)	9265	42.88	-8.54	-999	23.7	97531	1	0	0	7	7	2
2020	10	21	7	33	18.00	(*)	9609	42.88	-8.54	-999	23.7	97528	0	1	0	7	8	2
2020	10	21	7	33	19.00	(*)	10830	42.88	-8.54	-999	23.7	97528	1	1	1	8	9	3
2020	10	21	7	33	20.00	(*)	11418	42.88	-8.54	-999	23.7	97522	0	1	0	8	10	3
2020	10	21	7	33	20.00	(*)	11524	42.88	-8.54	-999	23.7	97536	1	0	0	9	10	3

In the table above, each column represents the following:

A: the year; B: the month; C: the day.

D: the hour; E: the minutes; F: the seconds.

G: the number of GPS satellites used by the detector.

H: the number of milliseconds since powering up the detector.

I: GPS latitude.

USC
UNIVERSIDADE DE SANTIAGO DE COMPOSTELA

J: GPS longitude.

K: GPS altitude (in meters).

L: the temperature (in Celsius).

M: the pressure (in pascals).

N, O and P: "1" if the corresponding counter recorded a hit; "0" otherwise. N corresponds to counter 1; O corresponds to counter 2; P corresponds to the coincidence between counters 1 and 2 (if we read 1 in column P, columns N and O have the same value).

Q, R and S: the cumulative of the three counters. Column Q corresponds to counter 1; column R corresponds to counter 2; column S corresponds to the coincidence between the two counters.

8.6 Data analysis and results

The two configurations in Figure 8.4 were used to study how the coincidence rate varied with a thickness of lead placed above the counters at different altitudes of the floors for the facility of the physics faculty, as previously mentioned. The collected data follow the Poisson distribution. The Poisson distribution shows how many times an event is probable to occur in a certain period (see Figure 8.5). It is, in other words, a count distribution. Especially when we have independent and random events with a vast number and the probability for each event is small and constant. Moreover, the detection time for the events is short compared with the half-life of the detected particles, especially for muons.

TimTrack algorithm explained in chapter 3 was used to analyze the data of the COSMIX detector. Several advantages are provided by using the TimTrack algorithm. First, it provides the best fit for the data distribution. The other advantage is that it forces the data to behave as an exponential distribution, which helps solve the dead time problem

USC UNIVERSIDADE DE SANTIAGO DE COMPOSTELA

for the detector (see the Appendix) without affecting the fit. Furthermore, the TimTrack algorithm allows us to choose the best fit of the data distribution according to the highest probability or the lowest uncertainty of the slope where all the analysis for the gathered data was done.

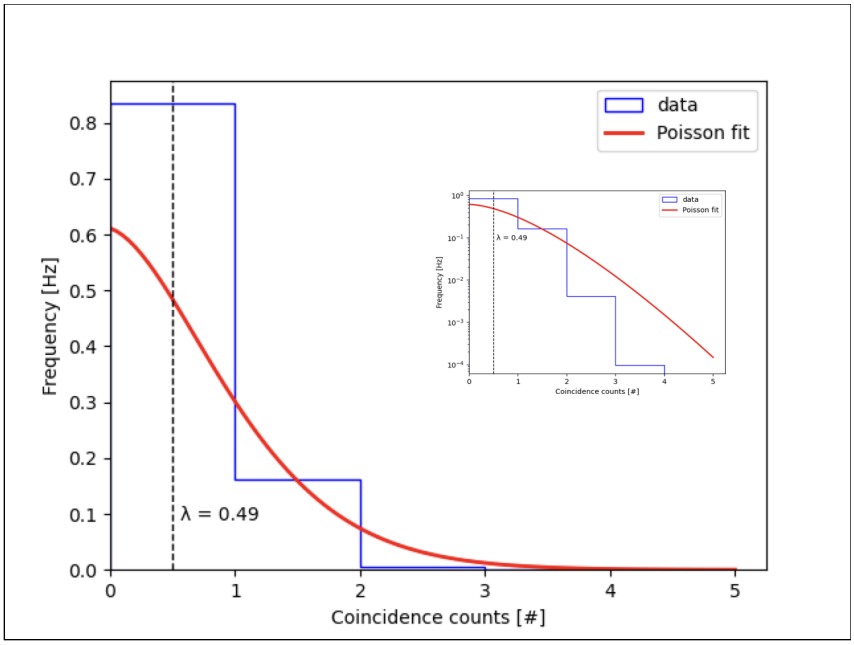

Figure 8.5: An example of a Poisson distribution of the histogram for the coincidence counts per second detected by the COSMIX detector. The y-axis for the inserted plot is in the logarithmic scale.

Figure 8.6 (left) shows an example of the TimTrack algorithm's fit for the detected rate (in logarithm scale) versus the time difference between two successive events without using lead layers and the histogram (right) for the time difference between the coincidence event and the next one, is also shown in the figure. The absolute value of the slope represents the detected rate of the detector.

USC
UNIVERSIDADE DE SANTIAGO DE COMPOSTELA

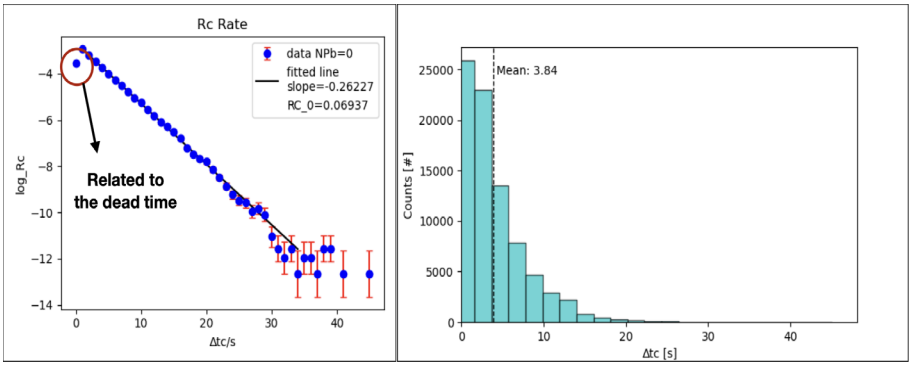

Figure 8.6: The distribution fit using the TimTrack algorithm (left) to find the coincidence rate for the COSMIX detector without using any absorbers. The best fit corresponded to the lowest uncertainty for the slope of the fit. The histogram of the time difference between the coincidence event and the next event (right).

The mean value for the histogram in Figure 8.6 (right) was calculated, representing the time needed to obtain one coincidence event, which means the coincidence rate of the detector equals $1/3.84\ s = 0.260\ (Hz)$. As we can see, the coincidence rate of the detector is compatible with the absolute value of the slope that we got by using the TimTrack algorithm.

The following figures as an example illustrate the results of the COSMIX detector at a certain altitude with different thicknesses of a lead layer placed over the two detectors in the vertical position.

USC
UNIVERSIDADE DE SANTIAGO DE COMPOSTELA

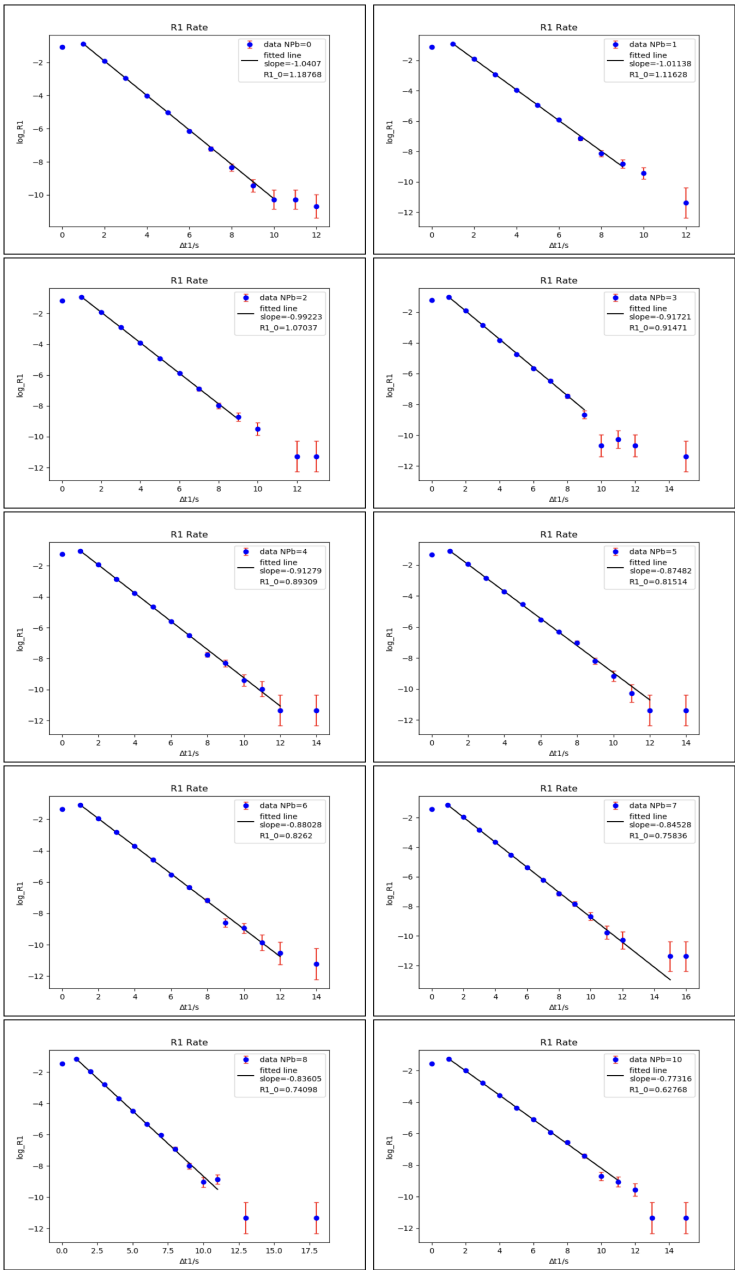

Figure 8.7: The distribution fit for the rate of detector 1 with different thicknesses of a lead layer in the vertical position.

USC
UNIVERSIDADE
DE SANTIAGO
DE COMPOSTELA

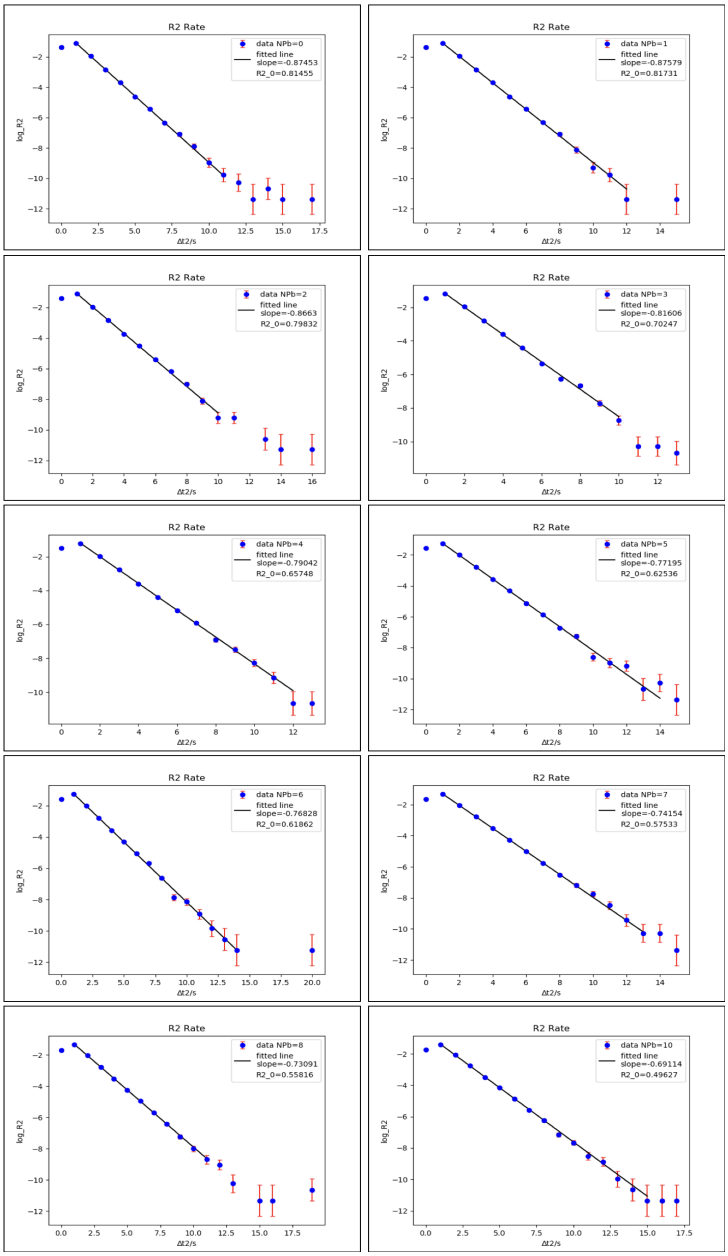

Figure 8.8: The distribution fit for the rate of detector 2 with different thicknesses of a lead layer in the vertical position.

USC
UNIVERSIDADE DE SANTIAGO DE COMPOSTELA

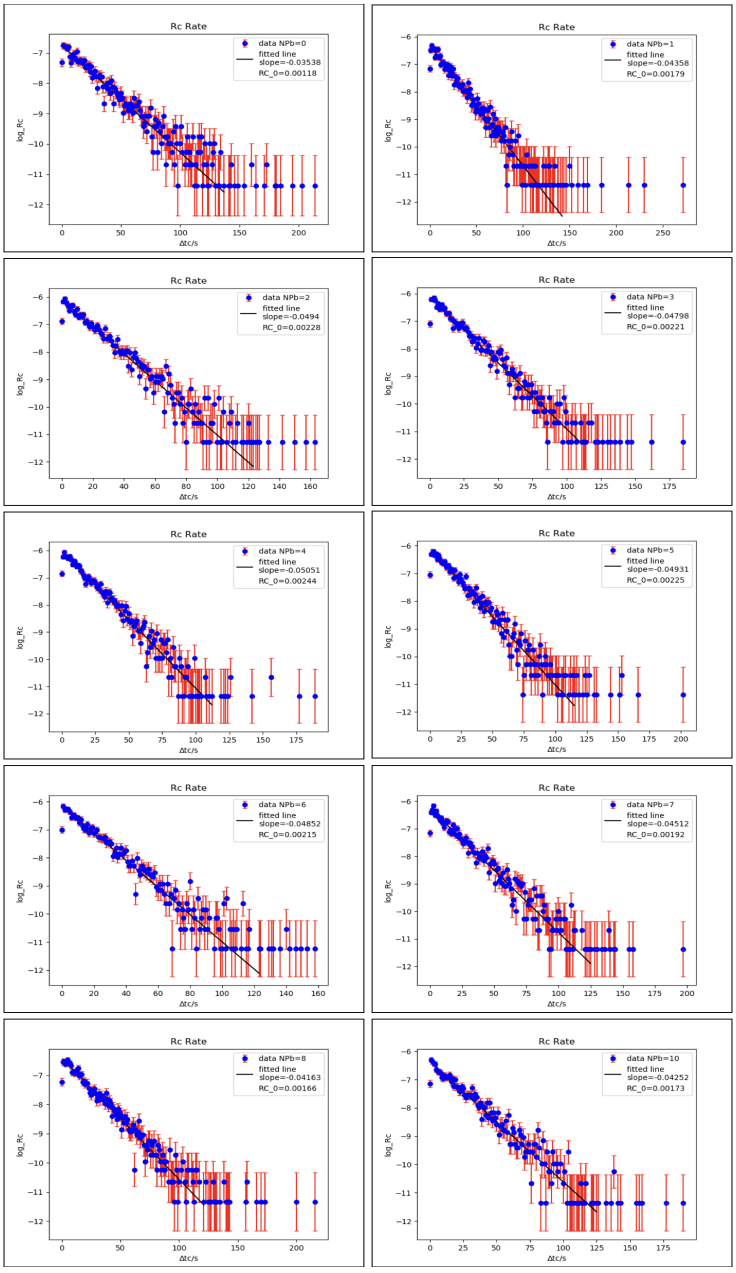

Figure 8.9: The distribution fit of the coincidence rate for the COSMIX detector with different thicknesses of a lead layer in the vertical position.

USC
UNIVERSIDADE
DE SANTIAGO
DE COMPOSTELA

Notes that in Figure 8.9 how the uncertainty (error bars) affects the fit slope, which is referred to as the detected particle rate. That's why we choose the best fit of the data distribution according to the lowest uncertainty of the fit slope.

Below we show the results obtained using the COSMIX detector in the horizontal configuration at all the levels using different thicknesses of lead layers added gradually on the top of both detectors. The normalized rate according to the corresponding rate without using any absorber for detector 1, detector 2 and coincidence rate, respectively, are shown in the following figures.

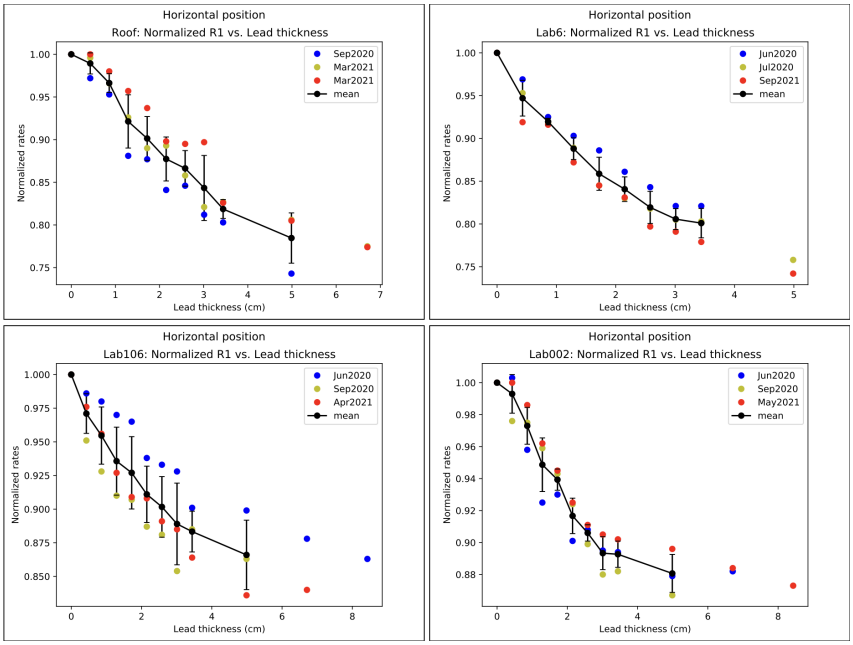

Figure 8.10: The normalized rate of detector 1 obtained by the horizontal position versus the lead thickness at all the altitudes in the physics faculty.

USC
UNIVERSIDADE DE SANTIAGO DE COMPOSTELA

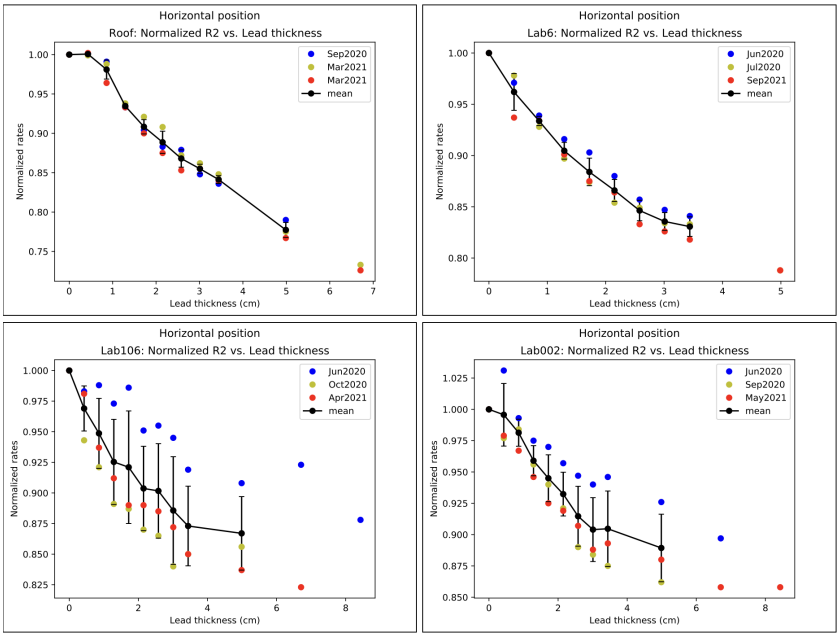

Figure 8.11: The normalized rate of detector 2 versus the lead thickness at all the levels obtained by the horizontal position.

USC
UNIVERSIDADE DE SANTIAGO DE COMPOSTELA

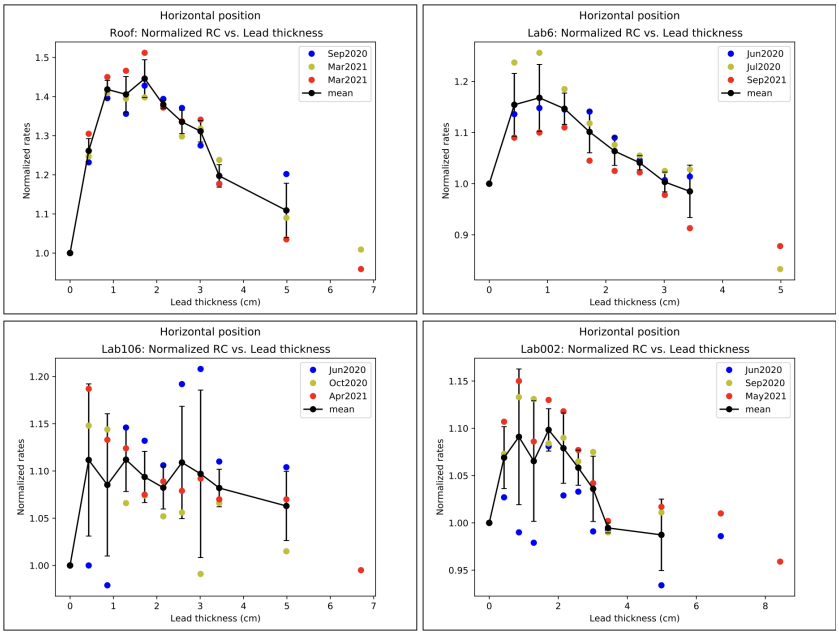

Figure 8.12: The normalized coincidence rate of the COSMIX detector where detector 2 placed over detector 1 versus the lead thickness obtained in the horizontal position at different floors of the physics faculty.

In the same manner, the following figures illustrate the results of the COSMIX detector obtained in the vertical configuration at different floors in the physics faculty using different thicknesses of lead layers added gradually over both detectors.

USC
UNIVERSIDADE DE SANTIAGO DE COMPOSTELA

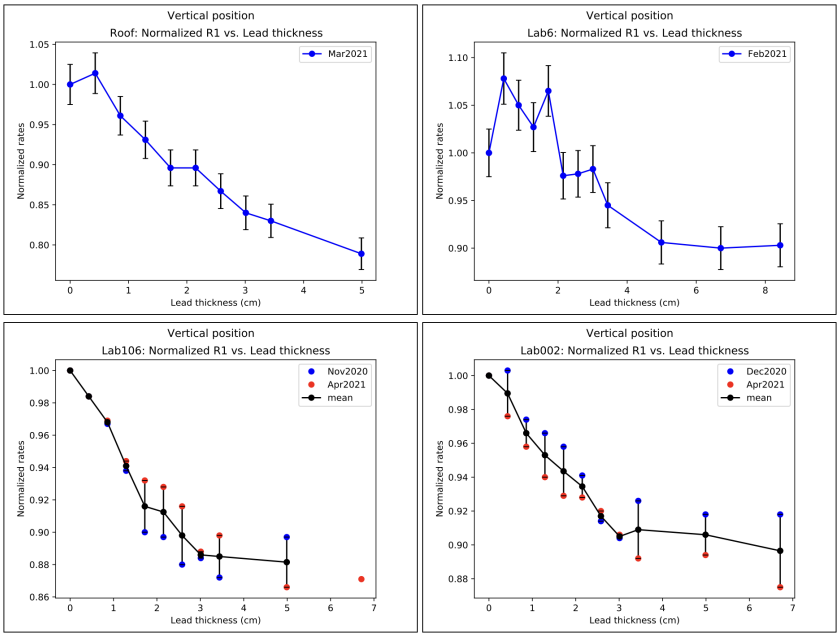

Figure 8.13: The normalized rate of detector 1 versus the lead thickness at all the levels obtained by the vertical position.

USC
UNIVERSIDADE DE SANTIAGO DE COMPOSTELA

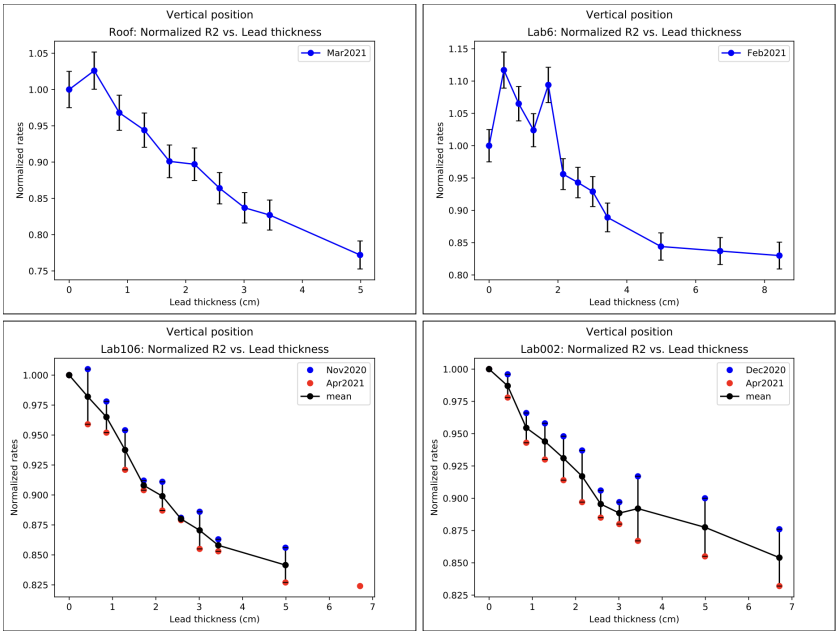

Figure 8.14: The normalized rate of detector 2 obtained by the vertical position versus the lead thickness at all the altitudes in the physics faculty.

USC
UNIVERSIDADE DE SANTIAGO DE COMPOSTELA

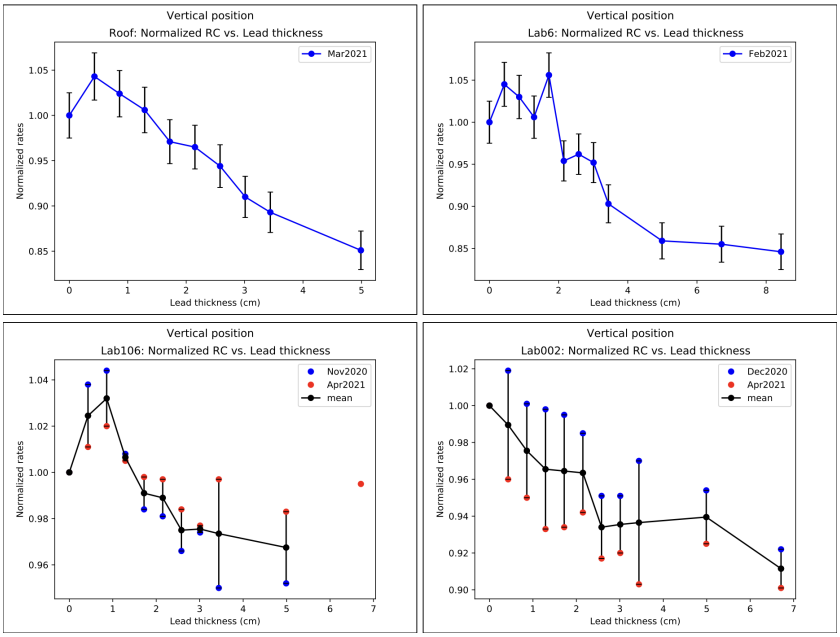

Figure 8.15: The normalized coincidence rate of the COSMIX detector where detector 2 placed over detector one versus the lead thickness obtained in the vertical position at different floors of the physics faculty.

Figure 8.16 illustrates the results of all the data collected in horizontal and vertical configurations at different altitudes of the physics building using different thicknesses of the lead layers for the rate of detector 1, the rate of detector 2 and the coincidence rate for the COSMIX detector.

Furthermore, the following Tables present a summary for all the data results of the COSMIX detector in both configurations, horizontal and vertical, at different altitudes using various thicknesses of the lead layers for the rate of detector 1, the rate of detector 2 and the coincidence rate.

USC
UNIVERSIDADE DE SANTIAGO DE COMPOSTELA

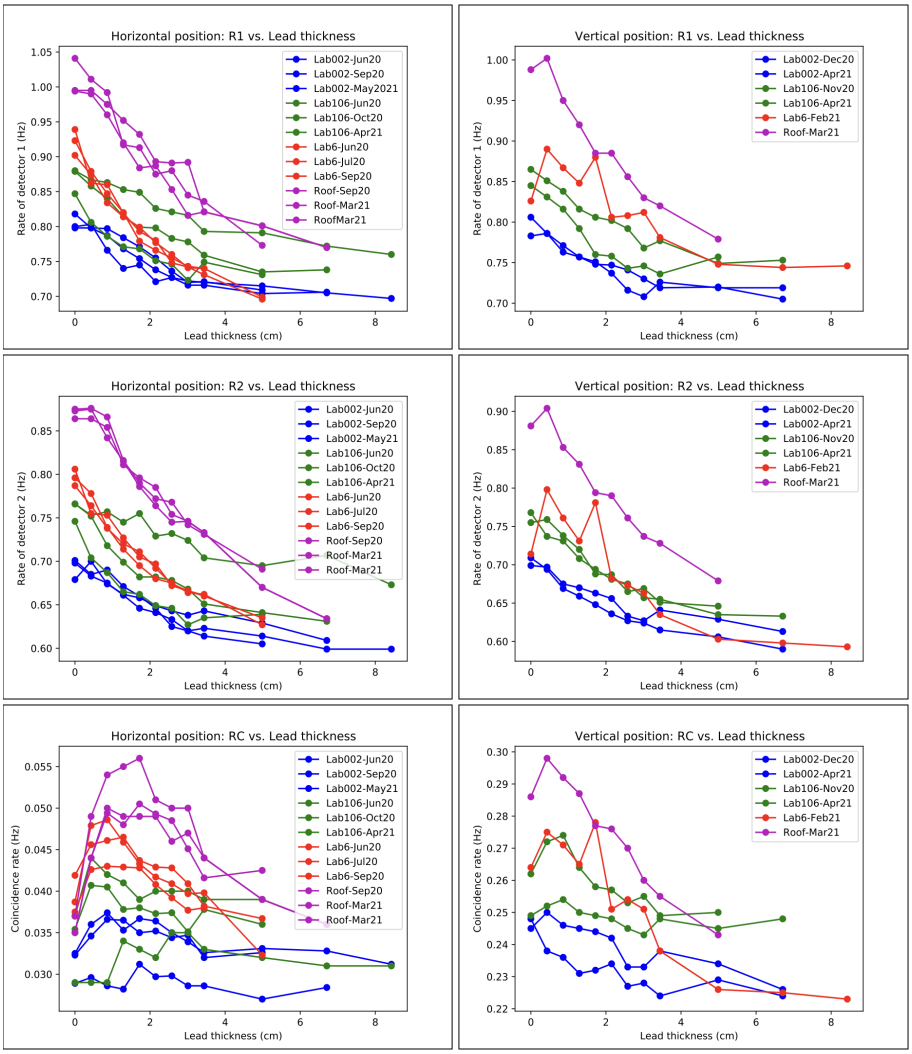

Figure 8.16: A summary of the results for all the gathered data in both positions at different levels using different thicknesses of the lead layers for the rate of detector 1, the rate of detector 2 and the coincidence rate of the COSMIX detector.

USC
UNIVERSIDADE DE SANTIAGO DE COMPOSTELA

Table 8.2: Represents a summary for all the results of the data in the horizontal configuration at different floors heights of the physics building using various thicknesses of the lead layers for the average rate of detector 1, the average rate of detector 2 and the average coincidence rate of the COSMIX detector.

	Horizontal configuration											
	Rate 1 (Hz)				Rate 2 (Hz)				Coincidence rate (Hz)			
xPb (cm)	Lab002	Lab106	Lab6	Roof	Lab002	Lab106	Lab6	Roof	Lab002	Lab106	Lab6	Roof
0	0.81 ± 0.01	0.87 ± 0.02	0.92 ± 0.02	1.01 ± 0.02	0.69 ± 0.01	0.76 ± 0.01	0.80 ± 0.01	0.87 ± 0.005	0.031 ± 0.002	0.034 ± 0.003	0.039 ± 0.002	0.036 ± 0.001
0.43	0.80 ± 0.002	0.84 ± 0.03	0.87 ± 0.01	1.0 ± 0.01	0.69 ± 0.01	0.74 ± 0.02	0.77 ± 0.01	0.87 ± 0.005	0.033 ± 0.003	0.038 ± 0.006	0.045 ± 0.002	0.046 ± 0.002
0.86	0.78 ± 0.01	0.83 ± 0.03	0.85 ± 0.01	0.98 ± 0.01	0.68 ± 0.01	0.72 ± 0.03	0.74 ± 0.01	0.85 ± 0.01	0.034 ± 0.004	0.037 ± 0.006	0.046 ± 0.002	0.051 ± 0.002
1.29	0.76 ± 0.02	0.81 ± 0.03	0.82 ± 0.002	0.93 ± 0.02	0.66 ± 0.004	0.70 ± 0.03	0.72 ± 0.01	0.81 ± 0.002	0.033 ± 0.004	0.038 ± 0.003	0.045 ± 0.002	0.051 ± 0.003
1.72	0.76 ± 0.01	0.81 ± 0.03	0.79 ± 0.01	0.91 ± 0.02	0.65 ± 0.01	0.70 ± 0.04	0.70 ± 0.01	0.79 ± 0.004	0.034 ± 0.002	0.037 ± 0.003	0.043 ± 0.0	0.052 ± 0.003
2.15	0.74 ± 0.01	0.79 ± 0.03	0.77 ± 0.01	0.89 ± 0.01	0.65 ± 0.003	0.69 ± 0.03	0.69 ± 0.01	0.77 ± 0.01	0.034 ± 0.003	0.036 ± 0.003	0.042 ± 0.001	0.05 ± 0.001
2.58	0.73 ± 0.004	0.78 ± 0.03	0.75 ± 0.004	0.87 ± 0.02	0.63 ± 0.01	0.69 ± 0.04	0.67 ± 0.001	0.75 ± 0.01	0.033 ± 0.002	0.037 ± 0.002	0.041 ± 0.001	0.048 ± 0.002
3.01	0.72 ± 0.002	0.77 ± 0.04	0.74 ± 0.001	0.85 ± 0.03	0.63 ± 0.01	0.67 ± 0.04	0.67 ± 0.001	0.74 ± 0.002	0.032 ± 0.003	0.037 ± 0.002	0.039 ± 0.001	0.047 ± 0.002
3.44	0.72 ± 0.002	0.77 ± 0.02	0.74 ± 0.004	0.83 ± 0.01	0.63 ± 0.01	0.66 ± 0.03	0.66 ± 0.001	0.73 ± 0.001	0.031 ± 0.002	0.037 ± 0.003	0.039 ± 0.001	0.043 ± 0.001
4.99	0.71 ± 0.004	0.75 ± 0.03	–	0.79 ± 0.01	0.62 ± 0.01	0.66 ± 0.03	–	0.68 ± 0.01	0.031 ± 0.003	0.036 ± 0.003	–	0.04 ± 0.002

USC
UNIVERSIDADE DE SANTIAGO DE COMPOSTELA

Table 8.3: summarizes all the data results in vertical configuration at different floors heights of the physics building using different thicknesses of the lead layers for the average rate of detector 1, the average rate of detector 2 and the average coincidence rate of the COSMIX detector.

	Vertical configuration											
	Rate 1 (Hz)				Rate 2 (Hz)				Coincidence rate (Hz)			
xPb (cm)	Lab002	Lab106	Lab6	Roof	Lab002	Lab106	Lab6	Roof	Lab002	Lab106	Lab6	Roof
0	0.79 ± 0.01	0.86 ± 0.01	0.83 ± 0.021	0.99 ± 0.025	0.70 ± 0.01	0.76 ± 0.01	0.71 ± 0.018	0.88 ± 0.022	0.247 ± 0.002	0.256 ± 0.01	0.264 ± 0.01	0.286 ± 0.01
0.43	0.79 ± 0.0	0.84 ± 0.01	0.89 ± 0.022	1.0 ± 0.025	0.70 ± 0.002	0.75 ± 0.01	0.80 ± 0.02	0.90 ± 0.023	0.244 ± 0.006	0.262 ± 0.01	0.275 ± 0.01	0.298 ± 0.01
0.86	0.77 ± 0.004	0.83 ± 0.01	0.87 ± 0.02	0.95 ± 0.024	0.67 ± 0.003	0.73 ± 0.004	0.76 ± 0.019	0.85 ± 0.021	0.241 ± 0.005	0.264 ± 0.01	0.271 ± 0.01	0.292 ± 0.01
1.29	0.76 ± 0.0	0.80 ± 0.01	0.85 ± 0.021	0.92 ± 0.023	0.66 ± 0.01	0.71 ± 0.01	0.73 ± 0.018	0.83 ± 0.021	0.238 ± 0.01	0.257 ± 0.01	0.265 ± 0.01	0.287 ± 0.01
1.72	0.75 ± 0.002	0.78 ± 0.02	0.88 ± 0.022	0.86 ± 0.022	0.66 ± 0.01	0.69 ± 0.003	0.78 ± 0.02	0.79 ± 0.02	0.238 ± 0.01	0.254 ± 0.005	0.278 ± 0.01	0.277 ± 0.01
2.15	0.74 ± 0.01	0.78 ± 0.02	0.81 ± 0.02	0.89 ± 0.022	0.65 ± 0.01	0.68 ± 0.003	0.68 ± 0.017	0.79 ± 0.02	0.238 ± 0.004	0.253 ± 0.005	0.251 ± 0.01	0.276 ± 0.01
2.58	0.73 ± 0.01	0.77 ± 0.02	0.81 ± 0.02	0.86 ± 0.021	0.63 ± 0.003	0.67 ± 0.01	0.67 ± 0.017	0.76 ± 0.019	0.23 ± 0.003	0.249 ± 0.004	0.254 ± 0.01	0.27 ± 0.01
3.01	0.72 ± 0.01	0.76 ± 0.01	0.81 ± 0.02	0.83 ± 0.021	0.63 ± 0.002	0.66 ± 0.01	0.66 ± 0.017	0.74 ± 0.018	0.231 ± 0.003	0.249 ± 0.01	0.251 ± 0.01	0.26 ± 0.01
3.44	0.72 ± 0.004	0.76 ± 0.02	0.78 ± 0.02	0.82 ± 0.021	0.63 ± 0.01	0.65 ± 0.002	0.64 ± 0.016	0.73 ± 0.018	0.231 ± 0.01	0.249 ± 0.001	0.238 ± 0.01	0.255 ± 0.01
4.99	0.72 ± 0.001	0.75 ± 0.004	0.75 ± 0.019	0.78 ± 0.0195	0.62 ± 0.01	0.64 ± 0.01	0.60 ± 0.015	0.68 ± 0.017	0.232 ± 0.003	0.248 ± 0.003	0.226 ± 0.01	0.243 ± 0.01
6.71	0.71 ± 0.01	–	0.74 ± 0.019	–	0.60 ± 0.01	–	0.60 ± 0.015	–	0.225 ± 0.001	–	0.225 ± 0.01	–
8.43	–	–	0.75 ± 0.019	–	–	–	0.59 ± 0.015	–	–	–	0.223 ± 0.01	–

Figure 8.17 depicts a summary of the coincidence rates for the gathered data of the COSMIX detector at all the floors utilizing different thicknesses of the lead layers.

Table 8.4, Table 8.5 and Figure 8.18 illustrate a summary for all the data results in horizontal configuration and vertical configuration at various altitudes of the physics building using different thicknesses of the lead layers for the normalized rate of detector 1, the normalized rate of detector 2 and the normalized coincidence rate of the COSMIX detector.

USC UNIVERSIDADE DE SANTIAGO DE COMPOSTELA

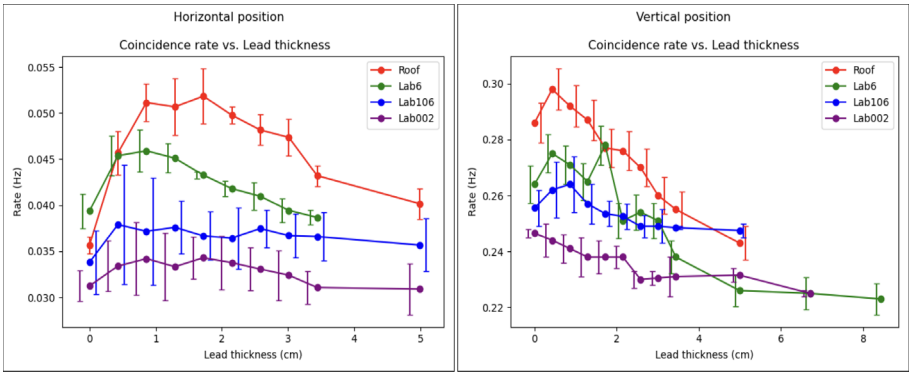

Figure 8.17: A comparison between the average coincidence rates for the COSMIX detector with both configurations for all the collected data.

Table 8.4: A summary of all the data results in horizontal configuration at different floors heights of the physics building using different thicknesses of the lead layers for the normalized average rate of detector 1, the normalized average rate of detector 2 and the normalized average coincidence rate of the COSMIX detector.

	Horizontal configuration											
	Normalized rate (R1)				Normalized rate (R2)				Normalized rate (RC)			
xPb (cm)	Lab002	Lab106	Lab6	Roof	Lab002	Lab106	Lab6	Roof	Lab002	Lab106	Lab6	Roof
0	1	1	1	1	1	1	1	1	1	1	1	1
0.43	0.99 ± 0.01	0.97 ± 0.01	0.95 ± 0.02	0.99 ± 0.01	1 ± 0.02	0.97 ± 0.02	0.96 ± 0.02	1 ± 0.0	1.07 ± 0.03	1.11 ± 0.08	1.15 ± 0.06	1.26 ± 0.03
0.86	0.97 ± 0.01	0.95 ± 0.02	0.92 ± 0.0	0.97 ± 0.01	0.98 ± 0.01	0.95 ± 0.03	0.93 ± 0.0	0.98 ± 0.01	1.09 ± 0.07	1.09 ± 0.08	1.17 ± 0.07	1.42 ± 0.02
1.29	0.95 ± 0.02	0.94 ± 0.03	0.89 ± 0.01	0.92 ± 0.03	0.96 ± 0.01	0.93 ± 0.03	0.90 ± 0.01	0.93 ± 0.0	1.07 ± 0.06	1.11 ± 0.03	1.15 ± 0.03	1.41 ± 0.05
1.72	0.94 ± 0.01	0.93 ± 0.03	0.86 ± 0.02	0.90 ± 0.03	0.95 ± 0.02	0.92 ± 0.05	0.88 ± 0.01	0.91 ± 0.01	1.10 ± 0.02	1.09 ± 0.03	1.10 ± 0.04	1.45 ± 0.05
2.15	0.92 ± 0.01	0.91 ± 0.02	0.84 ± 0.01	0.88 ± 0.03	0.93 ± 0.02	0.90 ± 0.03	0.87 ± 0.01	0.89 ± 0.01	1.08 ± 0.04	1.08 ± 0.02	1.06 ± 0.03	1.38 ± 0.01
2.58	0.91 ± 0.01	0.90 ± 0.02	0.82 ± 0.02	0.87 ± 0.02	0.91 ± 0.02	0.90 ± 0.04	0.85 ± 0.01	0.87 ± 0.01	1.06 ± 0.02	1.11 ± 0.06	1.04 ± 0.01	1.34 ± 0.03
3.01	0.89 ± 0.01	0.89 ± 0.03	0.81 ± 0.0	0.84 ± 0.04	0.90 ± 0.03	0.89 ± 0.04	0.84 ± 0.01	0.86 ± 0.01	1.04 ± 0.03	1.10 ± 0.09	1 ± 0.02	1.31 ± 0.03
3.44	0.89 ± 0.01	0.88 ± 0.02	0.80 ± 0.02	0.82 ± 0.01	0.90 ± 0.03	0.87 ± 0.03	0.83 ± 0.01	0.84 ± 0.0	0.99 ± 0.01	1.08 ± 0.02	0.99 ± 0.05	1.20 ± 0.03
4.99	0.88 ± 0.01	0.87 ± 0.03	–	0.78 ± 0.03	0.89 ± 0.03	0.87 ± 0.03	–	0.78 ± 0.01	0.99 ± 0.04	1.06 ± 0.04	–	1.11 ± 0.07

USC
UNIVERSIDADE DE SANTIAGO DE COMPOSTELA

Table 8.5: A summary for all the results of the data in vertical configuration at different floors heights of the physics building using various thicknesses of the lead layers for the normalized average rate of detector 1, the normalized average rate of detector 2 and the normalized average coincidence rate of the COSMIX detector.

	Vertical configuration											
	Normalized rate (R1)				Normalized rate (R2)				Normalized rate (RC)			
xPb (cm)	Lab002	Lab106	Lab6	Roof	Lab002	Lab106	Lab6	Roof	Lab002	Lab106	Lab6	Roof
0	1	1	1	1	1	1	1	1	1	1	1	1
0.43	0.99 ± 0.01	0.98 ± 0.0	1.08 ± 0.03	1.01 ± 0.03	0.99 ± 0.01	0.98 ± 0.02	1.12 ± 0.03	1.03 ± 0.03	0.99 ± 0.03	1.02 ± 0.01	1.05 ± 0.03	1.04 ± 0.03
0.86	0.97 ± 0.01	0.97 ± 0.0	1.05 ± 0.03	0.96 ± 0.03	0.95 ± 0.01	0.97 ± 0.01	1.07 ± 0.03	0.97 ± 0.03	0.98 ± 0.03	1.03 ± 0.01	1.03 ± 0.03	1.02 ± 0.03
1.29	0.95 ± 0.01	0.94 ± 0.0	1.03 ± 0.03	0.93 ± 0.03	0.94 ± 0.01	0.94 ± 0.02	1.02 ± 0.03	0.94 ± 0.03	0.97 ± 0.03	1.01 ± 0.0	1.01 ± 0.03	1.01 ± 0.03
1.72	0.94 ± 0.01	0.92 ± 0.02	1.07 ± 0.03	0.90 ± 0.03	0.93 ± 0.02	0.91 ± 0.0	1.09 ± 0.03	0.90 ± 0.03	0.96 ± 0.03	0.99 ± 0.01	1.06 ± 0.03	0.97 ± 0.03
2.15	0.93 ± 0.01	0.91 ± 0.02	0.98 ± 0.03	0.90 ± 0.03	0.92 ± 0.02	0.90 ± 0.01	0.96 ± 0.03	0.90 ± 0.03	0.96 ± 0.02	0.99 ± 0.01	0.95 ± 0.03	0.97 ± 0.03
2.58	0.92 ± 0.0	0.90 ± 0.02	0.98 ± 0.03	0.87 ± 0.03	0.90 ± 0.01	0.88 ± 0.0	0.94 ± 0.03	0.86 ± 0.03	0.93 ± 0.02	0.98 ± 0.01	0.96 ± 0.03	0.94 ± 0.03
3.01	0.91 ± 0.0	0.89 ± 0.0	0.98 ± 0.03	0.84 ± 0.03	0.89 ± 0.01	0.87 ± 0.02	0.93 ± 0.03	0.84 ± 0.03	0.94 ± 0.02	0.98 ± 0.0	0.95 ± 0.03	0.91 ± 0.03
3.44	0.91 ± 0.02	0.89 ± 0.01	0.95 ± 0.03	0.83 ± 0.03	0.89 ± 0.03	0.86 ± 0.01	0.89 ± 0.03	0.83 ± 0.03	0.94 ± 0.03	0.97 ± 0.02	0.90 ± 0.03	0.89 ± 0.03
4.99	0.91 ± 0.01	0.88 ± 0.02	0.91 ± 0.03	0.79 ± 0.03	0.88 ± 0.02	0.84 ± 0.01	0.84 ± 0.03	0.77 ± 0.03	0.94 ± 0.01	0.97 ± 0.02	0.86 ± 0.03	0.85 ± 0.03
6.71	0.90 ± 0.02	–	0.90 ± 0.03	–	0.85 ± 0.02	–	0.84 ± 0.03	–	0.91 ± 0.01	–	0.86 ± 0.03	–
8.43	–	–	0.90 ± 0.03	–	–	–	0.83 ± 0.03	–	–	–	0.85 ± 0.03	–

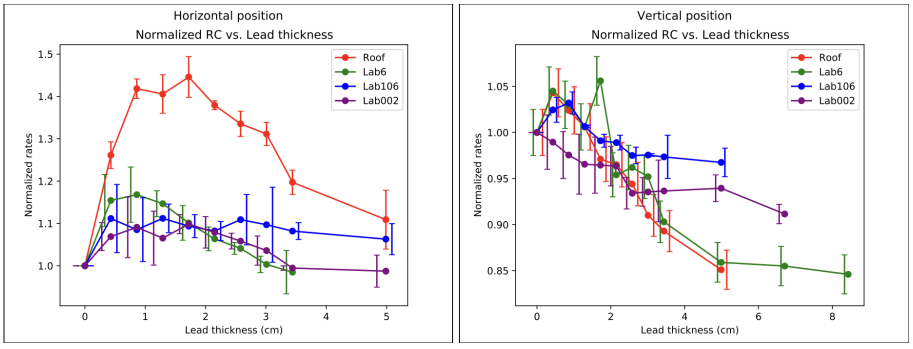

Figure 8.18: A comparison between the normalized coincidence rates for the COSMIX detector with the horizontal and vertical configuration for all the collected data.

USC UNIVERSIDADE DE SANTIAGO DE COMPOSTELA

The results were as our expectations. The highest value of the rate of coincidence was in the roof where the highest altitude and the value of the coincidence rate decreased with the decrease in the altitude and the lowest value of the coincidence rate was found at the ground level (Lab002), as shown in Figures 8.17 and 8.18. Whereas in the vertical configuration, there are fluctuations in the detector especially, in Lab6 and Lab106, which could be due to the instability of the background because many laboratories with a lot of electronic devices surround the laboratory and that might have an influence on the detector in that period.

Even though the fluctuations occurred in the detector, we could still see how the coincidence rate differed depending on the lead thickness placed above the counters. The coincidence rate increased continuously with lead thickness, peaking between 1 and 2 cm before dropping to roughly 75% of the peak value as lead thickness increased to around 5 cm.

The quick drop-off in the coincidence rate beyond the shower curve's peak revealed that the particles responsible for creating the groups of particles were not the same as those capable of easily penetrating 1 cm of lead.

8.7 Estimation of electron energy distribution in physics faculty at USC

This section focuses on the rates measured for detector S1 and detector S2 in vertical and horizontal configurations. First of all, we have estimated the average values of all the measurements done with both detectors with the associated uncertainties. The results are shown in Tables 8.6 and 8.7. They show the rates measured in both scintillators after subtracting the rate measured with a Pb brick 5 cm wide, assuming that thickness was enough to stop all the electromagnetic components; we assume that the decrease of the muon component is negligible. We may also assume that the electromagnetic component is dominated by the electrons, both positive and negative. We observe that

USC
UNIVERSIDADE
DE SANTIAGO
DE COMPOSTELA

the data obtained by both detectors are almost similar. Table 8.8 shows the result of the analysis we have done comparing the compatibility of both detectors. Finally, Table 8.9 shows the results of merging the data of both detectors providing a single sample with lower statistical errors.

Table 8.6: Shows the electromagnetic rates measured for detector S1 after subtracting the rate measured with a brick of lead 5 cm wide.

Electromagnetic rates for detector 1 with uncertainties									
NPb	xPb $[cm]$	$Roof_{ave}$ $[Hz]$	$Roof_{std}$ $[Hz]$	$L6_{ave}$ $[Hz]$	$L6_{std}$ $[Hz]$	$L106_{ave}$ $[Hz]$	$L106_{std}$ $[Hz]$	$L002_{ave}$ $[Hz]$	$L002_{std}$ $[Hz]$
0	0.00	0.22	0.03	0.18	0.07	0.11	0.03	0.09	0.01
1	0.43	0.21	0.02	0.16	0.03	0.09	0.03	0.08	0.01
2	0.86	0.18	0.02	0.14	0.03	0.08	0.04	0.06	0.02
3	1.29	0.14	0.02	0.11	0.03	0.06	0.04	0.05	0.02
4	1.72	0.11	0.03	0.10	0.06	0.04	0.04	0.04	0.01
5	2.15	0.10	0.02	0.07	0.04	0.03	0.04	0.03	0.01
6	2.58	0.08	0.02	0.06	0.04	0.02	0.04	0.02	0.01
7	3.01	0.06	0.04	0.05	0.05	0.01	0.04	0.01	0.01
8	3.44	0.04	0.02	0.04	0.04	0.01	0.03	0.01	0.01
Brick	5.00	0.00	0.02	0.00	0.04	0.00	0.03	0.00	0.01

USC UNIVERSIDADE DE SANTIAGO DE COMPOSTELA

Table 8.7: Displays the electromagnetic rates measured for detector S2 after subtracting the rate measured with a brick of lead 5 cm wide.

Electromagnetic rates for detector 2 with uncertainties									
NPb	xPb $[cm]$	$Roof_{ave}$ $[Hz]$	$Roof_{std}$ $[Hz]$	$L6_{ave}$ $[Hz]$	$L6_{std}$ $[Hz]$	$L106_{ave}$ $[Hz]$	$L106_{std}$ $[Hz]$	$L002_{ave}$ $[Hz]$	$L002_{std}$ $[Hz]$
0	0.00	0.20	0.02	0.15	0.06	0.11	0.03	0.08	0.01
1	0.43	0.20	0.02	0.16	0.04	0.09	0.03	0.08	0.01
2	0.86	0.18	0.02	0.13	0.03	0.07	0.04	0.06	0.01
3	1.29	0.14	0.02	0.10	0.03	0.06	0.04	0.05	0.01
4	1.72	0.11	0.02	0.11	0.06	0.05	0.04	0.04	0.01
5	2.15	0.10	0.02	0.06	0.03	0.03	0.04	0.03	0.01
6	2.58	0.08	0.02	0.05	0.03	0.03	0.04	0.02	0.01
7	3.01	0.07	0.02	0.04	0.03	0.02	0.04	0.01	0.01
8	3.44	0.05	0.01	0.03	0.03	0.01	0.04	0.01	0.02
Brick	5.00	0.00	0.02	0.00	0.03	0.00	0.03	0.00	0.01

Table 8.8: Presents the analysis results comparing the compatibility of both detectors.

Compatibility analysis of the rates for detectors 1 and 2 with uncertainties									
NPb	xPb $[cm]$	$Roof_{ave}$ $[Hz]$	$Roof_{std}$ $[Hz]$	$L6_{ave}$ $[Hz]$	$L6_{std}$ $[Hz]$	$L106_{ave}$ $[Hz]$	$L106_{std}$ $[Hz]$	$L002_{ave}$ $[Hz]$	$L002_{std}$ $[Hz]$
0	0.00	0.200	0.033	0.031	0.089	0.001	0.039	0.007	0.019
1	0.43	0.009	0.028	0.008	0.048	0.001	0.047	0.006	0.014
2	0.86	0.005	0.030	0.014	0.044	0.001	0.052	0.004	0.019
3	1.29	-0.002	0.028	0.012	0.045	0.001	0.054	0.000	0.019
4	1.72	0.001	0.032	-0.003	0.083	-0.001	0.060	0.002	0.016
5	2.15	-0.004	0.025	0.005	0.047	0.000	0.054	-0.003	0.017
6	2.58	0.002	0.030	0.004	0.053	-0.003	0.057	0.000	0.015
7	3.01	-0.008	0.039	0.009	0.058	-0.004	0.060	-0.003	0.015
8	3.44	-0.018	0.022	0.006	0.051	0.002	0.048	-0.004	0.017
Brick	5.00	0.000	0.027	0.000	0.053	0.000	0.048	0.000	0.017

USC
UNIVERSIDADE DE SANTIAGO DE COMPOSTELA

Table 8.9: Shows the results of combining the data of both detectors, giving in a single sample with lower statistical errors.

The weighted average of the rates for detectors 1 and 2 with uncertainties									
NPb	xPb $[cm]$	$Roof_{ave}$ $[Hz]$	$Roof_{std}$ $[Hz]$	$L6_{ave}$ $[Hz]$	$L6_{std}$ $[Hz]$	$L106_{ave}$ $[Hz]$	$L106_{std}$ $[Hz]$	$L002_{ave}$ $[Hz]$	$L002_{std}$ $[Hz]$
0	0.00	0.20	0.01	0.16	0.04	0.11	0.02	0.08	0.01
1	0.43	0.21	0.01	0.16	0.02	0.09	0.02	0.08	0.01
2	0.86	0.18	0.01	0.14	0.02	0.08	0.03	0.06	0.01
3	1.29	0.14	0.01	0.11	0.02	0.06	0.03	0.05	0.01
4	1.72	0.11	0.01	0.10	0.04	0.04	0.03	0.04	0.01
5	2.15	0.10	0.01	0.07	0.02	0.03	0.03	0.03	0.01
6	2.58	0.08	0.01	0.05	0.02	0.03	0.03	0.02	0.01
7	3.01	0.06	0.01	0.04	0.03	0.02	0.03	0.01	0.01
8	3.44	0.05	0.01	0.03	0.03	0.01	0.02	0.01	0.01
Brick	5.00	0.00	0.01	0.00	0.03	0.00	0.02	0.00	0.01

Figure 8.19 shows the attenuation of the measured electromagnetic component in the lead layers using the rates of both scintillators as a function of the lead thickness together with the weighted average.

USC UNIVERSIDADE DE SANTIAGO DE COMPOSTELA

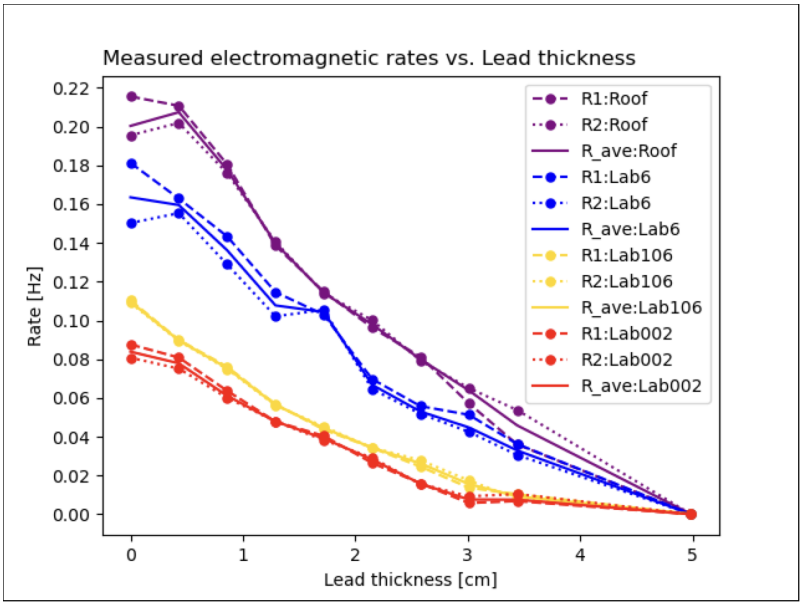

Figure 8.19: Represents the attenuation of electrons in the lead using the rate of detector one and detector two as a function of the lead thickness.

As passing through a given thickness of matter, electrons need minimum energy and we also considered it of interest to analyze the measured attenuation of electrons as a function of the energy threshold that electrons need to overcome a given lead thickness. Figure 8.20 shows the range of electrons in the lead adapted from the reference [108]. The figure also shows the energy thresholds corresponding to different numbers of the lead plates we used in our measurements.

USC
UNIVERSIDADE DE SANTIAGO DE COMPOSTELA

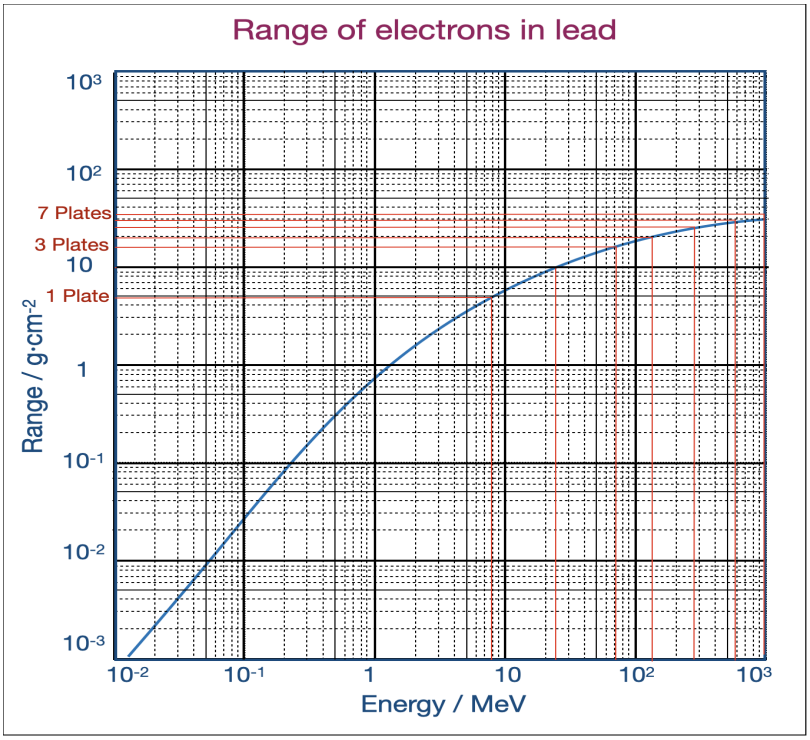

Figure 8.20: Shows the range of the electrons in several numbers of the lead plates used in our work as a function of the energy of the electrons.

Figure 8.21 shows the attenuation of electrons in the lead as a function of the energy thresholds estimated using Figure 8.20. We observe that the number of particles with an energy above the energy needed to go through the different number of lead plates follows approximately a linear behavior in all the levels of our data.

USC
UNIVERSIDADE DE SANTIAGO DE COMPOSTELA

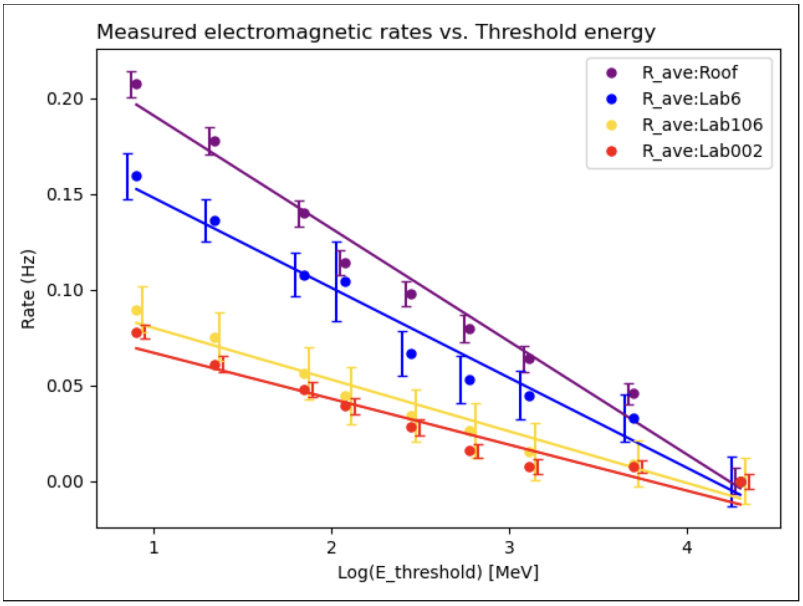

Figure 8.21: Illustrates the attenuation of electrons in the lead layers as a function of the estimated energy thresholds. The solid line represents the linear regression fit of the data for different levels.

Using the observed behavior, we have estimated the energy distribution of electrons in all the levels of the physics faculty building and a more accurate calculation of the associated rate of electrons. For this purpose, we made the following analysis.

Let us call $n(E)$ the energy distribution of electrons at any of the levels of the building. Then, the number of electrons above a given energy threshold E_i is:

$$N(E_i) = \int_{E_i}^{E_{max}} n(E)\, dE$$
$$= a - b \ln (E_i) \qquad (8.6)$$

USC
UNIVERSIDADE DE SANTIAGO DE COMPOSTELA

where E_{max} is the maximum energy of the electrons arriving to that level. Then $N(E_{max}) = 0$.

As we are working in MeV energy units, when $E_i = 1\ MeV$, we get:

$$N(1) = \int_1^{E_{max}} n(E)\, dE = a \tag{8.7}$$

Then, the parameter a of the linear fit represents the number of electrons with an energy greater than $1\ MeV$.

The $n(E)$ distribution can be deduced calculating the integral given in equation 8.5 in the interval $[E, E + dE]$. We get, step by step:

$$\int_E^{E+dE} n(E)\, dE = a - b\ln(E + dE) - (a - b\ln(E))$$

$$= n(E)\, dE$$

$$n(E)\, dE = b\,(\ln(E + dE) - \ln(E))$$

$$n(E) = b\left(\frac{\ln(E + dE) - \ln(E)}{dE}\right) = b\,.E^{-1} \tag{8.8}$$

We arrive to the very interesting a nice result:

$$n(E) = b\,.E^{-1}$$

Using the fact that the number of electrons with an energy greater than the E_{max} is zero, we can find the maximum energy E_{max} for the electrons as follows:

$$\int_{E_{max}}^{E_{max}} n(E)\, dE = a - b\ln(E_{max}) = 0$$

USC UNIVERSIDADE DE SANTIAGO DE COMPOSTELA

$$E_{max} = e^{a/b} \tag{8.9}$$

To find the values of variables a and b, we performed a linear regression fit to the data presented in Table 8.10. The results are shown in Table 8.10, together with the Chi-Square (χ^2) value of the fit, s and the probability p estimated as $p = 1 - CDF(s; NDF)$, where CDF is the cumulative distribution function associated with a chi-square distribution with NDF degrees of freedom. The last column shows the expected maximum energy of the electrons at every level. We made the fit in two fitting intervals with 9 and 8 points in order to analyze the consistency of our results. Both fits show compatible results inside the estimated uncertainties.

In order to see if there were other smaller but significant effects in our data, we also tried a second-order fit. The results are shown in Table 8.11, also with their statistical significance using the p-value test. We observe that the fit does not improve significantly with respect to the linear fit except in both the roof and the laboratory 002 levels. In any case, as we are mainly interested in estimating the electromagnetic background in laboratory 106, where the TRAGALDABAS detector is located, we consider the results obtained with the linear fit good enough for our purposes.

USC
UNIVERSIDADE DE SANTIAGO DE COMPOSTELA

Table 8.10: Shows the values for both parameters, a and b and the maximum energy of the electrons at different levels of the physics building.

Linear fit: $y = a + bx$							
Fit interval: [2, 10], NDF: 7							
Level	a	sa	b	sb	χ^2	$Probability$	E_{max} $[GeV]$
Roof	0.248	0.012	-0.025	0.002	4.10	0.77	19.5
L6	0.195	0.021	-0.020	0.003	1.02	0.99	14.5
L106	0.107	0.022	-0.012	0.003	0.49	1.00	9.6
L002	0.091	0.007	-0.010	0.001	7.34	0.39	6.9
Fit interval: [2, 9], NDF: 6							
Level	a	sa	b	sb	χ^2	$Probability$	E_{max} $[GeV]$
Roof	0.248	0.013	-0.025	0.002	4.09	0.66	19.2
L6	0.199	0.024	-0.021	0.004	0.91	0.99	11.7
L106	0.113	0.025	-0.013	0.004	0.25	1.00	5.7
L002	0.097	0.007	-0.012	0.001	4.21	0.65	4.2

USC UNIVERSIDADE DE SANTIAGO DE COMPOSTELA

Table 8.11: Illustrates the values for both parameters, a and b, when a second-order fit was applied for the data at different levels of the physics building.

Second order fit: $y = a + bx + cx^2$								
Fit interval: [2, 10], NDF: 6								
Level	a	sa	b	sb	c	sc	χ^2	*Probability*
Roof	0.301	0.031	-0.048	0.012	0.0021	0.0011	0.51	0.99
L6	0.238	0.057	-0.039	0.024	0.0017	0.0022	0.32	1.00
L106	0.137	0.058	-0.024	0.024	0.0010	0.0023	0.03	1.00
L002	0.123	0.017	-0.024	0.007	0.0011	0.0007	1.23	0.94
Fit interval: [2, 9], NDF: 5								
Level	a	sa	b	sb	c	sc	χ^2	*Probability*
Roof	0.281	0.027	-0.038	0.010	0.0011	0.0008	2.19	0.90
L6	0.226	0.047	-0.033	0.017	0.0011	0.0015	0.46	1.00
L106	0.136	0.049	-0.024	0.018	0.0010	0.0015	0.03	1.00
L002	0.123	0.014	-0.023	0.005	0.0011	0.0004	1.24	0.98

- Estimation of the electron background in the TRAGALDABAS detector

The rates of the electromagnetic background estimated in the previous paragraph do not represent the real rates existing in reality. Our measurements were affected by several factors as the inefficiencies in the detectors, their geometrical acceptances, changes in the air temperature or in the barometric pressure affecting the rates of the cosmic rays, among others.

Making the corrections of all these effects is not an easy task and is beyond the scope of our work. In order to make a realistic estimation of the real rates associated with our measurements, we proceed as follows. The high-energy electron contained in the atmosphere from cosmic origin was carefully studied in reference [P. Barker] in several

USC
UNIVERSIDADE DE SANTIAGO DE COMPOSTELA

places. One of them was Ann Arbor (Michigan) at a latitude of $42.28^{\circ}N$ and an altitude of $280\,m$ over the sea level. These values are quite similar to those at Santiago de Compostela, which is at a latitude of $42.87^{\circ}N$ and an altitude of $240\,m$ over the sea level. Although the mean rate of cosmic rays also depends on other factors as the mean atmospheric conditions or local geomagnetic field, we may assume at the first order of approximation that we could expect in our building in Santiago de Compostela the same rate of electrons that the ones measured at Ann Arbor. P. Barker got an integrated intensity of $52/m^2.s$ electrons with an energy above $10\ MeV$ of energy. Using this value, we can estimate the correction factor we need in our measurements for getting the same result in our measurements. Using the results obtained with the 9 points fit, we expect in our measurements a rate of $0.19 \pm 0.02/s$ for the electrons with energy above $10\ MeV$. If we make the rough estimation that any of our detectors have a surface of about $2.5 \times 10\ cm^2$, it provides a total rate of about $76 \pm 8/m^2.s$, not far away from the result obtained by P. Barker. In any case, in order to get results compatible with those in Ann Arbor, we will apply a factor of $0.68\ (= 52/76)$ to all our data. It is supposed that this factor accounts for all the efficiency and geometrical acceptance effects and gammas contamination not included in our results.

Considering the estimated energy distribution of electrons in Lab 106 on the first floor of the Faculty of Physics building, where the TRAGALDABAS detector is located, it is possible to make a rough estimation of the expected electron background in such detector.

The reconstruction efficiency of electrons in the TRAGALDABAS detector was estimated in the Ph.D. Thesis of Y. Fontenla [109]. He got the values given in Table 8.12.

A fit of the efficiency of form: $Eff = a + b \cdot Ln(logE - c)$ provides for the parameters the values: $a = 85.9 \pm 1.1$, $b = 22 \pm 0.6$ and $c = 1.38 \pm 0.1$. The result of the fit is shown in Figure 8.22.

USC
UNIVERSIDADE DE SANTIAGO DE COMPOSTELA

Table 8.12: Represents the estimation of the reconstruction efficiency of electrons in the TRAGALDABAS detector.

Energy [MeV]	Efficiency [%]
25	1
30	27
56	69
100	80
200	84
500	87

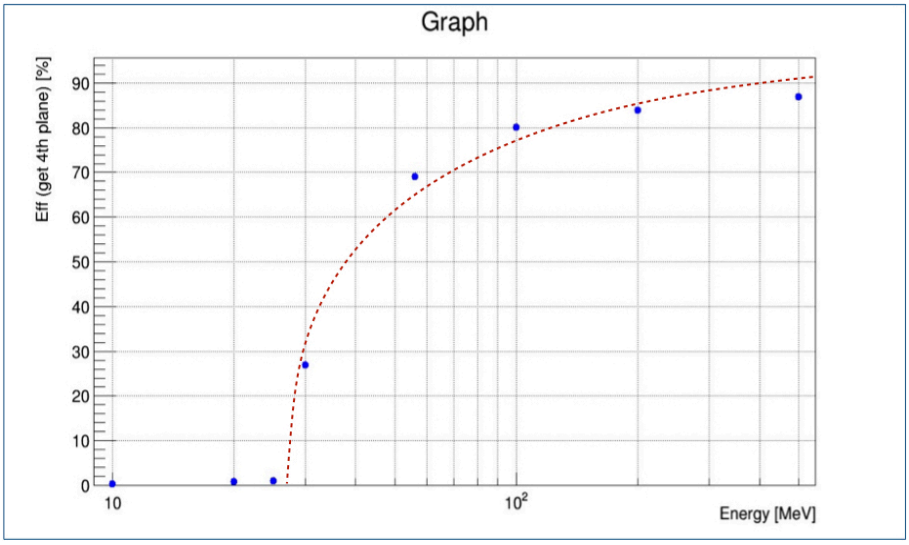

Figure 8.22: Shows the estimated TRAGALDABAS efficiency versus the energy of the electrons. The red dashed line represents the fit of the data given in Table 8.12.

Using the fit of the reconstruction efficiency of electrons in the TRAGALDABAS detector, we can estimate the expected efficiency of the detector in any range of energy of the arriving electrons.

USC UNIVERSIDADE DE SANTIAGO DE COMPOSTELA

As we have previously estimated the number of electrons we expect at different energy intervals, it is possible to make an estimation about the electron background we expect in the laboratory 106, where the TRAGALDABAS detector is placed. Our results are summarized in Table 8.13.

Table 8.13: Summary of the calculations for estimating the electron background in the TRAGALDABAS detector. Where E is the energy of electrons in MeV, the efficiency has been calculated using the fit described in the text, N is the expected rate of electrons estimated from the COSMIX data, sN contents their associated uncertainties, diff$N$ is a number of electrons in the different energy intervals, diff$R106$ is the expected rate per m^2 in Hz, in each energy interval at laboratory 106 after interpolating the efficiency between the lateral values. The last columns R_TR and sR_TR show the expected rates in the TRAGALDABAS detector, taking into account both its size and the geometrical acceptance and their corresponding uncertainties, where the uncertainty is the square root of the summation for all elements in the last column.

E/MeV	Log (E)	Eff/%	N/$m^2.s$	sN/$m^2.s$	diffN/$m^2.s$	diffR106/$m^2.s$	R_TR/s	sR_TR/s
10	1	0	24.4	4.0	2.2	0.0	0.0	0.0
18	1.25	0	22.2	4.1	2.2	0.0	0.0	0.0
32	1.5	38	20.0	4.3	2.2	0.8	0.3	0.1
56	1.75	63	17.8	4.5	2.2	1.4	0.6	0.1
100	2	75	15.6	4.7	2.2	1.7	0.7	0.2
178	2.25	83	13.4	5.0	2.2	1.8	0.8	0.3
316	2.5	89	11.2	5.2	2.2	2.0	0.8	0.4
562	2.75	93	9.0	5.5	2.2	2.1	0.9	0.5
1000	3	97	6.8	5.8	2.2	2.1	0.9	0.8
1778	3.25	100	4.6	6.1	2.2	2.2	0.9	1.2
3162	3.5	100	2.4	6.4	2.2	2.2	0.9	2.5
5623	3.75	100	0.2	6.7	0.2	0.2	0.1	2.8
6310	3.8	100	0.0	0.0	0.0	0.0	0.0	0.0
7079	3.85	100	0.0	0.0	0.0	0.0	0.0	0.0
Total expected rate of electrons in TRAGALDABAS detector:							6.9	4.1

USC UNIVERSIDADE DE SANTIAGO DE COMPOSTELA

For estimating the final results, we have considered that the detector has a surface of $1.8\,m^2$ and a geometrical acceptance of 0.23, corresponding to a distance of $1.8\,m$ between the external trigger planes. That is to say that only around one-fourth of the electrons arriving at the upper plane of the detector gives a signal in the lower plane. The final result for the expected rate of electrons in the TRAGALDABAS detector is around $6.9 \pm 4.1\ Hz$. As it is shown in Table 8.13, the big uncertainty in the total result comes mainly from the uncertainties in the estimation of the number of electrons at the highest energies, where the statistics in our data were smaller.

8.8 Discussion and outlook

The analysis of the gathered data for the COSMIX detector with the two configurations, vertical and horizontal, revealed some crucial conclusions and suggestions it could be summarized as follows:

1. Both data set configurations, vertical and horizontal, show a clear expected behavior of the absorbed rates for the data existing at all the Faculty of Physics building levels.

2. The data for laboratory L6 show a more dispersed behavior, maybe due to the multiple scatting effects due to the environment (floor, walls, devices, etc.) and the different location of the COSMIX detector in the laboratory for several reasons could not always be the same.

3. In all data sets, the behavior using 5 cm of lead absorber shows the clear absorption pattern expected, being all data sets statistically compatible. However, we observe a dispersion again on data sets corresponding to laboratories L6 and 106 that are not present at the roof, where no matter can produce dispersion and in the underground laboratory 002, where the matter above it seems to be enough to absorb these scattering effects. We propose to do these experiments again at laboratories L6 and 106 in the future either by blinding the COSMIX detector on sides to take only vertical rays or by increasing the

USC
UNIVERSIDADE
DE SANTIAGO
DE COMPOSTELA

separation of the detectors to reduce the acceptance for the inclined rays.

4. Using the tables existing in the literature of the range of electrons in the lead, it is possible to estimate the rate of electrons expected above given energy. With a detailed analysis of those behaviors, it is possible to estimate with good accuracy the energy distribution of the electrons in the four levels of the building analyzed in this work. As very interesting and unexpected results, we observe that in all the levels, the energy of the electrons follows a law of the form $n(E) = b/E$, being the number of electrons with energy higher than $1\,MeV$, $N(E > 1\,MeV)$ equal the parameter a. We did not find any reference to the E^{-1} behavior in the bibliography. Both parameters do allow quantifying the attenuation of the rate of electrons across the building (given by the a parameter) and the "cooling" of their energy distribution (given by the b parameter). According to the linear fits performed of the number of electrons above given energy cut as a function of the energy, it is effortless to estimate the maximum energy of the electrons at a given level an $E_{max} = e^{a/b}$.

The values obtained for both parameters, a and b and the energy limit E_{max} at the different levels analyzed and shown in Table 8.10.

5. Using the estimated rate of electrons in laboratory 106 and their energy distribution and the reconstruction efficiencies of electrons with the TRAGALDABAS detector, we have estimated the expected rate of the background of electrons measured by such detector, R_TR. We got the value to be around $6.9 \pm 4.1\,Hz$. Considering that the typical mean rate of the TRAGALDABAS detector is around $100\,Hz$, we do not expect the electron component in the data to be very much higher than around 10%. Improving this result would require taking more data with more than 8 absorber plates, including more data points between $3.4\,cm$ and $5\,cm$ of the lead absorber. It would significantly improve our fit and also inform us about the necessity or not of including high order terms in the energy distribution $n(E)$ of electrons.

USC UNIVERSIDADE DE SANTIAGO DE COMPOSTELA

Conclusions

This work covered several aspects related with the cosmic ray detection, focusing mainly on the Trasgo family detectors like TRAGALDABAS, TRISTAN and STRATOS. Trasgo is a family of particle detectors for cosmic ray measurements based on the Resistive Plate Chambers (RPCs) technology. TRAGALDABAS is a detection device located at the University of Santiago de Compostela in the Faculty of Physics. The detector TRISTAN achieved three journeys onboard the Spanish vessel Sarmiento de Gamboa and BIO Hesperides oceanographic vessel and was installed as a permanent location at the Spanish Antarctic Base Juan Carlos I in Livingston Island. STRATOS is a third detector of the family and was developed by the HIDRONAV Technology company and was built by LIP-Coimbra, specifically for atmospheric studies.

The work has been done using EnsarRoot as the main software tool for the analysis and simulation tasks related with all the Trasgo detectors. Several simulations and analysis tools were designed and tested in the TRAGALDABAS detector, which is devoted to studying cosmic radiations. The TimTrack algorithm is the standard particle reconstruction method for the Trasgo detector and it has been used for the fitting of experimental data and for getting the uncertainties and correlation coefficients of all the parameters. The CORSIKA package has been used for the systematic generation of cosmic ray showers induced by primary cosmic rays of different masses and at different energies. We also found the Google Sheet tool as a very interesting, flexible and powerful tool for preliminary data analysis, quality control and general behavior trends where a rigorous statistical analysis was considered unnecessary. We used all these tools for developing a significant number of programs that will stay as a computing and

USC
UNIVERSIDADE DE SANTIAGO DE COMPOSTELA

analysis infrastructure for future tasks and initiatives related to the Trasgo program.

Two main studies were carried out with two different configurations of the TRAGALDABAS detector: a first one composed by three RPC active planes without any material between them and a second one including 1 cm thick lead layer placed under the third plane. TimTrack was used for the track reconstruction. We compared our results with the ones obtained using real data taken with the same configurations. Specifically, we used our analysis to estimate the capability of the detector for separating electrons from muons. We used the results to make a first estimation of the electron content in the TRAGALDABAS data sample and their corresponding angular distribution.

Without using the lead radiator, we found that the ratio of the electrons from the total number of the detected particles is about 55% and the ratio of the muons about 45%. The probability of the most electrons is about 88% and 90% for the most muons. After using a lead layer, the ratio of the identified electrons becomes around 34% and the ratio of the detected muons is about 66%. The electron content is slightly higher than the expected value and can be a consequence of the radiator effect of the surrounding concrete existing in walls and ceilings. Also, the probability of being the detected particle of a specific particle was improved, where the probability of the most electrons became almost 100% and 94% for the most detected muons. As it could be expected, adding lead layers between detector planes improved the system's calorimetric capabilities and improved the separation of muons and electrons. We also made a first estimation of the angular distribution of events in the detector after acceptance corrections. A fit to the typical $\cos^n(\theta)$ behavior provides the value $n = 2.50 \pm 0.98$, slightly bigger than the typical value of around 2 measured by other experiments outdoors. The big uncertainty is a consequence of both the small statistic of corrected data that were available for our analysis. We also did not consider the fact that having the detector inside a building would require careful analysis.

USC
UNIVERSIDADE DE SANTIAGO DE COMPOSTELA

Unlike other typical cosmic ray stations, the high granularity of the Trasgo detectors provides the capability of detecting bundles or clusters of particles coming from the same primary cosmic ray. As has been already commented in the previous paragraph, they also offer the possibility of separating electrons and muons. These features might open new research possibilities either related to the study of the primary cosmic rays or, perhaps, direct analysis of the properties of the atmosphere. For this purpose, we used a previously existing program, improving the cluster-finding algorithm and including new variables. We created a big sample of events with H, He, C and Fe primaries ranging in energies between 1 GeV and 10^5 GeV. Among other studies, we determined the minimum energy needed by the analyzed primary nucleus to produce different particles or clusters of particles arriving at a ground 1.8 m^2 detector. As a main result, we found that muons and low energy electrons have approximately the same threshold energy, around 6 GeV, to produce 1 GeV electrons need at least 15 GeV of primaries. Mixed clusters composed of muons and electrons need 80 GeV and 2 muons need at least proton primaries with an energy above 300 GeV. We also estimated the energy of the maximum of the respective response functions. These results do allow to quantify the capability of the Trasgo detectors to scan the arrival of primary cosmic rays in different ranges of energies opening new research possibilities related to the variation of the solar activity and the interplanetary magnetic field. Also, several variables were sensitive to the height of the first interaction, offering also the possibility for the real-time measurement of the temperature of the high atmosphere. We also found that the expected rate of mixed and muon clusters is too small for allowing day-by-day studies with a significant research interest. However, we expect a rate of about 40 K electron clusters per day and it could be advisable a more careful analysis of their properties as estimating their total energy, their size, their opening angle, Etc. Electron clusters offer an indirect way of measuring the rate variation of high energy muons and their systematic analysis might open new perspectives for the regular survey of cosmic rays in the low energy region.

USC
UNIVERSIDADE DE SANTIAGO DE COMPOSTELA

We made a preliminary analysis of the effect of the pressure and temperature variation in the data taken by the TRISTAN detector along its first journey between Vigo (Spain) and Punta Arenas (Chile). We observe an apparent latitude effect in our data, but we do not observe a systematic effect in the pressure or temperature correction coefficients. A more deep analysis of the quality of the data is needed, as we know the data could be affected by an important malfunction of the cooling system during the journey and several extreme variations of the room temperature.

As a contribution to the STRATOS project, we made the first commissioning of the detector, obtaining, among other performances, a time resolution $\sigma_t = 226 \pm 7\ ps$ and a mean position resolution of $\sigma_x = 9.8 \pm 1.1\ mm$ and $\sigma_y = 15.2 \pm 2.0\ mm$ in X and Y directions respectively. Finally, we used a small compact and portable COSMIX detector, developed by the Univ. of Bordeaux, for direct measurement of the electrons and gammas background at laboratory 106 of the Faculty of Physics building, where the TRAGALDABAS detector is located. We also extended our study to three other levels of the building: the roof (at open-air), the second floor (laboratory 6) and the basement at ground level, laboratory 002. The task was not easy due to the small size of the detector, two scintillator bars of about $25\ cm^2$ size needing exposure times of one or several days and the difficulties of placing the detector always in the same position in the different laboratories, among others. We did not make the typical pressure corrections assuming that at first order, the pressure effect in the data taken during around two years would compensate themselves. We took data in two different configurations, with both detectors, one on top of the other (vertical configuration) and with both detectors placed side by side. In both configurations, we took data with several plates of lead on top of the detectors to study the development of the electromagnetic showers. In order to avoid the dead-time effect of the detector, we calculated the rates making an exponential regression on the distribution of time intervals between consecutive counts using the TimTrack algorithm. As the main result, we estimated that the energy distribution of the electromagnetic background $n(E)$ follows a law of

USC UNIVERSIDADE DE SANTIAGO DE COMPOSTELA

the form $n(E) = 1/E$ at all the building levels. Using the values obtained for laboratory 106 and the expected efficiency of the TRAGALDABAS detector for electrons of different energies, we estimate that the electron component expected at such detector is of the order of about $6.9 \pm 4.1\ Hz$. This result is far from compatible with the one measured directly in the TRAGALDABAS detector. The reason may be on both sides. On the one hand, the sample of the reconstructed data available of the detector was very small and the presence of a background of a few bad reconstructed tracks is not negligible. A better time reconstruction would be needed for better rejection of ghost combinations. On the other hand, in the COSMIX side, in the absence of a detailed acceptance analysis and considering the non-uniform distribution of the cosmic electrons, the correction performed using external data could have been too strict. Undoubtedly both methods should be improved. However, the existence of both of them would allow in the future the respective intercalibration and a better understanding of the cosmic ray background inside the building.

USC
UNIVERSIDADE DE SANTIAGO DE COMPOSTELA

USC
UNIVERSIDADE
DE SANTIAGO
DE COMPOSTELA

Resumo da tese en Galego

Introducción

Nas próximas páxinas resumimos o traballo realizado na detección de Raios Cósmicos con detectores de tipo TRASGO e tamén os resultados obtidos máis importantes. Este tipo de detectores foron deseñados específicamente para o estudo desta radiación ionizante característica; están basados na tecnoloxía de cámaras de placa resistiva, RPCs, un tipo de sensores gaseosos moi extendido na actualidade, relativamente baratos e con altas prestacións de eficiencia e resposta temporal.

Na actualidade están funcionando tres sistemas da chamada "Familia TRASGO": o detector TRAGALDABAS, na Facultade de Física da Universidade de Santiago de Compostela; o detector TRISTAN, que fixo xa dúas viaxes dende Vigo ata a base española Juan Carlos I na Antártida, onde se atopa a día de hoxe; e o detector STRATOS, máis recente e evolucionado, validado con datos no seu laboratorio de desenvolvemento no LIP-Coimbra, Portugal, e espérase que esté pronto operativo no entorno do aeroporto de Vigo.

O traballo resumido aquí analiza datos de Raios Cósmicos e prestacións operacionais dos tres sistemas mencionados, alén dun cuarto sistema independente e portátil co obxectivo de completar e complementar as medidas dos outros sistemas. Antes de presentar resultados, este traballo recolle unha descripción e evolución histórica do descubrimento e natureza dos Raios Cósmicos, unha descripción da tecnoloxía de RPCs e un resumo das ferramentas e métodos desenvolvidos e usados ao longo do traballo. E ademais da análise de datos reais, incluímos desenvolvementos e análise de simulacións, algo sempre de especial importancia en calquer experimento actual.

USC
UNIVERSIDADE DE SANTIAGO DE COMPOSTELA

Raios Cósmicos

Os chamados Raios Cósmicos foron descubertos por Victor Hess a comenzos do século XX. Hess atopou evidencias dunha radiación de partículas que chegaba ao nivel do chan e obtivo, anos máis tarde, o premio Nóbel polo seu descubrimento. Estos raios poden ter orixe solar, galáctico e incluso extragaláctico. Identificámolos como raios cósmicos primarios, e poden recorrer grandes distancias ata chegar ata nós. Poden verse influenciados por campos magnéticos, incluso o terrestre, chegando a quedar atrapados neles se non levan enerxía suficiente. Se consiguen evitalos e chegar ata a Terra, interaccionan na atmósfera xerando o que se chama unha chuveira de partículas (Extensive Air Showers) que chegan anta a superficie terrestre, constituíndo o que chamamos raios cósmicos secundarios, e cunha tasa aproximada de 180 partículas por metro cadrado e por segundo. A especie de partícula máis abundante no chan son os muóns, cunha distribución de chegada próxima á vertical. Os electróns e fotóns que chegan fano cunha distribución máis uniforme e en menor cantidade. Protóns, neutrinos e neutróns son o resto de partículas que chegan ata a superficie pero ou ben en cantidades moi pequenas ou ben sen case capacidade de interacción. Ademáis, a forma na que se agrupan todas estas partículas ao nivel do chan é un indicativo da natureza, enerxía e outras características do raio cósmico primario que produciu a chuvieira.

Detectores ou Cámaras de Placa Resistiva (RPCs) e a Familia TRASGO

Como xa introducimos, as RPCs son detectores gaseosos moi usados en experimentos de Física Nuclear e de Partículas. Foron desenvoltos e utilizados inicialmente como contadores e detectores de trigger na entrada de grandes espectrómetros. Porén, a mellora nos seus deseños permititu que a día de hoxe poidan usarse como detectores de tracking e, máis a miúdo, como detectores de tempo de voo, chegando a resolucións ben por baixo dos 100 ps.

USC
UNIVERSIDADE DE SANTIAGO DE COMPOSTELA

A base de funcionamento dunha RPC consiste en detectar a descarga eléctrica producida pola ionización da partícula incidente cando atravesa o gas activo, que se atopa sometido a unha alta diferencia de potencial. Dita ionización induce un sinal eléctrico nos electrodos de lectura que é atenuada e localizada grazas á presenza dun material de alta resistividade entre os electrodos e a zona activa. Despois, ese sinal é amplificado e tratado de forma axeitada por unha electrónica específica, chegando así a un sistema de adquisición de datos.

Os detectores da familia TRASGO cos que traballamos nesta tese son detectores de RPCs, con múltiples volumes activos e especialmente focados ao estudo dos Raios Cósmicos. Dita familia, o proxecto TRASGO (TRAcking reconStructinG mOdule) foi proposto por J.A. Garzón e colaboradores en 2011 co obxectivo de desenvolver novos sistemas de detección máis simples, modulares e económicos pero de altas prestacións. Dende aquela, foron xa cosntruídos varios detectores de tipo TRASGO. Sobre tres de eles presentamos prestacións e análise de datos neste traballo.

O primeiro sistema construído e operativo é o detector TRAGALDABAS. Consiste en 4 planos de RPCs de dobre gap, cunha separación aproximada de $50\ cm$ entre planos, e unha área de detección aproximada de $2\ m^2$ por plano, dividida en celas rectangulares. Implementa a electrónica e adquisición do experimento HADES do GSI/FAIR, e está situado tomando datos dende 2015 na Facultade de Física da USC.

O segundo sistema desenvolvido é o detector TRISTAN. Moi parecido ao anterior, este consta de 3 planos activos cunha área lixeiramente menor e coa mesma electrónica. Este detector tomou datos ao longo dunha viaxe de ida e volta dende Vigo a Punta Arenas, Chile, entre 2018 e 2019, e posteriormente noutro viaxe de ida ata a base antártica española Juan Carlos I, onde se atopa operativo na actualidade.

Por último, o terceiro detector de tipo TRASGO avaliado neste traballo, chamado STRATOS, ten unha estructura base similar aos anteriores

USC UNIVERSIDADE DE SANTIAGO DE COMPOSTELA

pero é máis novo e incorpora certas melloras mencionadas en detalle no seu correspondente capítulo.

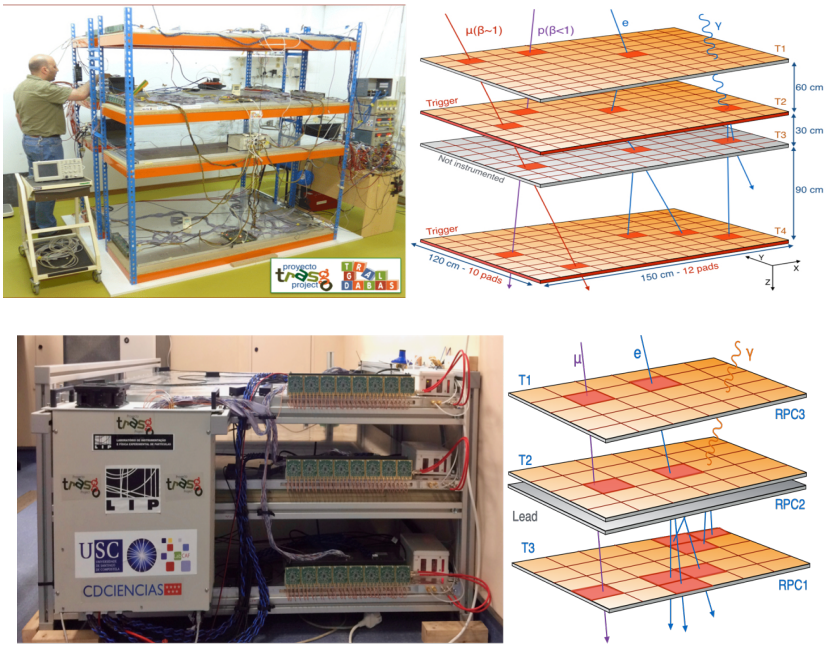

Figura 10.1: Fotografía dos tres detectores de tipo TRASGO avaliados neste traballo. Arriba: o detector TRAGALDABAS xunto cun esquema dos seus planos detectores. Centro: fotografía do sistema TRISTAN instalado na Antártida, tamén xunto co seu esquema de planos. Abaixo: fotografía do detector STRATOS recentemente desenvolvido no LIP-Coimbra.

USC UNIVERSIDADE DE SANTIAGO DE COMPOSTELA

O algoritmo de TimTrack

Un dos aspectos máis importantes na análise de datos experimentais é a reconstrucción de eventos. O algoritmo de TimTrack é o método de referencia de reconstrucción nos detectores de tipo TRASGO. Básase en mínimos cadrados para determinar con precisión os parámetros dinámicos das partículas a partir das medidas experimentais dos detectores. Estos parámetros agrúpanse nun vector ao que chamamos saeta (**s**). Dito vector contén as coordenadas de inicio de propagación da partícula, o tempo inicial respecto dun contador externo, as pendentes das traxectorias e a lentitude ou inversa da velociade. A vantaxa do método é que é capaz de unificar e manexar de forma conxunta todos os datos experimentais independentemente do sistema que os mida.

Dependendo do tipo de modelo que apliquemos ao TimTrack podemos distinguir entre método lineal e método non lineal. Foi aplicado aquí o método non lineal resolvéndoo de forma iterativa a partir dunha primeira estimación feita polo método lineal. O criterio de converxencia basouse en distancias euclídeas dentro da saeta.

TimTrack tamén pode ser usado como ferramenta de calibración ou como ferramenta de análise matemático de axuste de funcións. Precisamente esta última utilidade foi a que se usou na análise de datos dun pequeno sistema de referencia para medida de raios cósmicos, como comentaremos no seu correspondente apartado.

Análise de datos co detector TRAGALDABAS

Como xa mencionamos, este detector foi o primeiro da familia TRASGO. Trátase dun sistema de 4 planos, área activa de 1.5x1.2 m^2, cobertura angular de 5 sr e resolución temporal por plano por debaixo dos 300 ps. Leva dende 2015 tomando datos na Facultade de Física a unha tasa aproximada de 7 millóns de eventos por día.

USC
UNIVERSIDADE DE SANTIAGO DE COMPOSTELA

Neste traballo analizamos datos de TRAGALDABAS tanto reais coma simulados. Respecto a estos últimos, desenvolvéronse unha gran cantidade de simulacións usando o entorno EnsarRoot, e como xerador de eventos o paquete CRY. Foi desenvolvida non so a xeometría do detector, senon tamén a xeoetría do edificio da Facultade de Física co obxectivo de estudar a súa contribución á absorción de radiación, e tamén métodos de reconstrucción de eventos e traxectorias.

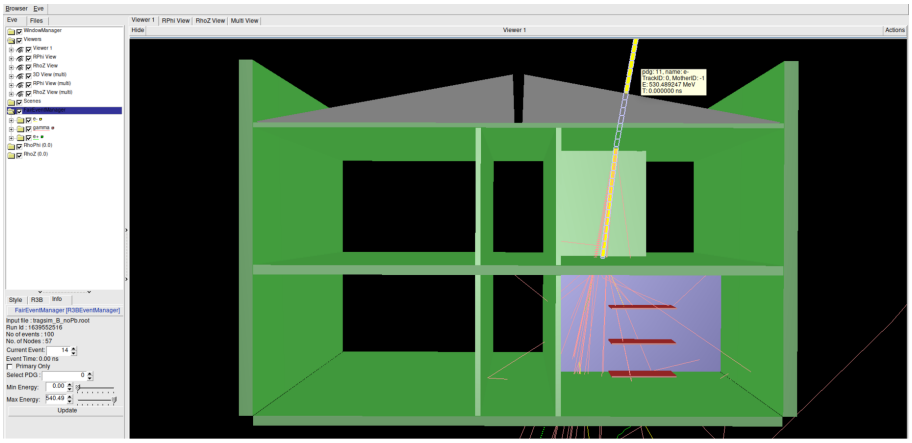

Figura 10.2: Visualización dun evento simulado de raios cósmicos incidindo sobre tres planos activos do detector TRAGALDABAS, situado na súa posición nominal dentro do edificio da Facultade de Física, cuxa estructura foi tamén simulada.

O obxectivo principal neste capítulo foi estimar a proporción ou cantidade de electróns e muóns detectados por TRAGALDABAS. Dito doutro xeito, facer unha identificación de partículas. Partindo de simulacións, analizáronse tres observables físicos para cada evento: a multiplicidade, o alcance ponderado e o χ^2 resultante da reconstrucción da traxectoria con TimTrack. Desenvolveuse un método que fenomenolóxicamente é capaz de aproximar a separación entre muóns e electróns. Dito método foi adaptado e evoluído dende a idea orixinal de Y. Fontenla e colaboradores en 2019, e aplicado por primeira vez en datos reais.

Analizáronse dúas configuracións diferentes do detector: por un lado, tres planos activos T1, T3 e T4, con trigger na coincidencia de T1 e T3;

USC UNIVERSIDADE DE SANTIAGO DE COMPOSTELA

e por outro, a mesma configuración pero insertando unha lámina de chumbo de 1 cm de grosos entre T3 e T4. O obxectivo desta lámina de Pb non foi outro que absorber a compoñente electrónica, incluso provocar pequenas chuvieiras EM, e así aumentar a capacidade de separación e identificación entre muóns e electróns, xa que os primeiros teñen a capacidade de atravesar a lámina sen apenas interaccionar.

Para a configuración sen a lámina de chumbo, obtívose a primeira instancia unha contribución aproximada de 50% electróns e 50% muóns, mentras que unha vez analizados os datos que incuían a lámina de Pb obtívose unha contribución final de 66% muóns e 34% electróns, mellorando significativamente a separación e achegando a probabilidade de acertar ata un 94%.

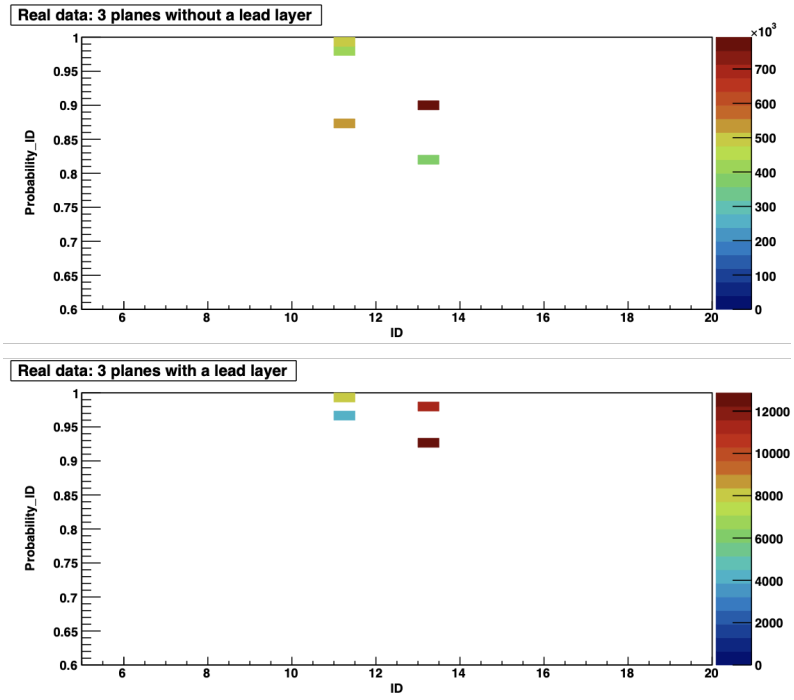

Figura 10.3: Separación entre electróns e muóns con TRAGALDABAS antes e despois de colocar a lámina de chumbo entre os dous últimos planos. Esta lámina aumenta significativamente o número de muóns identificados (electróns ID=11; muóns ID=13) e aumenta a probabilidade de ter acertado coa identificación.

USC UNIVERSIDADE DE SANTIAGO DE COMPOSTELA

Ademais da identificación de partículas, estudamos tamén a distribución angular de incidencia de raios cósmicos sobre TRAGALDABAS. O resultado obtido é lixeiramente diferente ao esperado "a ceo aberto", o que suxire que unha contribución non despreciable dos materiais do edificio da Facultade sobre a dirección final de incidencia sobre o detector. Dita distribución foi corrixida pola aceptancia xeométrica do detector, calculada mediante simulación, e axustada á coñecida distribución fenomenolóxica de Fluxo $\sim \cos^n(\theta)$, obténdose no noso caso unha potencia de $\boldsymbol{n = 2.497}$.

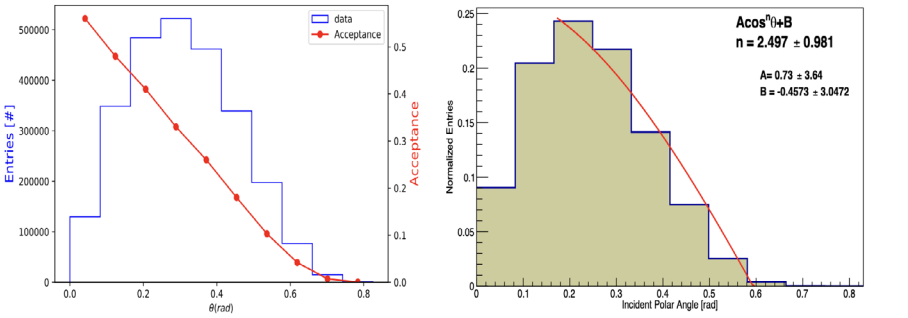

Figura 10.4: Esquerda: distribución angular de raios cósmicos medida con TRAGALDABAS e curva de aceptancia calculada. Dereita: distribución angular final corrixida e axustada a unha curva $\cos^n(\theta)$.

Análise de datos de TRISTAN ao longo do Océano Atlántico

TRISTAN é outro dos sistemas operativos da familia TRASGO. Trátase dun conxunto de 3 planos de RPCs, moi similar a TRAGALDABAS, que ademais incorpora por defecto unha lámina de chumbo de 1 cm entre os dous últimos planos cubrindo unha superficie aproximada do 40% do detector.

TRISTAN fixo xa dúas viaxes polo Océano Atlántico. A primeira delas foi un traxecto de ida e volta dende Vigo (España) ata Punta Arenas (Chile), extremo sur de Sudamérica, a bordo do buque Sarmiento de Gamboa. A súa segunda viaxe fíxoa a bordo do buque Hespérides, e foi, ata o de agora, un traxecto so de ida ata a base española Juan Carlos I na Antártida, que é onde se atopa operativo na actualidade. Este

USC UNIVERSIDADE DE SANTIAGO DE COMPOSTELA

traballo analiza datos da primeira parte da primeira viaxe ao longo de 38 días entre Novembro e Decembro de 2018 no seu traxecto entre Vigo e Punta Arenas.

O obxectivo era unha medida da tasa de cósmicos ao longo do percorrido e a súa correlación coas variables atmosféricas. Así, mediuse tamén a presión atmosférica e a temperatura ao longo do camiño. A tasa de raios cósmicos foi corrixida pola presión e temperatura de cada momento do día. Despois, corrixiuse esta tasa pola eficiencia calculada do detector, e finalmente tamén por aceptancia.

A figura a continuación amosa o percorrido seguido polo detector e a variación relativa da tasa de medida de raios cósmicos ao longo da viaxe, xa corrixida por presión atmosférica, temperatura, eficiencia e aceptancia.

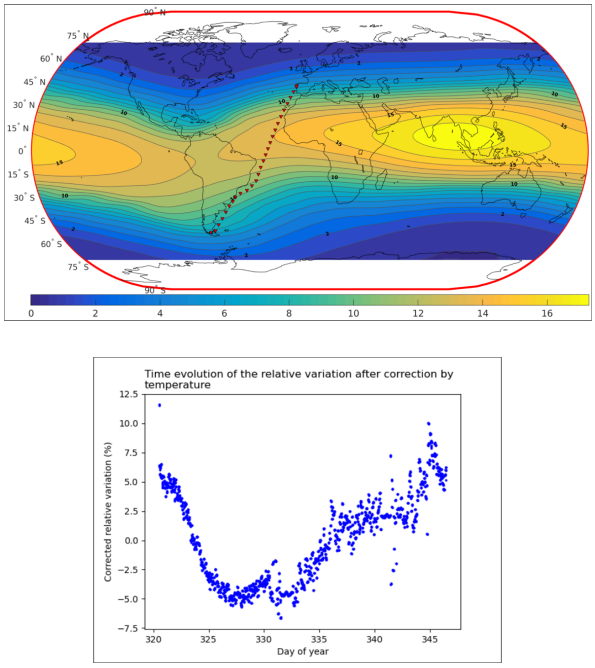

Figura 10.5: Arriba: representación do percorrido de TRISTAN na súa viaxe dende Vigo ata Punta Arenas. Cada triángulo representa un día de viaxe. Abaixo: variación relativa de raios cósmicos observada na viaxe. Pode verse claramente como a tasa é menor nas rexións da Terra próximas ao ecuador.

USC UNIVERSIDADE DE SANTIAGO DE COMPOSTELA

Calibracións e prestacións do detector STRATOS

A experiencia adquirida na construcción dos primeiros detectores da familia TRASGO levou aos equipos de traballo ao recente desenvolvemento do detector STRATOS. Conceptualmente similar aos anteriores sistemas, implementa unha lectura de sinal en forma de 64 strips longos por plano (mentras que tiñamos pads cadrados nos outros casos) e unha nova electrónica de amplificación e lectura, moito máis optimizada tanto en prestacións como en custe. Foi construído nos laboratorios do LIP-Coimbra, Portugal, e foi alí onde levamos a cabo as tarefas expostas a continuación.

O detector STRATOS foi calibrado en posición, tanto na súa dimensión lonxitudinal, onde a posición é calculada a partir da diferencia de tempos do mesmo sinal nos dous lados do mesmo strip de lectura, coma na súa dimensión transversal, que ven dada pola posición mesma do strip "centro de masas" da carga recollida. Foi pois tamén calibrado en carga e obtivéronse os parámetros de transformación dende unidades de ADC a valores físicos de carga, pC. A calibración en tempos foi tamén implementada e admais, dada as medidas de carga, a medida final temporal foi corrixida polo efecto que a carga produce na información de tempos (slewing correction). Por último, a eficiencia de detección do sistema tamén foi medida.

Despois de todos estos traballos, chegouse a unha resolución temporal de todo o sistema de **226 p**s, ben por baixo do criterio inicial de deseño establecido en 300 ps. As resolucións en posición e eficiencias obtidas para cada un dos planos de detección amósanse na táboa a continuación.

Plane	$\sigma_x(mm)$	$\sigma_y(mm)$	Efficiency (%)
1	10.80 ± 0.35	17.17 ± 0.45	92.1
2	6.97 ± 0.22	11.34 ± 0.29	91.7
3	7.03 ± 0.23	12.67 ± 0.33	92.1
4	11.33 ± 0.35	19.53 ± 0.49	92.5

USC UNIVERSIDADE DE SANTIAGO DE COMPOSTELA

Análise de clusters de partículas chegando ao nivel do chan

Unha das propiedades máis destacadas do tipo de detectores co que traballamos é a súa capacidade para detectar grupos ou clusters de partículas, medindo os seus tempos e direccións de chegada, o que permite formular hipóteses sobre a natureza da chuvieira e a orixe do raio cósmico primario. Con este último obxectivo, neste traballo fixemos simulacións de cósmicos primarios de diferentes natureza, enerxía e masa, e estudamos o comportamento das chuvieiras secundarias provocadas polos primeiros ao chegar ao chan.

Foi desenvolvido un método de definición de clúster e o seu correspondente método de búsqueda e identificación. Todas as propiedades dos clusters atopados foron coidadosamente analizadas e correlacionadas tamén coas propiedades do cósmico primario orixinal. Esto levou, entre outras cousas, a estimar a chamada Función de Resposta de hipotéticos detectores cara a detectión de ditos clusters.

En particular, en función do tipo de clúster que pode ser medido e identificado cun detector de tipo TRASGO de 1.8 m^2 de superficie activa, fíxose unha estimación da natureza, orixe, enerxía e fluxo do raio cósmico primario, e tamén do tipo, natureza, enerxía e dirección de propagación da chuvieira producida. Algúns dos resultados máis destacados son amosados a continuación.

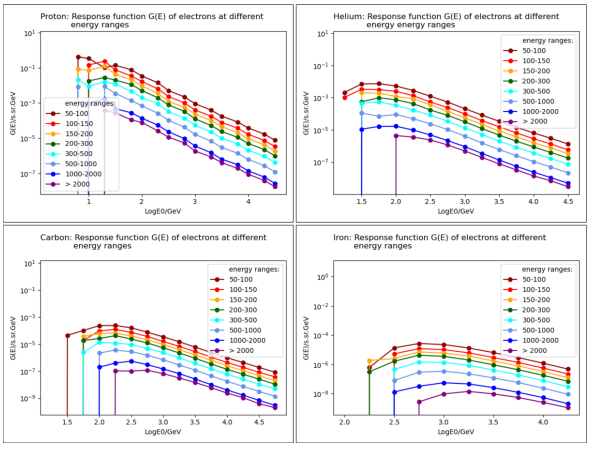

Análise de Raios Cósmicos co detector Cosmix

Como xa foi mencionado, o estudo de raios cósmicos secundarios proporciona unha información moi valiosa sobre diferentes fenómenos físicos. TRAGALDABAS, TRISTAN e STRATOS contribúen a estos estudos. Para dar máis seguridade ás medidas de estos sistemas completamos os experimentos con detección de cósmicos con un sistema diferente, pequeno e portátil, específicamente desenvolvido para medidas rápidas e simples: o detector Cosmix.

Cosmix consiste en dúas pequenas barras escintilantes de CsI(Tl) de 10 e 12 cm de lonxitude, con lectura por fotodiodos e unha electrónica moi simple con un sistema de coincidencias e un contador. Preséntase nun conxunto compacto (un pequeno maletín) o que permite facer medidas en calquer localización espacial.

Neste traballo usamos Cosmix para compementar os resultados de tasas de raios cósmicos medidos na Facultade de Física da Universidade de Santiago, facendo medidas en catro lugares distintos do edificio: a ceo aberto no tellado, nuha sala do terceiro piso, no mesmo laboratorio onde se atopa TRAGALDABAS no segundo andar, e nunha cuarta sala no soto do edificio. Medíronse ademais diferentes configuracións das barras de Cosmix e incluindo varios espesores de chumbo por riba das mesmas.

Ademais das propias tasas de cósmicos obtidas, se cadra o resultado máis destacado demostrado con este traballo é a enorme importancia que teñen os materiais dos edificios cando se trata de medidas de cósmicos no seu interior, en particular con TRAGALDABAS. Como exemplo, podemos afirmar que no tellado, a ceo aberto, as tasas son un 50% maiores que en calquer outra localización o interior do edificio, incluso nos casos con diferentes blindaxes de chumbo. Isto suxire que, por unha parte o edificio actúa como absorbente, e por outra, como radiador secundario producindo unha maior contribución de electróns ao conxunto de cósmicos no interior, modificando ademais a

USC
UNIVERSIDADE DE SANTIAGO DE COMPOSTELA

distribución angular dos mesmos, o que é consistente cos resultados obtidos con TRAGALDABAS.

Algunhas das tasas obtidas con Cosmix podemos velas nas táboas a continuación. Destaca, primeiro, a maior tasa medida sempre no tellado independentemente da configuración dos detectores, e tanto de forma individual coma en coincidencia, sendo constante en calquer outro punto do edificio, e segundo, a pouca reducción que producen na tasa os diferentes esperores de chumbo, o que da a entender que os propios materiais do edificio xa absorben a maior parte da contribución electrónica, chegando maioritariamente muóns, independentemente da localización interior.

	Horizontal configuration											
	Rate 1 (Hz)				**Rate 2 (Hz)**				**Coincidence rate (Hz)**			
xPb (cm)	Lab002	Lab106	Lab6	Roof	Lab002	Lab106	Lab6	Roof	Lab002	Lab106	Lab6	Roof
0	0.81 ± 0.01	0.87 ± 0.02	0.92 ± 0.02	1.01 ± 0.02	0.69 ± 0.01	0.76 ± 0.01	0.80 ± 0.01	0.87 ± 0.005	0.031 ± 0.002	0.034 ± 0.003	0.039 ± 0.002	0.036 ± 0.001
3.44	0.72 ± 0.002	0.77 ± 0.02	0.74 ± 0.004	0.83 ± 0.01	0.63 ± 0.01	0.66 ± 0.03	0.66 ± 0.001	0.73 ± 0.001	0.031 ± 0.002	0.037 ± 0.003	0.039 ± 0.001	0.043 ± 0.001

	Vertical configuration											
	Rate 1 (Hz)				**Rate 2 (Hz)**				**Coincidence rate (Hz)**			
xPb (cm)	Lab002	Lab106	Lab6	Roof	Lab002	Lab106	Lab6	Roof	Lab002	Lab106	Lab6	Roof
0	0.79 ± 0.01	0.86 ± 0.01	0.83 ± 0.021	0.99 ± 0.025	0.70 ± 0.01	0.76 ± 0.01	0.71 ± 0.018	0.88 ± 0.022	0.247 ± 0.002	0.256 ± 0.01	0.264 ± 0.01	0.286 ± 0.01
3.44	0.72 ± 0.004	0.76 ± 0.02	0.78 ± 0.02	0.82 ± 0.021	0.63 ± 0.01	0.65 ± 0.002	0.64 ± 0.016	0.73 ± 0.018	0.231 ± 0.01	0.249 ± 0.001	0.238 ± 0.01	0.255 ± 0.01

USC UNIVERSIDADE DE SANTIAGO DE COMPOSTELA

USC
UNIVERSIDADE
DE SANTIAGO
DE COMPOSTELA

Resumen de la tesis en Español

Introducción

En las próximas páginas se resume el trabajo realizado sobre detección de Rayos Cósmicos con detectores de tipo TRASGO y los resultados obtenidos más importantes. Este tipo de detectores fueron diseñados específicamente para el estudio de este tipo de radiación; están basados en la tecnología de cámaras de placa resistiva, RPCs, un tipo de detectores gaseosos muy extendidos en la actualidad, relativamente baratos y con altas prestaciones de eficiencia y respuesta temporal.

En la actualidad están funcionando tres detectores de la llamada familia TRASGO: el detector TRAGALDABAS, localizado en la Facultad de Física de la Universidad de Santiago de Compostela, España; el detector TRISTAN, que ha realizado ya dos viajes desde Vigo (España) hasta la base española Juan Carlos I en la Antártida, en donde se encuentra en la actualidad; y el sistema STRATOS, el más reciente y evolucionado, que ha tomado datos en su laboratorio de desarrollo en el LIP-Coimbra, Portugal, y muy pronto estará operativo en el entorno del aeropuerto de Vigo (España).

El trabajo resumido aquí analiza datos de Rayos Cósmicos y prestaciones operacionales de los tres sistemas mencionados, además de con un cuarto sistema independiente y portátil con el objetivo de completar y complementar las anteriores medidas. Antes de los mencionados resultados, se presenta una descripción y evolución histórica del descubrimiento y la naturaleza de los Rayos Cósmicos, una descripción de la tecnología de detectores de RPCs, y un resumen de las herramientas y métodos desarrollados y usados en este trabajo. Además, incluye no solo análisis de datos reales, sino también

USC
UNIVERSIDADE DE SANTIAGO DE COMPOSTELA

desarrollos y análisis de simulaciones, algo siempre muy importante en cualquier experimento actual.

Rayos Cósmicos

Los llamados Rayos Cósmicos fueron descubiertos por Victor Hess a principios del siglo XX. Hess encontró evidencias de una radiación de partículas que llegaban a nivel suelo terrestre, y años más tarde obtuvo el premio nobel de Física por su descubrimiento. Los rayos cósmicos son de origen solar, galáctico o extragalácticos, producidos en estrellas como el Sol, supernovas u otras fuentes extragalácticas como agujeros negros, enanas blancas y estrellas de neutrones. Los rayos cósmicos primarios recorren largas distancias y se ven influenciadas por campos magnéticos y en menor medida por los campos gravitatorios (si estos no son agujeros negros) hasta llegar a nuestro sistema solar. Primarios cargados se ven desviados por los campos magnéticos generados por el sol y por el campo magnético generado por la Tierra. Algunas partículas cósmicas cargadas se ven atrapadas por trampas magnéticas si su velocidad no es lo suficientemente altas o simplemente desviadas sin interaccionar con la Tierra. Si tienen la suficiente energía cinética como para evitar el campo magnético terrestre, interaccionan con la atmósfera de la Tierra generando una cascada atmosférica de partículas (Extensive Air Shower, EAS) y produciendo grandes cantidades de los llamados rayos cósmicos secundarios, que son los que llegan hasta la superficie terrestre. Éstos, llegan a un ritmo de unos 180 por metro cuadrado y por segundo, siendo en su mayoría muones, una partícula inestable muy penetrante y electrones y fotones de alta energía, o rayos gamma. Estos llegan a alcanzar energías una 50 veces mayores que las de los rayos X mas energéticos. Se pueden diferenciar varias partes en una cascada atmosférica: la primera interacción del cósmico con la parte alta de la atmósfera, el núcleo o core de la cascada y las diferentes componentes que la forman (hadrónica, electromagnética, muónica y nucleónica). Las partículas productos de las sucesivas interacciones llegan a nivel del suelo (muones, neutrones, electrones, fotones y en menor medida piones) o simplemente atraviesan la Tierra (neutrinos).

USC
UNIVERSIDADE DE SANTIAGO DE COMPOSTELA

Los rayos cósmicos secundarios mas abundantes a nivel del suelo decimos que son los muones; casi todos ellos llegan próximos a la dirección vertical. En el caso de los electrones y los rayos gamma, su distribución es mas uniforme, aunque los efectos que sufren al atravesar materiales son muy diferentes a los sufridos por los muones. Además, la forma en la que se agrupa la llegada de todos estos a la superficie terrestre es un indicativo de la naturaleza, propiedades y características de la partícula primara que dio lugar a la EAS.

Detectores de Placa Resistiva, Resistive Plate Chambers (RPCs), y la Familia Trasgo.

Las RPCs son detectores de tipo gaseoso ampliamente utilizados en experimentos de Física Nuclear y de Partículas. Fueron usados inicialmente como contadores o detectores de *trigger* a la entrada de grandes espectrómetros. Sin embargo, la posterior mejora en sus diseños permiten que puedan usarse como detectores de *tracking*, y más comúnmente como detectores de tiempo de vuelo, alcanzado resoluciones bien por debajo de 100 ps.

La base de un sistema de RPC consiste en detectar la descarga eléctrica producida por la ionización de la partícula incidente al atravesar el gas activo, el cual se encuentra sometido a una alta diferencia de potencial. Esta ionización induce una señal eléctrica en los electrodos de lectura, señal que es aplacada y localizada gracias a la inclusión de un material altamente resistivo entre los electrodos y la zona activa. Posteriormente, esa señal eléctrica es amplificada y tratada por una electrónica adecuada, y el resultado final es analizado en un sistema de adquisición.

En esta tesis hemos trabajado con detectores de la familia Trasgo. Estos detectores son del tipo RPC con múltiples volúmenes activos y que están enfocados al estudio de rayos cósmicos.
El proyecto – o también llamada familia – Trasgo (*TRAcking reconStructinG mOdule*) fue propuesto por J.A. Garzón y colaboradores en 2011 [60] con el objetivo de desarrollar detectores

USC UNIVERSIDADE DE SANTIAGO DE COMPOSTELA

simples, económicos y modulares, pero de altas prestaciones, basados en RPCs, y dedicados al estudio integral de Rayos Cósmicos y sus efectos asociados tales como las propiedades de la atmósfera terrestre. Durante estos años se han desarrollado y construido varios detectores tipo Trasgo, de los cuales, este trabajo presenta análisis de datos y prestaciones de tres de ellos.

El primer sistema construido y operativo es el detector TRAGALDABAS. Consiste en 4 planos de RPCs de doble gap, con una separación aproximada de $50\,cm$ entre ellos, y una área de detección por plano de cerca de $2\,m^2$ dividida en celdas rectangulares. Implementa la electrónica de Front-End y el sistema de adquisición de datos del experimento HADES del GSI. Está situado en la Facultad de Física de la Universidad de Santiago de Compostela, y lleva tomando datos desde 2015.

El segundo sistema de la familia Trasgo analizado en este trabajo es el detector TRISTAN. Muy similar a TRAGALDABAS, consta de 3 planos de RPCs con una área activa un poco menor que el primero, y prácticamente la misma electrónica. Este detector tomó datos durante un viaje de ida y vuelta desde Vigo (España) a la base española en la Antártida entre 2018 y 2019, y posteriormente en otro viaje solo de ida a la misma localización, donde se encuentra operativo en la actualidad.

El tercer detector de tipo Trasgo evaluado en este trabajo, STRATOS, tiene una estructura similar a los dos anteriores pero incorpora ciertas mejoras que serán mencionadas en su capítulo correspondiente.

USC
UNIVERSIDADE DE SANTIAGO DE COMPOSTELA

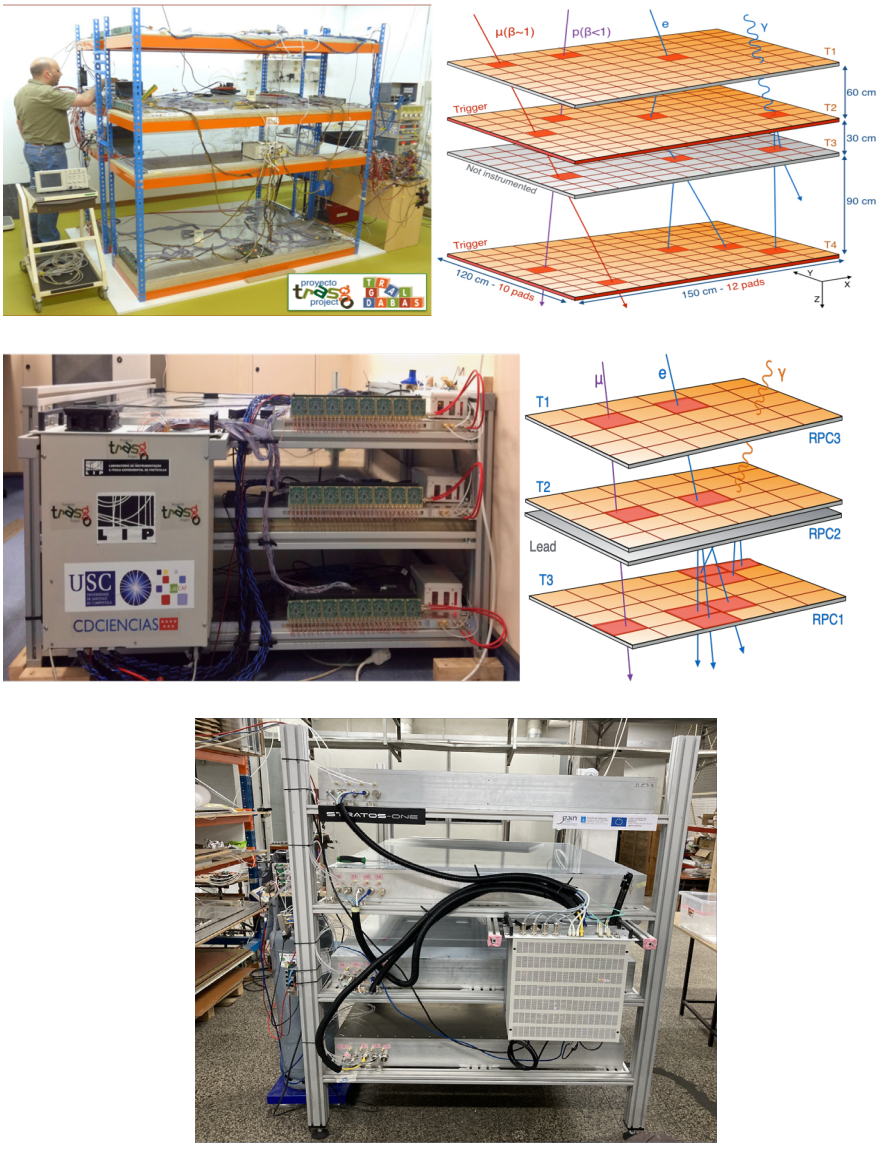

Figura 10.1: Fotografía de los tres detectores tipo Trasgo evaluados en este trabajo. Arriba: el detector TRAGALDABAS instalado en la Facultad de Física de la Universidad de Santiago de Compostela, junto con un esquema de sus planos detectores. Centro: fotografía del detector TRISTAN instalado en la Antártida, junto a su esquema de planos detectores. Abajo: fotografía del sistema STRATOS recientemente desarrollado en el LIP - Coimbra.

USC UNIVERSIDADE DE SANTIAGO DE COMPOSTELA

El algoritmo de TimTrack

Uno de los aspectos más importantes en el análisis de datos experimentales es la reconstrucción de los eventos. El algoritmo TimTrack está basado en el método de mínimos cuadrados y es la herramienta de reconstrucción de referencia en los detectores de la familia Trasgo [73, 74]. El objetivo de TimTrack es la determinación de los parámetros dinámicos de la partícula a partir de las medidas experimentales obtenidas de los detectores. Estos parámetros se agrupan en un vector llamado *saeta* (**s**).

El vector *saeta* contiene las coordenadas del inicio de la propagación de la partícula, el tiempo inicial respecto a un contador externo, las pendientes de la trayectoria según los ejes predefinidos *X* e *Y*, y la llamada lentitud o inversa de la velocidad. Una de las ventajas del método es que TimTrack es capaz de unificar todos los datos experimentales independientemente del tipo de detector que los mide. Si en un mismo experimento tenemos, por ejemplo, detectores RPC junto con plásticos centelleadores, TimTrack es capaz de manejarlos de manera conjunta.

La conexión entre el espacio de medidas experimentales y el espacio de los parámetros se realiza a través de un modelo **m**(**s**). Este modelo consta de tantas ecuaciones como datos experimentales. Dependiendo del tipo de detector y del problema a tratar tendremos una forma del modelo u otra. Los parámetros finales son obtenidos tras resolver una ecuación matricial que involucra la configuración del sistema y los pesos estadísticos.

Dependiendo del tipo de modelo que tengamos, podemos distinguir entre TimTrack lineal o no lineal. El TimTrack de tipo no lineal se resuelve de manera iterativa. El algoritmo de resolución es el mismo que el de cualquier problema de análisis de varias variables: proponemos una solución inicial y la vamos modificando hasta encontrar el mínimo. Para el criterio de convergencia, proponemos criterios basados en el módulo euclídeo de las *saetas*.

USC
UNIVERSIDADE DE SANTIAGO DE COMPOSTELA

TimTrack puede ser usado como herramienta de calibración, como algoritmo de reconstrucción de trayectorias o incluso como herramienta de análisis y ajuste matemático de funciones. En este trabajo se ha hecho uso de TimTrack tanto en la reconstrucción de la trayectoria de las partículas en los detectores como en el análisis de tasas de un cuarto sistema de detección usado como complemento a los sistemas de RPCs.

Análisis de datos reales y simulados con el detector TRAGALDABAS

Como se ha ya mencionado, TRAGALDABAS fue el primer detector operativo de la familia Trasgo. Se trata de un sistema de 4 planos de RPCs con una área activa de 1.5 x 1.2 m² por plano, una cobertura de ángulo sólido vertical de 5 sr y una resolución temporal global por debajo de 300 ps. Lleva desde 2015 tomando datos, excepto paradas de mantenimiento, en la Facultad de Física de la USC, a una tasa aproximada de 7 millones de eventos por día.

En este trabajo se ha hecho análisis de datos de TRAGALDABAS, tanto reales como simulados. Respecto a estos últimos, se han desarrollado un gran número de simulaciones sobre el detector dentro del entorno de software *EnsarRoot*, y usando como base de eventos el generador de rayos cósmicos *CRY*. Se ha trabajado también en la geometría del edificio de la facultad y en la mejora de los métodos de reconstrucción de eventos y trayectorias.

USC
UNIVERSIDADE DE SANTIAGO DE COMPOSTELA

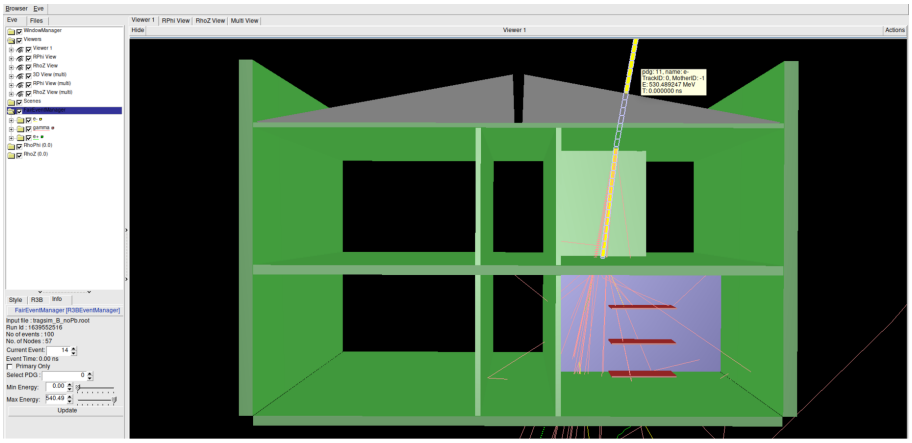

Figura 10.2: Visualización de un evento simulado de rayos cósmicos incidiendo sobre tres planos activos del detector TRAGALDABAS, situado en su posición nominal dentro del edificio de la Facultad de Física, cuya estructura está también simulada.

El objetivo principal del análisis de este capítulo ha sido intentar aproximar la cantidad de muones, electrones y otras partículas detectadas por TRAGALDABAS. Dicho de otro modo, hacer una identificación de partículas. A partir de simulaciones específicamente desarrolladas, se han analizado tres observables físicos, la multiplicidad total, el alcance ponderado y el χ^2 resultante de la reconstrucción de trayectorias con TimTrack, para así desarrollar un método que fenomenológicamente consiga diferenciar partículas de diferente naturaleza, principalmente muones y electrones. Dicho método ha sido adaptado y evolucionado a partir del primer trabajo realizado por Y. Fontenla y colaboradores sobre simulación, y ha sido aplicado por primera vez a datos reales.

Una vez refinado el método, ajustados sus parámetros con datos simulados y evaluado en detalle, fue aplicado a datos de TRAGALDABAS en dos configuraciones distintas: por un lado, tres planos activos, T1, T3 y T4, con *trigger* en coincidencia de T1 y T3; y por otro, la misma configuración pero con una lámina de Pb entre los planos T3 y T4. El objetivo de esta lámina de Pb de 1 cm de espesor no es otro que absorber la componente electrónica, o incluso provocar

USC UNIVERSIDADE DE SANTIAGO DE COMPOSTELA

pequeñas cascadas EM con origen en electrones o fotones de muy alta energía, para así aumentar la capacidad de separación entre electrones y muones, ya que estos últimos tienen capacidad suficiente como para atravesar dicha lámina sin desviarse ni interaccionar de forma significativa.

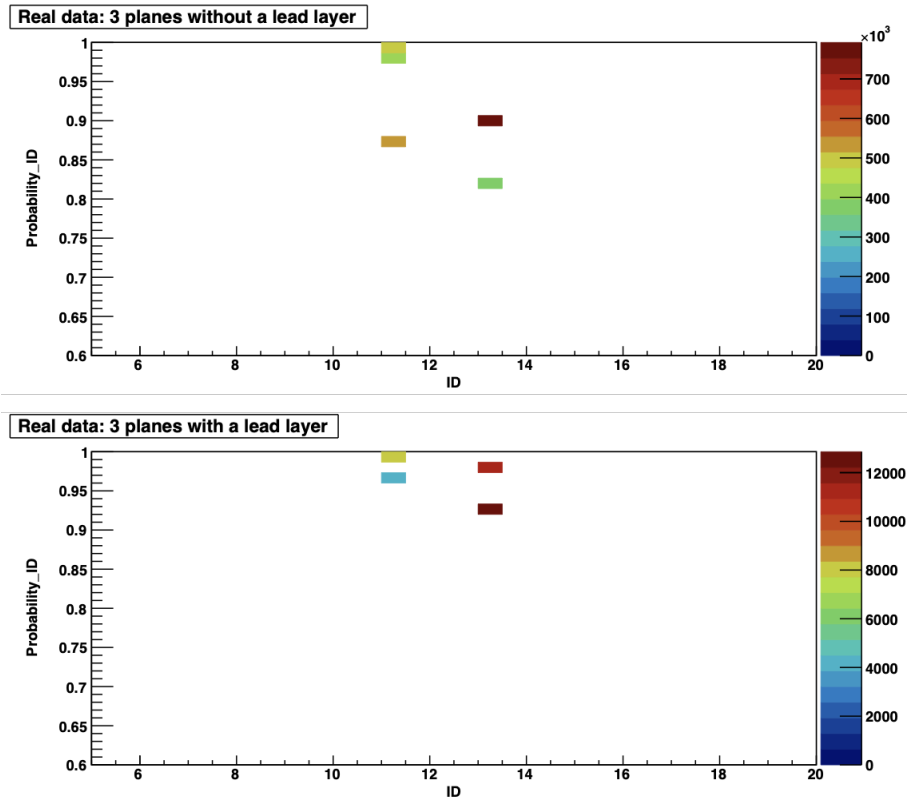

Figura 10.3: Separación entre electrones y muones con TRAGALDABAS antes y después de colocar la lámina de plomo entre los últimos planos. Se observa como la lámina aumenta sustancialmente el número de muones identificados (electrones ID=11; muones ID=13) y se mejora sustancialmente la probabilidad de haber acertado.

Para la configuración sin lámina de plomo, se obtuvo una contribución de aproximadamente 50% muones y 50% electrones, con una probabilidad de en torno a 90% de haber acertado con ser un muon mientras la probabilidad de que fuese un electrón la partícula

USC UNIVERSIDADE DE SANTIAGO DE COMPOSTELA

identificada como tal era del 88%. Una vez que se analizaron los datos de la configuración que incluye la lámina de Pb, se mejoró significativamente en la identificación de partículas, obteniéndose un **66% de muones** con una probabilidad de acierto próxima al 100% y un **34% de electrones** con probabilidad de acierto del 94%.

Además de la identificación y separación de partículas, se ha estudiado la distribución angular de incidencia de cósmicos sobre TRAGALDABAS. El resultado obtenido es ligeramente diferente al esperado "a cielo abierto", lo que sugiere una contribución no despreciable de los materiales del edificio de la Facultad a la dirección final de incidencia sobre el detector. La distribución angular medida ha sido corregida por la aceptancia geométrica del detector, obtenida a partir de datos simulados, y ha sido ajustada la conocida distribución fenomenológica de *Flujo* $\sim \cos^n(\theta)$, obteniéndose en nuestro caso una potencia de $\boldsymbol{n = 2.497}$.

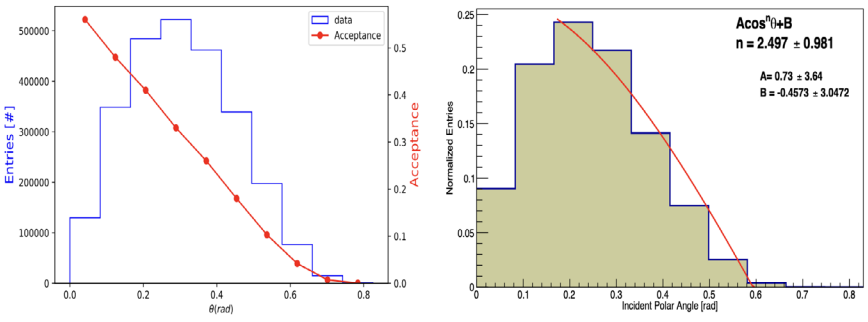

Figura 10.4: Izquierda: Distribución angular de Rayos Cósmicos medida con TRAGALDABAS y curva de aceptancia calculada. Derecha: distribución angular final corregida por aceptancia y ajustada a una curva $\cos^n(\theta)$.

Análisis de datos del detector TRISTAN a lo largo del Océano Atlántico

TRISTAN es otro de los detectores operativos de la familia Trasgo. Se trata de un conjunto de tres planos de RPCs, muy similar a TRAGALDABAS que además incluye por defecto una lámina de plomo de 1 cm cubriendo una superficie aproximada del 40% del

USC UNIVERSIDADE DE SANTIAGO DE COMPOSTELA

sistema con el objetivo de ayudar a una mejor separación de muones y electrones.

TRISTAN ha realizado dos viajes hasta la base española Juan Carlos I en la Antártida. El primero de los viajes fue un trayecto de ida y vuelta desde Vigo (España) hasta la Antártida, pasando por Punta Arenas, en Chile, a bordo del buque Sarmiento de Gamboa. El segundo viaje hasta la Antártida lo hizo a bordo del buque Hespérides, y es allí en donde se encuentra en la actualidad. En este trabajo se han analizado datos de la primera parte del primer viaje, en concreto a lo largo de 38 días entre noviembre y diciembre de 2018 en su trayecto entre Vigo y Punta Arenas.

El objetivo del trabajo de este capítulo ha sido obtener la tasa de medida de rayos cósmicos con TRISTAN en su viaje de Norte a Sur por el Océano Atlántico y su relación con las variables atmosféricas.

Se han estudiado la presión atmosférica y la temperatura a lo largo del viaje; se ha medido la tasa de cósmicos y se ha correlacionado y corregido por la presión y temperatura de cada momento del día. Posteriormente, se ha corregido esta tasa por la eficiencia obtenida del detector y por último, corregido también por aceptancia. Esta aceptancia ha sido calculada mediante simulaciones.

La figura a continuación muestra la trayectoria seguida por el detector y la variación relativa de tasa medida de rayos cósmicos a lo largo del viaje, ya corregida por presión atmosférica, temperatura, eficiencia y aceptancia.

USC
UNIVERSIDADE DE SANTIAGO DE COMPOSTELA

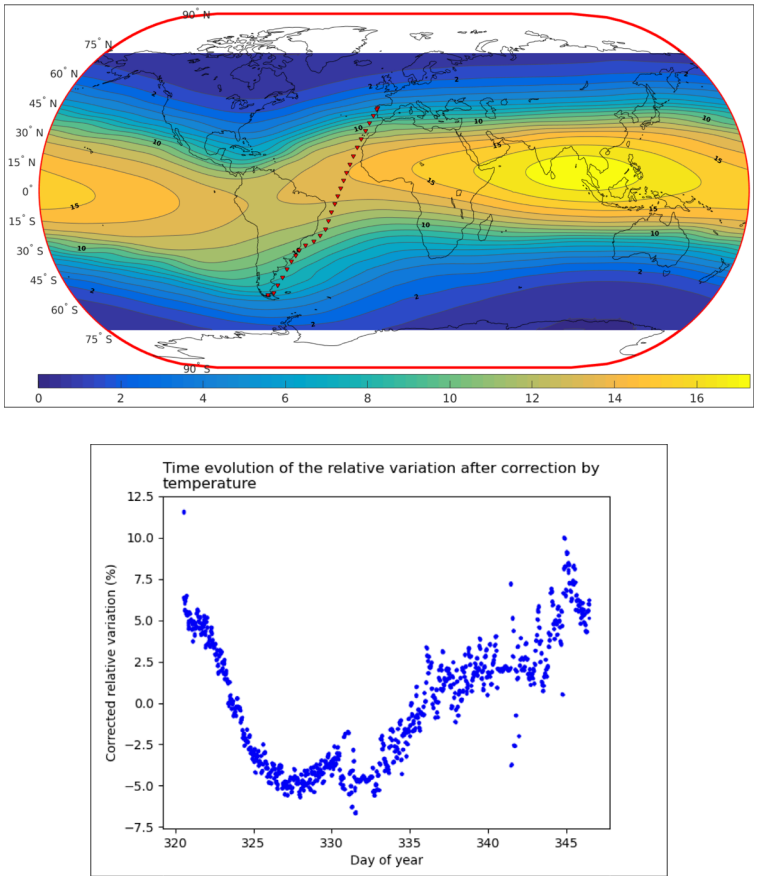

Figura 10.5: Arriba: representación de la trayectoria seguida por TRISTAN en su primer viaje de ida desde Vigo (España) a Punta Arenas (Chile). Cada triángulo representa un día de viaje. Abajo: variación relativa de Rayos Cósmicos observados a lo largo de ese viaje. Se puede ver claramente como la tasa de Rayos Cósmicos es menor en las regiones de la Tierra próximas al ecuador.

Calibraciones y medida de prestaciones del detector STRATOS

La experiencia adquirida en la construcción de los primeros detectores de la familia Trasgo ha llevado al reciente desarrollo del detector STRATOS. Conceptualmente muy similar a los otros dos sistemas anteriores, implementa lectura de señal en forma de 64 *strips* largos por plano (mientras que en los anteriores se leía en *pads* cuadrados) y una

USC UNIVERSIDADE DE SANTIAGO DE COMPOSTELA

electrónica de amplificación y lectura nueva, mucho más optimizada tanto en prestaciones como en precio. El sistema se ha construido en el laboratorio del LIP-Coimbra, Portugal, y es allí donde se han desarrollado las tareas resumidas a continuación.

El detector STRATOS ha sido calibrado en posición, tanto en dimensión longitudinal, en donde dicha posición se obtiene a partir de la diferencia de tiempos de la misma señal a ambos lados del mismo *strip* de lectura, como en dimensión transversal, calculada a partir de la posición misma del *strip* "centro de masas" de la carga recogida. También se ha calibrado en carga, y se han obtenido los parámetros de transformación de unidades desde unidades de ADC a valores físicos de carga, pC. La calibración en las medidas de tiempos del detector también fue desarrollada y además, dada la medida y calibración de la carga, la medida temporal final se ha corregido también por carga (*slewing correction*). Finalmente, la eficiencia del sistema también ha sido evaluada.

Respecto a los resultados obtenidos después de todas las calibraciones y correcciones, cabe destacar que se ha llegado a una resolución temporal de todo el sistema de $\boldsymbol{226\ ps}$, bien por debajo del criterio de aceptancia inicial del diseño establecido en $300\ ps$. Las resoluciones en posición y eficiencias obtenidas para cada uno de los planos de detección se muestran en la tabla a continuación.

Plane	$\sigma_x(mm)$	$\sigma_y(mm)$	Efficiency (%)
1	10.80 ± 0.35	17.17 ± 0.45	92.1
2	6.97 ± 0.22	11.34 ± 0.29	91.7
3	7.03 ± 0.23	12.67 ± 0.33	92.1
4	11.33 ± 0.35	19.53 ± 0.49	92.5

Análisis de clusters de partículas llegando al nivel del suelo

Una de las capacidades mas destacadas de los detectores tipo Trasgo es su capacidad para detectar grupos o clusters de partículas, midiendo sus tiempos y direcciones de llegada, lo que puede permitir formular

USC UNIVERSIDADE DE SANTIAGO DE COMPOSTELA

hipótesis sobre la naturaleza de la cascada y la masa y origen del cósmico primario. Con este último propósito, en este trabajo se han realizado simulaciones de rayos cósmicos primarios de diferentes naturalezas, energías y masas, y se ha estudiado el comportamiento de las cascadas secundarias provocadas por éstos al llegar al nivel del suelo.

Se ha desarrollado un método de definición de cluster de partículas a nivel de suelo y su correspondiente método de búsqueda e identificación de clusters. Todas las propiedades de los clusters identificados y analizados se han correlacionado con las propiedades del rayo cósmico primario. Asimismo, se ha obtenido la función de respuesta de hipotéticos detectores hacia dichos clusters.

En particular, en función del tipo de cluster de partículas que pueden ser medidos e identificados con un detector tipo Trasgo de 1.8 m² de superficie activa, se ha hecho una estimación de la naturaleza, origen, energía y flujo del cósmico primario, y también del tipo, naturaleza y energía de las cascadas atmosféricas producidas. Algunos de los resultados más destacados se resumen en la figura a continuación.

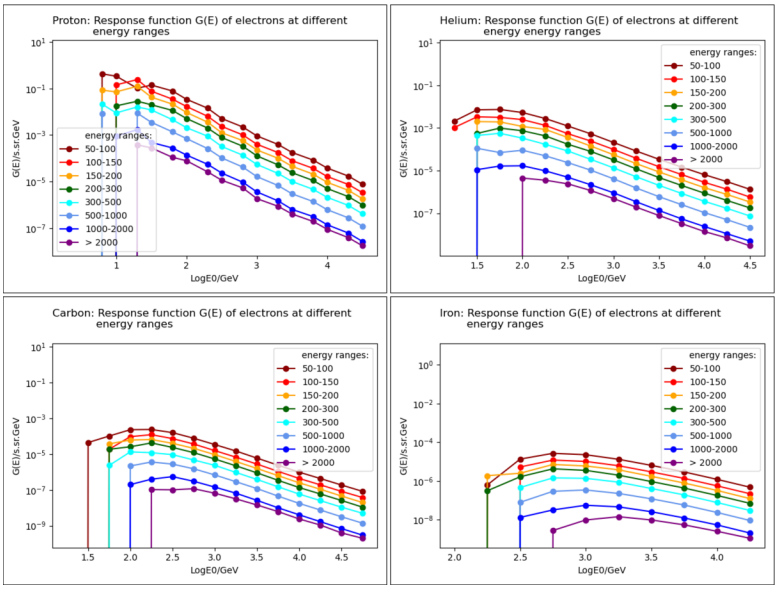

USC UNIVERSIDADE DE SANTIAGO DE COMPOSTELA

Análisis de Rayos Cósmicos con el detector Cosmix

Como se ha comentado ya, el estudio de Rayos Cósmicos secundarios proporciona información muy valiosa sobre diferentes fenómenos físicos. Tanto TRAGALDABAS, como TRISTAN como STRATOS han contribuido a estos estudios. Para dar más seguridad a las medidas de estos sistemas, se han completado los estudios con medidas de Rayos Cósmicos con un sistema diferente, pequeño y portátil, específicamente desarrollado para una medida simple y rápida de Rayos Cósmicos: el detector Cosmix.

Cosmix consiste en dos pequeñas barras centelladoras de CsI(Tl) de 10 y 12 cm de largo, leídas por fotodiodos y con una electrónica simple de adquisición terminada con un sistema de *trigger* y un contador. Se presenta en un conjunto compacto (un pequeño maletín) lo que permite hacer medidas en cualquier lugar.

Así, en este trabajo se ha usado Cosmix para complementar los resultados de tasas de rayos cósmicos en la Facultad de Física de la Universidad de Santiago de Compostela, haciendo medidas en cuatro localizaciones distintas del edificio: a cielo abierto en el tejado de la facultad; en una sala en el tercer piso del edifico; en el mismo laboratorio donde se encuentra TRAGALDABAS en el segundo piso de la facultad, y en una cuarta sala en el sótano del edificio. Se ha medido con diferentes configuraciones de las barras centelladores y diferentes configuraciones de *trigger*, y también se han hecho medidas incluyendo diferentes espesores de plomo encima de los detectores.

Además de las propias tasas medidas, el resultado más destacado al que se ha llegado en este trabajo es la demotración de la gran importancia que tienen los materiales del edificio en las medidas de cósmicos en su interior, en particular con el detector TRAGALDABAS. Como muestra, se puede afirmar que las tasas medidas en el tejado, a cielo abierto, son un 50% mayores que las medidas en cualquier piso interior del edificio, incluso los casos con diferentes blindajes de plomo. Esto sugiere que el edificio actúa, por una parte, como absorbente de una

USC UNIVERSIDADE DE SANTIAGO DE COMPOSTELA

gran cantidad de las cascadas atmosféricas a nivel del suelo, y por otra, como radiador secundario produciendo una mayor contribución de electrones al conjunto de cósmicos en el interior y modificando la distribución angular de los mismos, lo que es consistente con los resultados obtenidos con TRAGALDABAS.

Algunas de las tasas medidas con Cosmix se pueden ver en la tabla a continuación. Destacan dos resultados ya mencionados: primero, la mayor tasa medida siempre en el tejado – a cielo abierto – independientemente de la configuración de los detectores, y tanto de forma individual como en coincidencia, y como esa tasa es aproximadamente constante en cualquier otro punto dentro del edificio; y segundo, la poca reducción a la tasa que producen los espesores de plomo a las coincidencias dentro del edificio, lo que da a entender que los propios materiales del edificio ya absorben la mayor parte de la contribución electrónica, y llegan mayoritariamente muones a las salas de dentro del edificio, de forma muy similar independientemente de donde se encuentre esa sala.

	Horizontal configuration											
	Rate 1 (Hz)				**Rate 2 (Hz)**				**Coincidence rate (Hz)**			
xPb (cm)	Lab002	Lab106	Lab6	Roof	Lab002	Lab106	Lab6	Roof	Lab002	Lab106	Lab6	Roof
0	0.81 ± 0.01	0.87 ± 0.02	0.92 ± 0.02	1.01 ± 0.02	0.69 ± 0.01	0.76 ± 0.01	0.80 ± 0.01	0.87 ± 0.005	0.031 ± 0.002	0.034 ± 0.003	0.039 ± 0.002	0.036 ± 0.001
3.44	0.72 ± 0.002	0.77 ± 0.02	0.74 ± 0.004	0.83 ± 0.01	0.63 ± 0.01	0.66 ± 0.03	0.66 ± 0.001	0.73 ± 0.001	0.031 ± 0.002	0.037 ± 0.003	0.039 ± 0.001	0.043 ± 0.001

	Vertical configuration											
	Rate 1 (Hz)				**Rate 2 (Hz)**				**Coincidence rate (Hz)**			
xPb (cm)	Lab002	Lab106	Lab6	Roof	Lab002	Lab106	Lab6	Roof	Lab002	Lab106	Lab6	Roof
0	0.79 ± 0.01	0.86 ± 0.01	0.83 ± 0.021	0.99 ± 0.025	0.70 ± 0.01	0.76 ± 0.01	0.71 ± 0.018	0.88 ± 0.022	0.247 ± 0.002	0.256 ± 0.01	0.264 ± 0.01	0.286 ± 0.01
3.44	0.72 ± 0.004	0.76 ± 0.02	0.78 ± 0.02	0.82 ± 0.021	0.63 ± 0.01	0.65 ± 0.002	0.64 ± 0.016	0.73 ± 0.018	0.231 ± 0.01	0.249 ± 0.001	0.238 ± 0.01	0.255 ± 0.01

USC UNIVERSIDADE DE SANTIAGO DE COMPOSTELA

References

[1] Wulf, Theodor. "Beobachtungen über die Strahlung hoher Durchdringungsfähigkeit auf dem Eiffelturm." Physikalische Zeitschrift 11 (1910): 811-813.

[2] Hess, Viktor F. "Uber Beobachtungen der durchdringenden Strahlung bei sieben Freiballonfahrten." Phys. Zeits. 13 (1912): 1084-1091.

[3] "The Pierre Auger Cosmic Ray Observatory," *Nucl. Instruments Methods Phys. Res. Sect. A Accel. Spectrometers, Detect. Assoc. Equip.*, vol. 798, pp. 172–213, 2015, doi: https: //doi.org /10. 10 16/j.nima.2015.06.058.

[4] J. Garzon et al., "TRAGALDABAS. First results on cosmic ray studies and their relation with the solar activity, the Earth magnetic field and the atmospheric properties," 2017.

[5] J. P. Saraiva, A. Blanco, J. A. Garzón, D. Garcìa-Castro, L. Lopes and V. Villasante-Marcos, "The TRISTAN detector—2018–2019 latitude survey of cosmic rays," *J. Instrum.*, vol. 15, no. 09, pp. C09024–C09024, 2020, doi: 10.1088/1748-0221 /15/ 09 /c0 90 24.

[6] D. García-Castro *et al.*, "The TRASGO Project. Present Status and Results," *Phys. At. Nucl.*, vol. 84, no. 6, pp. 1070–1079, 2021, doi: 10.1134/S1063778821130093.

[7] D. García. PhD thesis, Universidad de Santiago de Compostela, Departamento de Física de Partículas.

USC UNIVERSIDADE DE SANTIAGO DE COMPOSTELA

[8] I. Garrigós. PhD thesis, Universidad de Santiago de Compostela, Departamento de Física de Partículas.

[9] P. D. Group *et al.*, "Review of Particle Physics," *Phys. Rev. D*, vol. 98, no. 3, p. 30001, Aug. 2018, doi: 10.1103/PhysRevD.98.030001.

[10] K. Greisen, "End to the Cosmic-Ray Spectrum?," *Phys. Rev. Lett.*, vol. 16, no. 17, pp. 748–750, Apr. 1966, doi: 10.1103/PhysRevLett.16.748.

[11] G. T. Zatsepin and V. A Kuzmʹin Upper Limit of the Spectrum of Cosmic Rays, Journal of Experimental and Theoretical Physics Letters 4 (1966), p.78–80.

[12] https://w3.iihe.ac.be/~aguilar/PHYS-467/PA3.html.

[13] M. Tanabashi et al. (Particle Data Group), "Review of Particle Physics," Phys. Rev. D, vol. 98, no. 3, p. 30001, Aug. 2018, doi: 10.1103/PhysRevD.98.030001.

[14] Maurin, D., F. Melot and Richard Taillet. "A database of charged cosmic rays." Astronomy & Astrophysics 569 (2014): A32.

[15] A. W. Strong, I. V Moskalenko and V. S. Ptuskin, "Cosmic-Ray Propagation and Interactions in the Galaxy," *Annu. Rev. Nucl. Part. Sci.*, vol. 57, no. 1, pp. 285–327, Oct. 2007, doi: 10.1146/annurev.nucl.57.090506.123011.

[16] J. R. Hörandel, "On the knee in the energy spectrum of cosmic rays," *Astropart. Phys.*, vol. 19, no. 2, pp. 193–220, 2003, doi: https://doi.org/10.1016/S0927-6505(02)00198-6.

USC
UNIVERSIDADE DE SANTIAGO DE COMPOSTELA

[17] B. Wiebel-Sooth and P. L. Biermann, Landolt-Börnstein, New Series vol. VI/3c (1999) 37.

[18] M. Wiedenbeck et al., Proc. of 28th Int. Cosmic Ray Conf., Tsukuba 4 (2003) 1899.

[19] A.M. Galper et al. The PAMELA experiment: a decade of cosmic ray physics in space. Journal of Physics: Conference Series, 798(1):012033, 2017.

[20] IceCube Observatory. https://icecube.wisc.edu/

[21] S. Chakraborty and I. Izaguirre. Star-forming galaxies as the origin of Ice Cube neutrinos: Reconciliation with Fermi-LAT gamma rays. https://arxiv.org/abs/hep-ph/9609357, 2016.

[22] L. Cremonesi. Cosmic-ray muon tomography for anti-terrorism applications. Master's thesis, University College London, 2011.

[23] W. Atkinson, "Single Event Effects from Ions Produced in Nuclear Reactions of CMOS with Cosmic Rays," Mar. 2021.

[24] A. A. Pacini, "Cosmic rays: bringing messages from the sky to the Earth's surface," Rev. Bras. Ensino FÃ\-sica, vol. 39, 2017, [Online]. Available:http://www.scielo.br/scielo.php?script=sci_arttext&pid=S1806-11172017000100406&nrm=iso.

[25] Gran Telescopio Milimétrico Alfonso Serrano. http:// www. lmtgtm.org.

[26] Yangbajing International Cosmic Ray Observatory in Tibet. http://www.ircip.cn/bbx/999722-999726.html?id=26645& newsid=639942.

USC UNIVERSIDADE DE SANTIAGO DE COMPOSTELA

[27] R. Bellotti *et al.*, "Measurement of the negative muon spectrum between 0.3 and 40 GeV/c in the atmosphere," *Phys. Rev. D*, vol. 53, no. 1, pp. 35–43, Jan. 1996, doi: 10.1103 /PhysRev D.53. 35.

[28] M. Circella, "Primary cosmic ray and muon measurements with CAPRICE," *Nucl. Phys. B - Proc. Suppl.*, vol. 100, no. 1, pp. 127–129,2001, doi: https://doi.org/10.1016/S0920-5632(01)01425-6.

[29] R. Bellotti and others, "Balloon measurements of cosmic ray muon spectra in the atmosphere along with those of primary protons and helium nuclei over mid latitude," *Phys. Rev. D*, vol. 60, p. 52002, 1999, doi: 10.1103/PhysRevD.60.052002.

[30] S. Haino *et al.*, "Measurements of primary and atmospheric cosmic-ray spectra with the BESS-TeV spectrometer," *Phys. Lett. B*, vol. 594, no. 1, pp. 35–46, 2004, doi: https: //doi . org / 10.1016/j.physletb.2004.05.019.

[31] M. Boezio *et al.*, "Energy spectra of atmospheric muons measured with the CAPRICE98 balloon experiment," *Phys. Rev. D*, vol. 67, no. 7, p. 72003, Apr. 2003, doi: 10.1103/PhysRevD.67 .072003.

[32] S. Coutu *et al.*, "Energy spectra, altitude profiles and charge ratios of atmospheric muons," *Phys. Rev. D*, vol. 62, no. 3, p. 32001, Jun. 2000, doi: 10.1103/PhysRevD.62.032001.

[33] T. Sanuki, M. Honda, T. Kajita, K. Kasahara and S. Midorikawa, "Study of cosmic ray interaction model based on atmospheric muons for the neutrino flux calculation," *Phys. Rev. D*, vol. 75, no. 4, p. 43005, Feb. 2007, doi: 10.1103/PhysRevD.75.043005.

USC UNIVERSIDADE DE SANTIAGO DE COMPOSTELA

[34] R. Cardarelli, R. Santonico, A. Di Biagio and A. Lucci, “Progress in resistive plate counters,” *Nucl. Instruments Methods Phys. Res. Sect. A Accel. Spectrometers, Detect. Assoc. Equip.*, vol. 263, no. 1, pp. 20–25, 1988, doi: https://doi.org/10.1016/0168-9002(88)91011-X.

[35] R. Santonico and R. Cardarelli, “Development of resistive plate counters,” *Nucl. Instruments Methods Phys. Res.*, vol. 187, no. 2, pp. 377–380, 1981, doi: https://doi.org/10.1016/0029-554X(81)90363-3.

[36] G. Cattani and the RPC group. The resistive plate chambers of the atlas experiment: performance studies. Journal of Physics: Conference Series, 280(1):012001, 2011.

[37] P. Baesso et al., “A high resolution resistive plate chamber tracking system developed for cosmic ray muon tomography,” J. Instrum., vol. 8, no. 08, pp. P08006–P08006, 2013, doi: 10.1088/1748-0221/8/08/p08006.

38] C. Lippmann. Detector physics of Resistive Plate Chambers. PhD thesis, Johann Wolfgang Goethe-Universität Frankfurt am Main, 2003.

[39] Nicholas Tsoulfanidis, ”Measurements and Detection of Radiation”, 2nd Edition (1995), University of Missouri-Rolla.

[40] J. Keuffel, Phys. Rev. 73(1948)531.

[41] V. V Parkhomchuck, Y. N. Pestov and N. V Petrovykh, “A spark counter with large area,” *Nucl. Instruments Methods*, vol. 93, no. 2, pp. 269–270, 1971, doi: https://doi.org/10.1016/0029-554X(71)90475-7.

USC UNIVERSIDADE DE SANTIAGO DE COMPOSTELA

[42] P. Cabanelas. Software development and performance analysis of the HADES Resistive Plate Chamber time-of-flight detector at GSI. PhD thesis, Universidad de Santiago de Compostela, Departamento de Física de Partículas, 2011.

[43] D. González-Díaz. Research and Developments on Timing RPCs. Application to the ESTRELA Detector of the HADES experiment at GSI. PhD thesis, Universidad de Santiago de Compostela, Departamento de Física de Partículas, 2006.

[44] G. Chiodini, M. R. Coluccia, E. Gorini, F. Grancagnolo and M. Primavera, "Laser beam characterization of the ATLAS RPC gas mixture," *Nucl. Phys. B - Proc. Suppl.*, vol. 172, pp. 284–288, 2007, doi: https://doi.org/10.1016/j.nuclphysbps.2007.08.013.

[45] M. Abbrescia *et al.*, "Eco-friendly gas mixtures for Resistive Plate Chambers based on tetrafluoropropene and Helium," *J. Instrum.*, vol. 11, no. 08, pp. P08019–P08019, 2016, doi: 10.1088/1748-0221/11/08/p08019.

[46] D. M. Rossi and H. Simon, "A closed-circuit gas recycling system for RPC detectors," *Nucl. Instruments Methods Phys. Res. Sect. A, Accel. Spectrometers, Detect. Assoc. Equip.*, vol. 661, no. Suppl1, pp. S230–S233, doi: DOI:101016/jnima201007053.

[47] J. Wang, "RPC performance at KLM/BELLE," *Nucl. Instruments Methods Phys. Res. Sect. A-accelerators Spectrometers Detect. Assoc. Equip. - NUCL INSTRUM METH PHYS RES A*, vol. 508, pp. 133–136, Aug. 2003, doi: 10.1016/S0168-9002(03)01335-4.

USC
UNIVERSIDADE DE SANTIAGO DE COMPOSTELA

[48] D. Piccolo *et al.*, "The RPC-based IFR system at BaBar experiment: preliminary results," *Nucl. Instruments Methods Phys. Res. Sect. A Accel. Spectrometers, Detect. Assoc. Equip.*, vol. 477, no. 1, pp. 435–439, 2002, doi: https://doi.org/10. 10 16/S0168-9002(01)01810-1.

[49] C. Bacci *et al.*, "Results from the analysis of data collected with a 50m2 RPC carpet at YangBaJing," *Nucl. Instruments Methods Phys. Res. Sect. A Accel. Spectrometers, Detect. Assoc. Equip.*, vol. 456, no. 1, pp. 121–125, 2000, doi: https://doi.org/10.1016/S0168-9002(00)00976-1.

[50] I. Crotty, J. Lamas Valverde, G. Laurenti, M. C. S. Williams and A. Zichichi, "The non-spark mode and high rate operation of resistive parallel plate chambers," *Nucl. Instruments Methods Phys. Res. Sect. A Accel. Spectrometers, Detect. Assoc. Equip.*, vol. 337, no. 2, pp. 370–381, 1994, doi: https://doi.org/10.1016/0168-9002(94)91105-3.

[51] I. Duerdoth *et al.*, "The transition from proportional to streamer mode in a resistive plate chamber," *Nucl. Instruments Methods Phys. Res. Sect. A Accel. Spectrometers, Detect. Assoc. Equip.*, vol. 348, no. 2, pp. 303–306, 1994, doi: https://doi.org/10.1016/0168-9002(94)90751-X.

[52] R. Cardarelli, A. Di Ciaccio and R. Santonico, "Performance of a resistive plate chamber operating with pure CF3Br," *Nucl. Instruments Methods Phys. Res. Sect. A Accel. Spectrometers, Detect. Assoc. Equip.*, vol. 333, no. 2, pp. 399–403, 1993, doi: https://doi.org/10.1016/0168-9002(93)91182-M.

USC
UNIVERSIDADE DE SANTIAGO DE COMPOSTELA

[53] M. Alviggi *et al.*, "First results of the cosmic rays test of the RPC of the ATLAS muon spectrometer at LHC," *Nucl. Instruments Methods Phys. Res. Sect. A Accel. Spectrometers, Detect. Assoc. Equip.*, vol. 518, no. 1, pp. 79–81, 2004, doi: https://doi.org/ 10.1016/j.nima.2003.10.029.

[54] M. Abbrescia *et al.*, "Study of long-term performance of CMS RPC under irradiation at the CERN GIF," *Nucl. Instruments Methods Phys. Res. Sect. A Accel. Spectrometers, Detect. Assoc. Equip.*, vol. 533, no. 1, pp. 102–106, 2004, doi: https://doi.org/ 10.1016/j.nima.2004.07.009.

[55] A. N. Akindinov *et al.*, "Latest results on the performance of the multigap resistive plate chamber used for the ALICE TOF," *Nucl. Instruments Methods Phys. Res. Sect. A Accel. Spectrometers, Detect. Assoc. Equip.*, vol. 533, no. 1, pp. 74–78, 2004, doi: https://doi.org/10.1016/j.nima.2004.07.004.

[56] M. Petrovici *et al.*, "Multistrip multigap symmetric RPC," *Nucl. Instruments Methods Phys. Res. Sect. A Accel. Spectrometers, Detect. Assoc. Equip.*, vol. 508, no. 1, pp. 75–78, 2003, doi: https://doi.org/10.1016/S0168-9002(03)01280-4.

[57] P. Fonte, A. Smirnitski and M. C. S. Williams, "A new high-resolution TOF technology," *Nucl. Instruments Methods Phys. Res. Sect. A Accel. Spectrometers, Detect. Assoc. Equip.*, vol. 443, no. 1, pp. 201–204, 2000, doi: https://doi.org/10. 1016/ S0 168-9002(99)01008-6.

[58] P. Fonte, R. Ferreira Marques, J. Pinhão, N. Carolino and A. Policarpo, "High-resolution RPCs for large TOF systems," *Nucl. Instruments Methods Phys. Res. Sect. A Accel. Spectrometers, Detect. Assoc. Equip.*, vol. 449, no. 1, pp. 295–301, 2000, doi: https://doi.org/10.1016/S0168-9002(99)01299-1.

USC
UNIVERSIDADE DE SANTIAGO DE COMPOSTELA

[59] A. Blanco *et al.*, "A large area timing RPC," *Nucl. Instruments Methods Phys. Res. Sect. A Accel. Spectrometers, Detect. Assoc. Equip.*, vol. 485, no. 3, pp. 328–342, 2002, doi: https://doi.org/10.1016/S0168-9002(01)02119-2.

[60] D. Belver, P. Cabanelas, D. Domínguez, J. A. Garzón, G. Kornakov, and M. F. Morales, "TRASGO: A proposal for a timing RPCs based detector for analyzing cosmic ray air showers,"*Nucl. Instruments Methods Phys. Res. Sect. A Accel. Spectrometers, Detect. Equip.*, vol. 661, pp. S163–S167, 2012, doi: https://doi.org/10.1016/j.nima. 2010.09.173.

[61] D. Belver *et al.*, "Performance of the Low-Jitter High-Gain/Bandwidth Front-End Electronics of the HADES tRPC Wall," *Nucl. Sci. IEEE Trans.*, vol. 57, pp. 2848–2856, Nov. 2010, doi: 10.1109/TNS.2010.2056928.

[62] H. Alvarez-Pol and others, "TRAGALDABAS: A new high resolution detector for the regular study of cosmic rays," *J. Phys. Conf. Ser.*, vol. 632, no. 1, p. 12010, 2015, doi: 10.1088/1742-6596/632/1/012010.

[63] A. Blanco *et al.*, "TRAGALDABAS: a new RPC based detector for the regular study of cosmic rays," *J. Instrum.*, vol. 9, p. C09027, Sep. 2014, doi: 10.1088/1748-0221/9/09/C09027.

[64] P. Assis *et al.*, "R&D for an autonomous RPC station in air shower detector arrays," *Proc. 32nd Int. Cosm. Ray Conf. ICRC 2011*, vol. 3, pp. 133–136, Jan. 2011, doi: 10.7529/ ICRC 2011 /V 03/0663.

USC
UNIVERSIDADE DE SANTIAGO DE COMPOSTELA

[65] A. Gil *et al.*, "Front-End electronics development for the new Resistive Plate Chamber detector of HADES," *J. Instrum.*, vol. 2, no. 11, pp. T11001–T11001, 2007, doi: 10.1088/1748-0221/ 2/ 11/t11001.

[66] Kornakov, G. (2012). New advances and developments on the RPC-TOF wall of the HADES experiment at GSI. PhD thesis. University of Santiago de Compostela.

[67] Laboratory of Instrumentation and Experimental Particle Physics:https://www.lip.pt

[68] D. Garcia-Castro *et al.*, *The TRISTAN detector. Cosmic ray survey between latitudes 38^{o}N and 53^{o}S along the Atlantic Ocean*. 2021.

[69] http://trb.gsi.de/

[70] L. Lopes *et al.*, "Resistive Plate Chambers for the Pierre Auger array upgrade," *J. Instrum.*, vol. 9, no. 10, pp. C10023–C10023, 2014, doi: 10.1088/1748-0221/9/10/c10023.

[71] J. J. Blanco and others, "ORCA (Antarctic Cosmic Ray Observatory): 2018 Latitudinal Survey," *PoS*, vol. ICRC2019, p. 1059, 2020, doi: 10.22323/1.358.1059.

[72] D. Garca Castro and J. A. Garzon, "The TRISTAN Antarctic Cosmic Ray detector.," *PoS*, vol. ICRC2019, p. 71, 2020, doi: 10. 22 32 3 /1.358.0071.

USC
UNIVERSIDADE DE SANTIAGO DE COMPOSTELA

[73] J. A. Garzón, P. Cabanelas, D. González Díaz, and T. Kurtukian, "TimTrack: A new concept for the tracking of charged particles with timing detectors," *Nucl. Instruments Methods Phys. Res. Sect. A Accel. Spectrometers, Detect. Assoc. Equip.*, vol. 629, no. 1, pp. 311–322, 2011, doi: https: //doi.org/ 10.1016/ j.nima. 2010.10.095.

[74] J. A. Garzón and P. Cabanelas, "TimTrack: A matrix formalism for a fast time and track reconstruction with timing detectors," *Nucl. Instruments \& Methods Phys. Res. Sect. A-accelerators Spectrometers Detect. Assoc. Equip.*, vol. 661, 2012.

[75] G. Audi, W. G. Davies, and G. E. Lee-Whiting, "A method of determining the relative importance of particular data on selected parameters in the least-squares analysis of experimental data," *Nucl. Instruments Methods Phys. Res. Sect. A Accel. Spectrometers, Detect. Assoc. Equip.*, vol. 249, no. 2, pp. 443–450, 1986, doi: https://doi.org/10.1016/0168-9002 (86) 90 700-X.

[76] L. Lyons, *Statistics for Nuclear and Particle Physicists*. Cambridge: Cambridge University Press, 1986.

[77] José Cuenca. Simulation and reconstruction algorithms for a commercial muon tomography system. PhD thesis, Universidad de Santiago de Compostela, Departamento de Física de Partículas, 2018.

[78] H. Álvarez Pol. Física computacional avanzada. Lecture notes at USC, 2017.

[79] E. Winsberg. Computer simulations in science. In Edward N. Zalta, editor, The Stanford Encyclopedia of Philosophy. Metaphysics Research Lab, Stanford University, summer 2018 edition, 2018.

USC UNIVERSIDADE DE SANTIAGO DE COMPOSTELA

[80] N. Metropolis and S. Ulam. The Monte Carlo Method. Journal of the American Statistical Association, 44(247):335–341, 1949.

[81] N. Metropolis, The Beginning of the Monte Carlo Method, Phil. Mag. 6-1 (1901), p. 198-227.

[82] D. Frenkel et B. Smit, Understanding Molecular Simulation, Academic Press 2002 (2001).

[83] J. Allison *et al.*, "Recent developments in Geant4," *Nucl. Instruments Methods Phys. Res. Sect. A Accel. Spectrometers, Detect. Assoc. Equip.*, vol. 835, pp. 186–225, 2016, doi: https://doi.org/10.1016/j.nima.2016.06.125.

[84] S. Agostinelli *et al.*, "Geant4—a simulation toolkit," *Nucl. Instruments Methods Phys. Res. Sect. A Accel. Spectrometers, Detect. Assoc. Equip.*, vol. 506, no. 3, pp. 250–303, 2003, doi: https://doi.org/10.1016/S0168-9002(03)01368-8.

[85] R. Brun and F. Rademakers, "ROOT — An object oriented data analysis framework," *Nucl. Instruments Methods Phys. Res. Sect. A Accel. Spectrometers, Detect. Assoc. Equip.*, vol. 389, no. 1, pp. 81–86, 1997, doi: https://doi.org/10.1016/S0168-9002(97)00048-X.

[86] D. Bertini, M. A-Turany, I. Koenig, and F. Uhlig, "The FAIR simulation and analysis framework," J. Phys. Conf. Ser., vol. 119, no. 3, p. 32011, 2008, doi: 10.1088/1742-6596/119/3/032011.

[87] http://www.ensarfp7.eu/

USC
UNIVERSIDADE DE SANTIAGO DE COMPOSTELA

[88] P. Cabanelas, H. Alvarez-Pol, E. Galiana, and Y. González-Rozas, "EnsarRoot: The framework for simulation and data analysis for ENSAR," *J. Phys. Conf. Ser.*, vol. 1024, p. 12038, 2018, doi: 10.1088/1742-6596/1024/1/012038.

[89] C. Hagmann, D. Lange, and D. Wright, "Cosmic-ray shower generator (CRY) for Monte Carlo transport codes," *2007 IEEE Nucl. Sci. Symp. Conf. Rec.*, vol. 2, pp. 1143–1146, 2007.

[90] MCNPX User's Manual, Version 2.5.0, Laurie Waters, ed., LA-CP-05-0369 (2005).

[91] P. Cabanelas, Y. Fontenla, and J. Garzon, *MIDAS: A particle identification tool for the TRAGALDABAS Cosmic Ray telescope.* 2019.

[92] S. Sagisaka, "Atmospheric effects on cosmic-ray muon intensities at deep underground depths," *Nuovo Cim. C*, vol. 9, no. 4, pp. 809–828, 1986, doi: 10.1007/BF02558081.

[93] R. R. S. De Mendonça, J.-P. Raulin, E. Echer, V. S. Makhmutov, and G. Fernandez, "Analysis of atmospheric pressure and temperature effects on cosmic ray measurements," *J. Geophys. Res. Sp. Phys.*, vol. 118, no. 4, pp. 1403–1409, 2013, doi: https://doi.org/10.1029/2012JA018026.

[94] Dorman, L. I. (2004), Cosmic Rays in the Earth's Atmosphere and Under- ground, Kluwer, Dordrecht, Netherlands.

[95] A. Dmitrieva, R. Kokoulin, A. Petrukhin, and D. Timashkov, "Corrections for temperature effect for ground-based muon hodoscopes," *Astropart. Phys. - ASTROPART Phys.*, vol. 34, pp. 401–411, Jan. 2011, doi: 10.1016/j.astropartphys.2010.10.013.

USC UNIVERSIDADE DE SANTIAGO DE COMPOSTELA

[96] S. Osprey *et al.*, "Sudden stratospheric warmings seen in MINOS deep underground muon data," *Geophys. Res. Lett.*, vol. 36, Mar. 2009.

[97] Tilav, S., Desiati, P., Kuwabara, T., Rocco, D., Rothmaier, F., Simmons, M., & Wissing, H. (2010). Atmospheric Variations as observed by IceCube. arXiv preprint arXiv:1001.0776.

[98] M. D. Berkova, A. V Belov, E. A. Eroshenko, and V. G. Yanke, "Temperature effect of the muon component and practical questions for considering it in real time," *Bull. Russ. Acad. Sci. Phys.*, vol. 75, no. 6, pp. 820–824, 2011, doi: 10.3103/ S 10 62 873811060086.

[99] A. Duperier, "The Meson Intensity at the Surface of the Earth and the Temperature at the Production Level," *Proc. Phys. Soc. Sect. A*, vol. 62, no. 11, pp. 684–696, 1949, doi: 10.1088/0370-1298/62/11/302.

[100] R. R. S. de Mendonça *et al.*, "THE TEMPERATURE EFFECT IN SECONDARY COSMIC RAYS (MUONS) OBSERVED AT THE GROUND: ANALYSIS OF THE GLOBAL MUON DETECTOR NETWORK DATA," *Astrophys. J.*, vol. 830, no. 2, p. 88, 2016, doi: 10.3847/0004-637x/830/2/88.

[101] V. L. Yanchukovsky and V. S. Kuzmenko, "Atmospheric effects of the cosmic-ray mu-meson component," Solar-Terrestrial Phys., vol. 4, no. 3, pp. 76–82, 2018.

[102] D. Belver. The Front-End Electronics of the HADES timing RPCs wall: design, devel- opment and performances analysis. PhD thesis, USC, 2009.

[103] https://www.iap.kit.edu/corsika/

USC UNIVERSIDADE DE SANTIAGO DE COMPOSTELA

[104] https://www.cenbg.in2p3.fr/grand-public-scolaires/les-rayons-cosmiques-au- lycee/cosmix/

[105] N. Arnaud et al., “Cosmic ray detectors for high schools in France,” Nucl. Part. Phys. Proc., vol. 273–275, pp. 1233–1238, 2016, doi: https://doi.org/10.1016/j.nuclphysbps.2015.09.196.

[106] P. Dunne, “Demonstrating cosmic ray induced electromagnetic cascades in the A-level laboratory,” Phys. Educ., vol. 34, no. 1, pp. 19–27, 1999, doi: 10.1088/0031-9120/34/1/015.

[107] Martin B R, Shaw G, 2008 Particle Physics (Chichester: John Wiley and Sons).

[108] K. Abdullah, FUNDAMENTALS IN NUCLEAR PHYSICS. 2014.

[109] Y. Fontenla. STUDIES ON THE COMPOSITION AND ENERGY OF SECONDARY COSMIC RAYS WITH THE TRAGALDABAS DETECTOR. PhD thesis, Universidad de Santiago de Compostela, Departamento de Física de Partículas, 2019.

USC
UNIVERSIDADE DE SANTIAGO DE COMPOSTELA

USC
UNIVERSIDADE
DE SANTIAGO
DE COMPOSTELA

Appendix

The acceptance in particle physics detectors

1 Introduction

Efficiency, acceptance, geometrical acceptability, and other terms are often used in nuclear and particle physics and, by extension, any subject where nuclear instrumentation is utilized. We present a brief review of those principles and associated topics in this appendix from a very general point of view.

2 Geometrical acceptance and mean acceptance

Let us call $j(\theta, \phi)$ the flux of particles that exist in a given region of space such that the number of particles $dn(\theta, \phi)$ arriving at a particular planar surface S inside a solid angle cone of size $d\omega$ at a given time[9] is given by:

$$dn(\theta, \phi) = j(\theta, \phi) \,.\cos\theta\, .S\,.d\omega \qquad (1)$$

A surface S could be a particle detector's surface, a telescope's surface, or any other planar surface inside a detector setup. Defined in that way, the dimensions of the flux are $[j(\theta, \phi)] = L^{-2}\,.sr^{-1}$. The definitions of the main variables are shown in Figure 1.

The total number N of particles traversing the surface S coming from the upper hemisphere, defined in this way, is:

[9] This definition can also be done per unit of time, energy, or any other measurable variable.

USC UNIVERSIDADE DE SANTIAGO DE COMPOSTELA

$$N = \int_{\theta=0}^{\pi/2} \int_{\phi=0}^{2\pi} j(\theta,\phi)\ .\ \cos\theta\ .\ S\ .\ d\omega$$

$$= \frac{1}{2} \int_{\theta=0}^{\pi/2} \int_{\phi=0}^{2\pi} j(\theta,\phi)\ .\ S\ .\ d(\cos^2\theta)\ .\ d\phi \qquad (2)$$

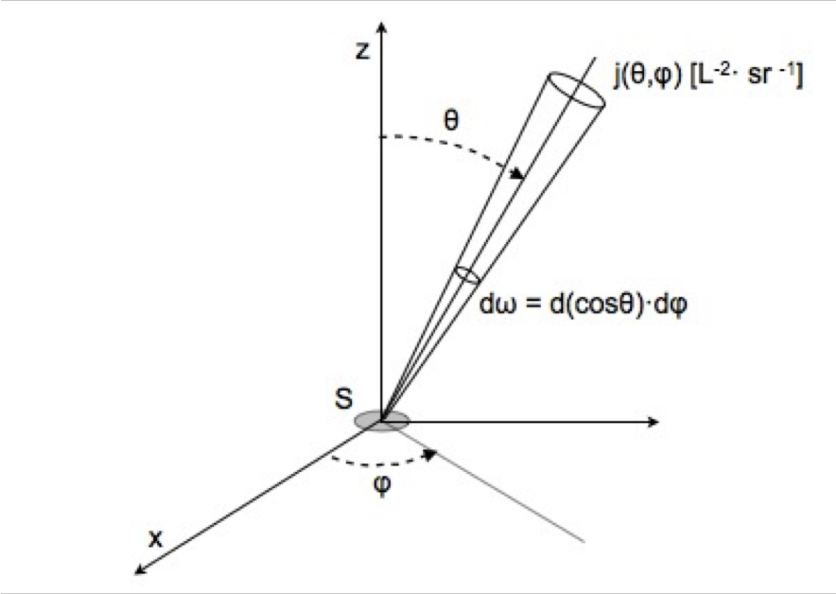

Figure 1: Definition of the main variables.

If the arriving particle distribution is uniform, $j(\theta,\phi) = j_0$, then we can write:

$$N = \frac{1}{2}\ .\ j_0\ .\ S\ .\int_{\theta=0}^{\pi/2} \int_{\phi=0}^{2\pi} d(\cos^2\theta)\ .\ d\phi$$

$$N = j_0\ .S\ .\pi \qquad (3)$$

USC UNIVERSIDADE DE SANTIAGO DE COMPOSTELA

The previous equations are no longer applicable if the detector is not perfect and does not detect all the particles arriving the surface S. A particle impinging on a detector may not be measured for various reasons. One reason could be that the particle collides with a dead region where the detector is not active for whatever reason (there is a frame or an empty region). Another reason could be that, despite hitting an active region, the detector lacks sensitivity in some regions or that the probability of detecting a particle varies depending on the particle's type, energy, or other variables. Figure 2 shows an example corresponding to a detector with strip readout where the detection regions have maximum and minimum efficiency at the high-efficiency and low-efficiency areas, respectively. The figure also illustrates the active and dead zones.

In Equation (1), we can include all the read-out effects as follows:

$$dm(\theta,\phi) = \alpha(\theta,\phi)\,.\,\epsilon(\theta,\phi)\,.\,dn(\theta,\phi)$$

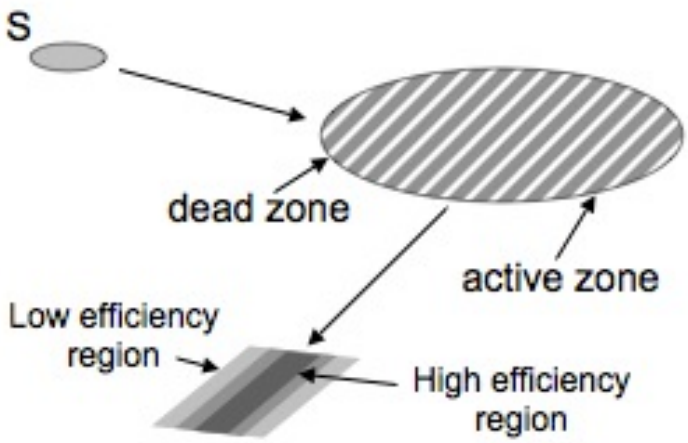

Figure 2: A strip detector with geometrical and read-out effects.

$$dm(\theta,\phi) = \alpha(\theta,\phi)\,.\,\epsilon(\theta,\phi)\,.\,j(\theta,\phi)\,.\cos\theta\;.S\,.\,d\omega \qquad (4)$$

USC UNIVERSIDADE DE SANTIAGO DE COMPOSTELA

where $m(\theta, \phi)$ denotes the number of particles detected by the detector, $\alpha(\theta, \phi)$, or *geometric acceptance*, represents the probability that a particle passes through the detector's active region, and $\epsilon(\theta, \phi)$, or *intrinsic efficiency*, refers the probability that such a particle is measured by the detector[10].

The concept of geometric acceptance is commonly extended to encompass other inefficiencies or any other effect dependent on the arrival direction and prevents correct particle measurement.

Mean acceptance, or simply *acceptance* is the average value of geometric acceptance integrated overall with the arrival directions. This concept can also include any other variable or circumstance that affects the overall number of events measured by the detector (as the dead time of the detector, inefficiency in the data acquisition (DAQ), etc..).

If m is the total number of particles recorded from N arriving particles, the acceptance α[11] can be defined as follows:

$$n = \alpha \, . N \tag{5}$$

Equation (4) can be used to estimate any of the magnitudes once the other magnitudes are well known. Because gathering sufficient data to estimate them is not always possible, alternative methods should be employed. In most cases, the geometric acceptance can be estimated using simulation or Monte Carlo (MC) techniques or approximating it with a simple formula in more intricate experimental setups. On the other hand, the intrinsic efficiency can be calculated in various ways: as a constant using the mean value, individually using a dedicated experiment, or parameterized using existing knowledge of the detector's behavior.

[10] Other particle features, such as type, energy, charge, and so on, may influence the efficiency.
[11] Acceptance can also be defined as a function of one or more variables, or in a specific solid angle region, over a particular energy range for a given type of particle.

USC UNIVERSIDADE DE SANTIAGO DE COMPOSTELA

It is possible to integrate $\epsilon(\theta, \phi)$ in the geometrical acceptance $\alpha(\theta, \phi)$ and work with only one magnitude for simplicity. Then we may express Equation (4) as follows:

$$dm(\theta, \phi) = \alpha(\theta, \phi) \, . j(\theta, \phi) \, . \cos\theta \, . S \, . d\omega \tag{6}$$

The geometrical acceptance now takes the form:

$$\alpha(\theta, \phi) = \frac{1}{j(\theta, \phi) \, . \cos\theta \, . S} \frac{dm(\theta, \phi)}{d\omega} \tag{7}$$

Equation (6) is integrated over all relevant variables in a solid angle Ω:

$$m = \alpha \, . \int_{\Omega} j(\theta, \phi) \, . \cos\theta \, . S \, . d\omega$$
$$= \alpha \, . N \tag{8}$$

where N is the integrated flux over the detector surface, note that particle fluxes with varying angular distributions $j(\theta, \phi)$ can result in different relationships between the total number of particles N and the number of measured particles m. The detector's acceptance is then a function of the particle distribution that arrives at it.

The geometric acceptability of a detector can be analyzed in the following manner. First, we generate a sample of N_0 events in the upper hemisphere[12] with a random uniform distribution of angles (θ, ϕ). Then, at different intervals $(\Delta\theta, \Delta\phi)$, we count the number m_0 of particles that have been detected based on the detector's geometry and characteristics. As a result, we get an estimate of the function:

[12] A uniform distribution sample of angles $\{\theta_i, \phi_i\}$ can be created by generating a sample of pairs of random numbers $\{r_i, s_i\}$ having a uniform distribution in $(0, 1)$ and defining: $\cos\theta_i = r_i$ and $\phi_i = 2\pi . s_i$.

USC UNIVERSIDADE DE SANTIAGO DE COMPOSTELA

$$m_0(\theta,\phi) = \alpha(\theta,\phi)\,.\,j_0\,.\cos\theta\,.\,S \tag{9}$$

with the condition of integration:

$$j_0 = \frac{1}{\pi}\,.\frac{N_0}{S} \tag{10}$$

If we define the following:

$$\begin{aligned}\rho_0(\theta,\phi) &= \frac{m_0(\theta,\phi)}{N_0} \\ &= \frac{1}{\pi}\,.\alpha(\theta,\phi)\,.\cos\theta\end{aligned} \tag{11}$$

The probability that a particle arriving at the detector with an angle (θ,ϕ) is measured by the detector[13] is given by $\rho_0(\theta,\phi)$.

The flux $j(\theta,\phi)$ of the arriving particles is sometimes unknown. The problem is determining it as accurately as feasible, for example, when measuring cosmic ray arrival distributions and their evolution over time. As previously indicated, this problem can be solved utilizing a set of experimental data $\{m(\theta,\phi)\}$ measured by the detector and estimating the geometrical acceptance.

Using the right-hand terms of Equation (11) and starting with Equation (4), we get:

$$m(\theta,\phi) = \frac{\pi\,.\,m_0(\theta,\phi)}{N_0}\,.j_0(\theta,\phi)\,.S \tag{12}$$

[13] It is obvious that if both efficiencies, α and ϵ, are identical to one, $\rho_0(\theta,\phi)$ is normalized and behaves like a good probability distribution.

USC UNIVERSIDADE DE SANTIAGO DE COMPOSTELA

Solving this equation, we get:

$$j(\theta,\phi) = \frac{N_0}{\pi \,.\, S} \,.\frac{m(\theta,\phi)}{m_0(\theta,\phi)} \tag{13}$$

To summarize, using the measured distribution of events $m(\theta,\phi)$ and the estimated distribution $m_0(\theta,\phi)$ of a sample of N_0 particles generated using a random uniform distribution, we may obtain the flux distribution $j(\theta,\phi)$ of a set of particles arriving at a detector.

We can also use Equation (11) to write:

$$j(\theta,\phi) = \frac{1}{\pi \,.\, S} \,.\frac{m(\theta,\phi)}{\rho(\theta,\phi)} \tag{14}$$

3 Dead time corrections

The definition given by Equation (1) can be generalized to include the time dt and an energy interval ΔE around given energy E or any other relevant variable as follows:

$$dn(\theta,\phi,E,t) = \, j(\theta,\phi,E,t) \,.\cos\theta \,.S \,.d\omega \,.dt \,.\Delta E \tag{15}$$

Other variables, such as dead time, can influence the number of particles measured by a detector during a given period of time. Because the detector or the readout system is busy after recording a previous event, some particles are lost due to this effect. The average ratio of dead time to total time is known as relative dead time.

Suppose we refer τ to the relative dead time of a given configuration. In that case, the total number of events recorded over a specific time period, integrated over all other variables, can be expressed as:

$$m_t = (1-\tau) \,.m \tag{16}$$

USC UNIVERSIDADE DE SANTIAGO DE COMPOSTELA

The acceptance is sometimes defined using the distribution of detected particles as a function of incoming angles and other relevant variables. Then, we can write the measured distribution of events as follows:

$$m(\theta,\phi) = \alpha(\theta,\phi)\,.\,\epsilon(\theta,\phi)\,.\,j(\theta,\phi)\,.\cos\theta\;.S \tag{17}$$

Considering the following:

$$j(\theta,\phi) = \rho(\theta,\phi)\,.N \tag{18}$$

as well as the *geometric acceptance* being defined as:

$$\alpha_g = \int_{\theta,\phi} \alpha(\theta,\phi)\,.\;\epsilon(\theta,\phi)\,.\;\rho(\theta,\phi)\,.\;\cos\theta\;.\;S\,.\;d\omega \tag{19}$$

after integrating into all the variables, we arrive at:

$$m = \alpha_g\,.N \tag{20}$$

In this way, knowing the geometrical acceptance, the total number of recorded events m directly provides the total number of events N.

USC
UNIVERSIDADE DE SANTIAGO DE COMPOSTELA

USC
UNIVERSIDADE
DE SANTIAGO
DE COMPOSTELA

Cosmic rays (CR) are high-energy atomic nuclei and other subatomic particles coming from outer space. After they travel through interstellar space, they collide with the Earth's atmosphere, producing up to billions of secondary particles, the so-called secondary cosmic rays. The main objective of this work is the comparative analysis of the cosmic rays measured in different locations by the two operative Trasgo-like detectors, TRISTAN and TRAGALDABAS, and make the first data commissioning for the newest STRATOS detector. For the intended study, all the calibration and correction tools necessary to obtain absolute rates and those for the study of correlations and joint analysis with detectors were developed and fine-tuned.